November 24, 2013 FERMILAB-CONF-06-284-T

Tevatron-for-LHC Report: Preparations for Discoveries

Salavat Abdullin[1], Darin Acosta[2], Shoji Asai[3], Oleksiy Atramentov[4,5], Howard Baer[5], Csaba Balazs[10], Paolo Bartalini[2], Alexander Belyaev[16], Ralf Bernhard[8], Andreas Birkedal[19], Volker Buescher[6 ¶], Richard Cavanaugh[2], Marcela Carena[1 †], Mu-Chun Chen[1], Christophe Clément[11], AseshKrishna Datta[9], Ytsen R. de Boer[12], Albert De Roeck[13], Bogdan A. Dobrescu[1 ¶], Alexey Drozdetskiy[2], Yuri Gershtein[5], Doug Glenzinski[1], Craig Group[2], Sven Heinemeyer[30], Michael Heldmann[6], Jay Hubisz[1], Martin Karlsson[14], Kyoungchul Kong[2], Andrey Korytov[2], Sabine Kraml[13], Tadas Krupovnickas[15], Remi Lafaye[13], Kenneth Lane[7], Fabienne Ledroit[17], Frank Lehner[8], Cheng-Ju Lin[1], Cosmin Macesanu[18], Konstantin T. Matchev[2], Arjun Menon[10,29], David Milstead[11], Guenakh Mitselmakher[2], Julien Morel[17], David Morrissey[20], Steve Mrenna[1 †], Jorge O'Farrill[5], Yuriy Pakhotin[2], Maxim Perelstein[21], Tilman Plehn[22], David Rainwater[23 ¶], Are Raklev[13,24], Michael Schmitt[25 ¶], Bobby Scurlock[2], Alexander Sherstnev[26], Peter Skands[1], Zack Sullivan[10], Tim M.P. Tait[10], Xerxes Tata[27], Ingo Torchiani[6], Benjamin Trocmé[17], Carlos Wagner[10,29], Georg Weiglein[31], Dirk Zerwas[28]

[1] *Fermilab*
[2] *University of Florida*
[3] *University of Tokyo*
[4] *Iowa State University*
[5] *Florida State University*
[6] *Universität Freiburg*
[7] *Boston University*
[8] *University of Zürich*
[9] *Harish-Chandra Research Institute*
[10] *Argonne National Lab.*
[11] *Stockholm University*
[12] *ITEP Moscow/Univ. of Twente*
[13] *CERN*
[14] *Lund University*
[15] *Brookhaven National Laboratory*
[16] *Michigan State University*
[17] *LPSC, Grenoble*
[18] *Syracuse University*
[19] *Univ. of California, Santa Cruz*
[20] *University of Michigan*
[21] *Cornell University*
[22] *MPI Munich*
[23] *University of Rochester*
[24] *University of Bergen*
[25] *Northwestern University*
[26] *Moscow State University*
[27] *University of Hawaii*
[28] *Université de Paris-Sud*
[29] *University of Chicago*
[30] *IFCA, Spain*
[31] *IPPP, Univ. of Durham*

Abstract

This is the "TeV4LHC" report of the "Physics Landscapes" Working Group, focused on facilitating the start-up of physics explorations at the LHC by using the experience gained at the Tevatron. We present experimental and theoretical results that can be employed to probe various scenarios for physics beyond the Standard Model.

¶ Convenors of the Physics Landscapes working group
† Organizers of the TeV4LHC Workshop

Contents

1 Introduction and Overview

The direct exploration of the energy frontier currently performed by the D0 and CDF experiments using $p\bar{p}$ collisions at $\sqrt{s} = 2$ TeV provided by the Tevatron is possible as a result of a long process of development involving many people. The existing sets of data, of over 1.5 fb^{-1} each, already contain information that will advance the understanding of the basic laws of physics. Within the next three years, many new aspects of physics beyond the Standard Model will be probed with four-times-larger data sets.

The capability of exploring the energy frontier will make a huge leap forward with the ATLAS and CMS experiments using pp collisions at $\sqrt{s} = 14$ TeV at the LHC, planned to start operating in 2008, only two years from now. This is a daunting endeavor, behooving the whole community of high-energy physicists to prepare.

The purpose of the TeV4LHC series of workshops, held at Fermilab, Brookhaven and CERN since 2004, is to facilitate the start-up of the physics explorations at the LHC by using experience built up at the Tevatron. This report describes the activities of the Physics Landscapes working group, focused on physics beyond the Standard Model. Three other TeV4LHC working groups, dealing with Higgs, QCD and electroweak/top physics, will summarize their activities in separate reports.

There are various experimental issues at the LHC that can be addressed using experience gained at the Tevatron. Furthermore, there are solutions to analysis problems for searches at CDF and D0 that can be transferred to CMS and ATLAS. In particular, many of the tools developed to facilitate Tevatron searches for new particles may be used at the LHC.

One should keep in mind though that the LHC is not a scaled-up Tevatron. Its pp collisions, as opposed to $p\bar{p}$ at the Tevatron, change the nature of the underlying processes. In fact, in certain cases there is a complementarity between the machines. For example, if a Z' boson exists such that a resonance will be discovered at the Tevatron in the dilepton invariant mass distribution, only a certain combination of Z' couplings to quarks may be measured. Observation of the same resonance at the LHC would provide a measurement of a different combination of Z' couplings to quarks. Putting together the two measurements would then allow the determination of the Z' couplings to up and down quarks separately.

In addition, it should be emphasized that the LHC environment will be much more challenging, with huge backgrounds and more stringent triggers. There are possible scenarios for physics beyond the Standard Model in which the Tevatron has a better capability than the LHC to discover certain new particles. For example, a weakly-coupled s-channel resonance that decays predominantly to b jets could be observable at the Tevatron if it is light enough, but may be too hard to distinguish from background at the LHC. Nevertheless, the much higher center-of-mass energy of the LHC leads to a truly impressive discovery potential. This report is intended to be a small step toward optimizing that potential.

A generic hurdle in assesing and optimizing the discovery potential of the LHC, as well as of

the Tevatron, is that it is impossible to reliably predict how physics looks at the TeV scale. Progress in theoretical high-energy physics has shown that the range of possibilities for physics at the TeV scale is much broader than was contemplated a decade ago. The only robust piece of information comes from the computation of the amplitude for longitudinal WW scattering [1], which shows that perturbative unitarity is violated unless certain new particles exist at the TeV scale. More concretely, at least one of the following statements must be true:

i) There is a Higgs boson with mass below about 700 GeV. This possibility is analyzed in the TeV4LHC report of the Higgs working group.

ii) There is no Higgs boson, but instead there are several spin-1 particles that couple to WW. These may be strongly coupled, as in the case of Technicolor (see Section 4.6), or weakly coupled, as in the case of the so-called Higgsless models (see Sec. 3.2). Note that unlike theories that are extensions of the Standard Model, which reduce to the Standard Model in some decoupling limit, the absence of the Higgs boson would imply that the electroweak symmetry breaking sector of the Standard Model is not realized in nature.

iii) Our current ability to compute cross sections breaks down at the TeV scale, either because of the complicated nature of some strongly-coupled field theory, or because quantum field theory is no longer a good description of nature at that scale. Evidently, either case would imply a most intriguing development for physics. Given that further progress in this direction would likely be data-driven, we will not discuss this possibility further.

Beyond the problem of unitarity in longitudinal WW scattering, there is little to guide us regarding what the ATLAS and CMS might observe. There are many well-motivated models that predict new particles which may be tested at the LHC, and it would be useful to analyze as many of them as possible in order to make sure that the triggers are well-chosen and that the physics analyses cover sufficient ground. Fortunately, ATLAS and CMS are multi-purpose discovery instruments, able to measure many different parameters in large classes of models. Moreover, any observation at CDF or D0 of physics beyond the Standard Model, as well as tighter limits on parameters in extensions of the Standard Model, would help the LHC experiments to focus on signatures likely to disentangle the correct description of nature at the TeV scale.

The next three Sections collect several self-contained contributions from individual authors. Each of these three sections starts with an introduction describing the connections between various contributions. Section 2 is focused on experimental aspects, such as the identification of simple and compound objects. Sec. 3 deals with experimental signatures associated with the cases where a single new particle will be accessible in the beginning at the LHC or Tevatron. Although this might sound like a simplistic scenario, it is realized in large regions of parameter space of many interesting models. Sec. 4 covers the more complicated cases of models where several new particles will be revealed at once. An important question tackled there is how to differentiate between models that lead to similar collider signatures, even though they have completely different origins. A classic example is pair production of heavy colored particles followed by cascade decays, which

occurs in supersymmetric models with R-parity, in models with universal extra dimensions, and in little Higgs models with T-parity. We conclude the report, in Section 5, with a brief summary of some of the striking results presented in Secs. 2, 3 and 4.

2 Experimental Aspects

After collecting an integrated luminosity of more than 1 fb^{-1}, searches at both Tevatron experiments CDF and DØ currently explore new territory beyond existing limits. At peak luminosities that are now reaching 2×10^{32} $cm^{-2}s^{-1}$, this requires the detectors, trigger systems and reconstruction algorithms to handle events at high rates and with high occupancy. With beam crossings producing up to $O(10)$ simultanuous interactions, these challenges are quite similar to what the ATLAS and CMS experiments will face at the LHC.

A lot of the knowledge and experience gained at Run II of the Tevatron can therefore serve as a basis for a quick startup of searches at the LHC. In this chapter, a number of examples with relevance to searches analyses are discussed to show how experimental techniques developed and refined at the Tevatron can be transferred to the LHC. This includes the reconstruction of leptons, jets and event quantities in a busy hadronic environment, the separation of new physics from huge jet backgrounds, and the modelling of backgrounds using data-driven methods.

Sections 2.1 through 2.4 discuss aspects of the reconstruction and identification of electrons, photons, muons, tau-leptons as well as jets and missing transverse energy. The discovery of any of the signals discussed in chapters 3 and 4 relies on the capability to reconstruct these objects efficiently. In addition it is crucial to model their efficiency and background correctly, which is a non-trivial challenge in the complex hadron-collider environment. Techniques for measuring efficiencies and energy scales of electrons, photons and muons are presented in sections 2.1 and 2.2. Sec. 2.3.1 shows how Tevatron data can be used to predict background rates to tau lepton reconstruction at the LHC. The modelling of jets and missing transverse energy is discussed in Section 2.4. In particular for jets, the Tevatron experiments play an important role in testing new generators that will be essential to model background from jet radiation at the LHC.

Finally, in the last section an example of an indirect search for new physics is summarized in full detail, including a discussion of the provisions necessary to trigger on the signal and study the various background processes.

2.1 Electron and Photon Reconstruction and Identification

Yuri Gershtein[1], Oleksiy Atramentov[2]

[1] *Florida State University*
[2] *Iowa State University*

2.1.1 Overview

Photon reconstruction at the Tevatron starts with finding clusters of energy in the electromagnetic calorimeter. For electrons, in addition to the calorimeter-seeded algorithms, a track-seeded algorithm exists, although it is used primarily for reconstruction of non-isolated electrons. For both reconstruction algorithms, however, the idea behind it is similar.

The main background to electrons and photons comes from jets. Also, a photon can be misidentified as an electron and vice versa. For example, $W\gamma$ events form a major background to multi-lepton SUSY searches when the W decays semi-leptonically and the photon undergoes convertion in the tracker [2], and to di-photon SUSY searches when the W decays into an electron and its track is not reconstructed [3]. For CDF's study on the exact composition of the electron fakes see Ref. [4].

Silicon trackers have revolutionized heavy flavor tagging at hadron colliders. However, the price one must pay for being able to tag heavy flavors is the large amount of material that electrons and photons must transverse before reaching the calorimeter. This introduces a significant problem for the Tevatron detectors, and will be an even bigger problem at the LHC, since both CMS and ATLAS detectors have much more material in the tracker (up to ~ 1.6 radiation lengths). We will discuss this in more detail in Sec. 2.1.2.

Having more than one radiation length of material in front of the calorimeter is already challenging, but experience at the Tevatron shows that the amount of material included in the Monte-Carlo (MC) simulation of the detector is significantly smaller than it is in reality. This and other effects lead to a substantial disagreement between the data and the MC at start-up.

In situ measurement of the material distribution and tuning of MC parameters is a long and elaborate process. However, analyses of the first data cannot wait for a perfect MC. It is therefore of utmost importance to develop algorithms to extract everything needed for the analyses (reconstruction and identification efficiency, energy scale and resolution, *etc*...) from the data itself. A lot of experience in this has been accumulated for electrons coming from Z, J/ψ, and Υ decays. Photons, on the other hand, present more of a challenge, since there is no clean and abundant resonant production of isolated photons at the Tevatron. One of the achievements of this series of workshops is the realization that at the LHC the $\mu\mu\gamma$ final state provides such a source. These issues are discussed in Sec. 2.1.3

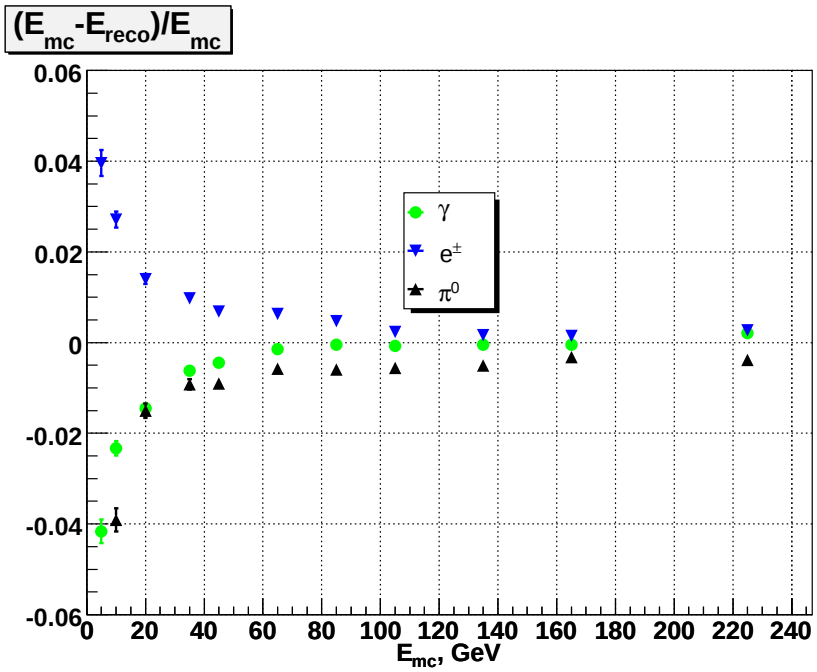

Fig. 2.1.1: Simulation of the linearity of the response of DØ detector to single electrons, photons, and neutral pions.

2.1.2 Effects of the Tracker Material

The large (up to 1.6 radiation lengths) amount of the material in front of the ECAL has a significant negative effect on reconstruction of electrons and photons. Electrons lose their energy by bremsstrahlung in material while curving in the magnetic field, which turns usually narrow EM showers into azimuthally wide sprays. This leads to a certain energy loss due to imperfect clustering. Even more important is the fact that the bremsstrahlung photons convert, and the resultant electrons curl in the magnetic field and do not reach the calorimeter. The combination of these two effects results in a non-linear energy scale for electrons that depends on the material distribution in front of the ECAL, and therefore on rapidity and (to a lesser extent) azimuth.

Photons, as opposed to electrons, propagate in the material in a different way. They stay totally intact until the first conversion. Therefore, for unconverted photons the material-induced non-linearity is not an issue. However, when a photon converts, its energy is shared between two electrons and the effect of the material is effectively doubled. As a result, the electron and photon energy scales are different and non-linear (see Fig. 2.1.1 for simulation of the DØ detector response).

2.1.3 Extraction of Efficiency and Energy Scale from Data

The experience of previous experiments, including the most recent from CDF and DØ at the Tevatron, is such that the amount of material included in the GEANT description of the detector is

severely underestimated by start-up time. First, the as-built detector is not the same as the as-drafted. Second, because the tracking system is complex and comprises so many elements, some of them end up inadequately implemented in the MC. The magnitude of the disagreement can be as large as a factor of two. For CDF, for example, in which three silicon detectors were build during Runs I and II, the amount of unaccounted material in the MC implementation of the last one at the start-up was only about 50% of the actual amount.

The above consideration makes it too risky to rely solely on the MC simulation for a proper description of electrons and photons in first analyses at the LHC. The plan for start-up should therefore be two-pronged:

A. Measure the amount of material in the tracker *in situ* using a combination of several methods (converted photon yields and distributions, mass of low-lying resonances and measurement of transverse momentum variation from the beginning to the end of electron tracks). The end result of this activity would be a MC simulation that describes the real detector.

B. In parallel to the work described in **A**, efficiencies, resolutions, and energy scales of electrons and photons should be measured for different detector regions and for different ID cuts.

The Tevatron experiments followed this strategy, using Z, Υ, and J/ϕ decays to calibrate electrons. At the LHC, both the center of mass energy and luminosity are high enough to provide a source of clean and isolated photons from radiative Z decays. A study using the detailed simulation of CMS detector showed [5] that using simple kinematic cuts on dilepton mass ($40 < m_{\mu\mu} < 80$ GeV) and photon-lepton separation ($\sqrt{\Delta\phi^2_{\mu\gamma} + \Delta\eta^2_{\mu\gamma}} < 0.8$) a reasonable signal-to-background ratio can be achieved (see Fig. 2.1.2).

When extracting detector performance from data, one should be wary of possible biases. For example, DØ measures the electron identification efficiency in $Z \to e^+e^-$ events using the "tag-and-probe" method. In this method one of the electrons is required to pass stringent identification criteria to improve purity of the sample while the other – the probe – is used to measure the efficiency. Here, the biases arise from correlations between the tag and the probe electrons. For example, in the early stages of electron identification, the efficiency turned out to be dependent on the primary vertex position, and since the selection of the tag biased the vertex distribution, the electron identification efficiency, obtained from the probe, was found to be shifted toward higher values. Although the full DØ MC simulation did not reproduce the effect exactly, it was enough to suggest a corrective action, i.e. it was chosen for the short term to parametrize efficiency as a function of both rapidity and vertex position while developing a new version of electron identification that did not have such a strong vertex dependence.

For energy scale measurements, the biases can arise from both instrumental and physics effects. As an example, let us consider photon energy scale measurement with $Z \to \mu\mu\gamma$ events. The instrumental effect comes from the photon energy resolution. The photon E_T spectrum in radiative Z decays falls sharply. Therefore, a sample of $\mu\mu\gamma$ events with large photon E_T will be enriched by events where the photon energy has been mis-measured, and the Z peak would shift

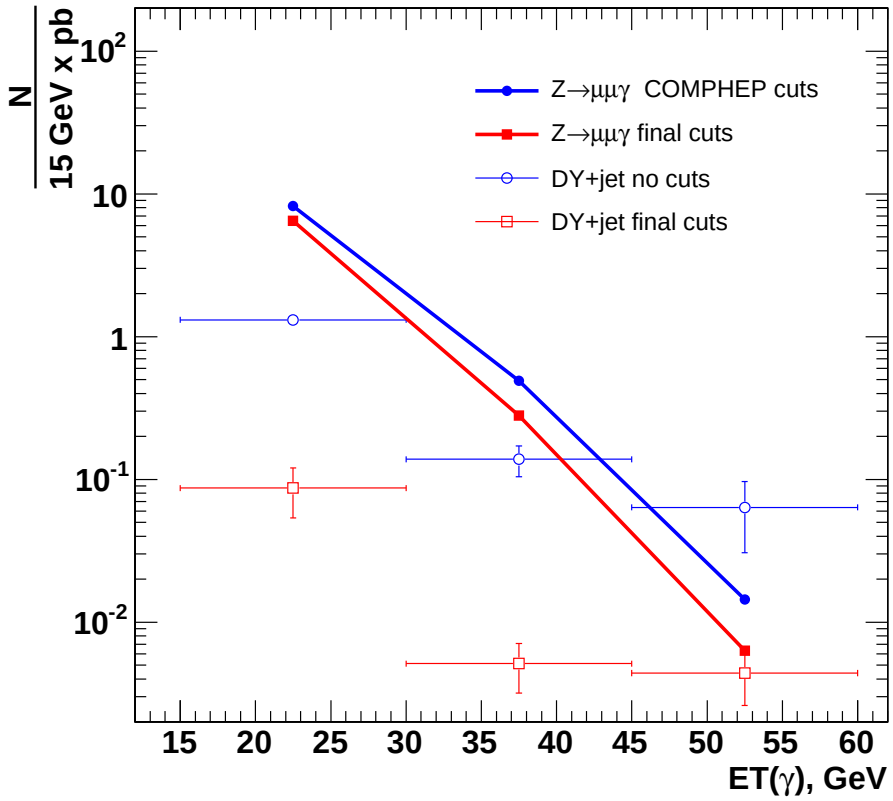

Fig. 2.1.2: Radiative Z decay signal and background yields before and after the cuts on event kinematics.

toward larger masses. The second effect arises from the large natural width of the Z. The importance of both effects can be estimated using a simple parametrized MC simulation (see Fig. 2.1.3). We fit the three body mass distribution in bins of photon transverse energy, first using generator level information (black points), and then smearing the generator information by the best energy resolution that one might expect at the LHC detector [6] (blue points). The red points correspond to the case in which we add an extra 2% constant term to the resolution function. The fitted values of the Z mass can be shifted by almost 0.4 GeV, which corresponds to a photon energy scale shift of 2%.

[6] $\frac{\sigma_E}{E} = \frac{0.027}{\sqrt{E}} \oplus \frac{0.155}{E} \oplus 0.0055$

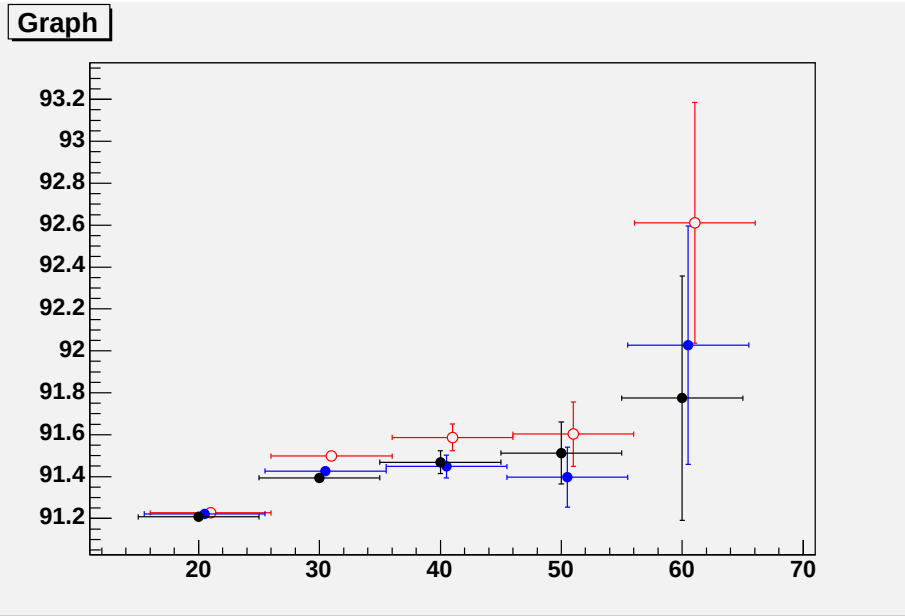

Fig. 2.1.3: Fitted value of the Z mass v. the photon E_T in GeV. See text for details.

2.2 Sensitivity of the Muon Isolation Cut Effic. to the Underlying Event Uncertainties

S. Abdullin[1], D. Acosta[2], P. Bartalini[2], R. Cavanaugh[2], A. Drozdetskiy[2], A. Korytov[2], G. Mitselmakher[2], Yu. Pakhotin[2], B. Scurlock[2], A. Sherstnev[3]

[1] *Fermi National Laboratory, Batavia, Illinois, USA*
[2] *University of Florida, Gainesville, Florida, USA*
[3] *Moscow State University, Moscow, Russia*

Uncertainties in predicting the muon isolation cut efficiency are studied by varying the PYTHIA parameters responsible for simulation of the underlying event. Study is performed on the example of the Standard Model Higgs search. The following processes are considered: $H \to ZZ \to 4\mu$, $\mathrm{ZZ} \to 4\mu$, *and* $t\bar{t} \to 4\mu + X$. *We show that an inclusive Z data sample will allow for a direct experimental measurement of the 4-muon isolation cut efficiencies associated with* $H \to ZZ \to 4\mu$ *and* $ZZ \to 4\mu$ *events with a systematic uncertainty of less than 2%.*

2.2.1 Introduction

In future searches for the Higgs boson at the LHC via its 4-muon decay channel, $H \to ZZ \to 4\mu$, the muon isolation cut plays a key role in suppressing many otherwise dominating backgrounds where all or some muons originate from hadronic decays ($\mathrm{t\bar{t}}$ and $\mathrm{Zb\bar{b}}$ are the most important processes in this category). Having reduced the $\mathrm{t\bar{t}}$ and $\mathrm{Zb\bar{b}}$ backgrounds to a negligible level, we also suppressing the ZZ background and signal. Therefore, one must worry about the efficiency of the muon isolation cut with respect to the ZZ background and Higgs boson signal and, even more, about the sensitivity of this efficiency to large theoretical uncertainties associated with a poor understanding of the underlying event (UE) physics. The UE is defined as [6] all the remnant activity from the same proton-proton interaction.

The goal of the studies presented here was not to optimize the muon isolation cut in order to maximize the signal-over-background significance, but rather to understand how well can we predict the isolation cut efficiency using the current Monte Carlo generators, and to develop a method of measuring the isolation cut efficiency using the experimental data themselves. The proposed technique of evaluating the isolation cut efficiency for ZZ events is based on sampling energy flow in cones of random directions in inclusive $\mathrm{Z} \to 2\mu$ data sample. At Tevatron, Z-boson di-muon data samples and random/complimentary cones are widely used for various calibration purposes, which was an original inspiration for us in developing the method we present further below. In these generator-level studies, we looked only at the tracker-based isolation cut.

The analysis presented in this subsection is done in accordance with official guidelines described in [6] for UE for a particular Monte Carlo generator with a particular set of model parameters. Only effects of the first order influencing UE in this model are considered.

2.2.2 Event Generation Parameters for PYTHIA

Higgs boson, $\mathrm{t\bar{t}}$ and Z-inclusive data samples were generated with PYTHIA 6.223 [7]. The ZZ data sample was generated at the matrix-element level with CompHEP [8] and, then, PYTHIA was used to complete the event simulation (parton shower development, UE, hadronization, and particle decays). The PYTHIA parameters that drive the UE simulation were consistently chosen to match those selected for the Data Challenge 2005 (DC05) CMS official production (see Table 2.2.2). Detailed discussion of the associated phenomenology and the corresponding references can be found elsewhere [6].

parameter	CDF	ATLAS	CMS (DC04)	CMS (DC05)	comment
PARP(82)	2	1.8	1.9	2.9	regularization scale of PT spectrum for MI
PARP(84)	0.4	0.5	0.4	0.4	parameter of matter distribution inside hadrons
PARP(85)	0.9	0.33	0.33	0.33	probability in MI for two gluons with color connections
PARP(86)	0.95	0.66	0.66	0.66	probability in MI for two gluons (as a closed loop)
PARP(89)	1800	1000	1000	14000	reference energy scale
PARP(90)	0.25	0.16	0.16	0.16	power of the energy-rescaling term
$\mathrm{pt}_{\text{cut-off}}$	3.34	2.75	2.90	2.90	final $\mathrm{pt}_{\text{cut-off}}$

Table 2.2.1: Parameters in PYTHIA for multi-parton interactions (MI) and UE for CDF, ATLAS and CMS.

The most critical parameter affecting the UE activity is $\mathrm{pt}_{\text{cut-off}}$, the lowest PT allowed for multi-parton interactions. The smaller $\mathrm{pt}_{\text{cut-off}}$ is, the larger is the number of tracks associated with the underlying event. The $\mathrm{pt}_{\text{cut-off}}$ value and its evolution with the center of mass energy of proton-proton collisions are defined via the following formula:

$$\mathrm{pt}_{\text{cut-off}} = \mathrm{PARP}(82) * (14000/\mathrm{PARP}(89))^{\mathrm{PARP}(90)}$$

The three parameters, PARP(82,89,90), have meaning only in this combination. The parameters PARP(89) and PARP(90) are fixed at 14,000 and 0.16, correspondingly. We decided to vary $\mathrm{pt}_{\text{cut-off}}$ by $\pm 3\sigma$, or $\pm 0.5\ \mathrm{GeV}$, which seems to be a sensible estimation of theoretical uncertainties arising from UE modeling [9]. Note that $\mathrm{pt}_{\text{cut-off}} = 3.34\ \mathrm{GeV}$, as extracted from CDF's Tune A of PYTHIA MI parameters, differs from the default values used by ATLAS ($2.75\ \mathrm{GeV}$) and CMS ($2.9\ \mathrm{GeV}$) by $\sim 0.5\ \mathrm{GeV}$ because it was done using a different PYTHIA parameter tuning model and is listed for completeness only in Table 2.2.2.

2.2.3 Monte Carlo sample production

Processes used in these studies were: $\mathrm{t\bar{t}}$ (PYTHIA parameter MSEL = 6); Higgs boson signal ($\mathrm{m_H} = 150$ GeV, PYTHIA parameters MSEL = 0, MSUB(102,123,124) = 1 with H allowed to decay to $\mathrm{Z}/\gamma*$ only, $\mathrm{Z}/\gamma*$ allowed to decay to $\mathrm{e}/\mu/\tau$ pair only and τ allowed to decay to e/μ only); ZZ (PYTHIA parameters MSEL = 0, MSUB(1) = 22 with $\mathrm{Z}/\gamma*$ allowed to decay to $\mathrm{e}/\mu/\tau$ pair only and τ allowed to decay to e/μ only); Z-inclusive (PYTHIA parameters MSEL = 0, MSUB(1) = 1 with Z allowed to decay to muon pair only). For Higgs boson signal, we used PHOTOS as a generator of bremsstrahlung photons.

Generator-level cuts:

- $\mathrm{t\bar{t}}$: at least four muons with $\mathrm{PT} > 7\ \mathrm{GeV}$ and $|\eta| < 2.4$;
- Higgs boson signal: at least four muons with $\mathrm{PT} > 7\,\mathrm{GeV}$ and $|\eta| < 2.4$; $5 < \mathrm{M_{inv}}(\mu^+\mu^-) < 150\ \mathrm{GeV}$ for 2 intermediate resonances ($\mathrm{Z}/\gamma*$);
- ZZ-sample: same as for signal;
- Z-inclusive: no user defined cuts.

2.2.4 Event selection

Event-selection cuts were further imposed on the produced Monte Carlo samples. These cuts were chosen to mimic those optimized for the future data analysis. There are two distinct sets of such cuts.

First, only "good muons" were selected. A muon was considered to be "good" if it had $\mathrm{PT} > 7$ GeV in the barrel region ($|\eta| < 1.1$) or $\mathrm{P} > 9$ GeV in the endcaps ($1.1 < |\eta| < 2.4$). This ensures that the muon reconstruction efficiencies are at their plateau, which helps minimize systematic uncertainties on the muon reconstruction efficiency.

Then, event-selection cuts similar to the full analysis cuts were applied. They are:

- At least 2 opposite sign muon pairs with invariant masses for all $\mu^+\mu^-$ pair permutations being greater than 12 GeV (this cut suppresses heavy-quark resonances).
- PT of all four selected muons must be greater than 10 GeV (signal-over-background optimization).
- invariant mass of the four muons must be greater than 110 GeV and less than 700 GeV (Higgs boson with $\mathrm{M} < 114.4\,\mathrm{GeV}$ is excluded at LEP, Higgs boson with mass over 700 GeV is strongly disfavored by theory and, also, would have too low a production cross section).
- $\mathrm{ISOL} = \sum \mathrm{PT_i}$ (PT with respect to the beam direction) should be less or equal to 0, 0, 1, 2 GeV for the four muons when the muons are sorted by the ISOL parameter. The sum runs over only charged particle tracks with PT greater then 0.8 GeV and inside a cone of radius $\mathrm{R} = \sqrt{(\Delta\phi)^2 + (\Delta\eta)^2} = 0.3$ in the azimuth-pseudorapidity space. A PT threshold of 0.8 GeV roughly corresponds to the PT for which tracks start looping inside the CMS Tracker. Muon tracks were not included in the calculation of the ISOL parameter.

2.2.5 Tracker-based muon isolation cut efficiency

Figures 2.2.1, 2.2.2 and 2.2.3 show the muon isolation cut efficiency averaged over all "good" muons (see section 3.2) for the $\mathrm{t\bar{t}}$ sample and the Higgs boson. For $\mathrm{t\bar{t}}$ background, we show two plots: one for muons originating from $\mathrm{W} \to \mu\nu$ and $\mathrm{W} \to \tau\nu \to \mu\nu\nu\nu$ decays and the other for muons originating from hadronic decays (typically, the former would tend to be isolated and the latter non-isolated). The average isolation efficiency per "good" muon is calculated as the ratio of the number of "good" muons with the isolation parameter ISOL below a particular threshold to the total number of "good" muons. Figure 2.2.4 shows the isolation cut efficiency for the least isolated muon out of four (Higgs boson sample). We use a cut at ISOL=2 GeV for such muons. One can see that this cut alone will have $\sim 80\%$ efficiency with $\pm 5\%$ uncertainty in a considered UE model.

Figure 2.2.5 compares the muon isolation cut efficiency curves for the main irreducible ZZ background and for the Higgs boson events. Clearly, these efficiencies are very similar.

Sensitivity to kinematical cuts Figure 2.2.6 demonstrates another very important feature of the tracker-based muon isolation cut: its efficiency is not very sensitive to the kinematical analysis cuts. The figure has two sets of efficiency curves: one is obtained for "good" muons and another for "good" muons passing further event selection cuts as described in section 3.2. One can hardly see any difference. Therefore, the conclusions of this analysis will not depend on the choice of the final event selection cuts.

Evaluation of the muon isolation cut efficiency from data using random-cone directions Figure 2.2.7 shows the isolation cut efficiency as calculated for random directions uniformly distributed in $\eta - \phi$ space ($|\eta| < 2.4$). The algorithm of the ISOL parameter calculation is the same as for "real" MC muons, except that now the ISOL parameter takes into account the sum of PT for tracks around random directions in the acceptance region. The Higgs boson Monte Carlo sample was used to make these plots. We see that the graphs obtained for the random cone (solid lines) and for "real" muons (dashed line; identical to Figures 2.2.3 and 2.2.6) look very similar. In fact, they agree within statistical uncertainties. This observation motivated us to investigate whether we can measure the isolation cut efficiency by using some distinct reference data sample and applying the random-cone technique. The reference data sample must have a large cross section (to provide good statistics), be relatively clean from backgrounds, and have a similar underlying structure to ZZ events. Inclusive $\mathrm{Z} \to \mu\mu$ seems to be just what we need. The cross section is ~ 1.6 nb, $\mathrm{Z} \to \mu\mu$ has a very clean signature.

Figure 2.2.8 shows the isolation cut efficiencies computed for random-cone directions in Z-inclusive Monte Carlo sample. One can see that the isolation cut efficiencies for muons in the ZZ sample are very well mimicked by the efficiencies calculated for random cones in the Z-inclusive sample. The variations in the UE $\mathrm{pt}_{\text{cut-off}}$ have nearly identical effects on both data samples.

4μ **Isolation cut efficiency per event** Efficiencies per event are listed in Table 2.2.5. We observe that the values for Signal, ZZ-background, and Z-inclusive using random-cone technique samples are in agreement with each other for all three tested UE scenarios. The range of efficiencies for the ZZ-background spans from ~ 0.72 to ~ 0.84. This range of $\pm 6\%$ absolute of the central value can be associated with the uncertainties on the 4-muon isolation cut efficiency arising from theoretical uncertainties on considered UE parameters in PYTHIA.

process/case	efficiency (default)	efficiency (-3σ)	efficiency ($+3\sigma$)
signal, $\mathrm{m_H} = 150$ GeV	0.775 ± 0.004	0.707 ± 0.005	0.812 ± 0.004
ZZ background	0.780 ± 0.004	0.721 ± 0.005	0.838 ± 0.004
4 RND muons, Z-inclusive events	0.762 ± 0.007	0.706 ± 0.007	0.821 ± 0.006
$\mathrm{t\bar{t}}$ background	0.016 ± 0.001	0.013 ± 0.001	0.015 ± 0.001

Table 2.2.2: Efficiency per event using different events samples: Higgs boson signal with $\mathrm{m_H} = 150$ GeV, ZZ background, Z-inclusive (4 RND muons), $\mathrm{t\bar{t}}$ background. "4 RND muons" means that for a particular process in each event 4 random cone directions were used to calculate the ISOL parameter and the corresponding values were treated as ones for "real" muons.

On the other hand, it appears possible to use the Z-inclusive sample to gauge the UE activity and evaluate the 4-muon isolation cut efficiency experimentally. There might be a small systematic shift of the order of $\sim 2\%$ in efficiencies between the ZZ and Z-inclusive samples, and this is a shift for calibration from data technique, which makes the result to a large degree independent from a particular UE scenario which would be actually realized in nature. For the three different UE simulations we used in these studies, we obtain the following offsets: 0.018 ± 0.008, 0.015 ± 0.009, 0.017 ± 0.007. Much larger Monte Carlo samples would be needed to pin it down more accurately. Meanwhile, conservatively, one may just ignore this correction and assign a 2% systematic uncertainty on the Z-sample-based estimate of the 4-muon isolation cut efficiency for ZZ-background and Higgs boson signal events. This uncertainty is already much smaller in comparison to the other systematics such as experimental uncertainties on the muon reconstruction efficiency, theoretical uncertainties associated with the choice of PDF's and QCD scale, etc.

The efficiency for accepting $\mathrm{t\bar{t}}$-events is of the order of 0.015 $\pm$ 0.001. Its sensitivity to the UE could not be studied due to lack of statistics, but it is not expected to be too large as it is dominated by the jet activity. In fact, if the reducible $\mathrm{t\bar{t}}$- and $\mathrm{Zb\bar{b}}$-backgrounds could not be suppressed well below the ZZ-background, one would need to study their sensitivity to the UE physics, as well as to the jet fragmentation modeling.

2.2.6 SUMMARY

The isolation cut efficiency per muon due to uncertainties in the considered UE models can vary as much as $\pm 5\%$ (the efficiency itself and its uncertainty strongly depend on how tight the ISOL cut is). The 4-muon isolation cut efficiency per event for $ZZ \to 4\mu$ background is measured to be $\sim (78 \pm 6)\%$.

To decrease these large uncertainties to a negligible level with respect to other systematic uncertainties, one can calibrate the isolation cut efficiency from data using Z-inclusive events ($Z \to 2\mu$) and the random-cone technique. We show that this indeed significantly decreases uncertainties associated with the poor understanding of the UE physics. There might be $\sim 2\%$ systematic shift in the 4-muon isolation cut efficiencies obtained this way. In principle, one can correct for this shift, but it does not appear to be necessary as this uncertainty is already very small.

The results and described techniques in this letter may be of interest for all analyses relying on lepton isolation cuts.

2.2.7 ACKNOWLEDGMENTS

We would like to thank M. Aldaya, P. Arce, J. Caballero, B. Cruz, G. Dissertori, T. Ferguson, U. Gasparini, P. Garcia, J. Hernandez, I. Josa, M. Konecki, P. Moisenz, E.R. Morales, N. Neumeister, A. Nikitenko, F. Palla and I. Vorobiev for their active participation in the analysis discussions and comments on this letter.

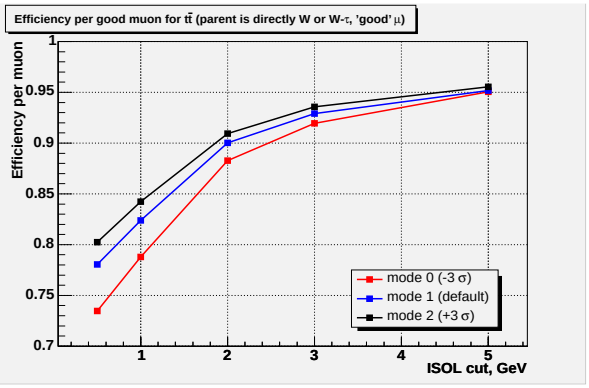

Fig. 2.2.1: Muon isolation cut efficiency averaged over selected muons whose parents are W bosons ($t\bar{t}$ events). The blue middle line is for the default MI $\mathrm{pt}_{\text{cut-off}}$, the black upper line is for downward -3σ variation of $\mathrm{pt}_{\text{cut-off}}$ value, the red lower line is for upward $+3\sigma$ variation.

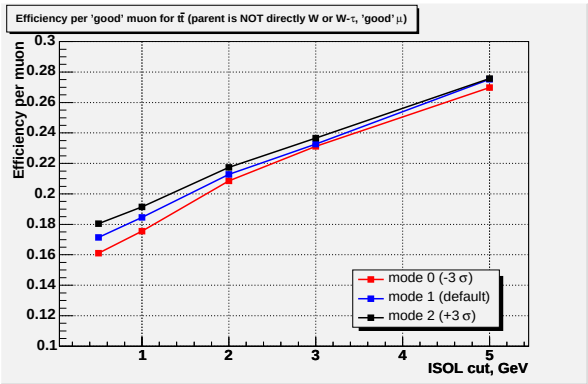

Fig. 2.2.2: Similar to Fig. 2.2.1 for muons from hadronic decays ($t\bar{t}$ events).

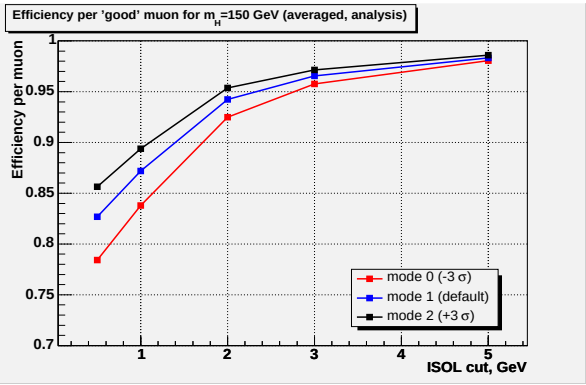

Fig. 2.2.3: Similar to Fig. 2.2.1 for Higgs boson events.

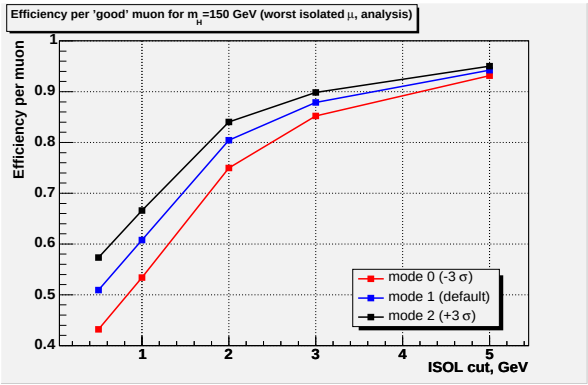

Fig. 2.2.4: Muon isolation cut efficiency for the least isolated muon from 4 selected ones in Higgs boson events.

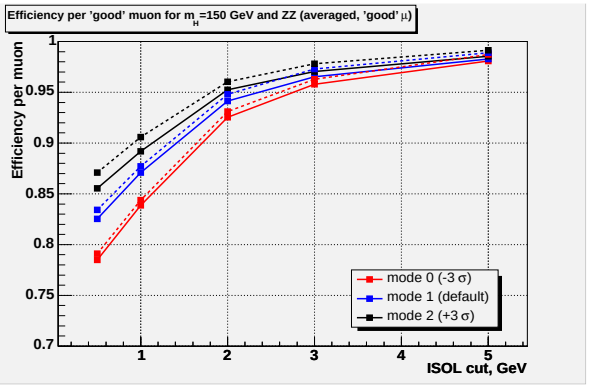

Fig. 2.2.5: Muon isolation cut efficiency averaged over 4 selected muons for signal events (solid lines, Fig. 2.2.3) and ZZ background (dashed lines). The blue middle line is for the default MI $\mathrm{pt}_{\text{cut-off}}$, the black upper line is for downward -3σ variation of $\mathrm{pt}_{\text{cut-off}}$ value, the red lower line is for upward $+3\sigma$ variation.

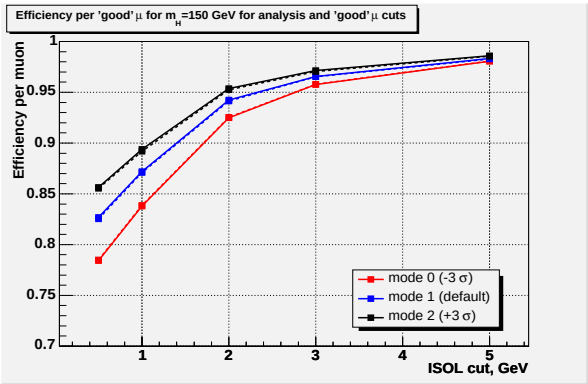

Fig. 2.2.6: Muon isolation cut efficiency averaged over 4 selected muons for signal events. Solid lines are for good muons from events after analysis cuts (see Fig. 2.2.3); dashed lines are for good muons from events before analysis cuts. There is no difference at statistical precision level for two graph sets. The blue middle line is for the default MI $\mathrm{pt}_{\text{cut-off}}$, the black upper line is for downward -3σ variation of $\mathrm{pt}_{\text{cut-off}}$ value, the red lower line is for upward $+3\sigma$ variation.

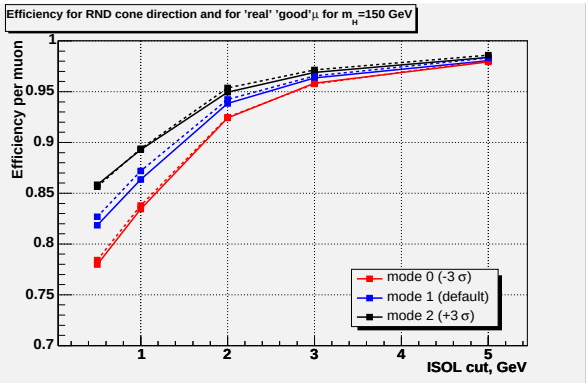

Fig. 2.2.7: Muon isolation cut efficiency for random-cone directions (solid lines) and for muons (dashed lines) for signal events. The blue middle lines are for the default MI $\mathrm{pt}_{\text{cut-off}}$, the black upper lines are for downward -3σ variation of $\mathrm{pt}_{\text{cut-off}}$ value, the red lower lines are for upward $+3\sigma$ variation.

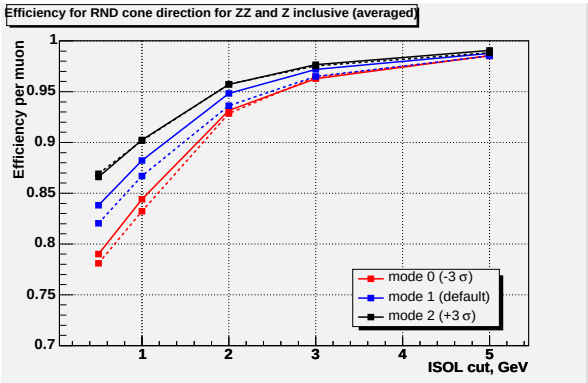

Fig. 2.2.8: Muon isolation cut efficiency for random-cone directions for Z-inclusive (dashed lines) and ZZ (solid lines) events. The blue middle lines are for the default MI $\mathrm{pt}_{\text{cut-off}}$, the black upper lines are for downward -3σ variation of $\mathrm{pt}_{\text{cut-off}}$ value, the red lower lines are for upward $+3\sigma$ variation.

2.3 τ-Identification, from DØ to ATLAS

Michael Heldmann, Ingo Torchiani

Freiburg University, Germany

2.3.1 Introduction

Excellent reconstruction and identification of all lepton species is crucial at the Large Hadron Collider (LHC). Tau leptons are the most difficult ones in this respect, since they produce neutrinos and hadrons among their decay products. Many different physics channels contain τ leptons in their final states. In particular the heaviest Higgs bosons in the Minimal Super Symmetric Model (MSSM) can be observed through their decays to τ leptons ($bbA^0/H^0 \rightarrow bb\tau\tau$, $H^{\pm} \rightarrow \tau^{\pm} + \nu_{\tau}$) and also the Standard Model (SM) Higgs produced through Vector Boson Fusion (VBF) can be observed when it decays to a τ pair. Additionally τ leptons can be an important signature for SUSY. Since it will not be possible to discriminate between prompt light leptons (electrons and muons) and leptons from τ-decays, the hadronic decay modes will have to be explored. Various characteristics of a τ-decay allow a discrimination against jets from QCD-events (QCD-jets) or heavy quark-jets (as from $\mathrm{t\bar{t}}$). This discrimination will be called τ-identification in the following.

For physics at the LHC many studies have been undertaken to evaluate the discovery potential in these channels. Since data from the LHC will not be available for at least one more year these studies had to rely on Monte Carlo simulation. Though a lot of work has been invested to provide a detailed description of the physics and detector effects, the potential uncertainty for such a complex variable like a multivariate discriminator between τ-jets and other jets might be substantial.

In terms of the similarities in physics environment and detector design, the Tevatron and DØ specifically is the best available tool to investigate the reliability of such Monte Carlo techniques to predict the performance of a given algorithm to separate between τ-jets and other jets.

Therefore an attempt has been made to estimate the uncertainty on the performance of the τ-identification algorithm used in ATLAS.

To accomplish this we try to establish a chain of understanding composed of the following steps:

- DØ Algorithm on DØ data
- DØ Algorithm on DØ MC
- DØ Algorithm on ATLAS MC
- ATLAS Algorithm on ATLAS MC
- Prediction for ATLAS Algorithm on ATLAS data

To implement this chain the strategy will be to select a signal and a background sample in DØ data and study the τ preselection as described below on these samples. After the selection we investigate a simple cut based τ-identification using three key variables, which have been implemented in ATLAS. Afterwards it will be shown to what extent these results are transferable to

ATLAS.

2.3.2 τ-reconstruction and identification in ATLAS

The reconstruction of τ-candidates in ATLAS is done by a package called "tauRec" [10]. The seeds for the building of tau candidates are provided by a sliding window cluster algorithm. It runs on $\Delta\eta \times \Delta\phi = 0.1 \times 2\pi/64$ calorimeter towers. Only clusters with $\mathrm{E_T} > 15\ \mathrm{GeV}$ are considered.

In Figure 2.3.1 the probability is shown for a true τ-jet within $|\eta| < 2.5$ to be reconstructed as a τ-candidate as a function of E_T for two different samples. E_T represents the transverse energy of the visible decay products. A true τ-jet is called reconstructed if a cluster is found with a barycenter within $\Delta\mathrm{R} < 0.3$ around the τ-jet direction. The efficiency rises from 20 % at 15 GeV over 88 % at 20 GeV and saturates at 98 % for $\mathrm{E_T} > 30\ \mathrm{GeV}$.

The reconstruction is followed by a step called identification. For the purpose of separating τ-jets from other jets a set of variables is calculated for each τ-candidate. The three most important of these variables are $\mathrm{R_{lem}}$, ΔE_T^{12} and $\mathrm{N_{Tr}}$.

- $\mathrm{N_{Tr}}$: number of tracks, extrapolated to the calorimeter, within $\Delta R < 0.2$ around the cluster barycenter, with $P_T > 2\ \mathrm{GeV}$
- $\mathrm{R_{lem}}$: transverse energy radius in the EM calorimeter layers

$$R_{em} = \frac{\sum_{i=1}^{n} E_{Ti}\sqrt{(\eta_i - \eta_{cluster})^2 + (\phi_i - \phi_{cluster})^2}}{\sum_{i=1}^{n} E_{Ti}} \tag{2.3.1}$$

  i runs over all electromagnetic calorimeters cells in the cluster with $\Delta\mathrm{R} < 0.4$,

- ΔE_T^{12} : transverse energy isolation

$$\Delta\mathrm{E_T^{12}} = \frac{\sum_{\mathrm{j=1}}^{\mathrm{n'}} \mathrm{E_{Tj}}}{\sum_{\mathrm{i=1}}^{\mathrm{n}} \mathrm{E_{Ti}}} \tag{2.3.2}$$

  j runs over all electromagnetic calorimeters cells in the cluster with $0.1 < \Delta\mathrm{R} < 0.2$,
  n' denotes their number, $\mathrm{E_{Tj}}$ is the transverse energy in cell j
  i runs over all electromagnetic calorimeters cells in the cluster with $\Delta\mathrm{R} < 0.4$,
  n denotes their number, $\mathrm{E_{Ti}}$ is the transverse energy in cell i

These three along with five other variables are combined into one discriminant using a likelihood ratio method, shown in Figure 2.3.2. A good separation between τ-jets and light jets can be obtained by tuning a cut on this single variable LLH2004 to the desired efficiency.

2.3.3 τ-reconstruction and identification in DØ

Reconstruction and identification of hadronically decaying τ-leptons has been used successfully at the DØ experiment in various analyses, e.g. a measurement of the $Z/\gamma^* \rightarrow \tau\tau$ cross section

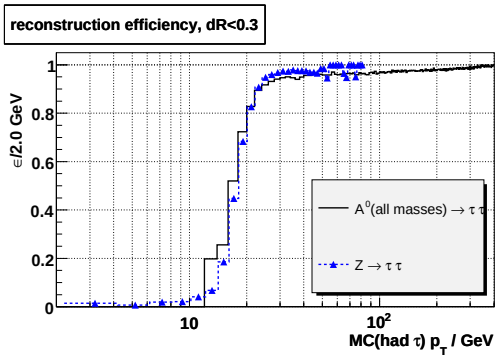

Fig. 2.3.1: Reconstruction efficiency for τ-jets as a function of E_T. Black is an average over signal samplesfrom $bbA^0/H^0 \rightarrow bb\tau\tau$ events, dotted is only a $Z^0 \rightarrow \tau\tau$ sample.

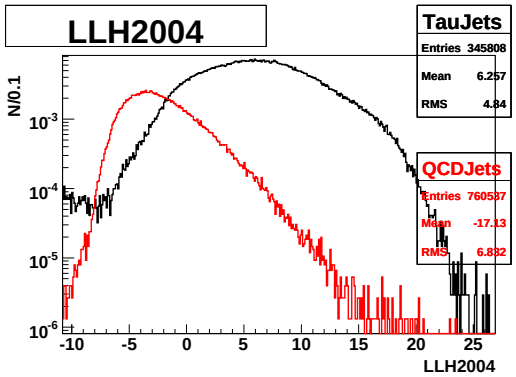

Fig. 2.3.2: LLH2004 distribution for τ-jets (black) and QCD-jets (red). Candidates with a LLH < -10 had variables outside the boundaries of histograms used when obtaining the PDFs. The LLH is applied after a preselection of $1 \leq \mathrm{N_{Tr}} \leq 3$. Due to statistical limitations, only one-dimensional distributions have been used. Nevertheless a good separation between τ-jets and QCD-jets is achieved.

[11]. The search for τ-candidates at DØ starts with the reconstruction of energy clusters in the calorimeter using a 0.3-cone algorithm seeded either by a calorimeter tower with a transverse energy of more then 1 GeV or a track with a transverse momentum of more than 5 GeV. For being considered as a τ-candidate, the total transverse energy in the cluster is required to be larger than 4 GeV or 2 GeV, respectively. In order to find energy deposits from neutral pions, a nearest-neighbor algorithm is used to reconstruct energy clusters in the electromagnetic calorimeter only. If the transverse energy of such an EM cluster is above 0.8 GeV it is regarded as a π^0 candidate.

In a second step tracks which are reconstructed in the central tracking system are associated to the calorimeter cluster. Up to three tracks can be assigned to a τ-candidate. Tracks are processed in the order of decreasing transverse momentum and have to fulfill the following requirements for being associated to the τ-candidate:

- The transverse momentum has to be larger than 1.5 GeV.
- The distance at the point of closest approach between first, second and third track has to be smaller than 2 cm.
- The invariant mass calculated from first and second track is smaller than 1.1 GeV.
- The invariant mass calculated from first, second and third track is smaller than 1.7 GeV.
- The charge of all tracks adds up to ± 1.

After this reconstruction process the tau candidates are classified into three types:

- τ**–type 1**: $\tau^{\pm} \rightarrow h^{\pm}\nu_{\tau}$ (π-like). The τ-candidate consists of a calorimeter cluster and one track, without any reconstructed EM cluster.
- τ**–type 2**: $\tau^{\pm} \rightarrow h^{\pm}\nu_{\tau} + (n\pi^0), n > 0$ (ρ-like). The τ-candidate consists of a calorimeter cluster, one track and at least one EM cluster.
- τ**–type 3**: $\tau^{\pm} \rightarrow h^{\pm}h^{\mp}h^{\pm}\nu_{\tau} + (n\pi^0), n \geq 0$ (3-prong). The τ-candidate consists of a calorimeter cluster and two or three tracks.

τ-candidates to which no track could be matched will not be discussed, since they are currently not used for physics analyses. After this classification the identification of hadronically decaying tau leptons and the rejection against background from QCD jets is performed using three neural networks, one for each τ–type. The neural nets consist of one input, one hidden and one output layer. The input and hidden layer contain as many nodes as input variables are used, while the output layer holds only a single node. Only the three most important input variables are discussed here, since they are comparable to variables used by ATLAS:

- **Profile:** $(E_T^1 + E_T^2)/E_T(0.5)$, E_T^i represents the transverse energy in the calorimeter tower with the highest and second highest transverse energy and $E_T(0.5)$ the transverse energy in a 0.5 cone around the τ-candidate.
- **Isolation:** $(E_T(0.5) - E_T(0.3))/E_T(0.3)$, where $E_T(x)$ represents the transverse energy in a x-cone around the τ-candidate.
- **Track isolation:** Scalar sum of p_T of tracks which are not associated to the tau, divided by the scalar sum of p_T of all tracks in a 0.5-cone around the τ-candidate.

A distribution of the output of the neural net is presented in Figure 2.3.3. It also shows $Z/\gamma^* \rightarrow \tau\tau$ signal, τ–type and track multiplicity, after a $\mu + \tau_{\mathrm{had}}$ selection, which uses the neural networks and is optimized for $Z/\gamma^* \rightarrow \tau\tau$ [12].

2.3.4 Signal and background selection

As a signal sample $Z^0 \rightarrow \tau\tau$ was chosen to provide true τ-jets. As a background sample $\mathrm{W} \rightarrow \mu\nu$ is used to provide light jets. $\mathrm{W} \rightarrow \mu\nu$ is used because it is an important background to many channels with τ final states and because it allows to obtain an unbiased jet-sample using a single μ trigger, down to rather low P_T.

$\mathrm{W} \rightarrow \mu\nu$ **sample** The selection cuts used to obtain the $\mathrm{W} \rightarrow \mu\nu$ sample were:

- $P_T(\mu) > 25$ GeV, $|\eta(\mu)| < 1.5$
- $P_T(jet) > 15$ GeV, $|\eta(jet)| < 1.0$
- $\not{E}_T > 20$ GeV, $\mathrm{m_T} > 30$ GeV
- $\mathrm{m}(\mu, \mathrm{track}) < 60$ GeV
- $\Delta\phi(\not{E}_T, jet) > 0.4$

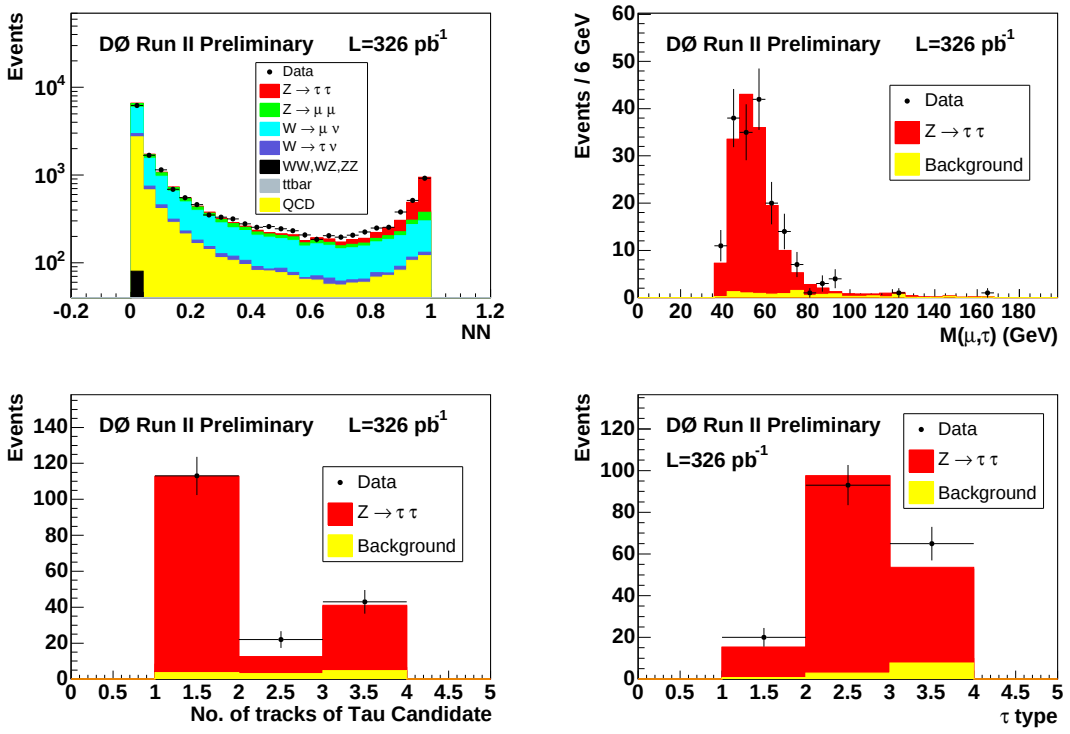

Fig. 2.3.3: Distribution of the output of the neural net used for the τ-identification at DØ taken from a $\mu + \tau_{had}$-selection for $p_T^\tau > 7$ GeV and distributions of the μ-τ_{had} invariant mass, track multiplicity and τ–type for $p_T^\tau > 25$ GeV after a selection optimized for $Z/\gamma^* \to \tau\tau$ [12].

Figure 2.3.4 shows the distribution of the transverse mass between $\not\!\!E_T$ and the muon after the selection for DØ data and Monte Carlo, where the dominating process is $\mathrm{W} \to \mu\nu$.

Since the rejection against jets will depend strongly on the kinematic variables (E_T and η) of the jets these are important. Figure 2.3.5 shows the comparison between data and Monte Carlo for the leading jet P_T and η after the $\mathrm{W} \to \mu\nu$ selection. Data and Monte Carlo agree within statistical errors.

Similar samples were produced for ATLAS using the same generator (PYTHIA). The same selection cuts were applied to make the samples as comparable as possible, see Figure 2.3.5.

$Z^0 \to \tau\tau$ **sample** The $Z^0 \to \tau\tau \to \mu + \mathrm{had}$ sample was selected in DØ Monte Carlo by requiring:

- $P_T\ (\mu) > 14\ \mathrm{GeV},\ |\eta(\mu)| < 1.5$
- $P_T\ (\tau) > 15\ \mathrm{GeV},\ |\eta(jet)| < 1.0$

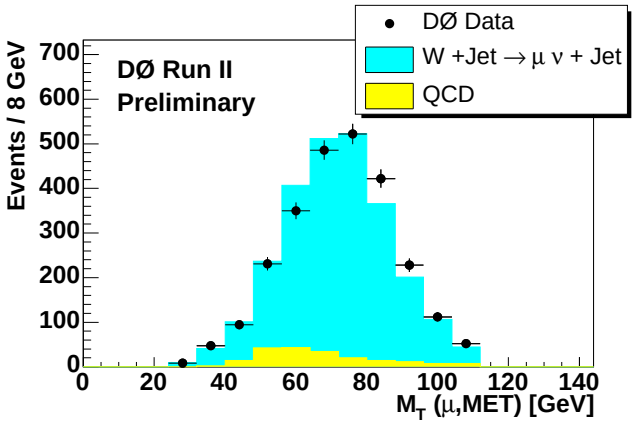

Fig. 2.3.4: Distribution of the transverse mass between the leading muon and $\not\!\!E_T$ after cuts described in the text. Shown are data (black dots), $\mathrm{W} \rightarrow \mu\nu$ (red) and QCD background (yellow).

2.3.5 Jet properties

A τ-selection, in one form or the other, makes use of the well known basic features of a hadronically decaying tau lepton: One (, two), or three tracks near the calorimeter cluster center and a corresponding energy deposition in the calorimeter.

Figure 2.3.6 shows the number of tracks within $\Delta\mathrm{R} < 0.3$ around the jet axis, for DØ and ATLAS. Every jet with $P_T > 15\ \mathrm{GeV}$ and $|\eta| < 1.0$ from the W+mu selection enters the plot. The track multiplicity is shown for tracks with $P_T > 1\ \mathrm{GeV}$. The comparison for DØ between Monte Carlo and data shows good agreement. Taus are, in most cases, selected only within jets having between one and three tracks.

The comparison with distributions for the same quantities obtained with simulated ATLAS data shows that the distributions are well comparable between the two experiments. Hence also some confidence can be derived for the modeling of these quantities for the prediction of backgrounds to τ final states in the ATLAS experiment.

2.3.6 Quantities used in Tau identification

Both DØ and ATLAS make use of several quantities to separate tau leptons from jets. To keep the environment simple we concentrate on three principal variables, defined in Section 2.3.3, which are important both for DØ and ATLAS. For the following comparisons all DØ discrimination variables were implemented in the ATLAS software framework, even though only three are used in this document. All are available in the official ATLAS software. In the implementation several details had to be faced that are consequences of the difference in detector layout. This included for example grouping ATLAS calorimeter cells to simulate a granularity and longitudinal segmentation similar to DØȦlso differences in noise levels and general activity had to be taken into account.

Figure 2.3.7 shows “Profile”, “Calorimeter Isolation” and “Track Isolation” for DØ data,

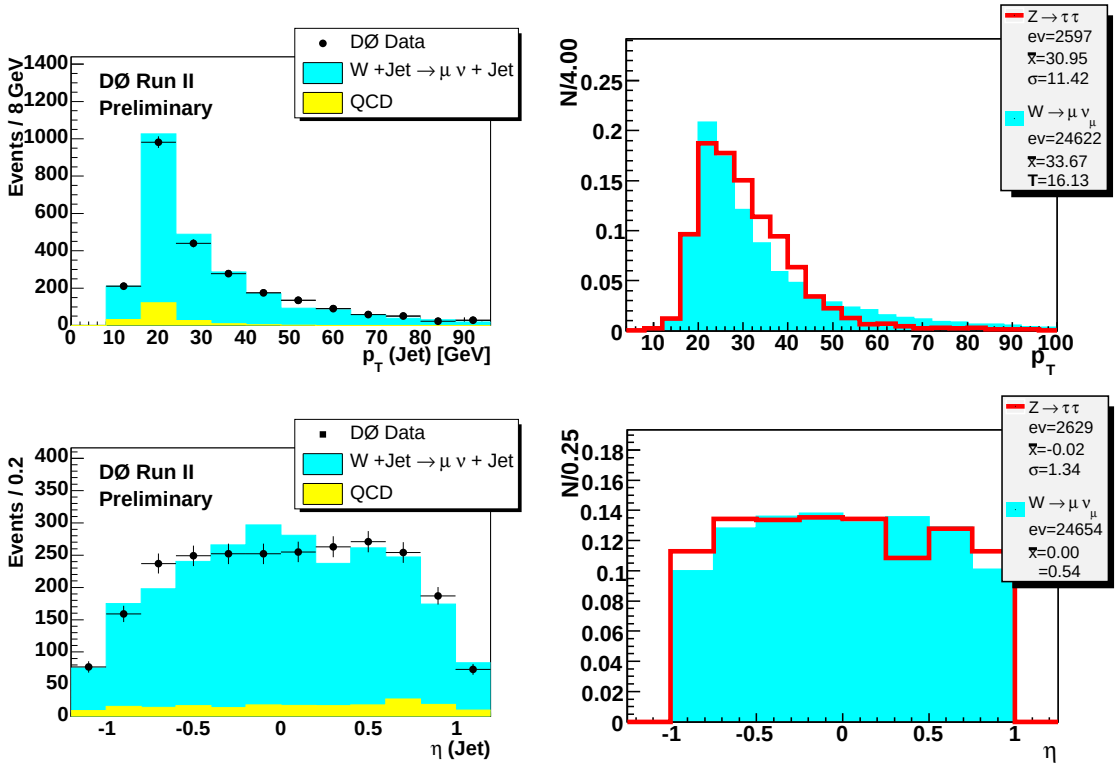

Fig. 2.3.5: Distribution of P_T and η for the leading jet for DØ (left) and ATLAS (right) in the $W \rightarrow \mu\nu$ sample. Distributions are given for DØ data, W $\rightarrow \mu\nu$ (cyan), QCD (yellow). For ATLAS P_T and η of the leading τ-jet are shown in red for $Z^0 \rightarrow \tau\tau$.

background and a possible signal in the left column. Modelling of these depends on complex details of jet fragmentation and detector simulation. Hence the agreement within statistical errors between data and Monte Carlo for DØ should be considered as very good. This shows that a high precision in the prediction of these variables can be achieved with current Monte Carlo event and detector simulations.

The right column of Figure 2.3.7 shows the same quantities for ATLAS Monte Carlo simulation. All three variables show a similar behavior for DØ and ATLAS. For “Profile” the agreement is very good and for “Calorimeter Isolation” reasonable. The “Track Isolation” shows the biggest discrepancy which we mainly attribute to the different P_T threshold on tracks which is 1 GeV for ATLAS and 0.4 GeV for DØ. This could explain the rather deep dip for low values of track isolation for jets.

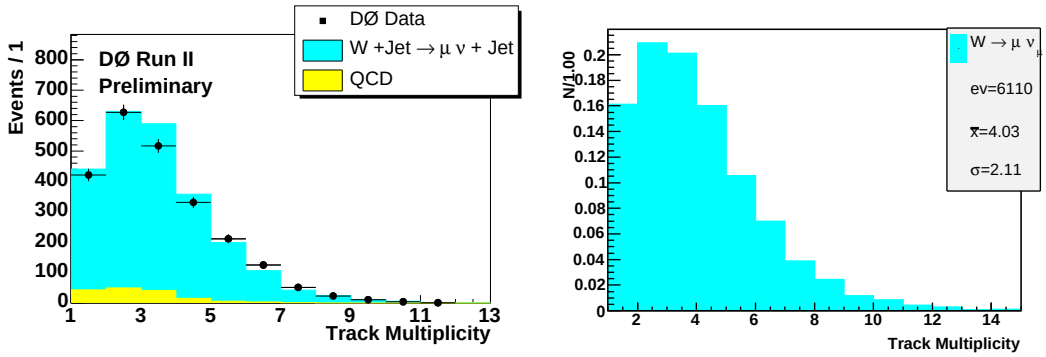

Fig. 2.3.6: Distribution of the track multiplicity for jets for DØ (left) and ATLAS (right). Distributions are given for DØ data, W $\rightarrow \mu\nu$ (cyan), QCD (yellow).

2.3.7 Simple "benchmark tau identification" based on three variables

To be able to judge the similarities and differences of the DØ and the ATLAS experiment with respect to τ-identification we decided to implement a very basic tau selection for both DØ and ATLAS. We choose a cut analysis on three variables, namely Profile, Isolation and Track Isolation. To obtain the optimal cut values a scan in these three variables has been performed, optimizing for the best rejection for all efficiencies. The performance of such an analysis on DØ data and MC is given in Figure 2.3.8, while Figure 2.3.9 gives a comparison between data and MC. Every point in the graph corresponds to a set of three cut values. For a given efficiency the highest point is the optimal set if cut values. For example, this simple method gives a rejection of ≈ 25 at 50 % efficiency. The right plot of Figure 2.3.9 shows the difference between the rejections obtained on data and MC for the same set of cuts on the before mentioned variables. Even though the input variables show a good agreement of MC and data, the analysis performs systematically worse on data than what is expected from MC. We assume this is due to significant correlations. It can be observed that the difference grows from 0 % at 80 % efficiency up to 60 % at 20 % efficiency. It should be noted that the usual DØ working point is at around 80 % , where the difference is smaller than 10 %. These differences are now translated into an uncertainty on the prediction of jet rejection in the ATLAS experiment.

2.3.8 Transfer to ATLAS

The left plot of Figure 2.3.10 shows the performance for the same kind of simple cut analysis as was used to produce Figure 2.3.8 but analyzing ATLAS Monte Carlo samples. It can be seen that the performance is roughly comparable to DØ results.

The right plot of Figure 2.3.10 shows the results of such a cut analysis using the "standard" ATLAS variables. The performance at higher efficiencies is very similar, while at lower efficiencies the "standard" ATLAS variables perform significantly better.

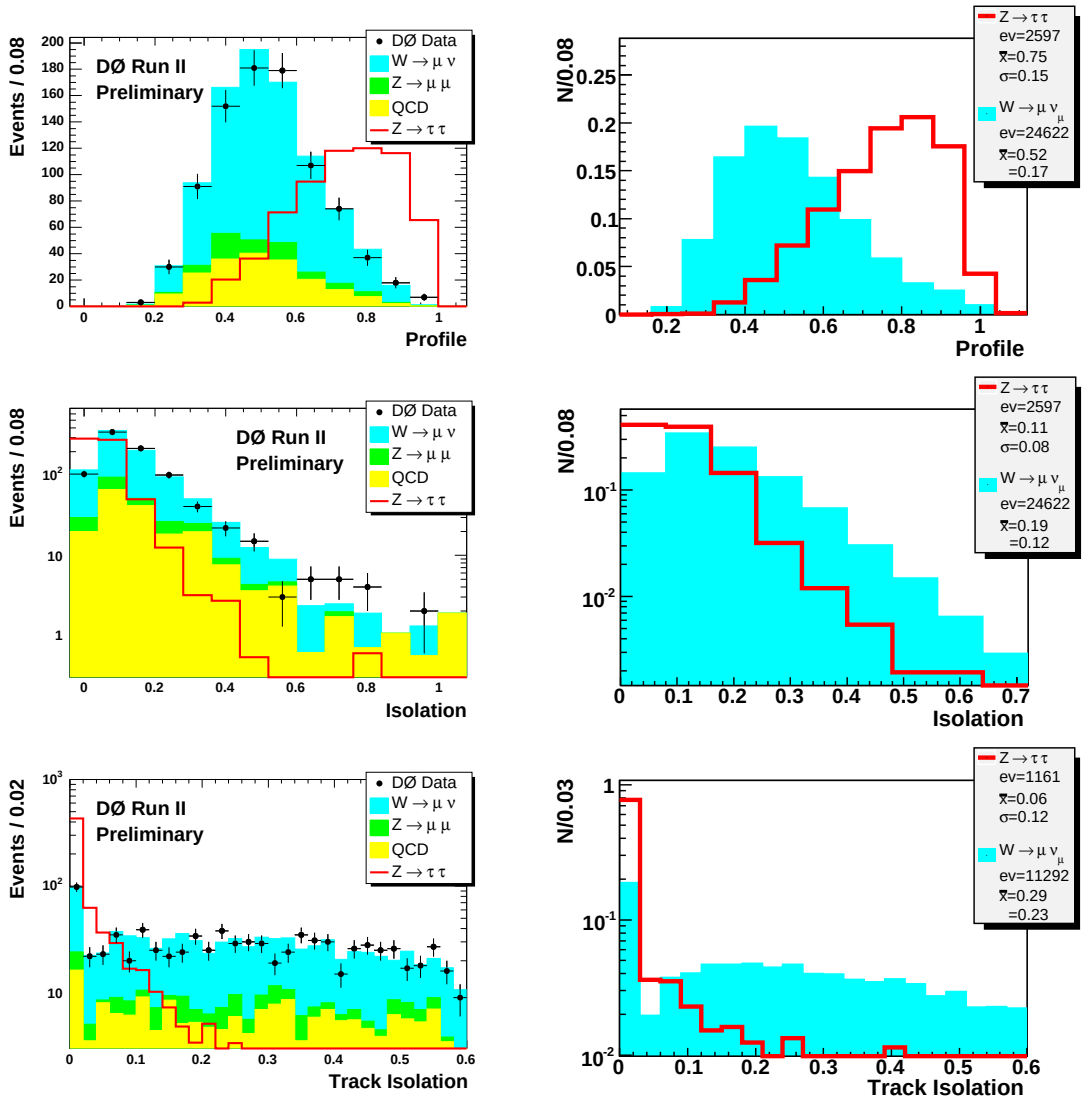

Fig. 2.3.7: Distributions of three key variables, τ-profile (upper row), τ-calorimeter isolation (middle row) and τ-track isolation (lower row). The left (right) column shows distributions for DØ (ATLAS). Distributions are given for DØ data (crosses), W $\rightarrow \mu\nu$ (cyan), $Z^0 \rightarrow \tau\tau$ (red), Z $\rightarrow \mu\mu$ (green) and QCD-jets (yellow).

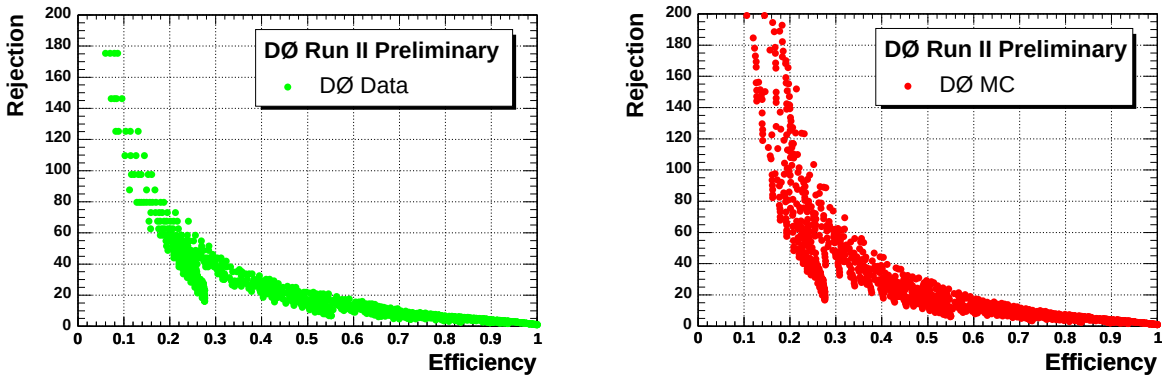

Fig. 2.3.8: Rejection against jets vs. efficiency for τ jets. Each point in the scatter plot stand for one possible combination of cuts of the three variables "Profile", "Isolation" and "Track Isolation". The efficiency is always determined on the $Z^0 \rightarrow \tau\tau$ MC sample. The left shows the performance on DØ $W^{\pm} \rightarrow \mu^{\pm}\nu$ data while the right plot the result of the same procedure on DØ $W^{\pm} \rightarrow \mu^{\pm}\nu$ MC.

Since the cuts were optimized separatly for DØ and ATLAS the exact cut values used to produce Figures 2.3.8 and 2.3.10 were not the same. Therefore it has been checked that the contribution of a certain variable to the rejection is very similar for ATLAS and DØ (not shown). Therefore the assumption, that results obtained for DØ using DØ variables are portable to ATLAS performance expectations, using ATLAS variables, seems justified.

Figure 2.3.11 shows the performance for ATLAS using the "standard" ATLAS method to identify tau leptons, which is a likelihood ratio method based on 8 variables (not all shown), including the three "standard" ATLAS variables we showed before. As expected, it can be seen that this method outperforms the three cut analysis significantly. The difference varies between 100 % and 50 % and again leaves the performance in the same order of magnitude.

Even though this improvement might result from additional variables, the assumption that their uncertainty behaves in a similar way can be made. This would mean that the differences seen in Figure 2.3.9 can be directly translated into an uncertainty on the prediction of rejection for the ATLAS experiment. Figure 2.3.12 shows the expected rejection obtained for ATLAS using the three cuts analysis (thick black line) and the "standard" approach (slashed black line). The uncertainty band given by the deviation at DØ between MC and data is shown as a thick grey line. The dotted black line shows the same uncertainty for the "standard" ATLAS τ-identification. In light gray the "worst" case is shown when including also the uncertainties on the deviation, assuming the worst performance within uncertainties.

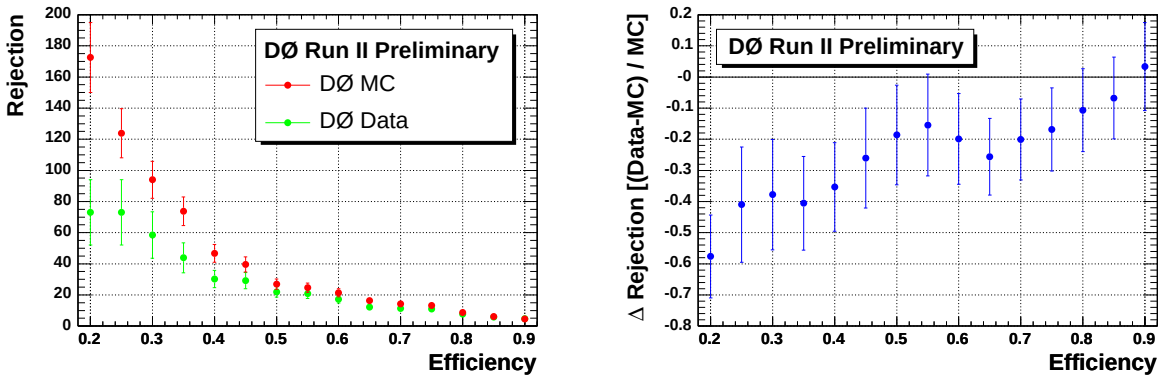

Fig. 2.3.9: Left figure shows "best" points from Figure 2.3.8 for MC and data. Right plot shows the relative difference.

2.3.9 Conclusion

Identification of hadronically decaying τ leptons is an important and challenging issue at both Tevatron and LHC experiments. To conduct feasibility studies at the LHC it is important to be able to estimate the uncertainty on the prediction of τ-identification performance. To obtain such an estimate, we selected $\mathrm{W} \rightarrow \mu\nu \ + \mathrm{jets}$ events in DØ data, DØ Monte Carlo and ATLAS Monte Carlo. We compared the τ-identification related properties of these jets between DØ MC and data. The comparison shows good agreement for all jet shape variables.

On the same sample a simplified τ-identification, based on three key variables, was studied. The cut values were optimized to yield highest rejection for a given efficiency. The efficiency was obtained from a $Z^0 \rightarrow \tau\tau$ Monte Carlo sample. The rejection was compared between Monte Carlo and DØ data and no significant discrepancies were found. Taking into account correlations the agreement is within one sigma deviation for efficiencies above 50 % and two sigma deviations for lower efficiencies.

To justify that these results are meaningful also for the ATLAS experiment, the DØ variables have been implemented in the ATLAS software as far as possible. It was found that the DØ variables perform in a very similar way on an ATLAS $\mathrm{W} \rightarrow \mu\nu$ sample, after the same preselection. Also for ATLAS a simplified τ-identification was optimized on ATLAS Monte Carlo. Regardless the obvious differences in detector and machine, it shows good agreement with the DØ results, in terms of the overall performance as well as the relative dependency on the variables.

This gives us confidence to quote an uncertainty between 0 % (at 90 % efficiency) and 50 % (at 20 % efficiency) for the prediction of rejection against jets in the ATLAS experiment.

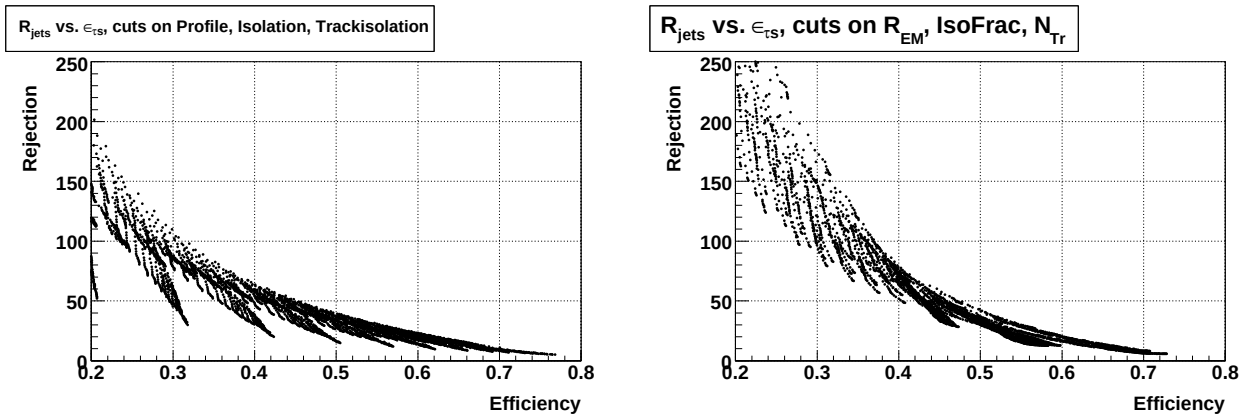

Fig. 2.3.10: Rejection against jets vs. efficiency for τ-jets on ATLAS samples. For the left (right) distribution DØ (ATLAS) variables have been used. Every point stands for a given combination of cuts on $\mathrm{R_{|em}}$, ΔE_T^{12} , $\mathrm{N_{Tr}}$.

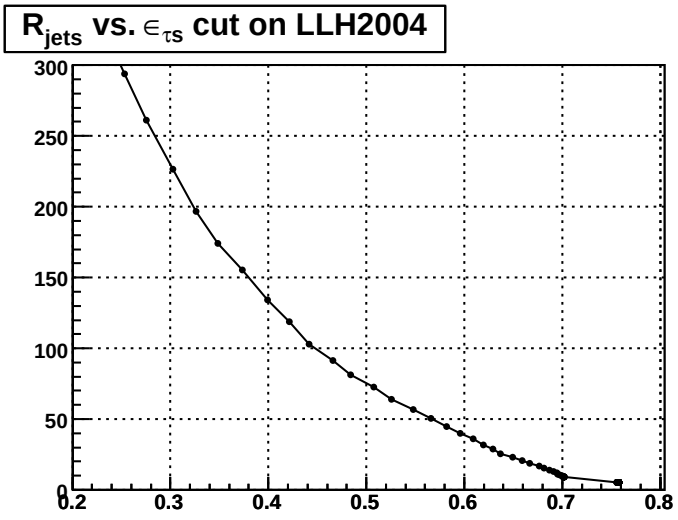

Fig. 2.3.11: Rejection against jets vs. efficiency for τ-jets on ATLAS samples using the ATLAS LLH.

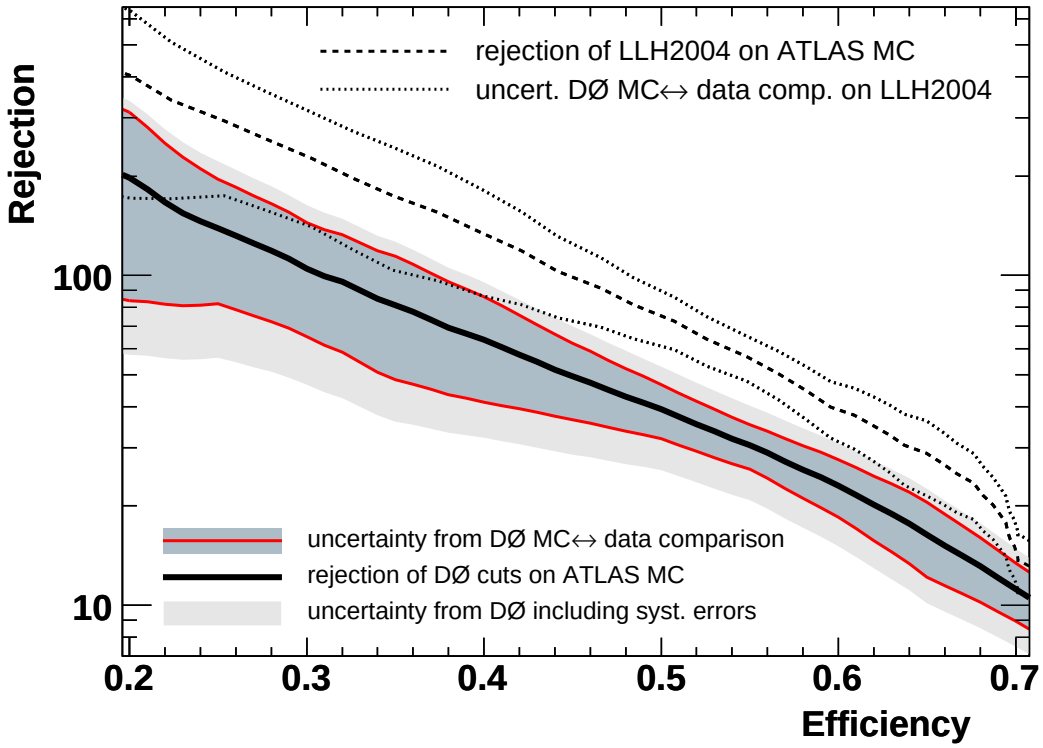

Fig. 2.3.12: Rejection against jets vs. efficiency for τ-jets on ATLAS samples using the ATLAS LLH including the uncertainties from DØ.

2.4 Jets and Missing E_T: Standard Model Background for SUSY searches at the LHC

S. Asai and T. Sasaki

University of Tokyo, E-mail: Shoji.Asai@cern.ch

The search for supersymmetry is one of the main purposes of the LHC. The Standard Model background processes are estimated with the Matrix Elements calculation, and we find out that the background contributions become larger than what we have expected, and that the distributions are similar to the SUSY signal. The careful studies of the Standard Model processes are useful using Tevatron Run-II data, especially studies of the slope of the P_T and missing E_T distributions of $W^{\pm}$ + jets, Z^0 + jets and $\mathrm{t\bar{t}}$ + jets.

2.4.1 Introduction

Supersymmetric (SUSY) Standard Models [13, 14] are promising extensions of the Standard Model(SM), because the SUSY can naturally deal with the problem of the quadratic Higgs mass divergence. Furthermore, the SUSY models provides a natural candidate for cold dark matter, and they have given a hint of the Grand Unification of gauge couplings around 2×10^{16} GeV. In these theories, each elementary particle has a superpartner whose spin differs by 1/2 from that of the particle. Discovery of these SUSY particles should open a window of new epoch, and is one of the important purposes of the LHC project [15, 16].

Dominant SUSY production processes at LHC are $\tilde{\mathrm{g}}\tilde{\mathrm{g}}$, $\tilde{\mathrm{g}}s$ and ss through the strong interaction. These production cross-sections, σ, do not strongly depend on the SUSY parameters except for masses of $\tilde{\mathrm{g}}$ and s [17, 18]. When these masses are 500 GeV, $\tilde{\mathrm{g}}\tilde{\mathrm{g}}$ is main production process, and total σ($\tilde{\mathrm{g}}\tilde{\mathrm{g}}$, $\tilde{\mathrm{g}}s$ and ss) is 100 pb. $\tilde{\mathrm{g}}\tilde{\mathrm{g}}$ production is dominate process for this case, since the population of gluon in the proton is very huge. σ becomes 3 pb for m_s=$m_{\tilde{\mathrm{g}}}$=1TeV. Even when these masses are 2 TeV, sizable production cross-section of about 20 fb is expected. $\tilde{\mathrm{u}}\tilde{\mathrm{u}}$ and $\tilde{\mathrm{u}}\tilde{\mathrm{d}}$ are main production processes for such a heavy case, since u and d quarks are valence quarks.

Decay modes of $\tilde{\mathrm{g}}$ and s are controlled by the mass-relation between each other, and are summarized in the Fig. 2.4.1. If kinematically possible, they decay into 2-body through the strong interaction. Otherwise, they decay into a Electroweak gaugino plus quark(s). Bino/Wino-eigenstates presented in this table become simply mass-eigenstate, ($\tilde{\mathrm{B}}^0 \sim \tilde{\chi}_1^0$, $\tilde{\mathrm{W}}^0 \sim \tilde{\chi}_2^0$, and $\tilde{\mathrm{W}}^{\pm} \sim \tilde{\chi}_1^{\pm}$), when m_0 is not too larger than $m_{1/2}$. In this case, Higgsino mass ($|\mu|$) becomes larger than gaugino mass at the EW scale, then Higgsino component decouples from lighter mass-eigenstates as already mentioned. Decay modes of third generation squarks ($\tilde{\mathrm{t}}_1$ and $\tilde{\mathrm{b}}_1$) are more complicated, since they have enough coupling to Higgsino due to non-negligible Yukawa couplings.

There are four leading decay modes of $\tilde{\chi}_2^0$ depending on mass spectrum. When the scalar lepton, $\tilde{\ell}^{\pm}$, is lighter than $\tilde{\chi}_2^0$, 2-body decay chain, $\tilde{\chi}_2^0 \to \ell\tilde{\ell}^{\pm}(\to \ell\tilde{\chi}_1^0)$ becomes dominant decay mode. Branching fraction of $\tilde{\chi}_2^0 \to \tau\tilde{\tau}_1$ is significantly large in the case of $\tan\beta \gg 1$. $\tilde{\chi}_2^0 \to \mathrm{h}\tilde{\chi}_1^0$ is

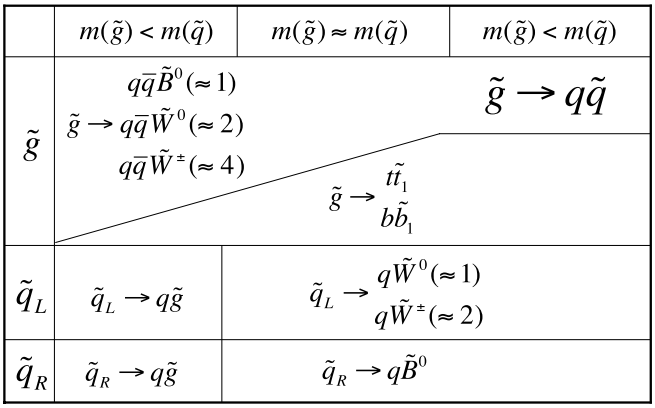

Fig. 2.4.1: Decay table of squarks and gluino:

dominant mode, if the mass difference between $\tilde{\chi}_2^0$ and $\tilde{\chi}_1^0$ is larger than Higgs boson mass. When the mass difference is smaller than m_{Z^0}, three body decay is main decay process. $\tilde{\chi}_1^{\pm}$ has three leading decay modes, $\tilde{\chi}_1^{\pm} \to \tilde{\ell}^{\pm}\nu$, $W^{\pm}\tilde{\chi}_1^0$ and $\mathrm{f}\bar{\mathrm{f}}'\tilde{\chi}_1^0$ as the similar manner to $\tilde{\chi}_2^0$.

$\tilde{\mathrm{g}}$ and/or s are copiously produced at the LHC, and the cascade decay follows after. The colored SUSY particles decays into the EW gauginos and jets as shown in the figure. Transverse momenta P_T of these jets are expected to be large due to the large mass-difference between the colored sparticles and EW gauginos. Cascade decay via scalar top and scalar bottom quarks also contributes, if they are significantly lighter than the other scalar quarks. Each event contains two $\tilde{\chi}_1^0$'s in the final state. If R-parity [19] is conserved, $\tilde{\chi}_1^0$ is stable, and it is neutral and weakly interacting and escape from the detection. Then missing transverse energy, $\not{E}_T$, carried away by two $\tilde{\chi}_1^0$'s plus multiple high P_T jets is the leading experimental signature of SUSY at LHC.

Also the other activities of additional jets, leptons and $\mathrm{b}\bar{\mathrm{b}}$ are possible, coming from the decays of $\tilde{\chi}_2^0$ and $\tilde{\chi}_1^{\pm}$. These additional informations are important to confirm SUSY signals, and to investigate its properties.

The following four SM processes can potentially have $\not{E}_T$ event topology with jets.

- $W^{\pm}$ + jets, $W^{\pm} \to \ell\nu$
- Z^0 + jets, $\mathrm{Z}^0 \to \nu\bar{\nu}, \tau + \tau^-$
- $\mathrm{t}\bar{\mathrm{t}}$ + jets
- Heavy flavor quarks (b,c) with semi-leptonic decay and the light flavor QCD jets with mis-measurement

Supersymmetry will be observed as an excess of these SM processes, and it should be discovered at LHC within one or two years (L=1-10 fb^{-1}) after the LHC starts, if $\tilde{\mathrm{g}}$ and s are lighter than about 2.0 TeV. Quick but well understanding of these SM processes plays important role in the discovery of SUSY, especially 'high P_T jet' and '$\not{E}_T$ ' measurements. These two subject are very important and we have good chance to study them with Tevatron Run-II data.

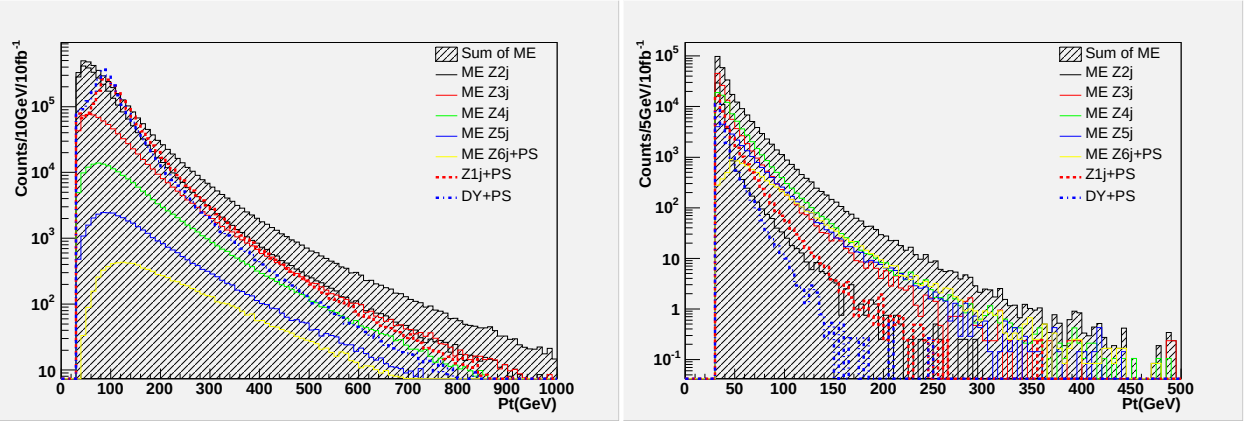

Fig. 2.4.2: P_T distribution of (a) the leading jet and (b) 4th jet. Red dotted shows the PS calculation and hatched histogram show the ME predictions. It is obtained after sum up of all different jet multiplicity samples as shown in colored histogram in both figures.

2.4.2 High P_T jets

High P_T jets and $\not\!\!E_T$ are vital for the SUSY search. The Parton Shower (PS) is the good model in the collinear and soft regions, since all leading logs are summed up. But the high P_T jets are not emitted in the PS model, and the high P_T jets should be estimated with the Matrix Element (ME) calculation.

260 million events are generated with the ALPGEN [20] for the SM processes mentioned above. Up to 6 quarks or gluons are emitted with the ME calculation in ALPGEN. The region of $P_T > 40$ GeV is covered with these partons. The produced events are fed into the PS generator (PYTHIA6.2 [7]) in order to evolute the QCD shower, which covers the soft and collinear regions. Special treatments are necessary in order to remove the double count of jet produced with the ME calculation and the PS jets. When the jet from the PS evolution emits into the phase space which is covered with the ME, the event is discarded [21]. This rejection factor is related to Sudakov factor. Figures 2.4.2 show the P_T distribution of the leading and 4th jets of Drell-Yan processes. In both figures the hatched histogram shows the ME predictions, and dotted line shows the predictions of the PS generator. The P_T distributions calculated with the PS model is softer than the ME prediction, and this difference becomes larger for higher jet-multiplicity. About 2nd order of magnitude is different for 4th leading jet as shown in Fig. 2.4.2.

The showered events are fragmented and decayed with the PYTHIA, and the detector effect is taken into account using the smearing Monte Carlo simulation of the ATLAS detector (ATLFAST [22]). The following event selections are applied, which are the standard selections for SUSY searches and not yet optimized depending on the sparticles mass.

- $\not\!\!E_T$ is larger than 100 GeV
- P_T is larger than 100 GeV for at least one jet
- Number of jets with $P_T > 50$ GeV is larger than or equal to 4.
- Transverse Sphericity is larger than 0.2, that means event are not back to back.
- If the event contains one isolated lepton (e or μ), whose P_T is larger than 10 GeV (defined as

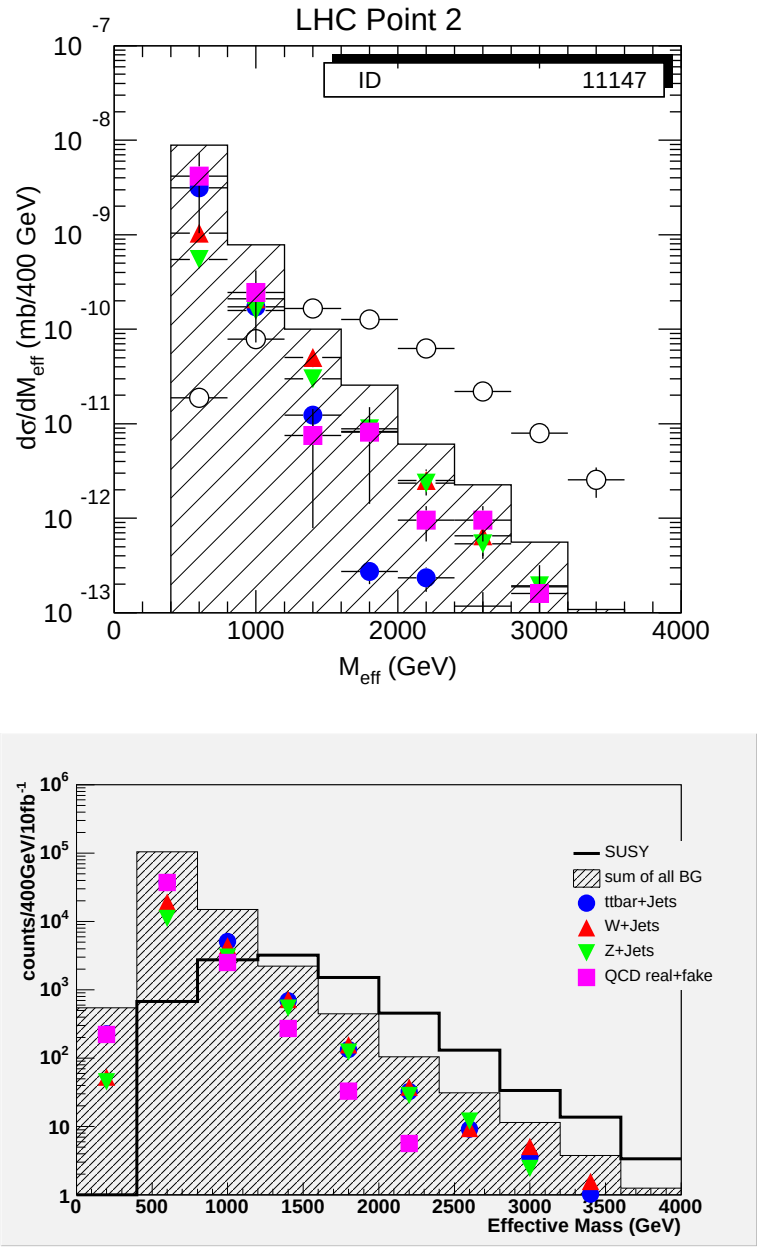

Fig. 2.4.3: Effective mass distributions of the SUSY signal and the SM background processes for no lepton mode: (a) Prediction with the PS model (b) Prediction with the ME. Mass of the scalar quarks and gluino is 1TeV in both figures.Blue circle, red triangle, green triangle and magenta box show the top,W,Z and QCD processes, respectively.

'one lepton mode'), the transverse mass between the lepton and $\not\!\!E_T$ is required to be larger than 100 GeV to reduce leptonic decay of the W boson. Event without the isolated lepton is also accepted as 'no lepton mode'.

The effective mass, which is define as $\not\!\!E_T + \sum_{4jets} P_T$, is a good variable, since the both $\not\!\!E_T$ and P_T of jets would have discrimination power between the SUSY signal and the SM background processes. Figures. 2.4.3 show the effective mass distributions of the SUSY signal, in which mass of squarks and gluino is 1 TeV, and the SM background processes. These are results of no lepton

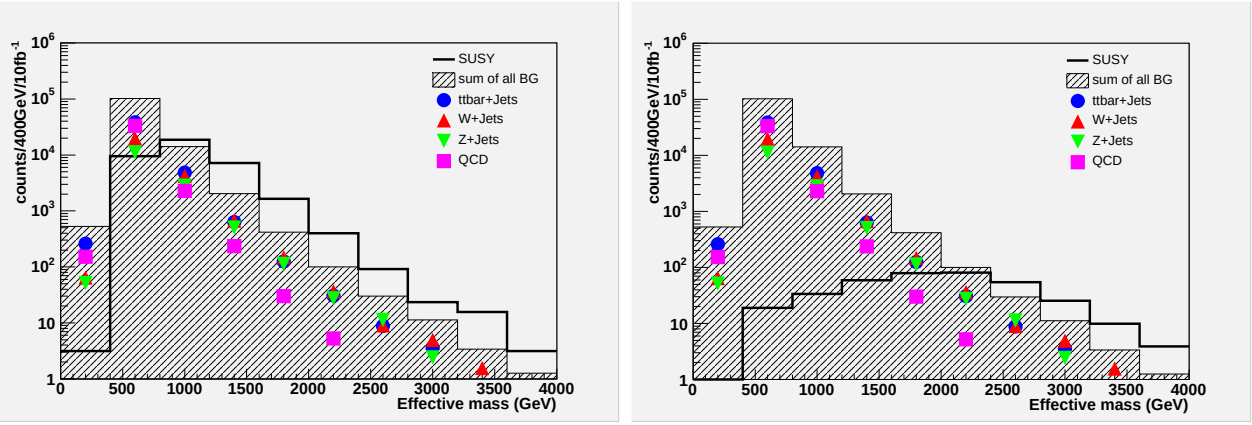

Fig. 2.4.4: Effective mass distributions of the SUSY signal and the SM background. The masses of both the squarks and gluino are (a) 700 GeV and (b) 1.5 TeV. Notation is the same as in Fig. 2.4.3.

mode after the selection criteria are applied. Left side figure shows the old results estimated with the PS model [22] and right shows the new results estimated with the ME + PS prediction.

(1) The SM background contributions become larger by factor 2-4 depending on the effective mass. They become the same order of the SUSY signal. There are many uncertainties in these estimations, for example effect of the higher order, choice of the various scales, and uncertainties of PDF. Especially the region of the 'high P_T' and 'high jet-multiplicity' are important and they have to be understood directly using real data. We will have enough luminosity to study these regions at Tevatron Run-II. (2) The slope of the distribution of the background is more gentle and the similar to that of the SUSY signal. Figures. 2.4.4 show the same distributions for the different SUSY mass scales. The slope of the background processes is very similar for the various SUSY mass scales, and they show we have to understand these slope well. Effect of the higher order, choice of the various scales are important to be understood. (3) Four types of background processes contribute at the same level.

The Z+jets and the QCD background processes can be significantly suppressed if one isolated lepton is required. Furthermore the transverse mass cut removes effectively the background including the leptonic decay of W boson (W+jets and tt+jets). Total number of background can be suppressed by factor about 20. On the other hand, the SUSY signal is reduced only by factor 2-5 depending the SUSY parameters. Fig. 2.4.5 shows the effective mass distribution for the one lepton mode. As you can see, clear excess will be observed. The dominant background processes are tt + jets and W +jets, which are more controllable than the QCD background processes.

2.4.3 Fake $\not\!\!E_T$

The missing transverse energy, $\not\!\!E_T$, is vital variable for SUSY searches. It is mainly produced with neutralino and neutrino, but also produced with the limited energy resolution of Hadronic jets. This is called as ' fake $\not\!\!E_T$ ' . The non-Gaussian response of the jet energy measurements

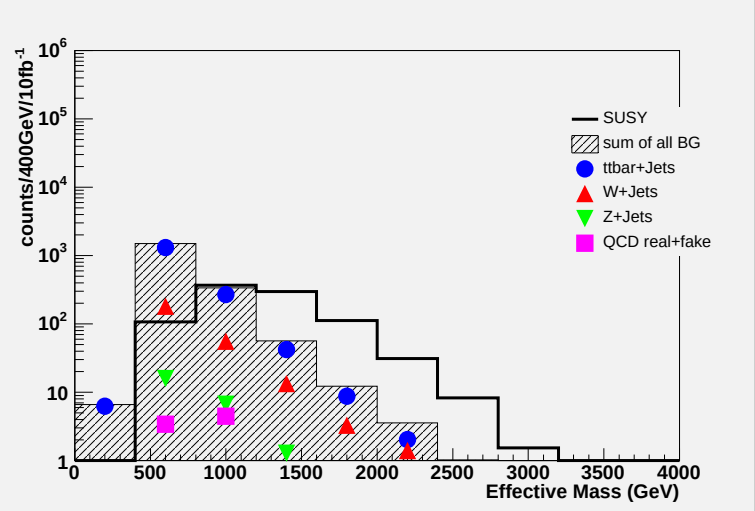

Fig. 2.4.5: Effective mass distributions of the SUSY signal and the SM background processes for one lepton mode: Notations are the same as in Fig. 2.4.3.

makes non-Gaussian tail in the fake $\not\!\!E_T$ distribution. Various detector components makes the different response(resolution) for the jet. Then the fake $\not\!\!E_T$ distribution becomes more complicated as shown in Fig. 2.4.6(a).

There are two important points:

- The resolution of the bulk part depends on the sum of energies deposited on the calorimeters, and also the dead material in front of or the inside of the calorimeters. If the event-topologies are different, the fraction of the energy in the various detector components becomes different, and the resolutions will be different.
- Distribution has a tail apart from the Gaussian as shown in the figure. This tail becomes dangerous background, since the QCD multi-jet processes have a huge cross-section.

Now the statistics of the simulated samples is very limited, and we can not conclude the shape/dependence of the tail. More careful studies of the tail are necessary, i.e. the dependence of the tail on the materials in front of the detectors, P_T of the jets, the contributions from the pileup and underlying. The dependence of the event-topologies is also important. The Fake $\not\!\!E_T$ points simply the direction of the jet, if jet multiplicity is small. $\not\!\!E_T$ is required not to point the jet direction for SUSY searches at Tevatron, and this selection removes the events including the large fake $\not\!\!E_T$. But the SUSY signals at LHC are, I have already mentioned, multi-jets topologies. Direction of the fake $\not\!\!E_T$ will be smeared in the multi-jets events. These studies using Tevatron run-II data are useful for the quick startup of the LHC.

2.4.4 Conclusions

The Standard Model background processes are estimated with the Matrix Elements calculation, and it is found out that the background contributions become larger than that we have expected.

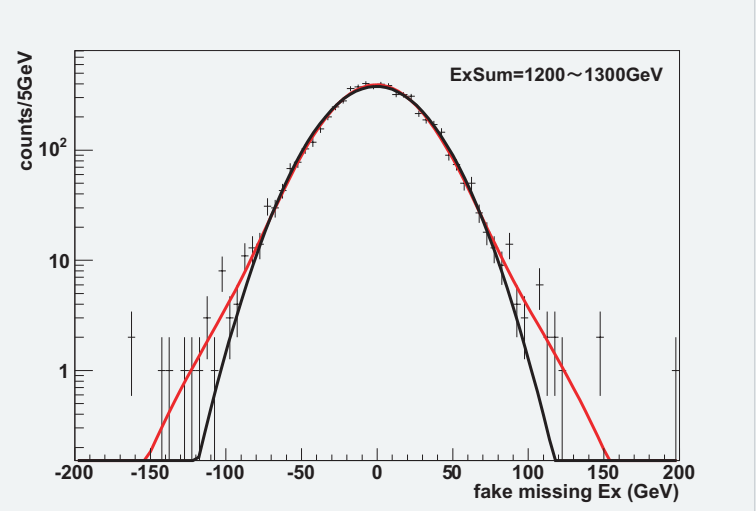

Fig. 2.4.6: Distributions of the fake missing Ex: points with error show the simulated results. Black and red lines show the fitted result with single and double Gaussian, respectively.

The distributions of the background processes are header and are similar to the SUSY signal. The careful studies of the Standard Model processes are useful using Tevatron Run-II data, especially studies of the slope of the P_T and missing E_T distributions of $W^{\pm}$ + jets, Z^0 + jets and $t\bar{t}$ + jets.

$\not\!\!E_T$ is the vital variable for SUSY searches and will be complicated distribution depending on the sum of the energies, the dead materials, and event-topologies. Detail studies using Tevatron Run-II are useful for quick start up of LHC.

2.5 Search for $B_s^0 \to \mu^+\mu^-$ and $B_d^0 \to \mu^+\mu^-$ Decays at the Tevatron

D. Glenzinski[1], C.-J. Lin[1], R. Bernhard[2] and F. Lehner[2]

[1] *Fermilab (CDF)*
[2] *University of Zürich (DØ)*

In the Standard Model (SM), Flavor-Changing Neutral Current (FCNC) decays are highly suppressed and can only occur through higher order diagrams. The decay rate for the FCNC decay $B_s^0 \to \mu^+\mu^-$ [7] is proportional to the CKM matrix element $|V_{ts}|^2$. The rate of $B_d^0 \to \mu^+\mu^-$ decays is further suppressed by the ratio of $|V_{td}/V_{ts}|^2$. The SM expectations for these branching fractions are $\mathcal{B}(B_s^0 \to \mu^+\mu^-) = (3.42 \pm 0.54) \times 10^{-9}$ and $\mathcal{B}(B_d^0 \to \mu^+\mu^-) = (1.00 \pm 0.14) \times 10^{-10}$ [23, 24], which are about two orders of magnitude smaller than the current experimental sensitivity. However, new physics contributions can significantly enhance these branching fractions. In the absence of an observation, any improvements to the limits can be used to set significant constraints on many SUSY models.

The best existing experimental limits are $\mathcal{B}(B_s^0 \to \mu^+\mu^-) < 4.1 \times 10^{-7}$ using $240\ \mathrm{pb}^{-1}$ of DØ data [25, 26] and $< 1.5 \times 10^{-7}$ using $364\ \mathrm{pb}^{-1}$ of CDF data [27] at the 90% confidence level (C.L.), and $\mathcal{B}(B_d^0 \to \mu^+\mu^-) < 8.3 \times 10^{-8}$ using 111 fb of Babar data [28] and $< 3.9 \times 10^{-8}$ using $364\ \mathrm{pb}^{-1}$ of CDF data [27] at the 90% confidence level.

In the following sections we briefly describe the analysis strategies employed by CDF and DØ in these $B_s^0 \to \mu^+\mu^-$ and $B_d^0 \to \mu^+\mu^-$ rare decay searches. Since the techniques employed are quite similar in the two experiments, we begin with a discussion of the general analysis strategy in section 2.5.1.

2.5.1 Analysis Strategy

General The CDF and DØ collaborations have published several papers describing searches for the rare $B_s^0 \to \mu^+\mu^-$ and $B_d^0 \to \mu^+\mu^-$ decays at the Tevatron [25, 26] [27, 29, 30]. Although they all use a very similar analysis strategy, we concentrate here on describing the most recent CDF and DØ analyses which yield the most stringent limits to date.

In general, the strategy is to collect the signal sample on a di-muon trigger that is as inclusive as possible. The analysis is simplified and the systematic uncertainties reduced by collecting both the signal and normalization ($B \to J/\psi X$) decays on the same trigger. Similarly, the reconstruction requirements are also chosen to be as loose possible while still maintaining a high purity so that the same $\mu^+\mu^-$ reconstruction requirements are made for both the signal and normalization modes. After a the pre-selection, four discriminating variables are used to further reduce the expected background while maintaining good signal efficiency. Both collaborations employ a "blind" analysis strategy when choosing the final selection criteria. For these optimizations the

[7] Throughout this section inclusion of charge conjugate modes is implicit.

signal mass region in the data is kept hidden, the backgrounds are estimated from the data mass sidebands, and the signal efficiency is estimated from Monte Carlo (MC) samples. Only after the final selection criteria have been chosen, and after the background estimates and MC modeling of the signal efficiency have both been verified using data control samples, is the data signal region revealed.

Event Selection and Optimization For $B_s^0 \to \mu^+\mu^-$ decays the final state is fully reconstructed. This yields invariant mass and vertex resolutions that are much better than for the partially reconstructed final states which dominate the background. In addition to the pre-selections requirements, four different variables are used to suppress the background. We exploit the long *B* lifetime and use $|\vec{L}|$, the 3D decay length of the di-muon pair relative to the primary interaction vertex. Combinatoric background and partially reconstructed *B* hadrons are removed with requirements on the 3D opening angle between the di-muon momentum ($\vec{p}^{\mu\mu}$) and decay length ($\vec{L}$) vectors, $\Delta\Theta$. Since *b*-quark fragmentation is hard, *B* hadrons carry most of the transverse momentum of the *b* quark, and thus are isolated. An Isolation variable [8], I, is therefore used to enhance the heavy flavor content of the sample and also to reject partially reconstructed *B* hadrons, which are less isolated since some of the daughter tracks are included in the isolation cone. The last variable is $M_{\mu\mu}$, the di-muon invariant mass.

To further enhance signal and background separation CDF constructs a multivariate likelihood ratio based on the input variables: I, $\Delta\Theta$, and $P(\lambda) = e^{-\lambda/c\tau_{B_{s(d)}}}$, where $\lambda = cM_{\mu\mu}|\vec{L}|/|\vec{p}^{\mu\mu}|$ and $\tau_{B_{s(d)}}$ is the world average $B_{s(d)}$ lifetime. The $P(\lambda)$ variable offers the same background discrimination as λ or $\vec{L}$ but with reduced sensitivity to the modeling of the vertex resolution. The likelihood ratio is then defined to be

$$L_R = \frac{\prod_i \mathbf{P}_s(x_i)}{\prod_i \mathbf{P}_s(x_i) + \prod_i \mathbf{P}_b(x_i)}, \tag{2.5.1}$$

where $x_1 = I$, $x_2 = \Delta\Theta$, $x_3 = P(\lambda)$, and $\mathbf{P}_{s(b)}(x_i)$ is the probability that a signal (background) event has an observed x_i. The probability distributions for the signal events are obtained from the signal MC and the background distributions are taken from the data sidebands. Using the procedure detailed in reference [27] CDF optimized the L_R and $\vec{p}_T^{\,\mu\mu}$ requirements as well as the width of the signal search window. The optimization resulted in this choice of final selection criteria: $L_R > 0.99$, $\vec{p}_T^{\,\mu\mu} > 4$ GeV/c, and a search window of ± 60 GeV/c^2 centered on the world average $B_{s,d}^0$ mass.

The expected number of background events in the CDF analysis is estimated by extrapolating the number of sideband events passing the pre-selection requirements to the signal window and

[8] The B-candidate isolation is defined as $I = |\vec{p}_T^{\,\mu\mu}|/(\sum_i p_T^i + |\vec{p}_T^{\,\mu\mu}|)$, where the sum is over all tracks with $\sqrt{\Delta\eta^2 + \Delta\phi^2} \leq 1$; $\Delta\phi$ and $\Delta\eta$ are the azimuthal angle and pseudorapidity of track i with respect to $\vec{p}^{\,\mu\mu}$. Only tracks that extrapolate within 5 cm of the di-muon vertex along the z-axis are included in order to exclude tracks orginating from other pp interactions which may have occured in the same bunch crossing.

then scaling by the expected rejection, κ, for a given L_R requirement. The parameter κ is determined from the background L_R distribution, which is generated by randomly sampling the $P(\lambda)$, $\Delta\Theta$, and I distributions from the data sidebands to improve statistical precision on κ. The procedure for estimating the background is cross-checked using control samples from the data: like sign $\mu^{\pm}\mu^{\pm}$ events, $\mu^+\mu^-$ events with $\lambda < 0$, and a fake-muon enhanced $\mu^+\mu^-$ sample in which at least one muon candidate fails the muon quality requirements. The background predictions are compared to the number of events observed in the search window for a wide range of L_R requirements. No statistically significant discrepancies are observed.

In the DØ analysis background is suppressed by making stringent requirements on the variables $\Delta\Theta$, I, and the transverse decay length significance, L_T/σ_{L_T}, where L_T is the projection of $\vec{L}$ onto the plane transverse to the beamline. The L_T-significance was found to have a better discriminating power than L_T alone. DØ optimizes the requirements on these three variables using the procedure described in reference [25, 26]. The optimization resulted in this choice of final selection criteria: $\Delta\Theta < 0.2$ rad, $I > 0.56$, and $L_T/\sigma_{L_T} > 18.5$. The width of the search window is ± 180 MeV/c^2 around the mean reconstructed B_s^0 mass. The background is estimated by interpolation using an unbinned likelihood fit to the sideband data.

Normalization Both collaborations choose to normalize the $\mathcal{B}(B_s^0 \to \mu^+\mu^-)$ to $B^+ \to J/\psi K^+$ decays rather than $B_s^0 \to J/\psi\phi$ decays. The reasons for this are that the B^+ decay yields larger statistics and the lifetime and branching ratio are well known from e^+e^- experiments. In contrast the B_s^0 branching ratio has only been measured at the Tevatron [31] with limited precision[9]. One might alternatively consider using the measured $\mathcal{B}(B^+ \to J/\psi K^+)$ and inferring $\mathcal{B}(B_s^0 \to J/\psi\phi)$ using $SU(3)$ symmetries. However, at present the theoretical uncertainties associated with these symmetry assumptions are about 20%, which is larger than the 13% uncertainties associated with the f_u/f_s needed for the $B^+ \to J/\psi K^+$ normalization. Moreover, the $B_s^0 \to J/\psi\phi$ final state presents additional challenges. For example, the reconstructed final state has four tracks, two from the $J/\psi \to \mu^+\mu^-$ decay and two from the $\phi \to K^+K^-$ decay, which results in larger kinematic differences with respect to the two-body $B_s^0 \to \mu^+\mu^-$ decays compared to the differences observed in the (effective) three-body $B^+ \to J/\psi K^+ \to \mu^+\mu^- K^+$ final state. The understanding of the efficiency for the $B_s^0 \to J/\psi\phi$ final state is further complicated by the presence of CP-even and CP-odd decay components with significantly different lifetimes.

[9] In addition, normalizing to this measured B_s^0 branching ratio is a bit disingenuous since in reference [31] $\mathcal{B}(B_s^0 \to J/\psi\phi)$ is determined by normalizing to $\mathcal{B}(B^+ \to J/\psi K^+)$.

Limit Setting Both CDF and DØ normalize to the $\mathcal{B}(B^+ \to J/\psi K^+)$ and calculate the upper limit on $\mathcal{B}(B_s^0 \to \mu^+\mu^-)$ using the following expression[10]:

$$\mathcal{B}(B_s^0 \to \mu^+\mu^-) \leq \frac{N_{B_s^0}^{ul}}{N_{B^+}} \cdot \frac{A_{B^+}}{A_{B_s^0}} \cdot \frac{\mathcal{B}(B^+ \to J/\psi(\to \mu^+\mu^-)K^+)}{(f_s/f_u) + R}, \tag{2.5.2}$$

where $N_{B_s^0}^{ul}(N_o, N_b)$ is the upper limit on the number of $B_s^0 \to \mu^+\mu^-$ decays observed at some confidence level given N_o observed events in the mass signal region when expecting N_b background events; N_{B^+} is the number of observed $B^+ \to J/\psi K^+$ candidates; $A_{B_s^0}$ and A_{B^+} are the total acceptance for the $B_s^0 \to \mu^+\mu^-$ and $B^+ \to J/\psi K^+$ decays, respectively, including trigger, reconstruction, and final selection efficiencies; the $\mathcal{B}(B^+ \to J/\psi K^+ \to \mu^+\mu^- K^+) = (5.88 \pm 0.26) \times 10^{-5}$ is taken from reference [32]; the fragmentation ratio f_s/f_u is taken from [11]; and $R = (\mathcal{B}(B_d^0 \to \mu^+\mu^-)/\mathcal{B}(B_s^0 \to \mu^+\mu^-)) \cdot (A_{B_d^0}/A_{B_s^0})$. Since the B_d^0 and B_s^0 are only $90\ \mathrm{MeV}/c^2$ apart, the factor R corrects for $B_d^0 \to \mu^+\mu^-$ "contamination" in the $B_s^0 \to \mu^+\mu^-$ signal region. In practice, the CDF $M_{\mu\mu}$ resolution of about $24\ \mathrm{MeV}/c^2$ is good enough to resolve the two states so that the $B_s^0 \to \mu^+\mu^-$ and $B_d^0 \to \mu^+\mu^-$ signal windows are chosen to have a small overlap. This overlap is ignored (ie. R is set to 0) when estimating the branching ratio limits. Similarly, DØ also conservatively sets $R = 0$. The $M_{\mu\mu}$ resolution of DØ is about $88\ \mathrm{MeV}/c^2$ so that the $B_s^0 \to \mu^+\mu^-$ and $B_d^0 \to \mu^+\mu^-$ final states can not be separately resolved. DØ chooses to interpret their result as a limit on $\mathcal{B}(B_s^0 \to \mu^+\mu^-)$ since, as discussed in section 2.5, $\mathcal{B}(B_d^0 \to \mu^+\mu^-)$ is expected to be CKM suppressed in most models. The experimental inputs and observed limits are summarized in Table 2.5.1.

2.5.2 Tevatron Combination

The most recent CDF and DØ results have been combined [33] properly accounting for the correlated uncertainties. The two measurements are summarized in Table 2.5.1. The single-event-sensitivity, *ses*, is defined as the $\mathcal{B}(B_s^0 \to \mu^+\mu^-)$ obtained when setting $N_{B_s^0}^{ul} = 1$ in equation 2.5.2. Despite using approximately 20% less luminosity, the DØ analysis maintains a slightly better *ses*, largely owing to their superior muon acceptance. On the other hand, the CDF analysis has a much smaller background expectation, even with 20% more luminosity, largely owing to their superior mass resolution. The expected limits are defined as the average limit obtained by summing over all possible experimental outcomes, N_o, weighted by their Poisson probability when expecting N_b background events. It is a measure of the exclusion power of given method assuming no signal is observed and takes into account the *ses* and background expectations.

The combined limit was obtained using a Bayesian technique [34, 35, 32] that parameterizes the uncertainties as gaussian distributions in the integration. A flat prior was used for the unknown $\mathcal{B}(B_s^0 \to \mu^+\mu^-)$ and it was verified that the resulting limit is insensitive to reasonable variations

[10] The expression for $\mathcal{B}(B_d^0 \to \mu^+\mu^-)$ is derived from equation 2.5.2 by replacing B_s^0 with B_d^0 and the fragmentation ratio f_u/f_s with $f_u/f_d = 1$.

[11] f_x is the fraction of weakly decaying B_x hadrons in b quark fragmentation. We use values from [32].

	CDF U-U	CDF U-X	DØ
Luminosity	$364\ \mathrm{pb}^{-1}$	$336\ \mathrm{pb}^{-1}$	$300\ \mathrm{pb}^{-1}$
$(A_{B^+}/A_{B_s^0})$	0.852 ± 0.084	0.485 ± 0.048	0.247 ± 0.019
N_{B^+}	1785 ± 60	696 ± 39	906 ± 41
N_b	0.81 ± 0.12	0.66 ± 0.13	4.3 ± 1.2
N_o	0	0	4
ses $(\times 10^7)$	1.04 ± 0.16	1.52 ± 0.25	0.59 ± 0.09
	(0.62 combined)		
expect. limit 90% C.L.	3.5×10^{-7}	5.6×10^{-7}	3.5×10^{-7}
	(2.0×10^{-7} combined)		
obsvd. limit 90% C.L.	(1.5×10^{-7} combined)		3.2×10^{-7}

Table 2.5.1: Summary of CDF and DØ results used to calculate the Tevatron combined limit on $\mathcal{B}(B_s^0 \to \mu^+\mu^-)$. The CDF analysis is divided in two separated search channels (U-U and U-X) with different muon acceptance. The *ses*, and expected and observed limits for the combination of the two CDF channels are given parathetically.

of the cut-off assumed in the definition of the prior. In the combination the uncertainties on the fragmentation ratio and the normalization branching ratios were added in quadrature and treated as fully correlated. All the other uncertainties were assumed to be uncorrelated. The resulting Tevatron combined limit is

$$\mathcal{B}(B_s^0 \to \mu^+\mu^-)_{comb.} < 1.2\,(1.5) \times 10^{-7} \text{ at a } 90\%\,(95\%)\,\text{C.L.} \tag{2.5.3}$$

assuming for the fragmentation ratio the standard PDG value [32] of $f_u/f_s = 3.71 \pm 0.41$. Using an evaluation of the fragmentation function based on Tevatron data alone ($f_u/f_s = 3.32 \pm 0.59$) would improve the limit by 10%.

The excellent CDF mass resolution allows them to carry out an independent search for $B_d^0 \to \mu^+\mu^-$ decays. As previously reported the resulting limit is $\mathcal{B}(B_d^0 \to \mu^+\mu^-) \leq 3.9 \times 10^{-8}$ at 90% C.L. An independent search is not possible for the DØ experiment. However, the DØ results can be interpreted as limits on $\mathcal{B}(B_d^0 \to \mu^+\mu^-)$ by assuming there is $B_s^0 \to \mu^+\mu^-$ contribution to the signal region. Interpreting the DØ results in this way and combining with the CDF limit gives

$$\mathcal{B}(B_d^0 \to \mu^+\mu^-)_{comb.} < 3.2\,(4.0) \times 10^{-8} \text{ at a } 90\%\,(95\%)\,\text{C.L.} \tag{2.5.4}$$

It should be stressed that the Tevatron combined limit on $\mathcal{B}(B_d^0 \to \mu^+\mu^-)$ is not independent of the B_s^0 limit, since the same DØ information is used in both.

2.5.3 Tevatron Outlook

The projected Tevatron reach for the DØ and CDF combined search for $B_s^0 \to \mu^+\mu^-$ decays is shown in Figure 2.5.1 as a function of the luminosity collected per experiment. The projection

assumes the analysis techniques are unchanged and that the trigger and reconstruction efficiencies are unaffected with increasing luminosity. If, then, each experiment collects 8 fb the Tevatron combination will allow for a "5σ discovery" down to $B_s^0 \to \mu^+\mu^-$ branching ratios of about 7×10^{-8} and for 90% C.L. exclusions down to branching ratios of about 2×10^{-8}. Both experiments are pursuing further improvements to the analysis sensitivity, which would push the Tevatron combined sensitivity to still lower branching ratios. Even if no signal is observed, the resulting stringent limit would eliminate a very large part of the high $\tan\beta$ parameter space in many supersymmetric models.

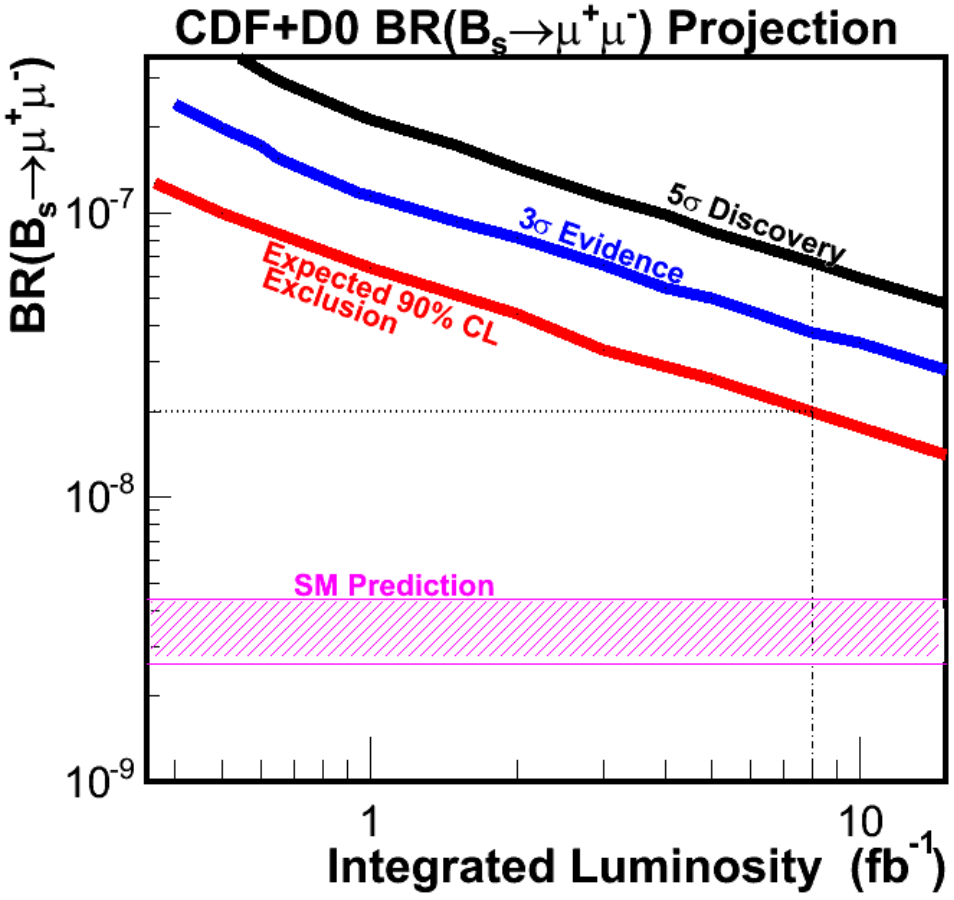

Fig. 2.5.1: The projected Tevatron combined reach for $\mathcal{B}(B_s^0 \to \mu^+\mu^-)$ as a function of the integrated luminosity collected by each experiment.

2.5.4 Relevance for LHC

At the Tevatron, the search for the decay $B_s^0 \to \mu^+\mu^-$ is a part of the core Run II physics program. An observation of $B_s^0 \to \mu^+\mu^-$ at the Tevatron would unambiguously signal the presence of new physics. At the LHC Atlas, CMS, and LHCb are all expected to have sensitivity down to the SM

branching ratio. In the following we discuss a few issues relevant for these future LHC analysis. In particular we offer comments concerning the mass resolution, background composition, choice of normalization mode, and trigger definitions.

Obviously a crucial aspect in the $B^0_{s,d} \to \mu^+\mu^-$ analysis is the experimental di-muon mass resolution. It's important for two reasons. First, an excellent mass resolution helps to reject background events in the signal region since high efficiency is maintained for narrow mass windows. The different background expectation numbers from DØ and CDF roughly reflect their mass resolutions. Second, it will be important to measure $\mathcal{B}(B^0_s \to \mu^+\mu^-)$ and $\mathcal{B}(B^0_d \to \mu^+\mu^-)$ separately, and this is most cleanly accomplished with mass resolutions that are small compared to $(M_{B^0_s} - M_{B^0_d}) = 90$ MeV/c^2. The ratio of these branching ratios can help in determining the flavor structure of any new physics which might be present. For minimal flavor violating (MFV) models, $\mathcal{B}(B^0_d \to \mu^+\mu^-)$ remains CKM suppressed relative to $\mathcal{B}(B^0_s \to \mu^+\mu^-)$. This is not necessarily true for non-MFV models such as R-parity violating SUSY, which can produce large enhancements, even for low values of $\tan\beta$, in either or both of the B^0_s and B^0_d FCNC decay rates.

The exact background composition at the Tevatron is not precisely known and is modeled from sideband data. It includes contributions from sequential semileptonic decays ($b \to c\mu^- X \to \mu^+\mu^- X$), gluon splitting ($g \to b\overline{b} \to \mu^+\mu^- X$), and fakes ($b \to \mu X$ + fake muon). Backgrounds from $B^0_{s,d} \to h^+h^-$ ($h^\pm = \pi^\pm, K^\pm$) are, at present, negligible. This will not be the case at the LHC, where these decays may form an irreducible background. Other exclusive decays from B_c (e.g. $B^\pm_c \to J/\psi(\to \mu^+\mu^-)\mu^\pm\nu$) or *B* baryons might also become important at the LHC. These types of backgrounds are difficult since they cannot be trivially estimated from the data sidebands, but instead require dedicated estimates that rely on a detailed understanding of the trigger performance and hadron-to-muon fake rates. It will thus be important to have a set of triggers which allow for the necessary studies.

Systematic effects can be minimized with an intelligent choice of the normalization decay. For the reasons discussed in Section 2.5.1, the Tevatron searches have normalized to the decay $B^+ \to J/\psi(\mu^+\mu^-)K^+$. This choice incurs a $\pm 13\%$ systematic uncertainty associated with the fragmentation ratio, f_u/f_s, which is correlated across all measurements. And although it is plausible to assume that the ratios determined from $e^+e^- \to Z^0 \to b\bar{b}$ experiments can be extrapolated to high energy $p\bar{p} \to b\bar{b}$ collisions, there is no strong theoretical argument in support of it. It is thus desirable to find a fragmentation independent normalization using a known B^0_s decay - e.g. $B^0_s \to J/\psi\phi$ decays. The present Tevatron searches suffer from a relatively low yield of $B^0_s \to J/\psi\phi$ decays. However, as the Tevatron dataset grows it is very likely that measurements on this important decay will considerably improve such that $B^0_s \to J/\psi\phi$ will become a well-known "standard" before LHC turns on. Given the large LHC datasets eventually available, it may be possible to normalize to one of the $B \to h^+h^-$ decays if an efficient trigger with a managable rate can be defined. The consideration of which normalization mode to choose should be coupled with the analysis trigger strategy.

The trigger plan for this analysis should be carefully considered. Generally speaking three types of triggers will be needed: A) one that collects the signal sample used for the analysis, B) a second that is unbiased with respect to the first so that the efficiency of trigger A can be determined, and C) a third that collects samples of heavy flavor hadronic decays (e.g. $B \to h^+h^-$). We'll briefly discussed issues relevant to each of these. The analysis is greatly simplified if trigger A simultaneously collects both the $B^0_{s,d} \to \mu^+\mu^-$ decays and the normalization decays. It is important to note that for the Tevatron results, the single largest correction in equation 2.5.2 comes from the ratio of trigger acceptance between the $B^0_s \to \mu^+\mu^-$ and normalization decay. This ratio is driven by the trigger requirements and reflects the fact that the $p_T(\mu)$ spectrum is softer for the $B^+ \to J/\psi(\to \mu^+\mu^-)K^+$ decays than for the two body $B^0_s \to \mu^+\mu^-$ decays. Thus the $B^+ \to J/\psi K^+$ trigger acceptance can have a much stronger dependence on the $p_T(B)$ than the $B^0_s \to \mu^+\mu^-$ acceptance. Depending on the trigger, this could be a source of significant systematic uncertainty, especially once model uncertainties associated with the $p_T(B)$ spectrum are folded-in. These effects should be considered when choosing a normalization mode. For example, normalizing to $B^0_s \to J/\psi\phi$ ($B \to h^+h^-$) decays would likely exacerbate (mitigate) these effects. The other two trigger paths must be designed to avoid introducing any kinematic bias relative to the requirements of trigger A. The principal aim of trigger B is to determine whether or not trigger A has any strong kinematic dependence which might effect the signal and normalization decay differently (e.g. $p_T(\mu)$ or $p_T(B)$ dependencies). Trigger C is used to collect clean $K^\pm$ and $\pi^\pm$ samples (e.g. from the decay $D^{+*} \to D^0\pi^+ \to K^-\pi^+\pi^+$) from which to determine the kaon- and pion-to-muon fake rates needed to accurately estimate the $B \to h^+h^-$ backgrounds. Ideally, large samples of $B \to h^+h^-$ decays would also be available for detailed study. Careful attention should be given to the expected rates of these triggers. It may happen that some or all of them may be rate limited at higher luminosities. If pre-scales are employed, care should taken to ensure that the data collected with triggers B and C have a luminosity profile similar to that of trigger A so that trigger efficiencies and backgrounds can be reliably estimated over the full range of relevant luminosities.

3 Particle-based Phenomenology

Let us assume that a signal for new physics will be observed at the Tevatron or the LHC. The question is how should one go about explaining what that signal is in a well defined theory. The simplest first attempt would be to try to fit the signal by assuming the existence of a single particle beyond the ones discovered already, in a Lorentz invariant quantum field theory. This is a good description at the TeV scale for many models that include several additional particles, with only one of them being relatively easy to discover.

If the signal cannot be convincingly explained by the existence of a single new particle, then one should attempt to explain it using several new particles. This situation occurs in a wide class of models where the signatures of different particles are correlated, for instance through cascade decays. We concentrate in this section on signatures produced by individual particles, leaving the discussion of models with multiple particles for Sec. 4.

The new particle is specified by its spin and its $SU(3)_c \times SU(2)_w \times U(1)_y$ charges. All other properties are described by some continuous parameters: mass, mixings and couplings. The number of types of new particles that are likely to be discovered at the Tevatron and the LHC is rather limited. The majority of the theories beyond the Standard Model discussed in the literature include only particles of spin 0, 1/2, 1, or 2. Higher-spin particles could exist, but they would require complicated strongly-coupled theories, or departures from quantum field theory (for a study of higher-spin particles at hadron colliders, see Ref. [36]).

Under $SU(3)_c$, new particles are most likely to transform as color singlets, triplets, octets, or sextets. Higher $SU(3)_c$ representations could exist, but would pose a variety of theoretical challenges. Under $SU(2)_w$, new particles may transform as singlets, doublets or triplets, while higher representations are not usually present in the models proposed so far.

Finally, the hypercharges of new particles are constrained by the requirement that the electric charge of any color-singlet (or of the ensuing hadrons in the case of colored particles) is an integer. Otherwise, the lightest particle with non-integer electric charge would be stable on cosmologial time scales, and would be ruled out for most interesting regions of parameter space by a variety of searches for stable charged particles.

We will not attempt to study here all these possible particles. We only display several representative examples, and urge the readers to analyze as many of the other cases before the start of the LHC. Sec. 3.1 describes the case of a heavy spin-1 particle that is a singlet under the Standard Model gauge group, usually referred to as a Z' boson, emphasizing the case where the Z' interacts with the quarks and leptons. Sec. 3.2 also discusses the collider implications of a Z' boson, but in the case where it couples exclusively to gauge bosons. Sec. 3.3 analyzes a heavy spin-1 particle that is color singlet and has electric charge ± 1, usually referred to as a W' boson

Sec. 3.4 presents a study of a spin-1/2 particle which is color-triplet, and has the same charges for the left- and right-handed components. This commonly referred to as a vectorlike quark. Sec. 3.5 deals with spin-0 particles that are $SU(2)_w$ triplets. Sec. 3.6 presents a study of

the collider signatures of a new electrically-charged particle which is stable enough to escape the detector.

3.1 Z' at the LHC

Fabienne Ledroit, Julien Morel, Benjamin Trocmé

Laboratoire de Physique Subatomique et de Cosmologie,
Grenoble, France

In this section, we develop a model independent determination of the ATLAS efficiency in detecting Z' bosons decaying to an electron-positron pair. This efficiency is then applied to the cross section predicted in the CDDT parameterization of Z' models, a model independent parameterization already used by CDF. We then derive the ATLAS Z' discovery potential in this framework. Finally we compare this potential to the results from LEP and the Tevatron.

The existence of an additional spin 1 neutral boson -denoted as Z' in this section- is predicted in many extensions of the Standard Model (SM), such as E_6 or $SO(10)$ Grand Unified Theories, extra dimensions theories, little Higgs models...
At the LHC, the Z' production process mainly consists in a quark-antiquark annihilation, the $u\bar{u}$ and $d\bar{d}$ cases being largely dominant in most models[12]. In all the following, only decays to known particles are considered; because of the high QCD backgound, there is very little hope to detect the hadronic decays of a Z' boson; with a large missing energy coming from two neutrinos, the $\tau^+\tau^-$ decay is also a very challenging channel. With the Drell Yan process as unique irreducible background and a very limited reducible background, the electron and muon channels are much more promising and can be considered as golden channels to discover a new neutral gauge boson. Up to Z' masses of about 5 TeV, the signature simply consists in a high invariant mass peak above the Drell Yan line shape.

In this section, the ATLAS potential in term of discovery of a Z' decaying to an electron-positron pair is studied. It is especially detailed in the CDDT parameterization[37] adopted by the CDF collaboration[38]; this parameterization takes into account both experimental limits and general theoretical assumptions to constrain the models with an additionnal neutral gauge boson. Given these, four classes of solutions are found, three parameters remaining totally free in the four classes; these parameters are the mass of the additionnal gauge boson, $M_{Z'}$, the global coupling strength, $g_{Z'}$, and a parameter x describing the relative coupling strength to the different fermions. An original method to extract a realistic efficiency depending on the model is presented. Since the reducible background is expected to be small, only the irreducible background was considered.

[12] In the following, the $s\bar{s}$, $c\bar{c}$, $b\bar{b}$ processes are ignored in order to ease the reading; the treatment of $u\bar{u}$ and $d\bar{d}$ events can be generalised to these marginal cases.

3.1.1 Samples

In order to study the reconstruction efficiency in a realistic context, several samples of $q\bar{q} \rightarrow \gamma/Z/Z' \rightarrow e^+e^-$ events were generated with PYTHIA[7], and simulated with GEANT 3 for the ATLAS detector response. The response of the particles with a pseudo-rapidity out of the range [-2.5,2.5] was not simulated. The events were then reconstructed in the official ATLAS reconstruction framework[39].

The samples were generated with two different Z' masses (1.5 TeV and 4 TeV) and for a variety models – SM like, E_6 derived models, Left-Right model – each model being fully determined by its coupling constants to the known fermions. The knowledge of the exact characteristics of these models, which can be found in [40], is not useful here since a model independent approach was chosen. The CTEQ5L parton distribution functions were used and initial/final state radiations were switched on. A total of 150,000 events with di-electron masses above 500 GeV and 15,000 above 2000 GeV were simulated.

3.1.2 Event selection

First the electron (positron) candidates are reconstructed using the standard ATLAS electron identification: additionally to criteria on shower shape and energy leakage, one requires to have a good track quality, with a total number of hits in the tracking detectors greater than 6. The absence of any additional track in a broad cone (0.05 in η and 0.1 in ϕ) around the matched track is also required in order to reduce the QCD and tau backgrounds.

Although being optimized on low energy electrons, these simple criteria lead to satisfactory results with reasonable angular and energy resolutions (see figure 3.1.1) and an acceptable efficiency; this procedure will have to be optimized in a near future but is good enough for our present purpose.

Only events with exactly two electrons candidates are kept; these two candidates were also required to be isolated in the calorimeter, i.e. with no cluster of transverse energy greater than 40 GeV in a cone of radius $\sqrt{(\Delta\phi)^2 + (\Delta\eta)^2}$ equal to 0.5.

Finally, the two reconstructed electrons must be of opposite charge and back to back in the transverse plane, the absolute difference of azimuthal angles having to be greater than 2.9 radians.

The typical efficiencies for this selection are detailed in table 3.1.1 for a sample of SM like Z' generated with a mass of 1.5 TeV.

At least two electrons with $\|\eta\| < 2.5$	(82.1$\pm$0.3)%
At least two identified and isolated electrons	(57.1$\pm$0.4)%
Electrons candidate of opposite charge	(53.4$\pm$0.4)%
Electrons candidate back to back	(45.9$\pm$0.4) %
Accepted events	(45.9$\pm$0.4)%

Table 3.1.1: Step by step event selection efficiency - SM like Z' with a mass of 1.5 TeV

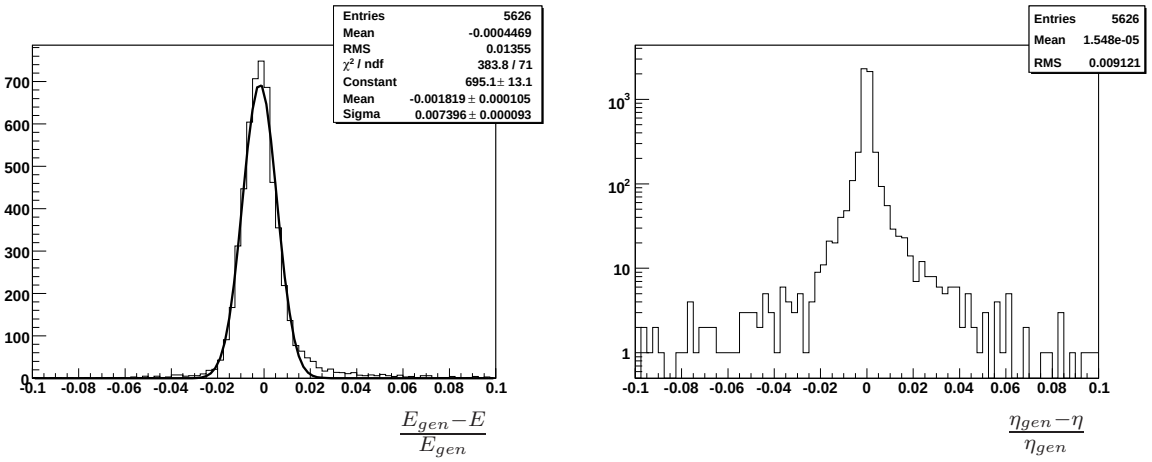

(a) Energy resolution

(b) Pseudo rapidity resolution.

Fig. 3.1.1: Reconstruction resolutions estimated by considering electrons/positrons decaying from a 1.5 TeV SM like Z' .

3.1.3 Model dependence of the efficiency.

With a full detector simulation and the use of the official ATLAS reconstruction framework, the efficiency estimate can be considered as realistic. Nevertheless, it strongly depends on the Z' mass and on the underlying model; therefore it cannot be used to derive any model independent limit. The different leptons kinematic characteristics, directly inducing different detector efficiencies, can be controlled by considering two characteristics of the model : the forward backward asymmetry (related to the coupling constants to quark and leptons), and the Z' boost distribution (related to the Z' mass and the coupling constants to quarks).

Introducing the angle $cos\theta^\star$ -the angle between the negative lepton and the incoming quark in the Z' rest frame-, the Z' production cross section is:

$$\frac{d\sigma}{d\cos\theta^\star} \propto \frac{3}{8}(1+\cos^2\theta^\star) + A_{FB}\cos\theta^\star \tag{3.1.1}$$

The A_{FB} coefficient depends on the boson coupling constants to incoming quarks and decay products and therefore strongly depends on the underlying model; this coefficient however vanishes when integrating over two $cos\theta^\star$ intervals symmetric around 0. Keeping in mind that flipping the $cos\theta^\star$ sign corresponds to swapping the electron and the positron, one can deduce the following property: in any positive (or negative) interval of pseudo rapidity in the Z' rest frame, the total number of leptons, electrons plus positrons, is independent of the A_{FB} coefficient. Therefore, if the detector is assumed to have equivalent detection and reconstruction efficiencies for electron and positron, the event selection efficiency does not depend on the A_{FB} coefficient; this however

does not mean that it is independent on the model, since the Z' boost still has to be taken into account. There is however a way to control this effect, as explained below. Notice that a forward/backward asymmetric efficiency does not spoil this result since the LHC is a pp collider, and hence the probability for the incoming quark to be forward is the same as the probability for the incoming antiquark.

The Z' boost can be deduced from its mass and its rapidity. The Z' rapidity distribution is represented on figure 3.1.2 (left) for two different models. Their shapes are different only due to the different u/d parton density functions in the proton and, because of different coupling constants of the Z' to u and d, due to the different fractions of di-electron coming from $u\bar{u}$ and $d\bar{d}$. When splitting each sample in two subsamples according on the incoming quark flavour, all Z' rapidity distributions become similar, independently of the model as can be seen on figure 3.1.2b.

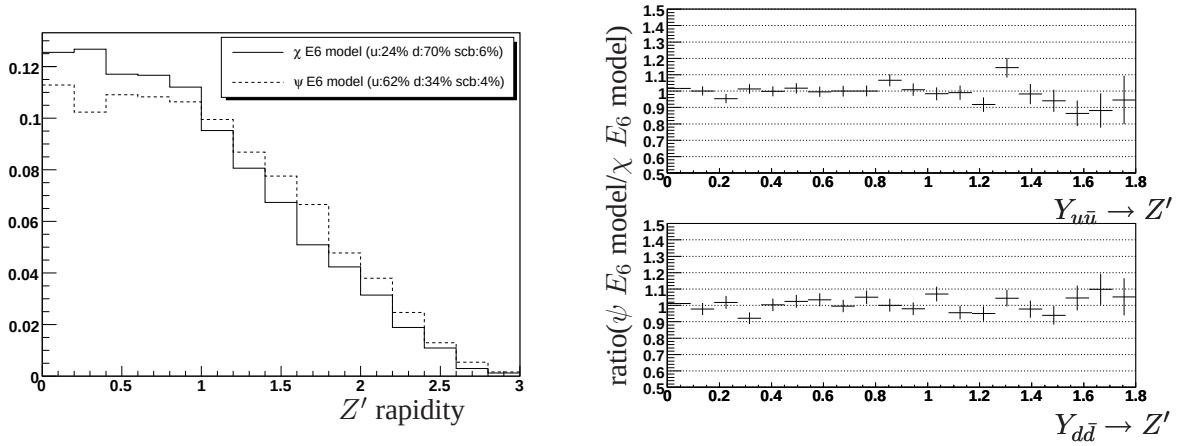

(a) Rapidity distributions (arbitrary scale).

(b) Rapidity ratios for the two models, considering $u\bar{u}$ and $d\bar{d}$ production separately.

Fig. 3.1.2: Z' rapidity for two different E_6 models in the mass range [1.48 TeV,1.52 TeV] ($M_{Z'} = 1.5$TeV)

The same is true for the leptons decaying from the Z' : for a given Z' mass, their kinematic properties only depend on the flavour of the incoming quarks. Consequently, an average reconstruction efficiency can be extracted event by event in any Z' model, with the only knowledge of the incoming quark flavour and the effective Z' mass. These efficiencies are summarized on figure 3.1.3 for the two main quark flavours, including the intermediate efficiencies for each selection step[13].

In both cases, one observes an increase of the number of events fully contained in the considered detector acceptance, when the di-electron mass becomes larger: this is a pure kinematic

[13]The variable bin size was chosen in order to optimize the number of events by bins.

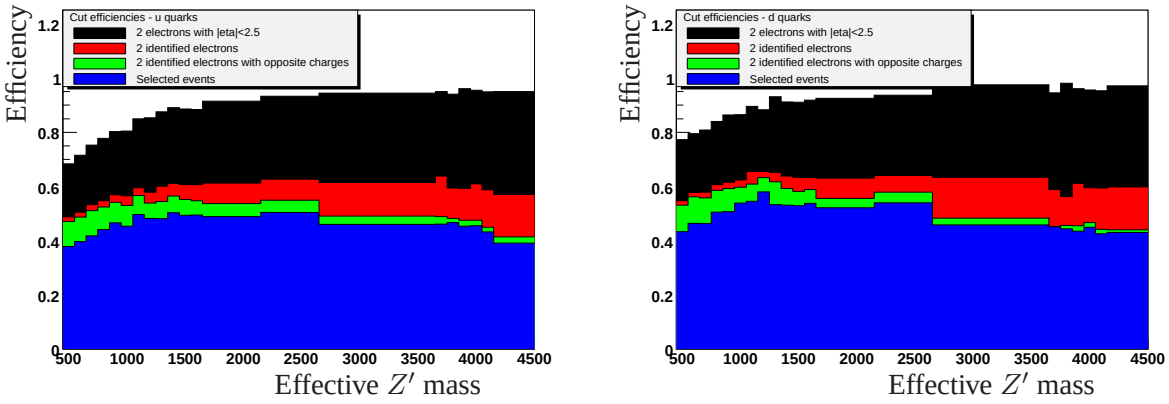

Fig. 3.1.3: Efficiencies for u and d flavours.

effect, the leptons being less boosted at large Z' mass. This effect is however counterbalanced by a degraded electron reconstruction efficiency; this can be explained by the fact that the electron identification algorithm is optimized on low energy electrons; there is some hope to recover from such effect by tuning the algorithm for higher energy objects. When the electron transverse momentum becomes larger, the detector charge identification is degraded, whereas the accuracy on the azymuthal angle measurement is improved. Consequently, at higher di-electron mass, the efficiency related to the charge criterion becomes lower and, on the opposite, the efficiency related to the acoplanarity becomes higher.
Finally, the reconstruction efficiency of the $d\bar{d} \rightarrow Z'$ is found to be always higher than the one of the $u\bar{u} \rightarrow Z'$. This can be explained by the particle density function differences, the d quark one being less peaked at low x, therefore inducing less boosted events, and consequently events which are more contained in the detector.
These efficiencies can be exploited in two ways:

- considering only a cross section production and ignoring the incoming quark flavour, the $u\bar{u}$ efficiency can be taken conservatively in order to derive a discovery reach or an exclusion limit.
- in the context of a given model, where the relative fractions of incoming u and d quarks are known, the discovery reach and exclusion limit can be precisely extracted.

With a limited number of generated and simulated Monte Carlo events, it is therefore possible to derive realistic limits with reasonable reconstruction efficiency in any model. In any case, this reconstruction efficiency is more realistic than the ones estimated with a fast detector simulation.

3.1.4 ATLAS discovery reach.

The four classes of CDDT solutions were considered with three different values of the $g_{Z'}$ coupling strength, and a wide range of x parameter values. The events generated by Pythia were efficiency weighted according to the incoming quark flavour and Z' mass, as explained in the previous section, in order to derive an effective production cross section. This procedure was also applied to the irreducible background. Then a significance estimator, called S_{12}[41], was used in order to extract the discovery reach in the $(x, g_{Z'}/M_{Z'})$ plane for several values of integrated luminosities. This estimator is defined by $S_{12} = \sqrt{S+B} - \sqrt{B}$ where S (resp. B) is the expected number of signal (resp. background) events; this definition is supposed to be more realistic than the usual $S/\sqrt{B}$ or $S/\sqrt{S+B}$.

The results are presented on figures 3.1.4 and 3.1.5 for two different values of luminosities : $400\ pb^{-1}$ and $100\ fb^{-1}$. The ATLAS discovery reach goes beyond the LEP exclusion limits in most scenarios, already in the first months of LHC running ($400\ pb^{-1}$ case); furthermore, with such a limited luminosity, it is also possible to probe regions of parameters space not yet excluded by CDF. The long term limits ($100\ fb^{-1}$ case), as for them, illustrate the very promising LHC discovery potential which is, as expected, far beyond the ultimate TeVatron one. This would be even more striking when including expected analysis refinements, such as : optimization of the electron reconstruction, performing a bump hunt analysis instead of a basic counting method, including the forward backward asymmetry measurement as done by CDF, ...

3.1.5 Conclusions.

The ATLAS Z' discovery reach has been presented in the context of the CDDT parameterization, by taking into account the efficiency, derived from a detector full simulation, independently of the model. The potential was found to be very promising, even with a limited amount of data.

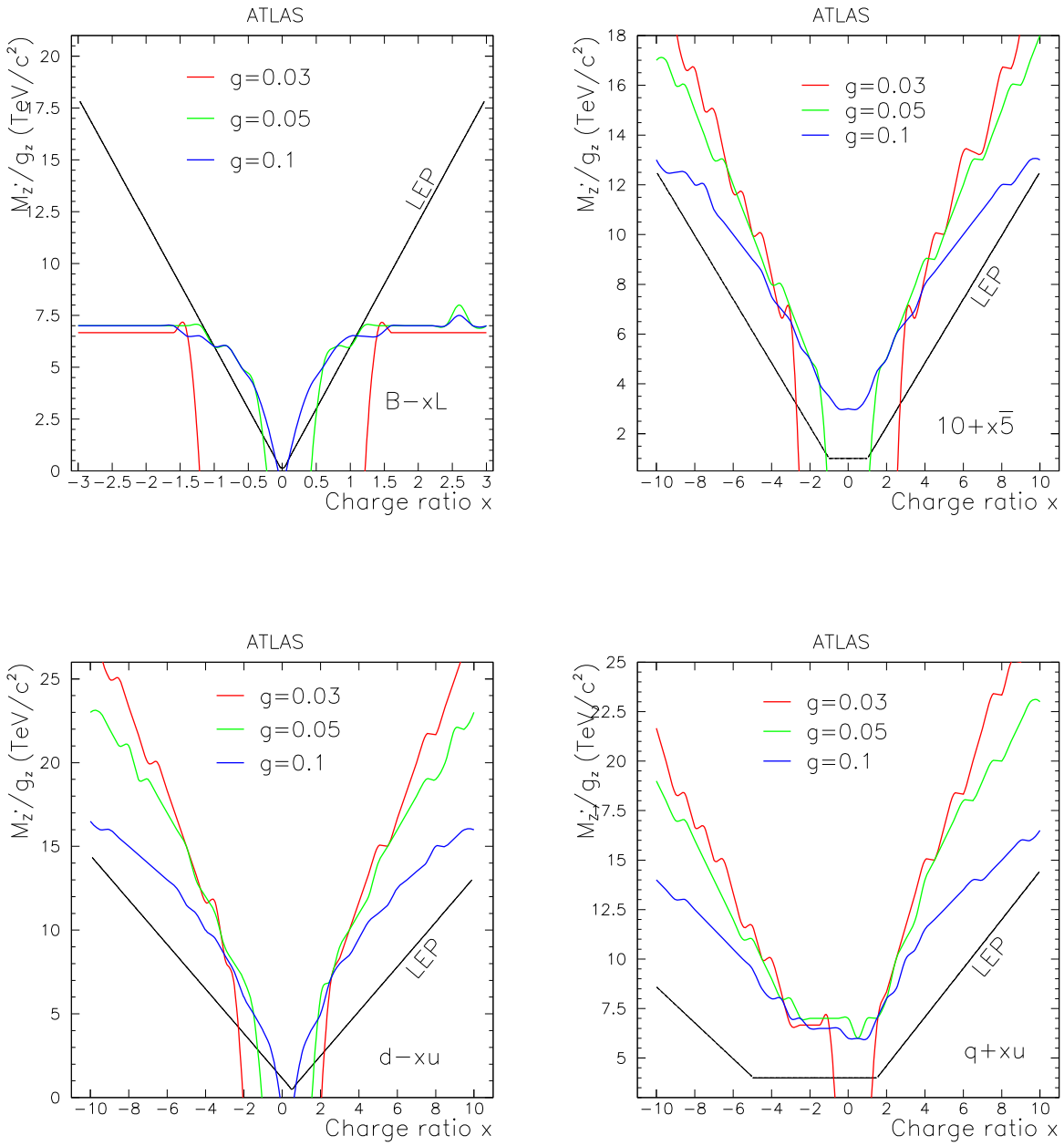

Fig. 3.1.4: ATLAS discovery reach with an integrated luminosity of $400\ pb^{-1}$ in the 4 classes of CDDT models.

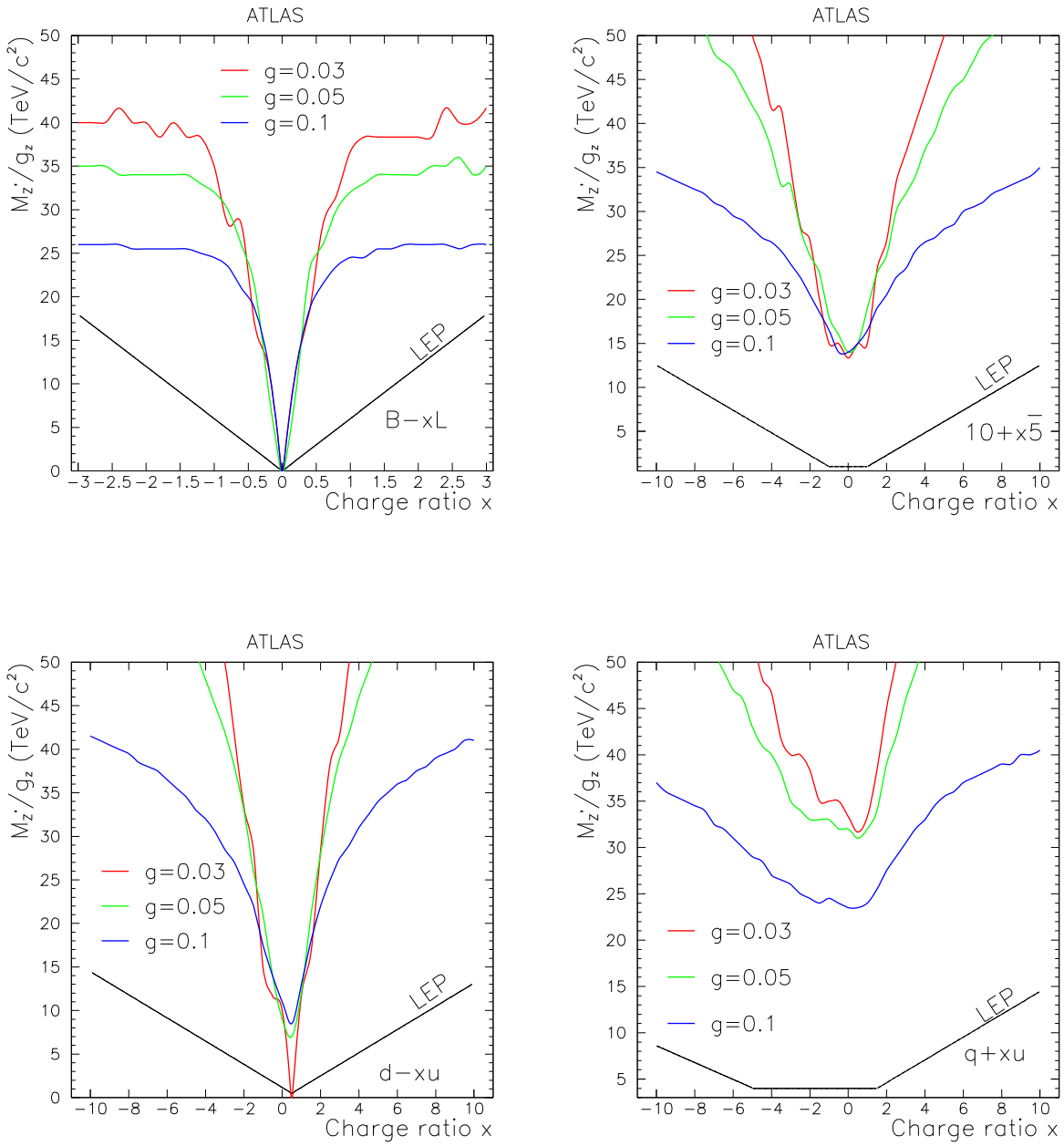

Fig. 3.1.5: ATLAS discovery reach with an integrated luminosity of 100 fb^{-1} in the 4 classes of CDDT models.

3.2 Phenomenology of Higgsless Models at the LHC and ILC

A. Birkedal[1], K. Matchev[2] and M. Perelstein[3]

[1] *Santa Cruz Institute for Particle Physics*

[2] *Institute for Fundamental Theory, University of Florida*

[3] *Institute for High-Energy Phenomenology, Cornell University*

We investigate the signatures of the recently proposed Higgsless models at future colliders. We focus on tests of the mechanism of partial unitarity restoration in the longitudinal vector boson scattering, which do not depend on any Higgsless model-building details. We study the LHC discovery reach for charged massive vector boson resonances and show that all of the preferred parameter space will be probed with 100 fb^{-1} of LHC data. We also discuss the prospects for experimental verification of the Higgsless nature of the model at the LHC. In addition, we present new results relevant for the discovery potential of Higgsless models at the International Linear Collider (ILC).

One of the greatest unsolved mysteries of the Terascale is the origin of electroweak symmetry breaking (EWSB). Within the usual description of the Standard Model (SM), a weakly coupled Higgs boson performs this task. However, it still has not been experimentally verified whether the electroweak symmetry is broken by such a Higgs mechanism, strong dynamics [42, 42, 43], or something else. This is one of the crucial questions particle physicists hope to answer in the upcoming experiments at the Large Hadron Collider (LHC) at CERN.

Experiments have already been able to put some constraints on theoretical ideas about EWSB. In theories involving EWSB by strong dynamics, the scale Λ at which new physics enters can be guessed from the scale at which massive gauge boson scattering becomes non-unitary. A simple estimate gives a value of

$$\Lambda \sim 4\pi M_W/g \sim 1.8 \text{ TeV}, \tag{3.2.1}$$

which is disfavored by precision electroweak constraints (PEC) [44, 45]. Thus, strong dynamics would seem to be largely ruled out as the source of EWSB. However, a new class of models, termed "Higgsless" [46, 47, 48, 49], have been able to raise the scale of strong dynamics, allowing agreement with PEC [50, 51, 52, 53].

Realistic Higgsless models contain new TeV-scale weakly coupled states accessible at the LHC. Among those, new massive vector bosons (MVB), heavy cousins of the W, Z and γ of the SM, which are of primary interest. It is those states which delay unitarity violation and hence allow the scale Λ to be raised [54]. Unfortunately, the details of the fermion sector of the theory are highly model-dependent. For instance, early Higgsless models did not allow sufficient change in Λ to agree with PEC [55, 56, 57, 58, 59, 60, 61], and modifications of the fermion sector were necessary. However, the basic mechanism by which Λ is raised is identical in all "Higgsless"

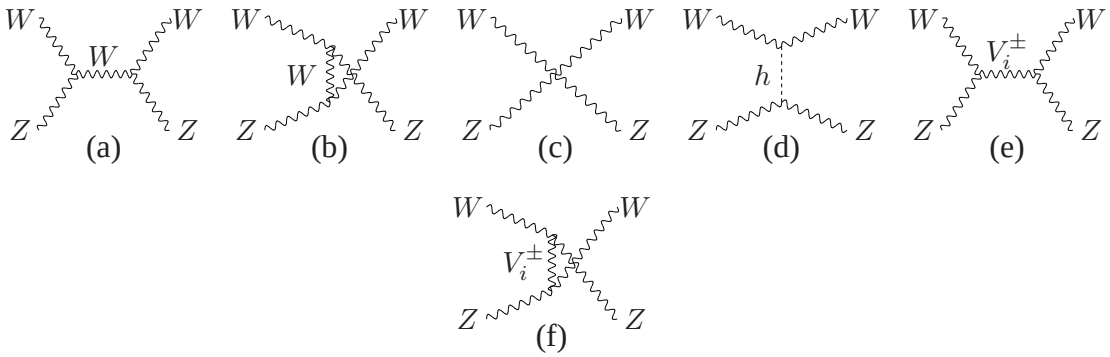

Fig. 3.2.1: Diagrams contributing to the $W^\pm Z \to W^\pm Z$ scattering process: (a), (b) and (c) appear both in the SM and in Higgsless models, (d) appears only in the SM, while (e) and (f) appear only in Higgsless models.

models, even regardless of the number of underlying dimensions [62, 63, 64, 65, 66, 67]. It is this mechanism which was studied in [68], focusing on its collider signatures. We review the analysis of Ref. [68] and present some new results relevant for the International Linear Collider (ILC). In Sec. 3.2.1 we derive a set of sum rules which should be obeyed by the couplings between the new MVBs and the SM W/Z gauge bosons. We identify discovery signatures of the new MVBs at the LHC which rely only on the couplings guaranteed by sum rules, and compare to the SM Higgs search signals. In Sec. 3.2.2 we discuss the LHC reach for charged MVBs and methods for testing the sum rules of Sec. 3.2.1 in order to identify the "Higgsless" origin of the MVB resonances. In Sec. 3.2.3 we discuss the corresponding Higgsless phenomenology at the ILC.

3.2.1 Unitarity sum rules

Consider the elastic scattering process $W_L^\pm Z_L \to W_L^\pm Z_L$. In the absence of the Higgs boson, this process receives contributions from the three Feynman diagrams shown in Figs. 3.2.1(a)–(c). The resulting amplitude contains terms which grow with the energy E of the incoming particle as E^4 and E^2, ultimately causing unitarity violation at high energy. In the SM, both of these terms are precisely cancelled by the contribution of the Higgs exchange diagram in Fig. 3.2.1(d). In Higgsless theories, the diagram of Fig. 3.2.1(d) is absent, and the process instead receives additional contributions from the diagrams in Figs. 3.2.1(e) and 3.2.1(f), where $V_i^\pm$ denotes the charged MVB of mass $M_i^\pm$. The index i corresponds to the KK level of the state in the case of a 5D theory, or labels the mass eigenstates in the case of a 4D deconstructed theory. Remarkably, the E^4 and E^2 terms can again be exactly cancelled by the contribution of the MVBs, provided that the following

sum rules are satisfied [68]:

$$g_{\mathrm{wwzz}} = g_{\mathrm{wwz}}^2 + \sum_i (g_{\mathrm{wzv}}^{(i)})^2, \tag{3.2.2}$$

$$2(g_{\mathrm{wwzz}} - g_{\mathrm{wwz}}^2)(M_{\mathrm{W}}^2 + M_{\mathrm{Z}}^2) + g_{\mathrm{wwz}}^2 \frac{M_{\mathrm{Z}}^4}{M_{\mathrm{W}}^2} = \sum_i (g_{\mathrm{wzv}}^{(i)})^2 \left[3(M_i^{\pm})^2 - \frac{(M_{\mathrm{Z}}^2 - M_{\mathrm{W}}^2)^2}{(M_i^{\pm})^2} \right].$$

Here $M_W(M_Z)$ is the $W(Z)$-boson mass and the notation for triple and quartic gauge boson couplings is self-explanatory. In 5D theories, these equations are satisfied exactly if all the KK states, $i = 1 \ldots \infty$, are taken into account. This is not an accident, but a consequence of the gauge symmetry and locality of the underlying theory. While this is not sufficient to ensure unitarity at all energies (the increasing number of inelastic channels ultimately results in unitarity violation), the strong coupling scale can be significantly higher than the naive estimate (3.2.1). For example, in warped-space Higgsless models [47, 50, 51, 52, 53] unitarity is violated at the scale [69]

$$\Lambda_{\mathrm{NDA}} \sim \frac{3\pi^4}{g^2} \frac{M_{\mathrm{W}}^2}{M_1^{\pm}}, \tag{3.2.3}$$

which is typically of order 5–10 TeV. In 4D models, the number of MVBs is finite and the second of the sum rules (3.2.2) is satisfied only approximately; however, our numerical study of sample models indicates that the sum rule violation has to be very small, at the level of 1%, to achieve an adequate improvement in Λ.

Considering the $W_L^+ W_L^- \to W_L^+ W_L^-$ scattering process yields sum rules constraining the couplings of the neutral MVBs V_i^0 (with masses denoted by M_i^0) [46]:

$$g_{\mathrm{wwww}} = g_{\mathrm{wwz}}^2 + g_{\mathrm{ww}_\gamma}^2 + \sum_i (g_{\mathrm{wwv}}^{(i)})^2, \tag{3.2.4}$$

$$4 g_{\mathrm{wwww}} M_{\mathrm{W}}^2 = 3 \left[g_{\mathrm{wwz}}^2 M_{\mathrm{Z}}^2 + \sum_i (g_{\mathrm{wwv}}^{(i)})^2 \, (M_i^0)^2 \right].$$

Considering other channels such as $W_L^+ W_L^- \to ZZ$ (see Fig. 3.2.2) and $ZZ \to ZZ$ does not yield any new sum rules. The presence of multiple MVBs, whose couplings obey Eqs. (3.2.2), (3.2.4), is a generic prediction of Higgsless models.

Our study of collider phenomenology in Higgsless models will focus on vector boson fusion processes. These processes are attractive for two reasons. Firstly, the production of MVBs via vector boson fusion is relatively model-independent, since the couplings are constrained by the sum rules (3.2.2), (3.2.4). This is in sharp contrast with the Drell-Yan production mechanism [58], which dominates for the conventional W' and Z' bosons but is likely to be suppressed for the Higgsless MVBs due to their small couplings to fermions, as needed to evade PEC [50, 51, 52, 53]. In the following, unless specified otherwise, we shall assume that the MVBs have no appreciable couplings to SM fermions. Secondly, if enough couplings and masses can be measured, these processes can provide a *test* of the sum rules, probing the mechanism of partial unitarity restoration.

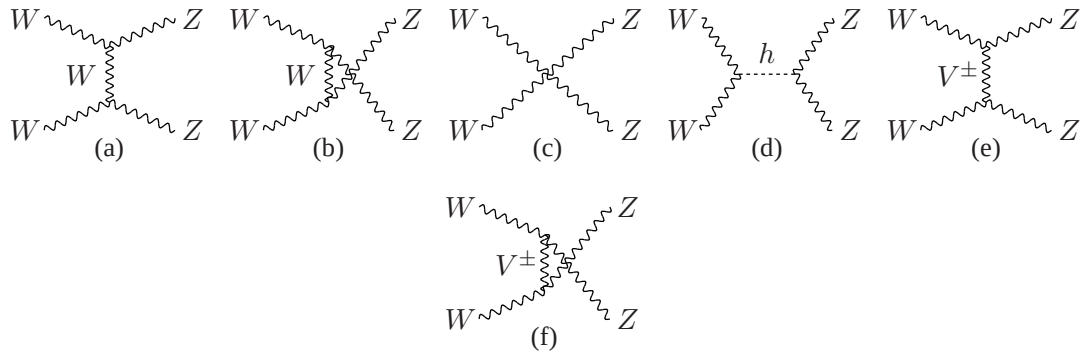

Fig. 3.2.2: Diagrams contributing to the $W^{\pm}W^{\mp} \to ZZ$ scattering process: (a), (b) and (c) appear both in the SM and in Higgsless models, (d) appears only in the SM, and (e) and (f) appear only in Higgsless models.

Eq. (3.2.3) indicates that the first MVB should appear below ~ 1 TeV, and thus be accessible at the LHC. For $V_1^{\pm}$, the sum rules (3.2.2) imply an inequality

$$g^{(1)}_{\rm WZV} \lesssim \frac{g_{\rm WWZ} M_{\rm Z}^2}{\sqrt{3} M_1^{\pm} M_{\rm W}}. \tag{3.2.5}$$

This bound is quite stringent: $g^{(1)}_{\rm WZV} \lesssim 0.04$ for $M_1^{\pm} = 700$ GeV. Also, sum rule (3.2.2) convergence requires $g^{(k)}_{\rm WZV} \propto k^{-1/2}\,(M_k^{\pm})^{-1}$. The combination of heavier masses and lower couplings means that the heavier MVBs may well be unobservable, so that only the V_1 states can be studied. The "saturation limit", in which there is only a single set of MVBs whose couplings saturate the sum rules, is likely to provide a good approximation to the phenomenology of the realistic Higgsless models. In this limit, the partial width of the $V_1^{\pm}$ is given by

$$\Gamma(V_1^{\pm} \to W^{\pm} Z) \approx \frac{\alpha\,(M_1^{\pm})^3}{144\,\sin^2\theta_W\,M_W^2}\,. \tag{3.2.6}$$

Given the couplings of the MVBs to the SM W and Z, we can now predict (at the parton level) the size of the new physics signals in the various channels of vector boson fusion. Fig. 3.2.3 provides an illustration for the case of $WW \to WW$ and $WZ \to WZ$. We show the expected signal for either a SM Higgs boson of mass $m_h = 500$ GeV, or the corresponding MVB V_1 of mass 500 GeV in the saturation limit. The sum rules (3.2.4) govern the signal in the $WW \to WW$ channel shown in the left panel of Fig. 3.2.3. However, the WW final state is difficult to observe over the SM backgrounds at the LHC: in the dilepton channel there is no resonance structure, while the jetty channels suffer from large QCD backgrounds. It is therefore rather challenging to test the sum rules (3.2.4). Notice that even if a WW resonance is observed, without a test of the sum rules (3.2.4), its interpretation is unclear, since the SM Higgs boson is *also* expected to appear as a WW resonance (see the left panel in Fig. 3.2.3).

We shall therefore concentrate on the $WZ \to WZ$ channel, in which the Higgsless model predicts a series of resonances as in Fig. 3.2.1(e), while in the SM the amplitude is unitarized by the t-channel diagram of Fig. 3.2.1(d) and has no resonance (see the right panel in Fig. 3.2.3). Conventional theories of EWSB by strong dynamics may also contain a resonance in this channel, but it is likely to be heavy (~ 2 TeV for QCD-like theories) and broad due to strong coupling. In contrast, the MVB resonance is very narrow, as can be seen from Fig. 3.2.3 and Eq. (3.2.6). In fact it is almost a factor of 20 narrower than a SM Higgs boson of the same mass. This is primarily due to the vector nature of the MVB and our assumption that it only has a single decay channel. We therefore conclude that a resonance in the $WZ \to WZ$ channel would be a smoking gun for the Higgsless model (for alternative interpretations involving extended Higgs sectors, see [70] and references therein). Finally, the $WW \to ZZ$ channel is a good discriminator as well, since it will exhibit a resonance for the case of the SM but not the Higgsless models (see Fig. 3.2.2). A comparison of the resonant structure of the three vector boson fusion final states is shown in Table 3.2.1.

Table 3.2.1: Comparison of the resonance structure of the SM and Higgsless models in different vector boson fusion channels.

Model	$WW \to WW$	$WZ \to WZ$	$WW \to ZZ$
SM	Yes	No	Yes
Higgsless	Yes	Yes	No

3.2.2 Collider phenomenology at the LHC

At the LHC, vector boson fusion processes will occur as a result of W/Z bremsstrahlung off quarks. The typical final state for such events includes two forward jets in addition to a pair of gauge bosons. The production cross section of $V_1^\pm$ in association with two jets is shown by the solid line in the left panel of Fig. 3.2.4. To estimate the prospects for the charged MVB search at the LHC, we require that both jets be observable (we assume jet rapidity coverage of $|\eta| \leq 4.5$), and impose the following lower cuts on the jet rapidity, energy, and transverse momentum: $|\eta| > 2$, $E > 300$ GeV, $p_T > 30$ GeV. These requirements enhance the contribution of the vector boson fusion diagrams relative to the irreducible background of the non-fusion $q\bar{q}' \to WZ$ SM process as well as Drell-Yan $q\bar{q}' \to V_1^\pm$. The "gold-plated" final state [71, 72, 73] for this search is $2j+3\ell$+$\not{E}_T$, with the additional kinematic requirement that two of the leptons have to be consistent with a Z decay. We assume lepton rapidity coverage of $|\eta| < 2.5$. The WZ invariant mass, m_{WZ}, can be reconstructed using the missing transverse energy measurement and requiring that the neutrino and the odd lepton form a W. The number of "gold-plated" events (including all lepton sign combinations) in a 300 fb^{-1} LHC data sample, as a function of m_{WZ}, is shown in Fig. 3.2.4 for

the SM (dotted), Higgsless model with $M_1^\pm = 700$ GeV (blue), and two "unitarization" models: Padé (red) and K-matrix (green) [74, 75] (for details, see Ref. [68]). A Higgsless model can be easily identified by observing the MVB resonance: for the chosen parameters, the dataset contains 130 $V_1^\pm \to W^\pm Z \to 3\ell + \nu$ events. The irreducible non-fusion SM background is effectively suppressed by the cuts: the entire dataset shown in Fig. 3.2.4 contains only 6 such events. We therefore estimate the discovery reach for $V_1^\pm$ resonance by requiring 10 signal events after cuts. The efficiency of the cuts for $500 \le M_1^\pm \le 3$ TeV is in the range $20 - 25\%$. We then find that with 10 fb^{-1} of data, corresponding to 1 year of running at low luminosity, the LHC will probe the Higgsless models up to $M_1^\pm \lesssim 550$ GeV, while covering the whole preferred range up to $M_1^\pm = 1$ TeV requires 60 fb^{-1}. Note, however, that one should expect a certain amount of reducible background with fake and/or non-isolated leptons.

Once the $V_1^\pm$ resonance is discovered, identifying it as part of a Higgsless model would require testing the sum rules (3.2.2) by measuring its mass $M_1^\pm$ and coupling $g^{(1)}_{WZV}$. The coupling can be determined from the total $V_1^\pm$ production cross section $\sigma_{\rm tot}$. However, we are observing the $V_1^\pm$ resonance in an exclusive channel, which only yields the product $\sigma_{\rm tot}\, BR(V_1^\pm \to W^\pm Z)$. A measurement of the total resonance width $\Gamma(V_1^\pm \to \text{anything})$ would remove the dependence on the unknown branching fraction BR. The accuracy of this measurement is severely limited by the poor missing energy resolution. Even though a Higgsless origin of the resonance can be ruled out if the value of $g^{(1)}_{WZV}$, inferred with the assumption of $BR = 1$, violates the bound (3.2.5), the LHC alone will not be able to settle the issue and precise measurements at an ILC appear to be necessary for the ultimate test of the theory.

3.2.3 Collider phenomenology at an ILC

Unlike traditional technicolor, Higgsless models offer new discovery opportunities for a lepton collider with a center-of-mass energy in the sub-TeV range. From Eq. (3.2.3) we have seen that the masses of the new MVBs are expected to be below 1 TeV, and they can be produced at an ILC through the analogous vector boson fusion process by bremsstrahlung of W's and Z's off the initial state e^+ and e^-. The V_1 production cross sections for vector boson fusion $e^+e^- \to V_1^\pm e^\mp \nu_e$ and $e^+e^- \to V_1^0 \nu_e \bar\nu_e$, as well as associated production $e^+e^- \to V^\pm W^\mp$, are shown in the left panel of Fig. 3.2.5. The horizontal lines correspond to the total cross sections of the continuum SM background. We see that for a large range of V_1 masses, ILC searches appear promising, already at the level of total numbers of events, before cuts and efficiencies. Furthermore, because of the cleaner environment of a linear lepton collider, one could use the dominant hadronic decay modes of the W and Z and easily reconstruct the invariant mass of the V_1 resonance, which provides an extra handle for background suppression (see the right panel in Fig. 3.2.5). Further detailed studies are needed to better evaluate ILC potential for testing the generic predictions (3.2.2) and (3.2.4) of the Higgsless models.

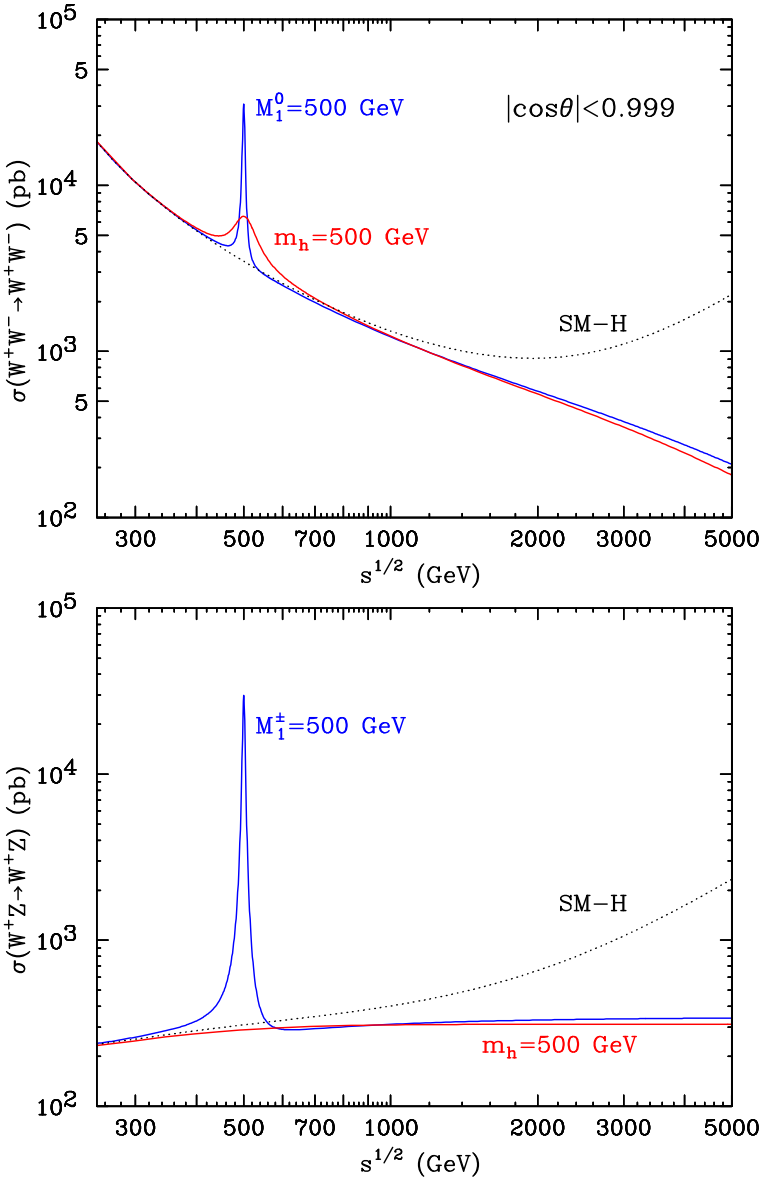

Fig. 3.2.3: Elastic scattering cross-sections for $WW \to WW$ (left) and $WZ \to WZ$ (right) in the SM without a Higgs boson (SM-H) (dotted), the SM with a 500 GeV Higgs boson (red) and the Higgsless model with a 500 GeV MVB (blue).

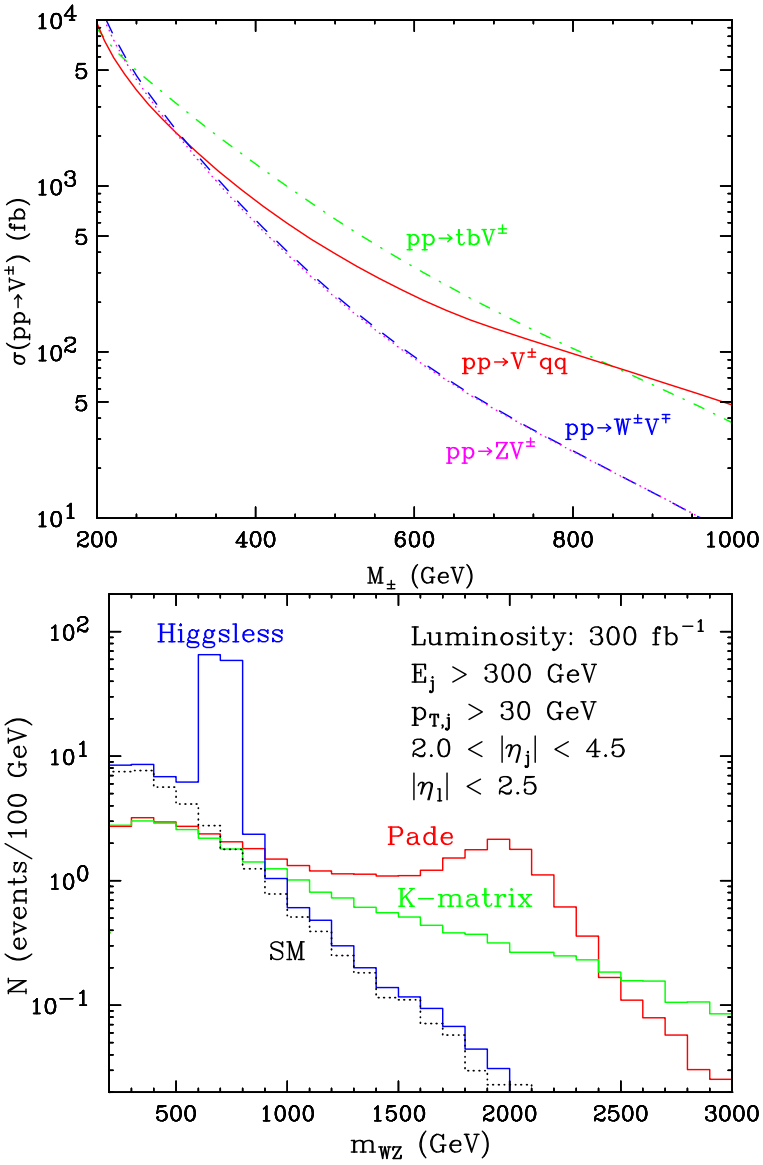

Fig. 3.2.4: Left: Production cross-sections for $V^{\pm}$ at the LHC. Here $tbV^{\pm}$ production assumes SM-like couplings to third generation quarks. Right: The number of events per 100 GeV bin in the $2j + 3\ell + \nu$ channel at the LHC with an integrated luminosity of 300 fb^{-1} and cuts as indicated in the figure. Results are shown for the SM (dotted), the Higgsless model with $M_1^{\pm} = 700$ GeV (blue), and two "unitarization" models: Padé (red) and K-matrix (green) [74, 75].

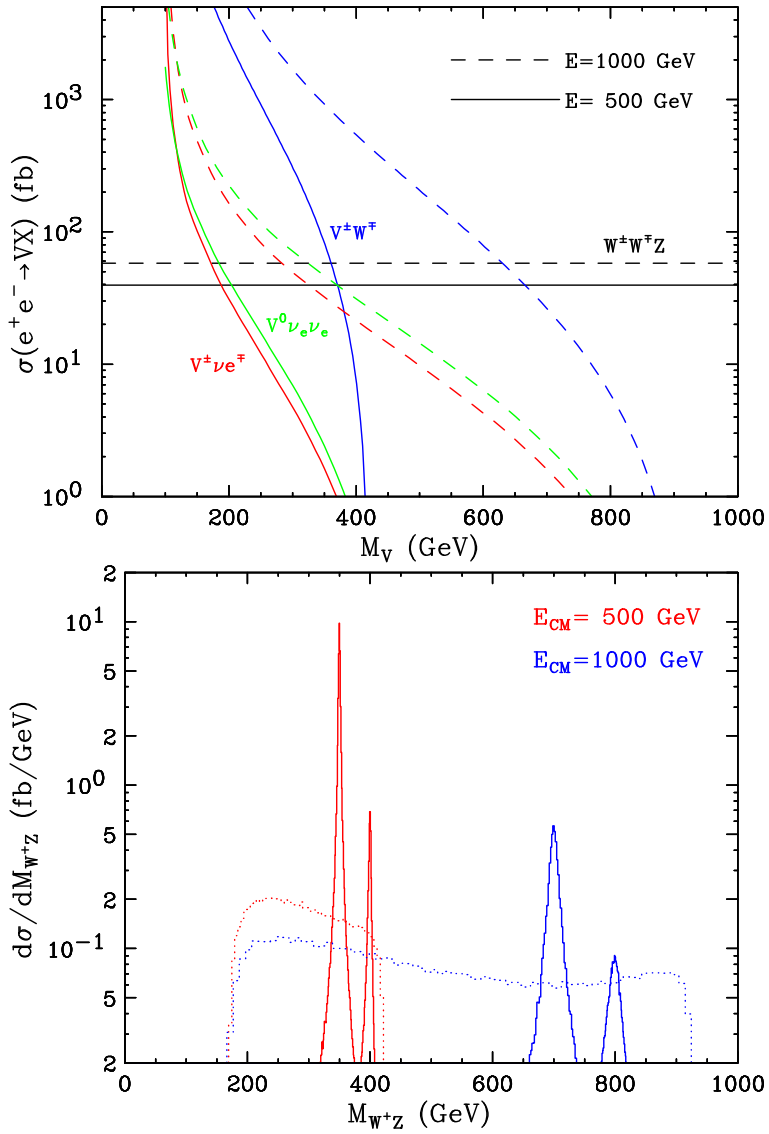

Fig. 3.2.5: Left: V_1 production cross-sections and the continuum SM background at an e^+e^- lepton collider of center of mass energy 500 GeV (solid) or 1 TeV (dashed). Right: WZ invariant mass distribution for Higgsless signals (solid) and SM background (dotted), at $E_{CM} = 500$ GeV (red, $M^{\pm} = 350, 400$ GeV) and $E_{CM} = 1$ TeV (blue, $M^{\pm} = 700, 800$ GeV).

3.3 Model independent searches for W' bosons

Zack Sullivan

High Energy Physics Division, Argonne National Laboratory
Argonne, Illinois 60439, USA

A new charged current interaction mediated by a particle with vector and/or axial-vector couplings to fermions is generically called a W' boson. Many classes of models of physics beyond the standard model predict the existence of W' bosons with a wide range of masses and couplings to fermions. From an experimental point of view, it is desirable to perform a search for these particles that is independent of any particular model. Fortunately, a completely model independent search for any finite-width W' boson exists [76].

The most general Lorentz invariant Lagrangian describing the coupling of a W' to fermions may be written as [77]

$$\mathcal{L} = \frac{1}{\sqrt{2}}\overline{f}_i\gamma_\mu\big(g_R e^{i\omega}\cos\zeta\, V^R_{f_i f_j}P_R + g_L \sin\zeta\, V^L_{f_i f_j}P_L\big)W' f_j + \text{H.c.}\,, \tag{3.3.1}$$

where ζ is a left-right mixing angle, and ω is a CP-violating phase that can be absorbed into V^R. In this notation, $g_{R(L)}$ are the right (left) gauge couplings, and $V^{R,L}_{f_i f_j}$ are generalized Cabibbo-Kobayashi-Maskawa (GCKM) matrices. In models where the W and W' mix, the mixing angle ζ is usually constrained to be small ($|\zeta| <$ a few $\times 10^{-5}$–10^{-2} [78]). Hence, searches are usually performed for purely right- or left-handed states, but that is not necessary in the analysis below.

In Ref. [76] the fully differential next-to-leading order (NLO) cross section for the production of a W' with arbitrary couplings, and decay into any pair of fermions was published. This paper proved that both the width and differential cross section factorize completely through NLO. Hence, a simple rescaling of naive right- or left-handed simulations can be mapped onto any arbitrary model as a function of generic couplings (denoted g'), W' mass, and W' total width. If the W' boson only decays into fermions (as in Fig. 3.3.1), then the W' width dependence is redundant.

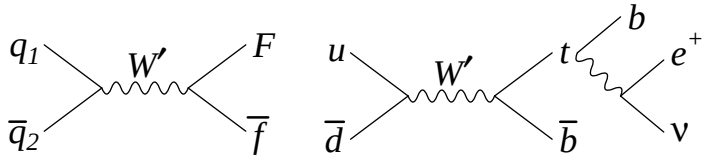

Fig. 3.3.1: Feynman diagram for W' production and decay into (left) any two fermions, and (right) the single-top-quark final state (Wbj).

It was demonstrated in Ref. [76] that the most effective model independent search for W' bosons at either the Tevatron or LHC (see also [79]) looks for the decay of the W' into the Wbj final state (Fig. 3.3.1). This final state allows a straight-forward peak search for the W' invariant

mass; and spin correlations provide the promise of disentangling the exact Dirac structure if a W' is found.

The cross section for a 700 GeV W' at the Tevatron is comparable to the single-top-quark cross section (see Fig. 3.3.2), but with a much smaller background. The CDF Collaboration looked for a mass peak in the run I single-top-quark analysis [80], and set a lower mass bound on W' bosons of 536(566) GeV assuming standard model-like couplings, where decays to right-handed neutrinos are (not) allowed. For pure left-handed W' bosons, the current best bound is 786 GeV [81] based on the decay into an electron and neutrino. Using the current single-top-quark bounds, an analysis of run II data could already surpass this limit for all W' bosons.

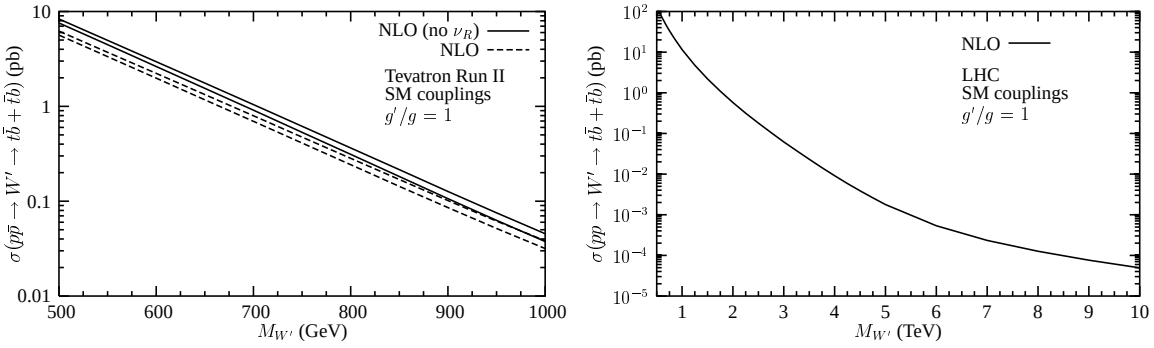

Fig. 3.3.2: Cross section at the (left) Tevatron and (right) LHC for W' boson production plus decay into the $t\bar{b}$ final state. Full theoretical error bands are shown for the Tevatron.

The s-channel production of single top quarks via W' bosons can occur at an extremely large rate at the LHC. In Fig. 3.3.2, the cross section for this channel is shown for SM-like couplings as a function of W' mass up to 10 TeV. In high-luminosity (100 fb^{-1}) years there could be 50 W' bosons produced with masses of 10 TeV that decay into this channel. The question is, can these be observed over the background?

In order to address this question, a fully simulated analysis of the signal and background was performed [79, 82]. The signal was evaluated using PYTHIA [83] run through the SHW detector simulation [84] with parameters updated to match the ATLAS detector [22]. The final state of interest contains a lepton (e or μ), 2 b-jets, and missing energy. The backgrounds come from $t\bar{t}$, t-channel single-top-quark production (i.e. tj), $Wjj, Wcj, Wb\bar{b}, Wc\bar{c}, WZ, Wt$, and s-channel single-top-quark production. As is apparent from Fig. 3.3.3, the most important of these are $t\bar{t}$, tj, and Wjj. The cross section for the backgrounds falls exponentially with $M_{bj\not{E}_T}$ the reconstructed invariant mass, and drops to less than one event above 3 TeV.

Unfortunately, the event generators do not currently model the tj or Wjj backgrounds correctly. In Fig. 3.3.3 matrix-element calculations are normalized to the correct fully-differential NLO calculations of the tj [85, 86] and Wjj [87] cross sections. The Tevatron will play an important role in validating these matching schemes.

Figure 3.3.4 shows that the LHC should have 5σ discovery reach for standard model-like W'

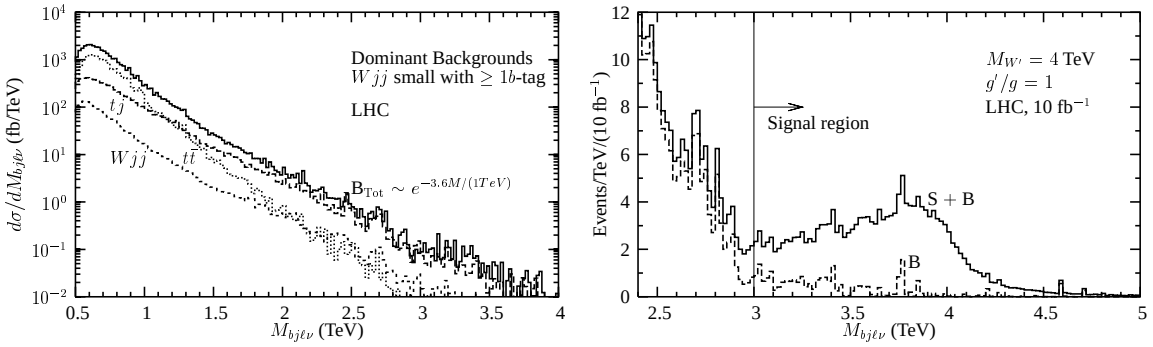

Fig. 3.3.3: (left) Dominant backgrounds for Wbj production at the LHC. After b-tagging the second jet, Wjj is roughly $1/5$ of the t-channel single-top-quark background tj. (right) Number of events expected per low-luminosity year (10 fb^{-1}) at the LHC in the Wbj-invariant mass final state vs. background.

bosons of 3.7 TeV in the first 10 fb^{-1}, and 4.7 TeV with 300 fb^{-1}. There is an effective hard cutoff in mass reach due to an almost exponentially falling parton luminosity above 5.5 TeV. While Fig. 3.3.2 shows a large cross section for 6–10 TeV, most events are produced well below resonance, and just add to the single-top-quark rate near the single-top threshold. More remarkable than mass reach is that couplings up to 20 times smaller than standard model-like couplings can be probed in the 1 TeV range. This allows complete coverage of Littlest Higgs parameter space in 1 year [79, 82]. Perturbative models based on ratios of couplings have effective couplings g' that do not differ from the standard model by more than a factor of 5, and typically average to $g' \approx g_{\rm SM}$ [79, 82]. Hence, these models will be accessible over the full mass reach.

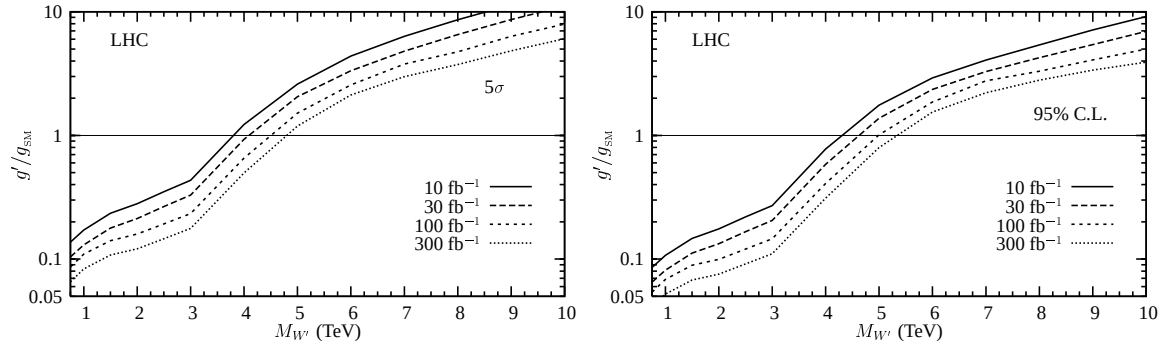

Fig. 3.3.4: Reach in relative coupling $g'/g_{\rm SM}$ at the LHC for 5σ discovery and 95% C.L. exclusion.

The most sensitive analysis of left-handed W' bosons completed so far looked for W' decay into an electron and neutrino [81]. While the reach is impressive, the lepton final state is not model independent. In particular, many new physics models have W' bosons with right-handed couplings, so this final state would never be produced. Leptophobic models, such as some versions of top color, also do not produce this final state.

The lepton final state suffers from several challenges in going to high energy. First, the back-

ground studies for LHC physics missed the dominant background of Wjj production [79, 82]. Valence-valence scattering opens a new production channel at the LHC that completely overwhelms the high-mass cross section, and is not produced by showering evolution of Wj production. Second, no mass can be reconstructed from fits to the transverse mass without huge data sets. Both problems are highlighted in Fig. 3.3.5, where a 4 TeV W' will produce at most 1 event above background per low-luminosity (10 fb^{-1}) year with a fairly flat transverse mass distribution. Finally, the prevalence of higher-order radiation makes it unlikely that a W' will be produced without additional jets, which will degrade reconstruction.

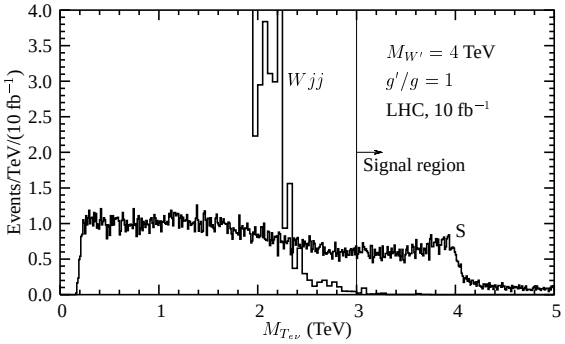

Fig. 3.3.5: Number of events expected per low-luminosity year at the LHC vs. the reconstructed transverse mass of the W', and the previously missed Wjj background.

There are several key issues affecting W' production for which Tevatron studies will provide vital assistance to the LHC effort.

- The real W background to all final states is much larger than estimated in the LHC TDRs. Since this background must be modeled by a mixture of Wj and Wjj events, it is vital to understand the performance and limitations of the new NLO and NLO-matched Monte Carlos in the context of the much simpler Tevatron environment.
- Similarly, single-top-quark production survives to much larger invariant masses than is predicted by the event generators used for the TDRs. The measurement of single-top-quark production at the Tevatron will provide a vital test of the methods and theoretical tools for modeling that background to new physics.
- How well high-energy leptons and jets will be measured is not a settled issue at the LHC. For W' bosons it has been assumed that only the $\sim$200 GeV b from top-quark decay can be tagged, but there is a TeV b jet recoiling against the top quark. Very little is known about high-energy b tagging. The Tevatron could provide valuable insight into the causes of the expected reduction of b-tagging efficiency at large E_T.

The Tevatron and LHC are complementary machines for W' searches. While the Tevatron can reach $\sim$900 GeV with 2 fb^{-1} of data [76], it will be a challenge for the LHC to go below 750 GeV in the Wbj final state because the background is rising exponentially. However, a 5.5 TeV

W' with standard-model couplings can be probed. For an indication of where several classes of models fall in the g'-$M_{W'}$ plane, including additional width effects, see Refs. [79, 82].

3.4 Vectorlike Quarks

Bogdan A. Dobrescu[1] and Tim M.P. Tait[2]

[1] *Fermilab, Batavia, IL 60510, USA*

[2] *Argonne National Laboratory, Argonne, IL 60439, USA*

3.4.1 Motivation

All observed elementary fermions are chiral: their left- and right-handed components have different charges under the $SU(2)_w \times U(1)_y$ gauge group. Additional chiral fermions could exist, but they would induce rather large one-loop contributions to electroweak observables, so that their number and properties are tightly restricted by the electroweak data. By contrast, if non-chiral fermions carrying Standard Model gauge charges exist, they would decouple from the observed particles in the limit where their masses are large compared to the electroweak scale. Non-chiral fermions are commonly called "vectorlike" because the Z and W bosons have vector couplings to them.

A particularly interesting type of vectorlike fermion is one that has the same gauge charges as the right-handed top quark. Such a vectorlike quark, usually labelled by χ, plays an essential role in the top-quark seesaw model [88, 89, 90, 91], where a Higgs doublet arises as a bound state of χ and the top-bottom doublet. The same vectorlike quark is used in little Higgs models [92, 93, 94], where it serves to cancel the top quark contribution to quadratic divergences of the Higgs mass.

From a phenomenological point of view, χ is interesting because of its potentially large mixing with the top quark. Here, we discuss the potential for discovery of χ at the LHC and the Tevatron. It should be mentioned, that although we limit our discussion to only up-type vectorlike quarks, down-type vectorlike quarks also appear in a variety of models, and may be phenomenologically interesting [95, 96, 97, 98]. The potential for their discovery at the LHC is evaluated in [99, 100].

3.4.2 Couplings of the χ quark

Let us concentrate on the top and χ quarks, ignoring the mixing with the first two generations of quarks (this can also be included, but the effects are expected to be small). We write down a low-energy effective theory whose parameters are sufficiently general to include the models mentioned above as particular cases.

Let us denote the gauge eigenstate quarks by a subscript 0. The gauge interactions of χ_{0_L}, χ_{0_R} and t_{0_R} are identical: they are all color triplets, $SU(2)_w$ singlets, and have hypercharge 4/3. The left-handed top quark, t_{0_L}, is part of an $SU(2)_w$ doublet of hypercharge 1/3. The effective Lagrangian includes two gauge invariant mass terms and two Yukawa interactions of χ_0 and t_0 to the Higgs doublet. Given that $SO(2)$ transformations that mix χ_R and t_R are not physically

observable, one can arrange that either one of the mass parameters or one of the Yukawa couplings vanishes. Therefore, after electroweak symmetry breaking, the quark mass matrix and Higgs boson interactions are given by

$$\mathcal{L} = -\left(\overline{t}_{0_L}\ ,\ \overline{\chi}_{0_L}\right)\begin{pmatrix} 0 & \lambda_\chi\left(v_h + h/\sqrt{2}\right) \\ m_{\chi t} & m_{\chi\chi}\end{pmatrix}\begin{pmatrix} t_{0_R} \\ \chi_{0_R}\end{pmatrix} + \text{h.c.}\ , \tag{3.4.1}$$

where h is the Higgs boson and $v_h \simeq 174$ GeV is the Higgs VEV. The two mass parameters, $m_{\chi t}$ and $m_{\chi\chi}$, and the λ_χ Yukawa coupling are taken to be real parameters, as their complex phases can be absorbed by U(1) transformations of the quark fields. Hence, there are only three real parameters that describe the mass sector of heavy t and χ quarks.

To relate the parameters in the Lagrangian to physical observables, we transform the gauge eigenstates $t_{0_L}, t_{0_R}, \chi_{0_L}, \chi_{0_R}$ to the mass eigenstates t_L, t_R, χ_L, χ_R, where t is the top quark observed at the Tevatron, of mass $m_t \approx 175$ GeV, and χ is a new quark of mass m_χ, which remains to be measured. The relation between the two bases depends on two angles, θ_L and θ_R, but θ_R is not related to any physical observable, as explained above. The mixing angle θ_L affects the electroweak interactions of the top quark as well as the Yukawa couplings of the Higgs boson. We use s_L and c_L as short-hand notation for $\sin\theta_L$ and $\cos\theta_L$, respectively.

The relations between the physical parameters m_t, m_χ and θ_L and the initial parameters $\lambda_\chi, m_{\chi t}, m_{\chi\chi}$ are given by

$$m^2_{t,\chi} = \frac{1}{2}\left[m^2_{\chi\chi} + m^2_{\chi t} + \lambda^2_\chi v^2_h \mp \sqrt{\left(m^2_{\chi\chi} + m^2_{\chi t} + \lambda^2_\chi v^2_h\right)^2 - 4\left(\lambda_\chi v_h m_{\chi t}\right)^2}\right] \tag{3.4.2}$$

for the masses, and by

$$s_L = \frac{1}{\sqrt{2}}\left(1 - \frac{m^2_{\chi\chi} + m^2_{\chi t} - \lambda^2_\chi v^2_h}{m^2_\chi - m^2_t}\right)^{1/2}\ . \tag{3.4.3}$$

for the mixing angle. Note that in the limit of $m_\chi \to \infty$, the mixing vanishes ($s_L \to 0$) so that the new physics decouples from the Standard Model.

The interactions of t and χ with the electroweak gauge bosons, which depend on θ_L, can be computed straightforwardly. There are charged current interactions,

$$\begin{aligned} t - \overline{b} - W^+_\mu \quad &: \quad -i\frac{g}{\sqrt{2}} c_L \gamma_\mu P_L\ , \\ \chi - \overline{b} - W^+_\mu \quad &: \quad -i\frac{g}{\sqrt{2}} s_L \gamma_\mu P_L\ , \end{aligned} \tag{3.4.4}$$

where $P_L = (1-\gamma_5)/2$ is the left-handed projector and $g \equiv e/\sin\theta_W$ is the $SU(2)_w$ gauge coupling. The charge-conjugate interactions have the same vertex factors. The neutral current interactions contain the photon interactions, which are standard for both t and χ, as demanded

by gauge invariance under $U(1)_{EM}$. The Z boson interactions with the left-handed quarks are modified, and include t-χ flavor-changing neutral currents:

$$\begin{aligned}
t_L - \overline{t}_L - Z_\mu &: -i\frac{e}{\sin\theta_W\cos\theta_W}\left(\frac{1}{2}c_L^2 - \frac{2}{3}\sin^2\theta_W\right)\gamma_\mu P_L \,, \\
t_L - \overline{\chi}_L - Z_\mu &: -i\frac{e}{\sin\theta_W\cos\theta_W}\frac{1}{2}s_L c_L \gamma_\mu P_L \,, \\
\chi_L - \overline{\chi}_L - Z_\mu &: -i\frac{e}{\sin\theta_W\cos\theta_W}\left(\frac{1}{2}s_L^2 - \frac{2}{3}\sin^2\theta_W\right)\gamma_\mu P_L \,,
\end{aligned} \tag{3.4.5}$$

and the $\overline{t}_L - \chi_L - Z_\mu$ interaction is the same as the $t_L - \overline{\chi}_L - Z_\mu$ interaction given above. The interactions of t_R and χ_R are with the Z boson are identical with those of the right-handed top quark in the Standard Model.

The Higgs interactions with t and χ can be expressed in terms of θ_L, m_t/v and m_χ/v:

$$\begin{aligned}
h^0 - \overline{t}_L - t_R &: -ic_L^2\frac{m_t}{v\sqrt{2}} \\
h^0 - \overline{t}_L - \chi_R &: -ic_L s_L\frac{m_\chi}{v\sqrt{2}} \\
h^0 - \overline{\chi}_L - t_R &: -ic_L s_L\frac{m_t}{v\sqrt{2}} \\
h^0 - \overline{\chi}_L - \chi_R &: -is_L^2\frac{m\chi}{v\sqrt{2}}
\end{aligned} \tag{3.4.6}$$

The charge-conjugate vertex factors are the same as their counter-parts given above.

3.4.3 Decays of the χ quark

The charge-current interactions allow for the $\chi \to W^+ b$ decay, while the flavor-changing neutral-current interactions allow for the $\chi \to Zt$ decay, assuming that m_χ is above ~ 250 GeV. These Higgs interactions allow decays of χ into a top and a Higgs boson, which competes with the $\chi \to Zt$ and $\chi \to Wb$ decays for some regions of parameter space. In the heavy χ limit, the decay widths are given by

$$\begin{aligned}
\Gamma(\chi \to W^+ b) &\simeq \frac{s_L^2 m_\chi^3}{32\pi v^2} \,, \\
\Gamma(\chi \to Zt) \simeq \Gamma(\chi \to ht) &\simeq \frac{c_L^2}{2}\,\Gamma(\chi \to W^+ b) \,.
\end{aligned} \tag{3.4.7}$$

Clearly the $\chi \to W^+ b$ decay is dominant, but if c_L is not much smaller than unity, then the decay $\chi \to ht$ could be very interesting. In the presence of the χ quark the bounds from precision

electroweak measurements on the mass of the Higgs boson are considerably loosened [101]. It is likely that the Higgs boson is heavier than about 180 GeV, and it decays most of the time to W^+W^- and ZZ.

For $m_\chi > 350$ GeV, we will consider the LHC signal induced by the decay $\chi \to ht$ followed by $h \to ZZ$ with one of the Z bosons decaying leptonically. Previous studies in the context of the little Higgs model [102], have assumed a light Higgs boson (m_H= 120 GeV), which leads to a signal harder to see at the LHC.

For $m_\chi < 350$ GeV, which is the region of interest at the Tevatron, χ decays predominantly to Wb, and would look like a heavier top quark.

3.4.4 Single-χ production at the LHC

Both single-χ and χ-pair productions are possible at the Tevatron and the LHC. We first discuss single-χ production, which has the advantage for large χ masses that only one massive quark must be produced, and thus parton luminosity and phase space are favorable. However, it has the feature that the process is only possible because of the mixing between the χ and the top quarks, and thus the cross section depends strongly on the mixing angle, $\sigma \propto s_L^2$. The difference in the mass of the final state objects implies that single-χ production is usually the dominant production for large χ masses, reachable by the LHC, whereas χ-pair production is usually dominant for lower χ masses, testable at the Tevatron.

The process proceeds through the t-channel exchange of a W boson from any light quark in one of the colliding hadrons to a bottom quark in the other one. The final state thus consists of a single χ quark and a jet which tends to be in the forward region of the detector. This process has been considered in the past, particularly in the little Higgs context [94, 93, 103]. We point out here that there is another process of single-χ production (though one that does not interfere with the W-exchange process) not usually considered in the literature in which a t-channel Z boson is exchanged between a light quark and a top quark in the initial state, resulting from gluon splitting. This process is important [104], and should be included in phenomenological studies of single-χ production.

The LHC discovery potential with 300 fb^{-1}, estimated in Ref. [102] (without the inclusion of the Z-exchange contribution) and assuming that the three branching fractions shown in Eq (3.4.7) are in the proportions 2:1:1 (corresponding to $s_L \ll 1$), reaches about 1 TeV for the $\chi \to Zt$ decay, and 2 TeV for $\chi \to Wb$, with some dependence on the model parameters as expected for single-χ production.

Another interesting signature at the LHC is provided by single-χ production followed by the decay $\chi \to ht$. Given that the Higgs boson mass in this model is not tightly constrained by electroweak fits, and the leptonic decays of gauge bosons allow for clean event reconstruction, a clear signature of the process would be obtained from the case $h \to ZZ$.

The event topologies are complex and their reconstruction from jets and leptons leads to

some combinatorial background. The topologies with two, three or four leptons in the final state, originate from either a Z or t decay, are quite promising. The case with one lepton has overwhelming background, especially if there is some misidentification of jets as leptons. The case with five leptons has a cross section which is too low to lead to an observable signal. The events can be selected to contain at least two leptons of the same flavor and opposite charge, and at least 2 non b-tagged jets. Because of the massive parent particles, all of these objects are expected to be central and at relatively large p_T. The W, Z, and top resonances provide an excellent means to unravel the structure of the events, and should prove efficient to reduce the dominant backgrounds, $t\bar{t}$, $Wjt\bar{t}$ and $Zt\bar{t}$.

3.4.5 Pair production

Recently, it has been shown [105] that with 100 fb^{-1}, a 1 TeV top-like quark can be discovered at the LHC in the channel $gg, qq \to T\bar{T} \to W^+bW^-\bar{b}$. Pair production of χ quarks with their subsequent decays leads to very complex events containing many jets and leptons. Since more center of mass energy is required to produce a pair of heavy quarks, the mass reach will be in general lower than for single production. However, the production cross section is through the strong force, and does not depend on any of the other parameters than the χ mass.

Furthermore, detector resolution, efficiencies, and combinatorial effects make it difficult to reconstruct these events. The case with one lepton in the final state, dominated by $\chi\chi \to Wb\ Wb \to \ell\nu\ jj$, has been studied by [105]. Here, we consider only the case with two leptons in the final state, $\chi\chi \to Wb\ Zt \to jjb\ \ell\ell\ jjb$, as other cases are limited by statistics or by combinatorial backgrounds.

The principal backgrounds for the $\chi\chi \to Wb\ Zt \to jjb\ \ell\ell\ jjb$ channel are $t\bar{t}$, $WWjt\bar{t}$ and $Zt\bar{t}$. The main components are $t\bar{t}$ production and $Zt\bar{t}$, as they have respectively a high cross section and similar event topology. The $WWt\bar{t}$ background has a low cross section and can be strongly suppressed by the requirement of recontruction of the intermediate resonance. The events will contain 2 leptons of the same flavor and opposite charge, whose invariant mass should reconstruct close to the Z boson mass. In addition, we expect 2 b-tagged jets and at least 4 untagged jets, two of which will reconstruct a W.

Acknowledgments: We would like to thank Georges Azuelos for many helpful discussions, and for describing to us the plans of the ATLAS collaboration to search for vectorlike quarks.

3.5 Triplet Higgs Boson

Mu-Chun Chen

Fermi National Accelerator Laboratory, Batavia, IL, USA

The Standard Model requires a Higgs boson to explain the generation of fermion and gauge boson masses. Precision electroweak measurements suggest that the Higgs boson must be relatively light, $m_H < 219\,GeV$. Currently, experimental data overwhelmingly support the SM with a light Higgs boson. The simplest version of the Standard Model with a single Higgs boson, however, has the theoretical problem that the Higgs boson mass is quadratically sensitive to any new physics which may arise at high energy scales. Little Higgs models are a new approach to understanding the hierarchy between the TeV scale of possible new physics and the electroweak scale. These models have an expanded gauge structure at the TeV scale which contains the Standard Model $SU(2) \times U(1)$ electroweak gauge groups. The LH models are constructed such that an approximate global symmetry prohibits the Higgs boson from obtaining a quadratically divergent mass until at least two loop order. The Higgs boson is a pseudo-Goldstone boson resulting from the spontaneous breaking of the approximate global symmetry and so is naturally light. We present in this talk, which is based on the work done in Ref. [106, 107, 108], the one-loop electroweak precision constraints in the Littlest Higgs model (LLH) [109], which contains a gauged $[SU(2) \otimes U(1)]_1 \otimes [SU(2) \otimes U(1)]_2$ symmetry as its subgroup. We include the logarithmically enhanced contributions from both fermion and scalar loops, and emphasize the role of triplet scalars in constructing a consistent renormalization scheme.

Precision electroweak measurements give stringent bounds on the scale of little Higgs type models. One of the strongest bounds comes from fits to the ρ parameter, since in the LLH model the relation $\rho = 1$ is modified at the tree level. A special feature of the SM with the assumption of one Higgs doublet is the validity of the tree level relation, $\rho = 1 = \frac{M_W^2}{M_Z^2 c_\theta^2}$ due to the tree level custodial symmetry. There is thus a definite relation between the W-boson mass and the Z-boson mass. Of course, one can equivalently choose any three physical observables as the input parameters in the gauge sector. If we choose G_μ, M_Z and α as the three input parameters in the gauge sector, the W-boson mass, M_W, then is predicted in the usual way via muon-decay,

$$M_W^2 = \frac{\pi\alpha}{\sqrt{2} G_\mu s_\theta^2} \left[1 + \Delta r \right] , \tag{3.5.1}$$

where Δr summarizes the one-loop radiative corrections, and it is given in terms of the gauge boson self-energy two point functions as,

$$\begin{aligned} \Delta r &= -\frac{\delta G_\mu}{G_\mu} - \frac{\delta M_W^2}{M_W^2} + \frac{\delta\alpha}{\alpha} - \frac{\delta s_\theta^2}{s_\theta^2} \\ &= \frac{\Pi^{WW}(0) - \Pi^{WW}(M_W)}{M_W^2} + \Pi^{\gamma\gamma\,\prime}(0) + 2\frac{s_\theta}{c_\theta}\frac{\Pi^{\gamma Z}(0)}{M_Z^2} - \frac{\delta s_\theta^2}{s_\theta^2} \, . \end{aligned} \tag{3.5.2}$$

The counter term for the weak mixing angle s_θ which is defined through the W- and Z-boson mass ratio, $s_\theta^2 = 1 - \frac{M_W^2}{M_Z^2}$, is then given by,

$$\frac{\delta s_\theta^2}{s_\theta^2} = \frac{c_\theta^2}{s_\theta^2}\left[\frac{\Pi^{ZZ}(M_Z)}{M_Z^2} - \frac{\Pi^{WW}(M_W)}{M_W^2}\right] . \tag{3.5.3}$$

Both of the two point functions, $\Pi^{WW}(M_W)$ and $\Pi^{WW}(0)$, have identical leading quadratic m_t dependence, $\frac{\sqrt{2}G_\mu}{16\pi^2}3m_t^2\left(1 + 2\ln\frac{Q^2}{m_t^2}\right)$, and thus their difference is only logarithmic.The two-point function, $\Pi^{\gamma\gamma\prime}(0)$, is also logarithmic in m_t. However, in the counter term $\delta s_\theta^2/s_\theta^2$, the difference between $\Pi^{WW}(M_W)$ and $\Pi^{ZZ}(M_Z)$ is quadratic in m_t. The prediction for M_W^2 thus depends on m_t quadratically in this case.

While the Standard Model requires three input parameters in the weak sector, a model with $\rho \neq 1$ at tree level, such as the LLH model, requires an additional input parameter in the gauge-fermion sector, which can be taken to be the VEV of the Higgs triplet, v'. Many of the familiar predictions of the Standard Model are drastically changed by the need for an extra input parameter [110, 111]. We choose as our input parameters the muon decay constant G_μ, the physical Z-boson mass M_Z^2, the effective lepton mixing angle s_θ^2 and the fine-structure constant $\alpha(M_Z^2)$ as the four independent input parameters in the renormalization procedure. The ρ parameter, defined as, $\rho \equiv M_{W_L}^2/(M_Z^2 c_\theta^2)$, where s_θ^2 is the effective leptonic mixing angle at the Z-resonance, and the W-boson mass, which is defined through muon decay, are then derived quantities. Since the loop factor occurring in radiative corrections, $1/16\pi^2$, is similar in magnitude to the expansion parameter, v^2/f^2, of chiral perturbation theory, the one-loop radiative corrections can be comparable in size to the next-to-leading order contributions at tree level. We compute the loop corrections to the ρ parameter which are enhanced by large logarithms; we focus on terms of order $1/(16\pi^2)\ln(M^2/Q^2)$, where $Q \sim M_Z$ and $M \sim f \sim \mathcal{O}(TeV)$. At the one-loop level, we have to take into account the radiative correction to the muon decay constant G_μ, the counterterm for the electric charge e, the mass counterterm of the Z-boson, and the counterterm for the leptonic mixing angle s_θ^2.

The effective leptonic mixing angle is defined through the ratio of the vector to axial vector parts of the Zee coupling,

$$4s_\theta^2 - 1 = \frac{\mathrm{Re}(g_V^e)}{\mathrm{Re}(g_A^e)}, \tag{3.5.4}$$

which differs from the naive definition of the Weinberg angle in the littlest Higgs model, $s_W^2 = g'^2/(g'^2 + g^2)$, by,

$$\Delta s_\theta^2 \equiv s_W^2 - s_\theta^2 = -\frac{1}{2\sqrt{2}G_\mu f^2}\left[s_\theta^2 c^2(c^2 - s^2) - c_\theta^2(c'^2 - s'^2)(-2 + 5c'^2)\right] . \tag{3.5.5}$$

The W-boson mass is defined through muon decay,

$$M_W^2 = \frac{\pi\alpha}{\sqrt{2}G_\mu s_\theta^2}\left[1 + \Delta r_{\text{tree}} + \Delta r'\right] \ , \tag{3.5.6}$$

where Δr_{tree} summarize the tree level corrections due to the change in definition in the weak mixing angle as well as the contributions from exchange of the heavy gauge bosons,

$$\Delta r_{\text{tree}} = -\frac{\Delta s_\theta^2}{s_\theta^2} + \frac{c^2 s^2}{\sqrt{2}G_\mu f^2} \ , \tag{3.5.7}$$

and the one-loop radiative corrections are collected in $\Delta r'$,

$$\begin{aligned} \Delta r' &= -\frac{\delta G_\mu}{G_\mu} - \frac{\delta M_W^2}{M_W^2} + \frac{\delta\alpha}{\alpha} - \frac{\delta s_\theta^2}{s_\theta^2} \\ &= \frac{1}{M_W^2}\left[\Pi^{WW}(M_W) - \Pi^{WW}(0)\right] + \Pi^{\gamma\gamma}(0)' - \frac{c_\theta}{s_\theta}\frac{\Pi^{\gamma Z}(M_Z)}{M_Z^2} \ . \end{aligned} \tag{3.5.8}$$

When deriving this equation, we have used

$$\frac{\delta s_\theta^2}{s_\theta^2} = \text{Re}\left\{\frac{c_\theta}{s_\theta}\left[\frac{\Pi^{\gamma Z}(M_Z)}{M_Z^2} - \frac{v_e}{2s_\theta c_\theta}\left(\frac{a_e^2 - v_e^2}{a_e v_e}\Sigma_A^e(m_e^2) + \frac{\Lambda_V^{Zee}(M_Z)}{v_e} - \frac{\Lambda_A^{Zee}(M_Z)}{a_e}\right)\right]\right\} \ , \tag{3.5.9}$$

where Σ_A^e is the axial part of the electron self-energy and $\Lambda_{V,A}^{Zee}$ are the vector and axial vector parts of the $Ze\overline{e}$ vertex corrections. This follows from the fact that the counter term for s_θ^2 is formally related to the wave function renormalizations for γ and Z. The dominant contribution, $\Pi^{\gamma Z}(M_Z)$, depends on m_t only logarithmically. Due to this logarithmic dependence, the constraint on the model is weakened. On the other hand, the scalar contributions become important as they are quadratic due to the lack of the tree level custodial symmetry.

We find that the one-loop contribution to Δr, due to the SU(2) triplet scalar field, Φ, scales as

$$\frac{1}{16\pi^2}\frac{v'^2}{v^4}M_\Phi^2 \ . \tag{3.5.10}$$

In the limit $v^{'} = 0$ while keeping f fixed, which is equivalent to turning off the coupling $\lambda_{h\Phi h}$ in the Coleman-Weinberg potential, the one loop contribution due to the SU(2) triplet, Δr_Z^s, vanishes. The large f limit of the scalar one-loop contribution, Δr_Z^s, vanishes depending upon how the limit $f \to \infty$ is taken [106, 107, 108]. As f approaches infinity, the parameter μ^2 (thus v^2) can be kept to be of the weak scale by fine-tuning the unknown coefficient in the mass term μ^2 in the Coleman-Weinberg potential while all dimensionless parameters remain of order one. The scalar one-loop contribution in this limit does *not* de-couple because M_Φ^2 increases as f^2 which compensates the $1/f^2$ suppression from v'^2/v^2. In this case, the SM Higgs mass m_H is of the weak scale v. On the other hand, without the fine-tuning mentioned above, v can be held constant while varying f, if the

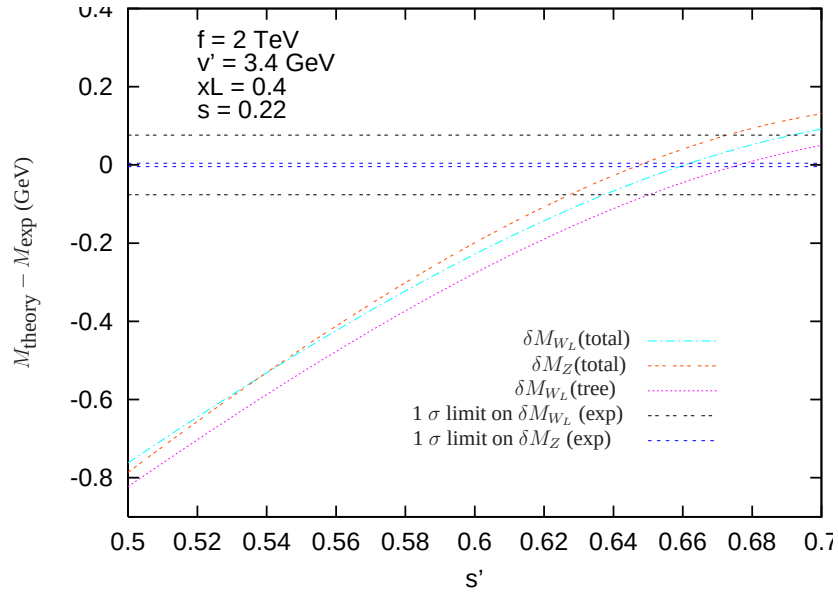

Fig. 3.5.1: Prediction for M_{W_L} as a function of the mixing angle s' at the tree level and the one-loop level. Also plotted is the correlation between M_Z and s' for fixed s, v' and f. The cutoff scale f in this plot is $2\ TeV$, the $SU(2)$ triplet VEV $v' = 3.4\ GeV$, the mixing angle $s = 0.22$, and $x_L = 0.4$.

quartic coupling λ_{h^4} (thus λ_{Φ^2}) approaches infinity as f^2/v^2. This can be done by taking $a \sim f^2/v^2$ while keeping a' finite and s and s' having specific values. The scalar one-loop contribution then scales as

$$\Delta r_Z^s \sim \frac{1}{v^2}(\frac{v'}{v})^2 M_\Phi^2 \sim (\frac{1}{v^2})(\frac{\lambda_{h\Phi h}}{\lambda_{\Phi^2}})^2 \frac{v^2}{f^2}\lambda_{\Phi^2} f^2 \to \frac{\lambda_{h\Phi h}^2}{\lambda_{\Phi^2}} \quad . \tag{3.5.11}$$

Since the coupling constant λ_{Φ^2} must approach infinity in order to keep v constant as we argue above, the scalar one-loop contribution Δr_Z^s thus vanishes in the limit $f \to \infty$ with v held fixed and no fine tuning. In this case, $m_H \sim \mu$ scales with f.

We analyze the dependence of the W-boson mass, M_{W_L}, on the mixing between $SU(2)_1$ and $SU(2)_2$, described by s', the mixing between $U(1)_1$ and $U(1)_2$, described by s, the mixing parameter in $t - T$ sector, x_L, and the VEV of the $SU(2)$, v'. The predictions for M_{W_L} with and without the one-loop contributions for $f = 2$ TeV is given in Fig. 3.5.1, which demonstrates that a low value of f ($f \sim 2\ TeV$) is allowed by the experimental restrictions from the W and Z boson masses, provided the VEV of the $SU(2)$ triplet scalar field is non-zero. This shows the importance of the $SU(2)$ triplet in placing the electroweak precision constraints. In order to have experimentally acceptable gauge boson masses, however, the parameters of the model must be quite finely tuned, regardless of the value of the scale f. On the other hand, the prediction for M_{W_L} is very sensitive to the values of s' as well as v'.

The non-decoupling of the SU(2) triplet scalar field shown in Fig. 3.5.2 implies the impor-

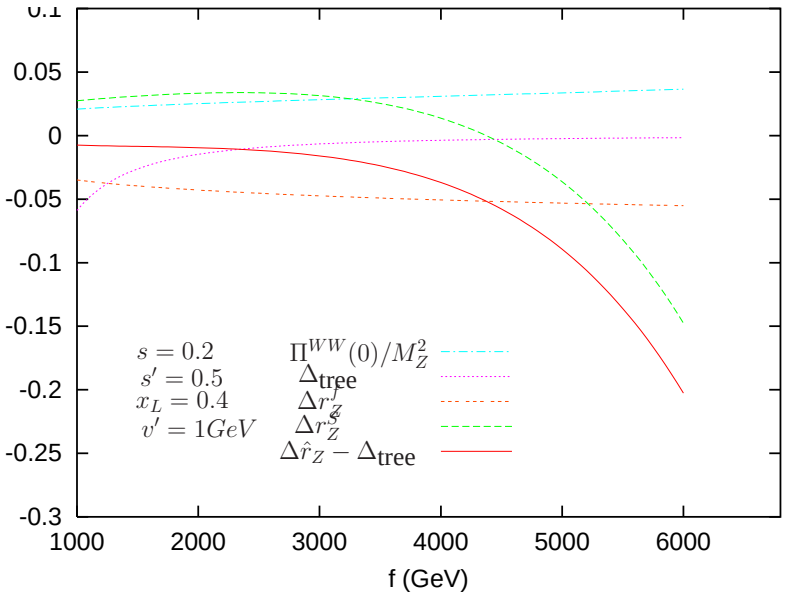

Fig. 3.5.2: The tree level correction, Δ_{tree}, the fermionic and scalar contributions to the one loop correction, Δr_Z^f and Δr_Z^S, the total one loop correction, $\Delta\hat{r} - \Delta_{\text{tree}}$, and $\Pi^{WW}(0)/M_Z^2$ as functions of the cutoff scale f at fixed s, s', x_L and v'.

tance of the inclusion of the scalar one-loop contributions in the analyses. In the region below $f = 4\ TeV$, where the tree level corrections are large, the vector boson self-energy is about half of the size of the tree level contributions, but with an opposite sign. (Other one-loop contributions roughly cancel among themselves in this region). Due to this cancellation between the tree level correction and the one-loop correction, there is an allowed region of parameter space with low cut-off scale f. Fig. 3.5.2 also shows that the tree level contribution of the LH model get smaller as f increases, as is expected. In order to be consistent with experimental data, the triplet VEV v' must approach zero as f goes to infinity. Our results emphasize the need for a full one loop calculation.

The forth input parameter in the gauge sector is needed in any new models where a $SU(2)_L$ triplet with a non-vanishing VEV is present. In addition to the littlest Higgs model, models of this kind include the SM with a triplet Higgs and the left-right symmetric model based on $SU(2)_L \times SU(2)_R \times U(1)_{B-L}$. A unique collider signature of models with a triplet Higgs is the decay of the doubly charged component of the triplet into same sign di-leptons, $\phi^{--} \to \ell^-\ell^-$. The Tevatron and the LHC thus have the capability to discover a triplet Higgs if its mass is of the order of a TeV. This decay mode is unique in the sense that it does not exist in MSSM or other extensions of the SM having only Higgs doublets or singlets. It is interesting to note that the operator which leads to the decay $\phi^{--} \to \ell^-\ell^-$ also contributes to the LH Majorana neutrino masses. This thus provides an interesting possibility of probing the neutrino mixing parameters at collider experiments.

3.6 Expected Signatures of Charged Massive Stable Particles at the Tevatron

C. Clément[a], Y. de Boer[b,c], M. Karlsson[d], D. Milstead[a]

[a] *Stockholm University, Stockholm, Sweden*

[b] *Institute for Theoretical and Experimental Physics, Moscow, Russia*

[c] *University of Twente, Enschede, the Netherlands*

[d] *Lund University, Lund, Sweden*

The expected signatures of a range of charged massive stable particles produced in proton-antiproton collisions at 2 *TeV centre-of-mass energy were investigated using QCD-based models. The fragmentation properties of jets containing* R*-hadrons formed from stable stops and gluinos allow discrimination between* R*-hadron and Standard Model jets. Interactions of stable massive particles in material were shown to give sensitivity to the species of scattering particle.*

3.6.1 Introduction

Many candidate theories beyond the SM predict the presence of charged massive stable[14] particles (CMSPs). Different types of CMSPs arise in a number of scenarios of SUSY, Universal Extra Dimensions, leptoquarks, and various unification models.

One of the primary tasks of the Tevatron and LHC programs is therefore to demonstrate or disprove the existence of CMSPs. A number of experimental searches have been performed at the Tevatron and other colliders[112, 113, 114, 115, 116, 117, 118] and much preparatory work is underway at the LHC[119, 120, 121, 122, 123]. The extracted exclusion limits are dependent on the models used for the cross-sections and span up to approximately 200 GeV in mass in the most optimistic scenarios. One typical search strategy which has been employed is to use time-of-flight information to isolate slow moving muon-like tracks. However, hadronic CMSPs (usually referred to as R-hadrons in the context of SUSY[15]) can evade detection in this way through charge exchange interactions[124, 125, 126, 127] with passive detector material. For example, a charged R-hadron can convert to a neutral state through nuclear interactions in the calorimetry and thus not be recorded in the muon chambers. However, since the available charge exchange reactions depend on the species of R-hadron undergoing scattering, charge exchange interactions also offer a possibility to differentiate between CMSP scenarios.

As part of this workshop the detector signatures of stable staus, gluinos and stops were studied as a means to develop analysis tools for the possible discovery and quantification of these sparticles. The selected sparticles are predicted to be stable in a number of scenarios. The observ-

[14] The term stable is taken to refer to particles which do not decay over a time scale corresponding to their passage through a typical detector.

[15] In this paper, the term R-hadron refers to an exotic hadron containing an unspecified sparticle, while the terms $\mathrm{R}_{\tilde{g}}$-hadron and $\mathrm{R}_{\tilde{q}}$-hadron refer to particles containing a gluino and squark, respectively.

ables studied here are relevant for any generic search for a colourless particle with charge $\pm e$, a charge $\pm\frac{2}{3}e$ colour triplet, or an electrically uncharged colour octet state. QCD-based models were used to study the production mechanisms, fragmentation properties and subsequent scattering in matter of the sparticles. In performing this work several potential experimental challenges were highlighted which may need to be addressed in order to discover CMSPs or definitively exclude their presence at either the Tevatron or the LHC.

3.6.2 Theoretical Background

The topic of CMSPs was recently brought to the fore by the emergence of the theory of Split-SUSY[128, 129] in which the gluino can be stable. Within this approach, the hierarchy problem and the fine-tuning of the Higgs mass are accepted. SUSY is still necessary to unify the gauge couplings, but by accepting the fine-tuning of the Higgs mass, Split-SUSY proposes a way to break the symmetry at scale above 1000 TeV. The scalar particles, except for a single neutral Higgs boson acquire masses at this high scale. Chiral symmetries assure that the fermions possess masses around the TeV scale. Split-SUSY still provides a dark matter candidate and furthermore, possesses none of the difficulties in describing electric dipole moments[130, 131] or flavour changing neutral currents[132] which challenge the Minimal Supersymmetric Standard Model. A further consequence of Split-SUSY is that the gluino can then become meta-stable since it decays through a squark and the decay is therefore suppressed. For values of squark masses above around 10^6 GeV, a produced gluino can form a $R_{\tilde{g}}$-hadron which is sufficiently stable so as to propagate through a Tevatron detector. The potential of the Tevatron and the LHC to discover stable gluons has been investigated in a number of works[133, 134, 123, 122]. In addition to Split-SUSY, stable gluinos also arise in other SUSY scenarios[124, 135, 136, 137, 138, 139] including GMSB.

In the context of GMSB, it is, however, more common that searches are performed for meta-stable staus[137, 140]. A very light gravitino as a LSP which couples very weakly to the other particles is a characteristic of GMSB models. The NLSP is usually a neutralino or one of the sleptons. If the mixing of the stau states $\tilde{\tau_L}$ and $\tilde{\tau_R}$ is non-negligible then the lightest stau $\tilde{\tau_1}$ can also become lighter than the other sleptons and the neutralino and therefore be the only NLSP. The lifetime of the NLSP depends on the gravitino mass (or equivalently the SUSY breaking scale) and meta-stable staus can be expected over a sizable part of the parameter space open to the Tevatron and LHC.

Long lived charged particles are also predicted in five-dimensional SUSY[141]. In this model the Standard Model is embedded in a supersymmetric theory with a compactified extra dimension. In this scenario, a stable stop with mass around 200 GeV is predicted.

CMSPs are also predicted in a number of alternative exotic scenarios. Theories of leptoquarks[142], Universal Extra Dimensions[143], certain unification models[144], and theories which postulate new SM fermions[145, 146, 147]. Magnetic monopoles are a further type of CMSP which have been sought. The existence of Dirac Monopoles addresses the question of electric charge quantisation[148,

149] and Dirac Monopoles are themselves predicted within unification models[150, 151].

3.6.3 R-hadrons in Jets

Fragmentation of R-hadrons

Hard scattering events for $p\bar{p}$ interactions are simulated using the leading order generator PYTHIA/JETSET 6.3[152]. The effects of initial and final state QCD radiation are described in PYTHIA by leading logarithm parton showers. In PYTHIA the fragmentation of partons into hadrons follows the Lund string model[153]. The hadronisation of gluinos and stops was performed within JETSET using special routines for this purpose[154]. A Peterson fragmentation function parameter[155], extrapolated to the R-hadron mass region under study, was used. The fragmentation parameter is computed according to

$$\frac{\epsilon_{\tilde{q}\tilde{g}}}{\epsilon_b} = \frac{m_b^2}{m_{\tilde{q}\tilde{g}}^2} \tag{3.6.1}$$

Since a gluino is a colour octet, two colour strings are attached to it and a gluino-induced jet is thus expected to possess a larger particle multiplicity than a jet initiated by a squark.

Mesonic states and baryonic states are produced in the hadronisation model. Furthermore, neutral $R_{\tilde{g}}$-hadrons can be formed as gluino ball ($\tilde{g}g$) states. The probability $P_{\tilde{g}g}$ of forming a gluino ball in the hadronisation step is set by default to 0.1 within PYTHIA. However, the fraction of gluino balls is *a priori* unknown and any comprehensive search strategy should therefore also consider scenarios in which CMSPs are produced dominantly as neutral states.

Each state is set stable and it has been predicted [127] that the mass splitting is sufficiently small so as to exclude the decay into a low lying neutral mass state.

Jet Properties of R-hadrons

Searches for stable staus and sleptons often impose isolation criteria either in calorimeter or tracking systems to reject background. Since a R-hadron is produced within a jet, searches cannot rely on isolation. However, measurements of R-hadrons in a jet could then be used to distinguish between R-hadrons and staus. Furthermore, the jet structure can be used to characterise R-hadrons and as a search tool. This can be particularly useful in scenarios in which the R-hadron is not recorded in a muon system owing to the effects of nuclear interactions.

Samples of pair produced gluinos and stop-antistops with masses of 300 GeV/c^2 were studied and compared with QCD dijet events. The distribution $\frac{1}{N_{jet}}\frac{dn_{ch}}{dz}$ is shown in Fig. 3.6.1 for different intervals of jet transverse momentum. Here, z is a fragmentation variable $z = p_{ch}/p_{jet}$ defined for all charged particles which are reconstructed within a jet. The variable z is formed from momenta of the charged particle (p_{ch}) and the jet (p_{jet}). N_{jet} and n_{ch} are the number of jets and charged particles, respectively. A minimum cut on the jet transverse energy of 20 GeV has also been applied.

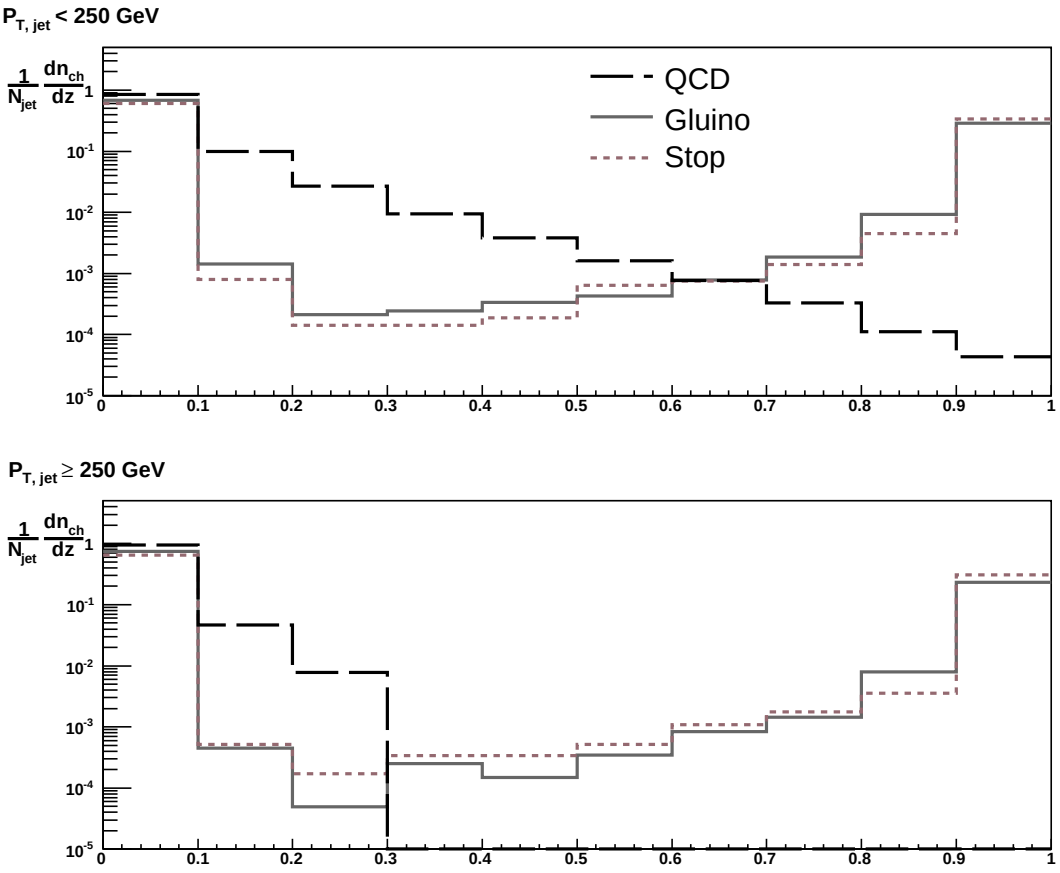

Fig. 3.6.1: The distribution of $(1/N_{jet})(dn_{ch}/dz)$ for charged particles in jets in R-hadron and QCD events. The distributions are shown for two intervals of jet transverse momentum.

Jets were found using a cone algorithm[156] in the pseudorapidity region $|\eta| < 2$. The jets were formed from stable particles produced following hadronisation and a cone radius of R=0.7 was used.

The z distribution for the QCD sample shows an expected behaviour with a large rate of low momentum particles produced from QCD radiation and leading particles. The R-hadron samples show a large rate of low momentum tracks but in addition a leading R-hadron populates the high z region.

The dependence of $\frac{1}{N_{jet}}\frac{dn_{ch}}{dz}$ on the jet transverse momentum can be used to discriminate signal from background. Fig. 3.6.1 shows evidence of the classic scaling violations for the QCD dijet case with the depopulation of the high z region, as would be expected from perturbative QCD[157]. However, for the R-hadron samples, the peak at high z remains relatively constant.

Since R-hadrons can be produced in pairs, the correlation between leading R-hadrons can offer further discrimination. The distribution $z_{1L}z_{2L}$ is shown in Fig. 3.6.2. Here z_{1L} and z_{2L} are the values of z for the leading particles in the first and second jets, respectively. The normalisation is arbitrarily chosen to provide same-sized samples of QCD and R-hadron 2-jet events. The R-hadron distributions remain peaked above 0.9 while the QCD spectra now peaks at around 0.05. The stop sample peaks at a higher value of z than the gluino sample, as would be expected from the different colour string topologies associated with the different types of sparticle.

The multiplicity of gluino and stop jets is shown in Fig. 3.6.3. The multiplicity falls with mass as less phase space is available for QCD emissions. The gluino multiplicity exceeds that from stop jets. An enhanced multiplicity at low momentum would be expected owing the different QCD colour factors involved in hadronising squark and gluinos[158].

The fine details of the fragmentation spectra presented here are subject to a number of theoretical uncertainties such as those due to the treatment of the gluino constituent mass and the choice of the gluino fragmentation function. However, the gross features of the distributions presented would not be expected to be sensitive to these effects.

While the golden channel for observing a CMSP would be a slow penetrating particle, the study of jet properties would provide supplementary information regarding the fragmentation of a heavy coloured object in the case of a discovery. Furthermore, it could also act as a component of a search strategy in its own right for events not containing a slow muon-like candidate. Such events could arise due to charge exchange interactions as described in section 3.6.4. However, there would be important experimental issues to address. An inefficiency in a muon detector could lead to the measurement of a R-hadron like z spectra for heavy quark production. Of greater importance would be the triggering of R-hadrons which were not recorded as muons. Since the energy deposition due to a R-hadron is likely to be maximally around 15 GeV this may not be enough to trigger on an event. Thus, an event with two R-hadron jets and no muon signature would not be recorded unless there was evidence of a third jet arising from a higher order process. Three-jet processes and their implication for Tevatron limits in the case $R_{\tilde{g}}$-hadron production have

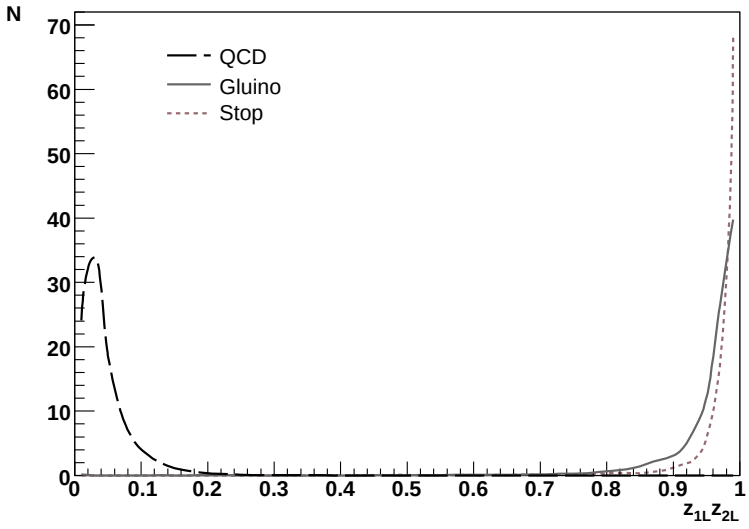

Fig. 3.6.2: The distribution of $z_{1L}z_{2L}$ for leading charged particles in events containing two jets. Distributions are shown for R-hadron and QCD events. The distributions are normalised to contain the same yield of two-jet events.

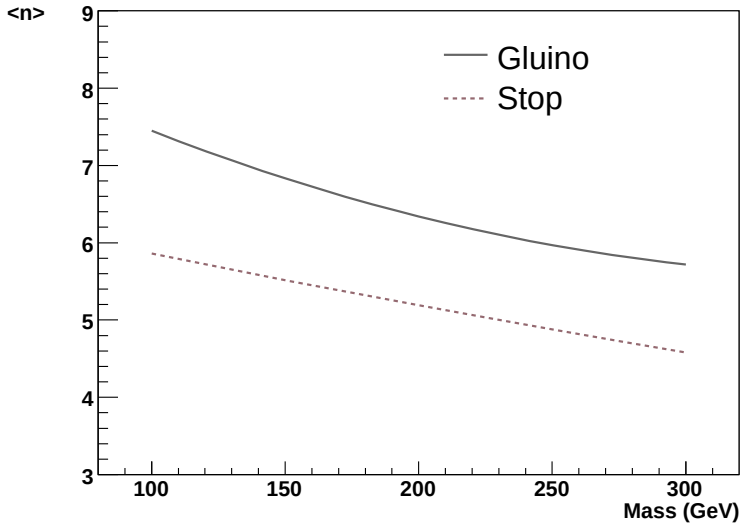

Fig. 3.6.3: The average multiplicity of gluino and stop jets as a function of sparticle mass.

already been considered in[133].

3.6.4 Scattering of CMSPs in Matter

Modelling CMSP scattering

Non-coloured CMSPs such as staus are usually treated as heavy muons when modelling their propagation through a detector. Continuous ionisation and repeated elastic Coulomb scatterings with nuclei are handled by modified GEANT routines[159].

However, the situation is more complicated for R-hadrons for which electromagnetic and hadronic energy loss are important. Calculations of the fine details of R-hadron nuclear scattering in matter are uncertain, and a number of models have been proposed in the literature[124, 125, 126, 127]. Although the phenomenology and predictions differ between the various approaches, some generic, well-motivated features of R-hadron scattering exist.

The probability of an interaction between a heavy coloured parton in the R-hadron and a quark in the target nucleon is low since the cross-section varies with the inverse square of the parton mass according to perturbative QCD. When modelling the scattering of a R-hadron in material, one can thus use the central picture of a stable non-interacting gluino accompanied by a coloured hadronic cloud of light constituents, which are responsible for the interactions. The effective interaction energy is therefore small and equivalent to the interactions of a pion of energy of around several GeV with a stationary nucleus.

A further feature of R-hadron scattering is that, following multiple scatterings, a mesonic R-hadron will almost always have converted into a baryonic state[127]. This is due to phase space suppression for baryon-to-meson conversion and the lack of available pions, with which the R-baryon must interact in order to give up its baryon number. The available baryon states are S^0, S^+,S^-, and S^{++}. The state S^{--}, if formed from either a squark or gluino R-hadron, would possess negative baryon number and would immediately interact to become a meson[16].

An important consequence of the nuclear reactions is that they allow a $R_{\tilde{g}}$-hadron to reverse the sign of its charge in nuclear interactions. However, a hadron containing a stop-like squark can not reverse the sign of its charge through hadronic interactions alone. Charge reversal could nevertheless take place for $R_{\tilde{q}}$-hadrons via the oscillation of intermediate $M^0_{\tilde{q}}$ and $M^0_{\bar{\tilde{q}}}$-states which could be formed in the calorimeter. Since u-type sflavour violation involving the third generation is largely unconstrained it has been shown that extremely rapid oscillations over the scale of a detector are conceivable[160], as are minimal oscillations.

Thus, an observation of R-hadrons which reverse the sign of their charge and which form a doubly charged state could, on the basis of fundamentally allowed and forbidden reactions indicate the existence of a $R_{\tilde{g}}$-hadron or a $R_{\tilde{t}}$-like hadron in which oscillations have occured, thereby providing information concerning the squark couplings. The observation of a doubly charged state

[16] In this paper R, M and S are generic labels used to denote a hadron, meson, and a baryon, respectively. When appropriate, a superscript denotes the charge and a subscript denotes the species of heavy sparticle.

and no charge reversal processes could be used to identify a $R_{\tilde{t}}$-like hadron if a lower limit on the rate of charge reversal processes for gluino R-hadrons can be calculated. A further way of discriminating between stop and gluino R-hadron hypotheses would be to use information on the charges of the tracks before scattering. A pair of charged $R_{\tilde{t}}$,$R_{\tilde{t}}$ would always have unlike signs unlike an equivalent pair of charged $R_{\tilde{g}}$-hadrons which can either have like or unlike charges.

The model[127] for scattering which is used in this study is implemented in GEANT-3[159]. The model provides a simple and general framework of simulating nuclear interactions of heavy hadrons. The total cross-section is set constant for gluino R-meson and R-baryon interactions to 24mb and 36mb, respectively, based on arguments from quark counting and the values obtained from low energy hadron-hadron scattering. The relative fraction of 2-2 and 2-3 processes is determined by a phase space factor. Since it would be impossible to calculate individual Clebsch-Gordon coefficients for each matrix element for each reaction, the matrix elements are assumed to be the same. A $R_{\tilde{g}}$-hadron will typically interact around 10 occasions as it propagates through the calorimeter systems of the Tevatron and LHC experiments. For this work, GEANT-3 scattering routines for $R_{\tilde{g}}$-hadrons were adapted to simulate the scattering of $R_{\tilde{t}}$-hadrons within the framework of the existing model.

Signatures of CMSPs after Scattering

Both CDF[115] and D0[118] have used time-of-flight information to search for CMSPs. One advantage of this technique is that it is highly effective in suppressing background and a search becomes largely a counting exercise when systematic uncertainties are under control. Furthermore, it is possible to reconstruct the mass of a CMSP from timing information alone. This has been studied at the Tevatron[118] and in preparatory physics studies for the LHC[120, 161].

As previously mentioned in section 3.6.4, the propagation of a stau presents fewest experimental difficulties. However, R-hadron scattering is subject to a number of experimental challenges. Charge exchange processes can lead to tracks which possess oppositely signed electric charge in the inner and muon tracking chambers. Similarly, the production of doubly charged states following nuclear scattering gives rise to tracks in which the inner track appears to have twice the transverse momentum of the track reconstructed in the muon system. The response of track reconstruction software to such tracks would be a critical experimental issue in any search. Should these effects be prominent, they may well already have impeded searches for R-hadrons at many colliders. A study of the discovery potential of ATLAS to $R_{\tilde{g}}$-hadrons using tracks which have reversed the sign of their electric charge has already been performed[122]. The Tevatron offers the possibility to develop such searches using collision data.

For this workshop, a toy MC implementing the resolution of D0 tracking systems was used in order to gain an estimate of the expected visibility of CMSP tracks and in particular of R-hadrons which have undergone charge exchange. The resolutions of the muon and inner tracking chambers were parameterized according to ref. [162]. An additional 25% smearing was applied to the muon

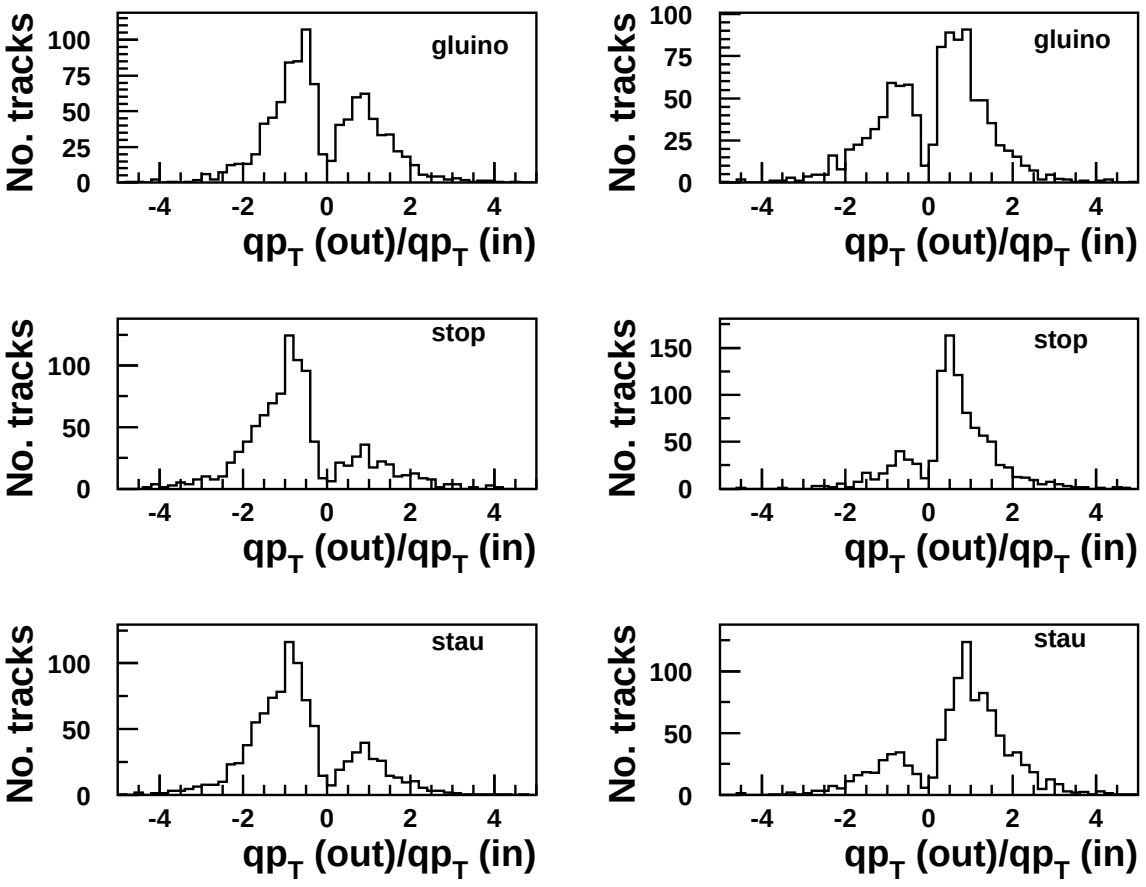

Fig. 3.6.4: The ratio $r = \frac{qp_T(in)}{qp_T(out)}$ for gluino and stop R-hadrons and staus. Distributions are shown for tracks with positively (right) and negatively (left) charged inner tracks.

resolution terms and a charge misidentification rate of around 20% was assumed.

Nuclear interactions involving stop and gluino R-hadrons were calculated using the model[127] described in section 3.6.4. A thickness of $11\lambda_T(\pi)$ was assumed to model the D0 calorimetry.

Pairs of staus, stops and gluinos were generated using PYTHIA and subjected to acceptance cuts necessary for them to be identified as slow moving particles[118].

- The scaled speed of the CMSP β was required to be less than 0.65.
- The CMSPs were restricted to the central pseudorapidity region ($|\eta| < 1.5$).
- The CMSP transverse momentum was required to be greater than 15 GeV.

Fig. 3.6.4 shows the ratio $r = \frac{qp_T(out)}{qp_T(in)}$, where q is the charge of the CMSP and $p_T(in)$ ($p_T(out)$) is the momentum in the inner (muon) tracking chamber. Negative values of r would

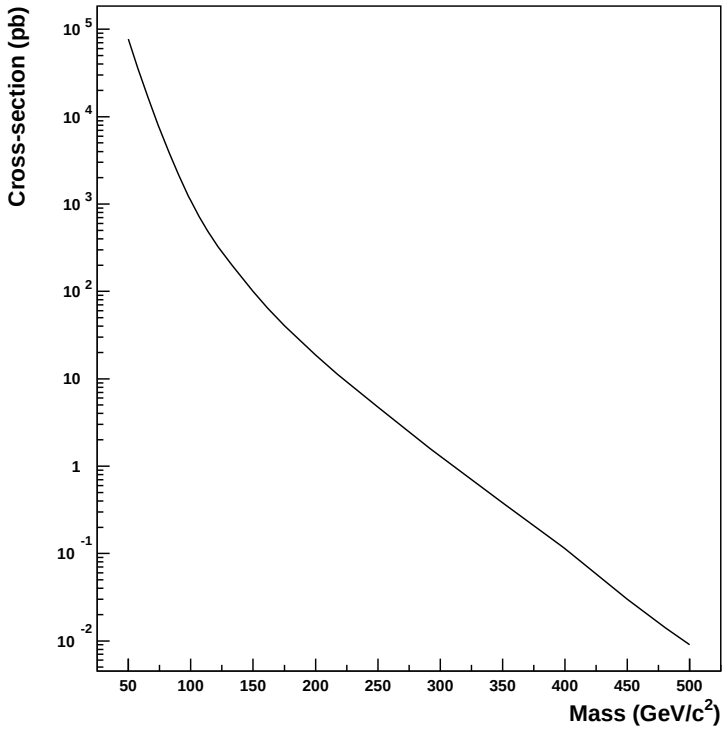

Fig. 3.6.5: The NLO cross-section for gluino pair production as a function of gluino mass.

denote evidence of charge 'flipping'. Spectra are shown for stop and gluino R-hadrons and staus, and are shown for the cases in which the inner track has negative and positive charge.

Interesting features emerge following scattering. The gluino spectra shows a substantial (approximately 50%) rate of charge 'flipping'. A lower rate of charge reversal is expected for positively charged inner tracks than negatively charged tracks since there are two possible positive charge states for the emerging R-hadron: $S^{+}_{\tilde{g}}$ and $S^{++}_{\tilde{g}}$. In this model, the stop R-hadrons undergo minimal mixing of neutral mesino states, and the only 'flipping' which arises comes from charge misidentification. Maximal mixing would bring the stop spectra close to the gluino one. A further feature of the stop and gluino spectra is that the average momentum of the positive tracks in the muon system is lower than the negative tracks. This arises due to the presence of the doubly charged state which would be reconstructed with half of the transverse momentum of the singly charged state. The staus flip purely from charge misidentification.

It is interesting to study the expected rate of tracks arising in a Split-SUSY scenario in which the gluino is stable. Using next-to-leading QCD calculations[163, 164] in a Split-SUSY scenario[122], the cross-section for the pair production of gluinos is shown in Fig. 3.6.5. For an accumulated luminosity of 2 fb^{-1} several thousand gluinos could be expected for 300 GeV mass.

For a luminosity of 2 fb^{-1}, the expected yield of gluino R-hadron tracks passing the acceptance cuts described above is shown in Fig. 3.6.6. The expected yields of tracks which reverse the sign of their charge are also shown. The total yield of charge reversing tracks and the amount of tracks undergoing positive-to-negative and negative-to-positive changes are shown. In an optimistic scenario, several hundred tracks would be accumulated at 300 GeV mass. However, it should be again be pointed out that this represents a best-case scenario and detector effects will undoubtedly degrade any signal. Nevertheless, if an excess could be observed and charge reversal could be established, it would be striking evidence for the existence of R-hadrons.

3.6.5 Summary

The existence of stable, heavy, charged particles has been predicted within a number of different scenarios of physics beyond the Standard Model. One of the tasks of the Tevatron and LHC programs will be to discover and characterise these particles or to exclude their production.

In this work, experimental signatures of long-lived staus, stops and gluinos were studied. The fragmentation of stops and gluinos in jets allows discrimination from QCD jets. Hadronic interactions of R-hadrons with matter were considered. These give rise to challenging experimental effects which can assist and impede any search. Charge exchange processes provide striking signatures of tracks which change the sign of their charges. Rates of such processes were estimated and expected track yields were estimated for the D0 detector.

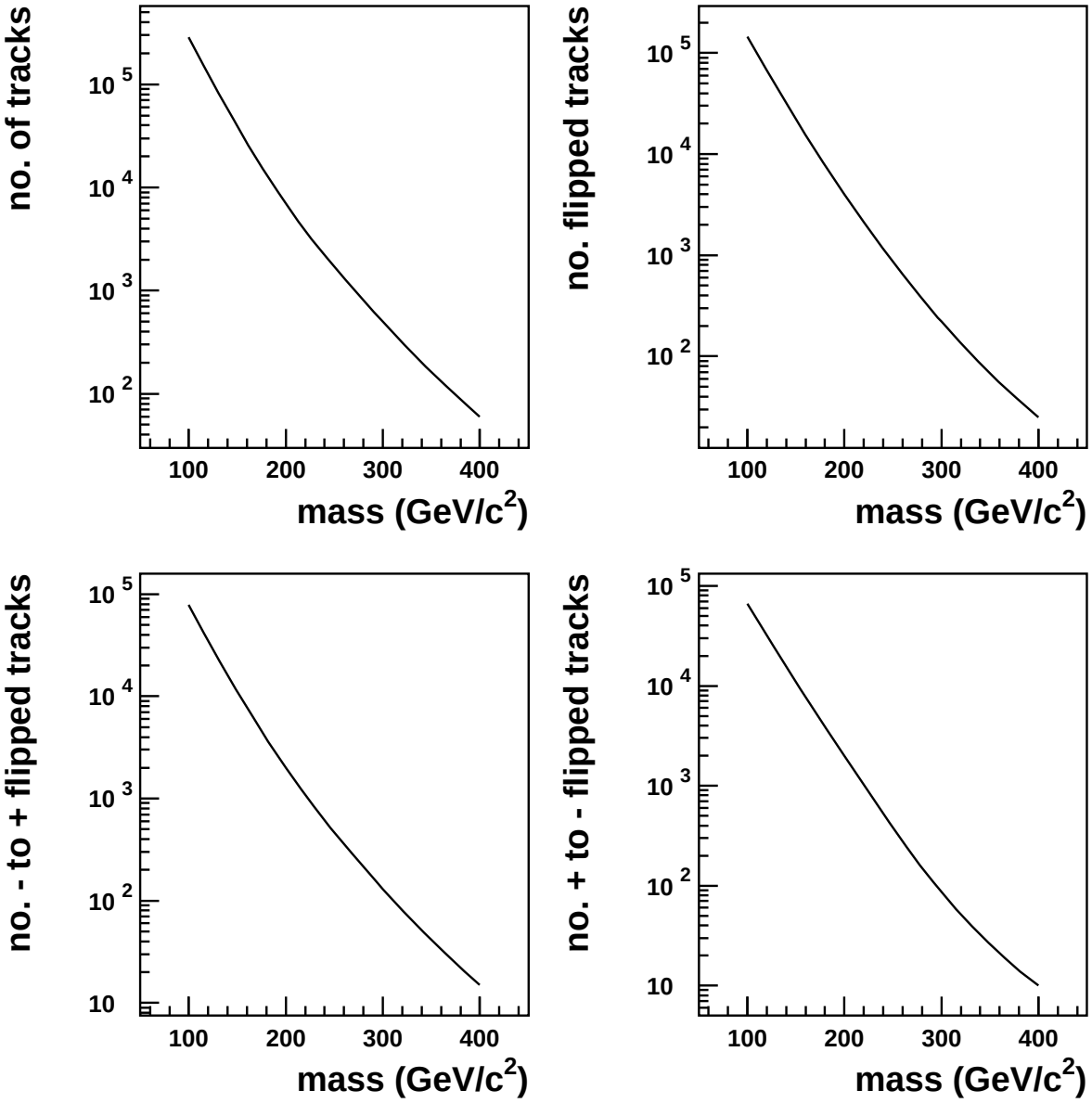

Fig. 3.6.6: The yield of gluino R-hadron tracks expected for 2fb^{-1} and the yields of tracks which change the sign of their charge.

4 Model-based Phenomenology

In addition to the particle-based approach to phenomenology, there is considerable focus on specific models of new physics, or classes of models, and their phenomenological implications, both at colliders and in cosmology and astrophysics, and indeed where these fields intersect. This approach is not exactly tuned to how experimental searches at colliders tend to be conducted, but is still of great value as many of the mainstream models are highly motivated by a variety of theoretical and phenomenological arguments. The recent proliferation of new classes of models has, however, muddied the waters somewhat. Unless one closely follows these trends, it is easy to become lost in the landscape.

A complicating factor is the realization that models of new physics which incorporate dark matter candidates typically yield collider signatures of cascade decays of heavy particles through lighter ones down to SM particles plus the dark matter. That is, many very different types of new physics can appear in experiments with the classical SUSY signature of high-multiplicity leptons, jets and missing energy. This realization presented a phenomenological crisis, and drives much of the current effort to glean more information from cascade decays and other data to disentangle a signature from a largish set of possible explanations. The first contribution of this chapter, Sec. 4.1, addresses this problem.

Much effort is still directed, however, at the initial fleshing-out of production and decay channels, and in creating generators for these processes which can be used for practical phenomenology. Sections 4.3,4.4,4.5 and 4.6 do this for extra-dimensional, Little Higgs T-parity, and technicolor models, the last via a "straw-man" framework meant to establish a working language for generic signatures anticipated by technicolor models. It is especially notable because Tevatron has significant potential to observe these signatures, and Run I data contains a few interesting hints which have not yet been followed up on in Run II.

Sec. 4.7 on slepton mass measurement improves existing techniques for determing supersymmetric lepton partner masses at the LHC, in cases where established techniques would have considerable difficulty. The technique should be extendible to other types of models as well, and would be important for formulating statements about dark matter from collider data on new observed states.

Moving even further in this direction, Sections 4.8,4.9 and 4.11 address specifically the issue of combining data from Tevatron, LHC and a future international linear collider (ILC) to connect supersymmetry, dark matter and cosmology in both general mSUGRA and electroweak baryogenesis scenarios.

The final two contributions, Sections 4.12 and 4.13, deal exclusively with SUSY scenarios. The first is a guide to SUSY tools publicly available for phenomenology, while the second is a brief description of the leading scheme for how collider data from various machines but especially the Tevatron can be used to determine where in SUSY parameter space nature lies if SUSY is indeed discovered by current experiments.

4.1 Spin Determination at the LHC

AseshKrishna Datta[1]*, Kyoungchul Kong*[2] *and Konstantin T. Matchev*[2]
[1] *MCTP, University of Michigan, Ann Arbor, USA* [17]
[2] *Institute for Fundamental Theory, Physics Dept., University of Florida, USA*

We contrast the experimental signatures of low energy supersymmetry and the model of Universal Extra Dimensions and discuss methods for their discrimination at LHC. We consider on-shell cascade decay from squarks or KK quarks for two different types of mass spectrum: a degenerate case (UED) and SPS1a. For the dilepton invariant mass, we find that it is difficult to discriminate two models for both mass spectra, although for some parameter space in MSSM, it can be used. We also investigate the possibility of differentiating the spins of the superpartners and KK modes by means of the asymmetry method of Barr. In the case of the SPS1a mass spectrum, we conclude that the UED model can not fake the SUSY asymmetry through the entire parameter space.

4.1.1 Introduction

With the highly anticipated run of the Large Hadron Collider (LHC) at CERN we will begin to explore the Terascale in earnest. There are very sound reasons to expect momentous discoveries at the LHC. Among the greatest mysteries in particle physics today is the origin of electroweak symmetry breaking, which, according to the Standard Model, is accomplished through the Higgs mechanism. The Higgs particle is the primary target of the LHC experiments and, barring some unexpected behavior, the Higgs boson will be firmly discovered after only a few years of running of the LHC. With some luck, a Higgs signal might start appearing already at Tevatron Run II.

The discovery of a Higgs boson, however, will open a host of new questions. As the first fundamental scalar to be seen, it will bring about a worrisome fine tuning problem: why is the Higgs particle so light, compared to, say, the Planck scale? Various solutions to this hierarchy problem have been proposed, and the most aesthetically pleasing one at this point appears to be low energy supersymmetry (SUSY). In SUSY, the problematic quadratic divergences in the radiative corrections to the Higgs mass are absent, being cancelled by loops with superpartners. The cancellations are enforced by the symmetry, and the Higgs mass is therefore naturally related to the mass scale of the superpartners.

While the solution of the hierarchy problem is perhaps the most celebrated virtue of SUSY, supersymmetric models have other side benefits. For one, if the superpartners are indeed within the TeV range, they would modify the running of the gauge couplings at higher scales, and gauge coupling unification takes place with astonishing precision. Secondly, a large class of SUSY models, which have a conserved discrete symmetry (R-parity), contain an excellent dark matter candidate: the lightest neutralino $\tilde{\chi}_1^0$. One should keep in mind that the dark matter problem is by far the

[17] Current address: Harish-Chandra Research Institute, Allahabad, India

most compelling *experimental* evidence for particles and interactions outside the Standard Model (SM), and provides a completely independent motivation for entertaining supersymmetry at the TeV scale. Finally, R-parity implies that superpartners interact only pairwise with SM particles, which guarantees that the supersymmetric contributions to low energy precision data only appear at the loop level and are small. In summary, supersymmetric extensions of the SM are the primary candidates for new physics at the TeV scale. Not surprisingly, therefore, signatures of supersymmetry at the Tevatron and LHC have been extensively discussed in the literature. In typical scenarios with superpartners in the range of a few TeV or less, already within the first few years of running the LHC would discover a signal of new physics in several channels. Once such a signal of physics beyond the Standard Model is seen, it will immediately bring up the question: is it supersymmetry or not?

The answer to this question can be approached in two different ways. On the theoretical side, one may ask whether there are well-motivated alternatives to low-energy supersymmetry, which would give similar signatures at hadron colliders. In other words, if the new physics is not supersymmetry, what else can it be? Until recently, there were no known examples of other types of new physics which could "fake" supersymmetry sufficiently well. The signatures of supersymmetry and its competitors (Technicolor, new gauge bosons, large extra dimensions, etc.) were sufficiently distinctive, and there was little room for confusion. However, it was recently realized that the framework of Universal Extra Dimensions (UED), originally proposed in [143], can very effectively masquerade as low-energy SUSY at a hadron collider such as the LHC or the Tevatron [165]. It therefore became of sufficient interest to try to prove SUSY at the LHC from first principles, without resorting to model-dependent assumptions and without theoretical bias. The experimental program for proving SUSY at a *lepton* collider was outlined a long time ago [166] and can be readily followed to make the discrimination between SUSY and UED [167, 168, 169, 170]. Recently there has been a lot of interest regarding the "inversion" problem and spin measurements at LHC [171, 172, 173, 174, 175, 176, 177, 178, 179, 180, 181, 182] (see also Sec. 4.13). However, as we shall see below, the case of hadron colliders is much more challenging.

4.1.2 UED versus SUSY

The couplings of the SM particles and their superpartners are equal, being related by supersymmetry and the generic collider signatures of supersymmetric models with weakly-interacting massive particle (WIMP) lightest SUSY particles (LSPs) is missing energy. In UED, KK-parity guarantees the lightest KK particle (LKP) is stable and UED can explain dark matter problem [183, 184, 185, 186, 187]. The new couplings are also the same as SM couplings. Therefore the above two features are common to both SUSY and UED and cannot be used to distinguish the two cases. We see that while R-parity-conserving SUSY implies a missing energy signal, the reverse is not true: a missing energy signal would appear in any model with a dark matter candidate, and even in models which have nothing to do with the dark matter issue, but simply contain new neutral quasi-stable particles, e.g. gravitons [188, 189, 190]. Similarly, the equality of couplings is a celebrated test of

SUSY, but we see that it is only a necessary, not sufficient, condition to prove supersymmetry. In addition, the measurement of superpartner couplings in order to test the SUSY relations is a very challenging task at a hadron collider. For one, the observed production rate in any given channel is sensitive only to the product of the cross-section times the branching fractions, so any attempt to measure the couplings from a cross section would have to make certain assumptions about the branching fractions. An additional complication arises from the fact that at hadron colliders all kinematically available states can be produced simultaneously, and the production of a particular species in an exclusive channel is rather difficult to isolate. The couplings could also in principle be measured from the branching fractions, but that also requires a measurement of the total width, which is impossible in our case, since the Breit-Wigner resonance cannot be reconstructed, due to the unknown momentum of the missing LSP (LKP).

The fundamental difference between SUSY and UED is first the number of new particles, and second their spins. The KK particles at $n = 1$ are analogous to superpartners in SUSY. However, the particles at the higher KK levels have no analogues in $N = 1$ supersymmetric models. Discovering the $n \geq 2$ levels of the KK tower would therefore indicate the presence of extra dimensions rather than SUSY. However, these KK particles can be too heavy to be observed. Even if they can be observed at LHC, they can be confused with other new particles [178, 179] such as Z' or different types of resonances from extra dimensions [191].

The second feature – the spins of the new particles – also provides a tool for discrimination between SUSY and UED: the KK partners have identical spin quantum numbers as their SM counterparts, while the spins of the superpartners differ by $1/2$ unit. However, spin determination may in some cases be difficult at the LHC (or at hadron colliders in general), where the parton-level center of mass energy E_{CM} in each event is unknown. In addition, the momenta of the two dark matter candidates in the event are also unknown. This prevents the reconstruction of any rest frame angular decay distributions, or the directions of the two particles at the top of the decay chains. The variable E_{CM} also rules out the possibility of a threshold scan, which is one of the main tools for determining particle spins at lepton colliders. We are therefore forced to look for new methods for spin determinations, or at least for finding spin correlations[18]. The purpose of this paper is to investigate the prospects for establishing SUSY at the LHC by discriminating it from its look-alike scenario of Universal Extra Dimensions by measuring spins [19] of new particles in two models [20].

[18]Notice that in simple processes with two-body decays like slepton production $e^+e^- \to \tilde{\mu}^+\tilde{\mu}^- \to \mu^+\mu^-\tilde{\chi}_1^0\tilde{\chi}_1^0$ the flat energy distribution of the observable final state particles (muons in this case) is often regarded as a smoking gun for the scalar nature of the intermediate particles (the smuons). Indeed, the smuons are spin zero particles and decay isotropically in their rest frame, which results in a flat distribution in the lab frame. However, the flat distribution is a necessary but not sufficient condition for a scalar particle, and UED provides a counterexample with the analogous process of KK muon production [167], where a flat distribution also appears, but as a result of equal contributions from left-handed and right-handed KK fermions.

[19]Another recent work [182] showed how one can clearly distinguish a SUSY gluino from a UED heavy gluon partner at the LHC.

[20]The same idea can apply in the case of Little Higgs models since the first level of the UED model looks like the

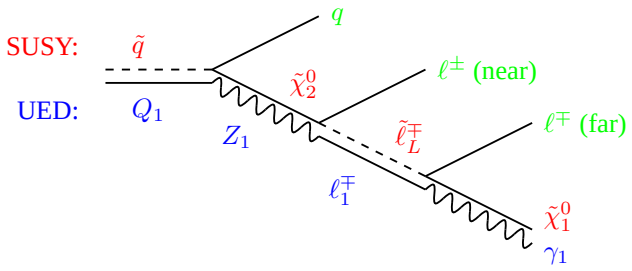

Fig. 4.1.1: Twin diagrams in SUSY and UED. The upper (red) line corresponds to the cascade decay $\tilde{q} \to q\tilde{\chi}_2^0 \to q\ell^\pm\tilde{\ell}_L^\mp \to q\ell^+\ell^-\tilde{\chi}_1^0$ in SUSY. The lower (blue) line corresponds to the cascade decay $Q_1 \to qZ_1 \to q\ell^\pm\ell_1^\mp \to q\ell^+\ell^-\gamma_1$ in UED. In both cases the observable final state is the same: $q\ell^+\ell^- \not{E}_T$.

4.1.3 Spin Determination in Squark/KK Quark Cascade Decay

As discussed in the previous section, the second fundamental distinction between UED and supersymmetry is reflected in the properties of the individual particles. Recently it was suggested that a charge asymmetry in the lepton-jet invariant mass distributions from a particular cascade (see fig. 4.1.1) can be used to discriminate SUSY from the case of pure phase space decays [176] and is an indirect indication of the superparticle spins. (A study of measuring sleptons spins at the LHC can be found in [177]). It is therefore natural to ask whether this method can be extended to the case of SUSY versus UED discrimination. Following [176], we concentrate on the cascade decay $\tilde{q} \to q\tilde{\chi}_2^0 \to q\ell^\pm\tilde{\ell}_L^\mp \to q\ell^+\ell^-\tilde{\chi}_1^0$ in SUSY and the analogous decay chain $Q_1 \to qZ_1 \to q\ell^\pm\ell_1^\mp \to q\ell^+\ell^-\gamma_1$ in UED. Both of these processes are illustrated in Fig. 4.1.1. Blue lines represent the decay chain in UED and red lines the decay chain in SUSY. Green lines are SM particles.

Dilepton Invariant Mass

First we will look for spin correlations between the two SM leptons in the final state. In SUSY, a slepton is a scalar particle and therefore there is no spin correlation between the two SM leptons. However in UED, a slepton is replaced by a KK lepton and is a fermion. We might therefore expect a different shape in the dilepton invariant mass distribution. To investigate this question, we first choose a study point in UED (SPS1a in mSUGRA) with $R^{-1} = 500$ GeV taken from [165, 196] and then adjust the relevant MSSM parameters (UED parameters) until we get a matching spectrum. So the masses are exactly same and cannot be used for discrimination.

In Fig. 4.1.2 we show invariant mass distributions in UED and SUSY for two different types of mass spectra. In Fig. 4.1.2(a), all UED masses are adjusted to be the same as the SUSY masses in SPS1a ($m_0 = 100$ GeV, $m_{1/2} = 250$ GeV, $A_0 = -100$, $\tan\beta = 10$ and $\mu > 0$) while in

new particles in the Little Higgs [192, 193, 194, 195].

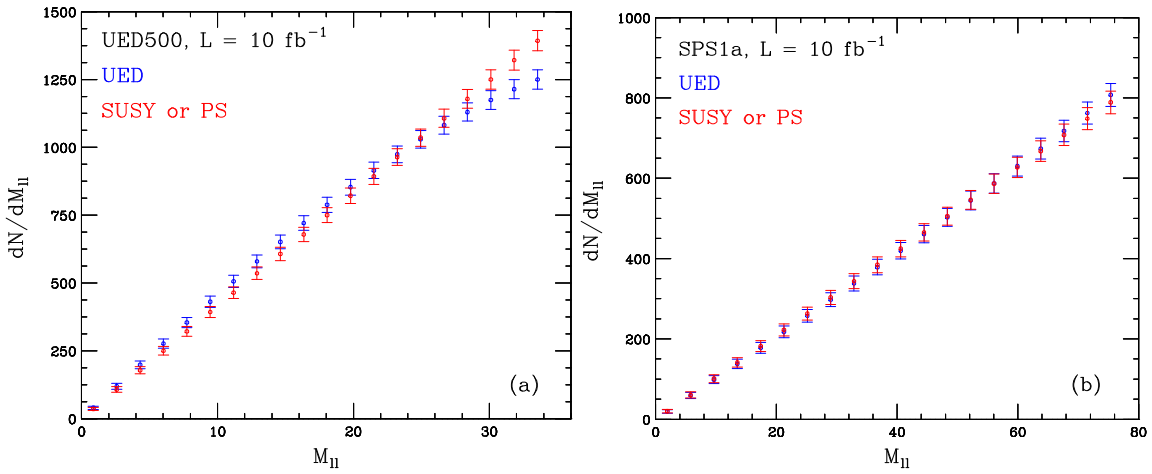

Fig. 4.1.2: Comparison of dilepton invariant mass distributions in the case of (a) UED mass spectrum with $R^{-1} = 500$ GeV (b) mass spectrum from SPS1a. In both cases, UED (SUSY) distributions are shown in blue (red). All distributions are normalized to $\mathcal{L} = 10$ fb^{-1} and the error bars represent statistical uncertainty.

Fig. 4.1.2(b) the SUSY masses are replaced by KK masses for $R^{-1} = 500$. In both cases, UED (SUSY) distributions are shown in blue (red). Squark/KK quark pair-production cross sections are taken from Ref. [180] and the relevant branching fractions are obtained from Ref. [165] for UED and Ref. [197] for SUSY. All distributions are normalized to $\mathcal{L} = 10$ fb^{-1} and the error bars represent statistical uncertainty. For SUSY, the distribution is the same as that in the case of pure phase space decay since the slepton has no spin. As we see, the two distributions are identical for both UED and SUSY mass spectrum even if the intermediate particles in UED and SUSY have different spins. Small differences in the distributions will completely disappear once the background, radiative corrections and detector simulation are included.

The invariant mass distributions for UED and SUSY/Phase space can be written as [180, 181]

$$\begin{aligned} \text{Phase Space} : \frac{dN}{d\hat{m}} &= 2\hat{m} \\ \text{SUSY} : \frac{dN}{d\hat{m}} &= 2\hat{m} \\ \text{UED} : \frac{dN}{d\hat{m}} &= \frac{4(y+4z)}{(1+2z)(2+y)}\left(\hat{m} + r\,\hat{m}^3\right) \end{aligned} \tag{4.1.1}$$

where the coefficient r in the second term of the UED distribution is defined as

$$r = \frac{(2-y)(1-2z)}{y+4z}\,, \tag{4.1.2}$$

$\hat{m} = \frac{m_{\ell\ell}}{m_{\ell\ell}^{max}}$ is the rescaled invariant mass, $y = \left(\frac{m_{\tilde{\ell}}}{m_{\tilde{\chi}_2^0}}\right)^2$ and $z = \left(\frac{m_{\tilde{\chi}_1^0}}{m_{\tilde{\ell}}}\right)^2$ are the ratios of masses involved in the decay; y and z are less than 1 in the case of on-shell decay. From Eq. 4.1.1, there

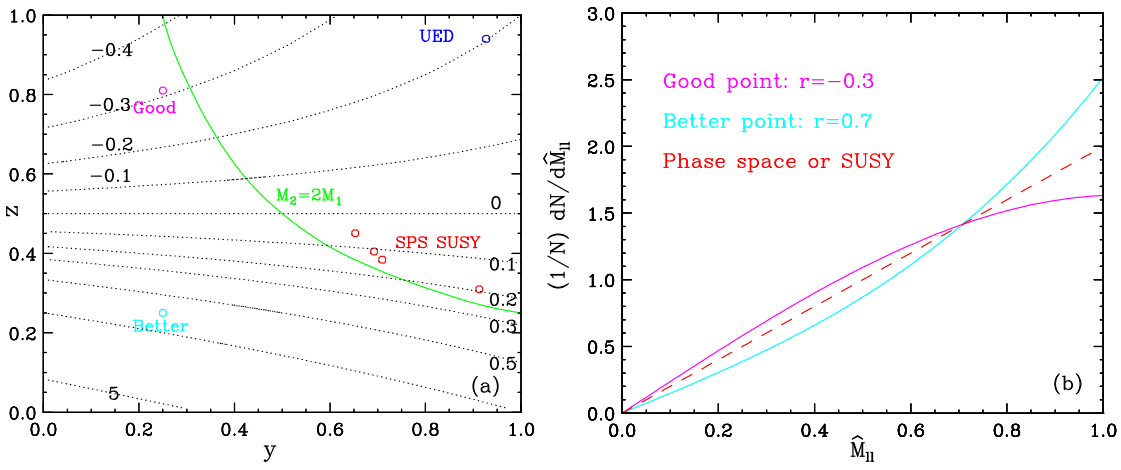

Fig. 4.1.3: (a) Contour dotted lines represent the size of the coefficient r in Eq. 4.1.2. UED is the blue dot in the upper-right corner since y and z are almost 1 due to the mass degeneracy. The red dots represent several snowmass points: SPS1a, SPS1b, SPS5 and SPS3, from left to right. The green line represents gaugino unification, so all SUSY benchmark points lie close to this line. r is small for both UED and snowmass points. (b) The dashed line represents the dilepton distribution in SUSY or pure phase space. Solid cyan (magenta) line represents dilepton distribution in UED for $r = -0.3$ ($r = 0.7$).

are two terms in UED. The first term is phase-space-like and the second term is proportional to $\hat{m}^3$. So we see that whether or not the UED distribution is the same as the SUSY distribution depends on the size of the coefficient r in the second term of the UED distribution. Note that the UED distribution becomes exactly the same as the SUSY distribution if $r = 0.5$. Therefore we scan (y, z) parameter space, calculate the coefficient r and show our result in Fig. 4.1.3(a). In Fig. 4.1.3(a), contour dotted lines represent the size of the coefficient r in Eq. 4.1.2. UED is the blue dot in the upper-right corner since y and z are almost 1 due to the mass degeneracy, while red dots represent several snowmass points [198]: SPS1a, SPS1b, SPS5 and SPS3, from left to right. The green line represents gaugino unification so all SUSY benchmark points are close to this green line. As we can see, r is small for both UED and snowmass points. This is why we did not see any difference in the distributions from Fig. 4.1.2. If the mass spectrum is either narrow (UED mass spectrum) or generic (mSUGRA type), the dilepton distributions are very similar and we cannot extract any spin information from this distribution. However, away from the mSUGRA model or UED, we can easily find regions where the coefficient r is large and the spin correlation is big enough so that we can see a shape difference. We show two points (denoted by 'Good' and 'Better') in Fig. 4.1.3(a) and show the corresponding dilepton distributions in Fig. 4.1.3(b). For the 'Good' point, the mass ratio is $m_{\tilde{\chi}_1^0} : m_{\tilde{\ell}} : m_{\tilde{\chi}_2^0} = 9 : 10 : 20$ and for the 'Better' point, $m_{\tilde{\chi}_1^0} : m_{\tilde{\ell}} : m_{\tilde{\chi}_2^0} = 1 : 2 : 4$. In Fig. 4.1.3(b), the dashed line represents dilepton distribution in SUSY or pure phase space and the solid cyan (magenta) line represents the dilepton distribution in UED for $r = -0.3$ ($r = 0.7$). Indeed, for larger r, the distributions look different, but background

and detector simulation need to be included. Notice that in the mSUGRA model, the maximum of the coefficient r is 0.4.

Lepton-Jet Invariant Mass - Charge Asymmetry

Now we look at spin correlations between q and ℓ in Fig. 4.1.1. In this case, there are several complications. First of all, we don't know which lepton we need to choose. There are two leptons in the final state. The lepton we call 'near' comes from the decay of $\tilde{\chi}_2^0$ in SUSY or Z_1 in UED, while the other lepton we call 'far' comes from the decay of $\tilde{\ell}$ in SUSY or ℓ_1 in UED. The lepton-quark invariant mass distributions $m_{\ell q}$ turns out to be useful. The spin of the intermediate particle (Z_1 in UED or $\tilde{\chi}_2^0$ in SUSY) governs the shape of the distributions for the near lepton. However, in practice we cannot distinguish the near and far lepton, and one has to include the invariant mass combinations with both leptons (it is impossible to tell near and far leptons event-by-event, but there can be an improvement for the selection [181].). Second, we do not measure jet (quark) charge. Therefore we do not know whether a particular jet (quark) came from the decay of a squark or an anti-squark. This doubles the number of diagrams that we need to consider. These complications tend to wash out the spin correlations, but a residual effect remains, which is due to the different number of quarks and anti-quarks in the proton, which in turn leads to a difference in the production cross-sections for squarks and anti-squarks [176]. Most importantly, we do not know which jet is actually the correct jet in this cascade decay chain. We pair produce two squarks (or KK quarks) and each of them decays to one jet. Once initial-state radiation (ISR) is included, there are many jets in the final state. For now, as in [180], we assume that we know which jet is the correct one and choose it. One never knows for sure which is the correct jet, although there can be clever cuts to increase the probability that we picked the right one [181]. There are two possible invariant distributions in this case: $\left(\frac{d\sigma}{dm}\right)_{q\ell^+}$ with positively charged leptons and $\left(\frac{d\sigma}{dm}\right)_{q\ell^+}$ with negatively charged leptons. In principle, there are 8 diagrams that need to be included (a factor of 2 from quark/anti-quark combination, another factor of 2 from sleptons with different chiralities, and a factor 2 from the ambiguity between near and far leptons).

For this study, as in the dilepton case, we first start from a UED mass spectrum and adjust the MSSM parameters until we get perfect spectrum match. In this case, Z_1 does not decay into a right-handed lepton. There are 4 contributions and they all contribute to both $\left(\frac{d\sigma}{dm}\right)_{q\ell^+}$ and $\left(\frac{d\sigma}{dm}\right)_{q\ell^+}$ distributions which are in fig. 4.1.4,

$$\begin{aligned}\left(\frac{d\sigma}{dm}\right)_{q\ell^+} &= f_q\left(\frac{dP_2}{dm_n}+\frac{dP_1}{dm_f}\right)+f_{\bar{q}}\left(\frac{dP_1}{dm_n}+\frac{dP_2}{dm_f}\right)\\ \left(\frac{d\sigma}{dm}\right)_{q\ell^-} &= f_q\left(\frac{dP_1}{dm_n}+\frac{dP_2}{dm_f}\right)+f_{\bar{q}}\left(\frac{dP_2}{dm_n}+\frac{dP_1}{dm_f}\right)\ ,\end{aligned} \tag{4.1.3}$$

where P_1 (P_2) represents the distribution for a decay from a squark or KK quark (anti-squark or anti-KK quark) and f_q ($f_{\bar{q}}$) is the fraction of squarks or KK quarks (anti-squarks or anti-KK quarks) and by definition, $f_q + f_{\bar{q}} = 1$. The quantity f_q tells us how much squarks or KK quarks are

produced compared to the anti-particles. For the UED mass spectrum and SPS1a, $f_q \sim 0.7$ [180]. These two distributions in UED (SUSY) are shown in Fig. 4.1.4(a) (Fig. 4.1.4(b)) in different colors. The distributions are normalized to $\mathcal{L} = 10 fb^{-1}$ and the very sharp edge near $m_{q\ell} \sim 60$ GeV ($m_{q\ell} \sim 75$ GeV) is due to the near (far) lepton. However, once the background and detector resolutions are included, these clear edges are smoothed out.

Now with these two distributions, a convenient quantity, 'asymmetry' [176] is defined below

$$A^{+-} = \frac{\left(\frac{d\sigma}{dm}\right)_{q\ell^+} - \left(\frac{d\sigma}{dm}\right)_{q\ell^-}}{\left(\frac{d\sigma}{dm}\right)_{q\ell^+} + \left(\frac{d\sigma}{dm}\right)_{q\ell^-}} \,. \tag{4.1.4}$$

Notice that if $f_q = f_{\bar{q}} = 0.5$, $\left(\frac{d\sigma}{dm}\right)_{q\ell^+} = \left(\frac{d\sigma}{dm}\right)_{q\ell^+}$ and A^{+-} becomes zero. This is the case for pure phase space decay. Zero asymmetry means we don't obtain any spin information from this decay chain, i.e., if we measure a non-zero asymmetry, it means that the intermediate particle ($\tilde{\chi}_2^0$ or Z_1) has non-zero spin. So for this method to work, f_q must be different from $f_{\bar{q}}$. This method does not apply at a $p\bar{p}$ collider such as the Tevatron since a $p\bar{p}$ collider produces the same amount of quarks as anti-quarks. The spin correlations are encoded in the charge asymmetry [176]. However, even at a pp collider such as the LHC, whether or not we measure a non-zero asymmetry depends on parameter space. E.g., in the focus point region, gluino production dominates and the gluino produces equal amounts of squarks and anti-squarks. Therefore we expect $f_q \sim f_{\bar{q}} \sim 0.5$ and any asymmetry will be washed out.

Our comparison between A^{+-} in the case of UED and SUSY for the UED mass spectrum is shown in Fig. 4.1.5(a). We see that although there is some minor difference in the shape of the asymmetry curves, overall the two cases appear to be very difficult to discriminate unambiguously, especially since the regions near the two ends of the plot, where the deviation is the largest, also happen to suffer from poor statistics. Notice that we have not included detector effects or backgrounds. Finally, and perhaps most importantly, this analysis ignores the combinatorial background from other jets in the event, which could be misinterpreted as the starting point of the cascade depicted in Fig. 4.1.1. Overall, Fig. 4.1.5 shows that although the asymmetry (Eq. 4.1.4) does encode some spin correlations, distinguishing between the specific cases of UED and SUSY appears to be challenging.

Similarly in Fig. 4.1.5(b), we show the asymmetry for UED and SUSY for a mass spectrum of mSUGRA point SPS1a. In this case, the mass spectrum is broad compared to the UED spectrum and $\tilde{\chi}_2^0$ in SUSY (Z_1 in UED) does not decay into left-handed sleptons ($SU(2)_W$ KK leptons). Unlike the narrow mass spectrum, here we experience larger mass splittings, as expected in typical SUSY models, and the asymmetry distributions appear to be more distinct than the case shown in Fig. 4.1.5(a), which is a source of optimism. These results have been recently confirmed in Ref. [180]. It remains to be seen whether this conclusion persists in a more general setting, and once the combinatorial backgrounds are included [181]. Notice that comparing (a) and (b) in Fig. 4.1.4, the signs of the two asymmetries have changed. The difference is the chirality of sleptons or KK leptons. In Fig. 4.1.4(a) (Fig. 4.1.4(a)), left-handed sleptons or $SU(2)_W$-doublet

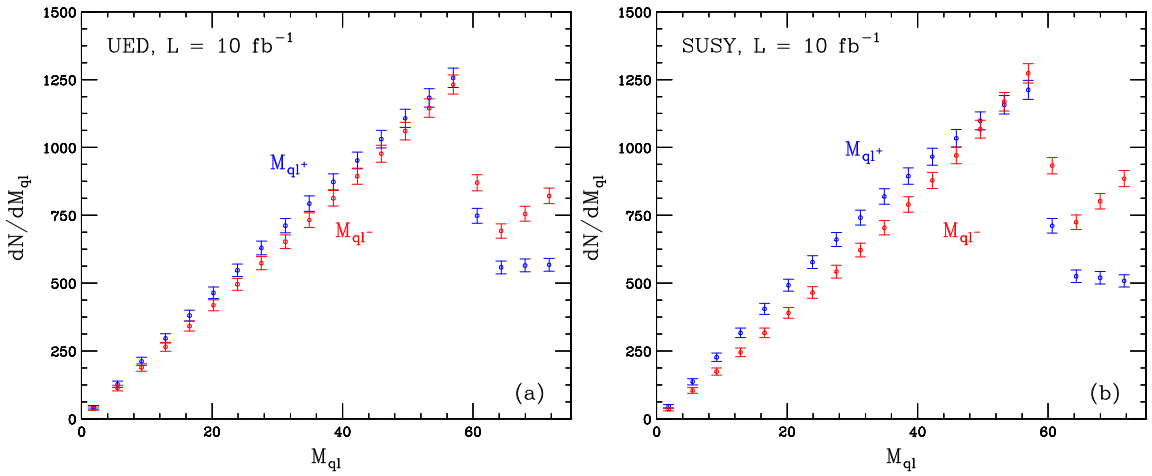

Fig. 4.1.4: $\left(\frac{dN}{dm}\right)_{q\ell^+}$ (blue) and $\left(\frac{dN}{dm}\right)_{q\ell^+}$ (red) in the case of (a) UED and (b) SUSY for UED mass spectrum with $R^{-1} = 500$ GeV. q stands for both a quark and an anti-quark, and $N(q\ell^+)$ ($N(q\ell^-)$) is the number of entries with a positively (negatively) charged lepton. The distributions are normalized to $\mathcal{L} = 10fb^{-1}$. A very sharp edge near $m_{q\ell} \sim 60$ GeV ($m_{q\ell} \sim 75$ GeV) is due to the near (far) lepton. Once background and detector resolutions are included, these clear edges are smoothed out.

KK leptons (right-handed sleptons or $SU(2)_W$-singlet KK leptons) are on shell and the asymmetry starts positive (negative) and ends negative (positive). By looking at the sign of the asymmetry, we can determine which chirality was on-shell.

What we did so far was, first choose a study point in one model and adjust parameters in other models until we match the mass spectra. However, not all masses are observable and sometimes we get fewer constraints than the number of masses involved in the decay. So what we need to do is to match endpoints in the distributions instead of matching mass spectra, and ask whether there is any point in parameter space which is consistent with the experimental data. In other words, we have to ask which model fits the data better. We consider three kinematic endpoints: $m_{q\ell\ell}$, $m_{q\ell}$ and $m_{\ell\ell}$ (see Fig. 4.1.1). In principle, we can find more kinematic endpoints such as the lower edge. Here we are conservative and take upper edges only [199, 200, 201]. In the case of an on-shell decay of χ_2^0 and $\tilde{\ell}$, these three kinematic endpoints are written in terms of the invariant masses

$$\begin{aligned} m_{q\ell\ell} &= m_{\tilde{q}}\sqrt{(1-x)(1-yz)} \\ m_{q\ell} &= m_{\tilde{q}}\sqrt{(1-x)(1-z)} \\ m_{\ell\ell} &= m_{\tilde{q}}\sqrt{x(1-y)(1-z)} \end{aligned} \tag{4.1.5}$$

where $m_{\tilde{q}}$ is the squark or KK quark mass and $x = \left(\frac{m_{\tilde{\chi}_2^0}}{m_{\tilde{q}}}\right)^2$, $y = \left(\frac{m_{\tilde{\ell}}}{m_{\tilde{\chi}_2^0}}\right)^2$ and $z = \left(\frac{m_{\tilde{\chi}_1^0}}{m_{\tilde{\ell}}}\right)^2$ are the ratios of masses in the cascade decay chain. By definition, x, y and z are each less than 1.

We are now left with 2 free parameters, f_q and x, from which we solve for y, z and $m_{\tilde{q}}$. We

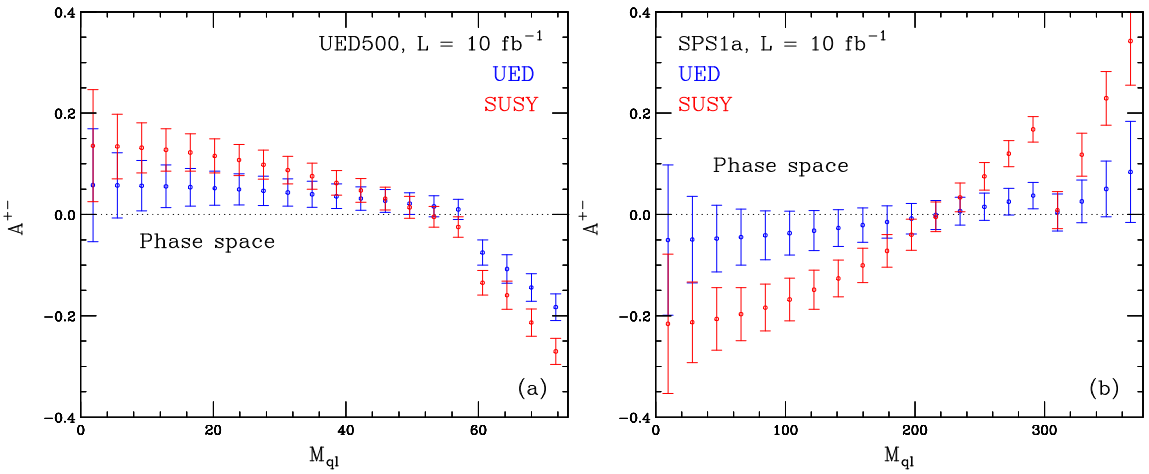

Fig. 4.1.5: Asymmetries for UED (SUSY) are shown in blue (red) in the case of (a) a UED mass spectrum with $R^{-1} = 500$ GeV and (b) the SPS1a mass spectrum. The horizontal dotted line represents pure phase space. The error bars represent the statistical uncertainty for $\mathcal{L} = 10$ fb^{-1}.

minimize χ^2,

$$\chi^2 = \sum_{i=1}^{n} \frac{(x_i - \mu_i)^2}{\sigma_i^2}\,, \tag{4.1.6}$$

between the two asymmetries in the $(x,\ f_q)$ parameter space to see whether we can fake a SUSY asymmetry in a UED model. x_i is the theory prediction and μ_i is the experimental value with uncertainty σ_i. $\chi^2_{dof} = \chi^2/n$ is the 'reduced' χ^2 or χ^2 for n degrees of freedom.

Our result is shown in Fig. 4.1.6(a). We found a minimum χ^2 of around 3 in the region where all KK masses are the same as the SUSY masses in the decay and f_q is large. This means that χ^2 is minimized when we have a perfect match in mass spectrum. The red circle is the point SPS1a.

Now since we don't yet have experimental data, we generated data samples from SPS1a assuming $10 fb^{-1}$ and construct the asymmetries in SUSY and UED in Fig. 4.1.6(b). We included a 10% jet energy resolution. Red dots represent data points and the red line is the SUSY fit to the data points. The blue lines are the UED fits to data points for two different values of f_q. For SUSY, χ^2 is around 1 as we expect. We can get better χ^2 for UED, from 9.1 to 4.5, by increasing f_q. It is still too large to fit to the Monte Carlo. So our conclusion for this study is that a particular point like SPS1a can not be faked throughout the entire parameter space of UED. However, we need to check whether this conclusion will remain the same when we include the wrong jet assignment, i.e. jets which have nothing to do with this decay chain [181]. Notice that the clear edge at $m_{q\ell} \sim 300$ GeV in Fig. 4.1.5(b) disappeared in Fig. 4.1.6(b) after including jet energy resolution. From Fig. 4.1.5, we see that SUSY has a larger asymmetry.

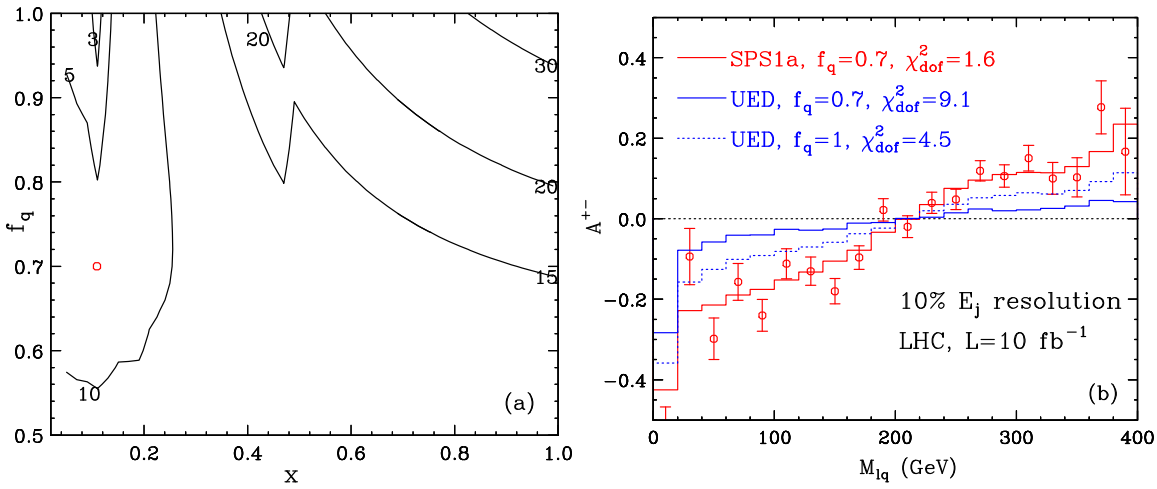

Fig. 4.1.6: (a) The contour lines show χ^2 in (x, f_q) parameter space and the red dot represents the SPS1a point. χ^2 is minimized when $f_q \sim 1$ and x are the same as for SPS1a. (b) Red dots represent the data points generated from SPS1a with $\mathcal{L} = 10$ fb^{-1} including a 10% jet energy resolution. χ^2-minimized UED (SUSY) fits to the Monte Carlo are shown in blue (red). Since the Monte Carlo was generated from SUSY, a small χ^2 for the SUSY fit is expected. χ^2 for UED fits is 9.1 (blue sold) and 4.5 (blue dotted) for $f_q = 0.7$ and f_q=1, respectively.

4.1.4 Conclusions

The fundamental difference between UED and SUSY is 1) the number of partners of SM particles and 2) the spins of new particles. The second level of KK particles can be confused with e.g. a Z' and its existence is not a direct proof of UED, although the smoking gun for UED is degeneracy in resonance masses. Therefore to discriminate these two models, we need to measure the spins of new particles. Two methods are discussed in this paper and the key was a mass spectrum. First in the dilepton mass, with a narrow mass spectrum (UED type) and a mass spectrum from mSUGRA model, UED and SUSY predict very similar distributions. In some regions of MSSM parameter space away from the mSUGRA, the spin correlation becomes more important and the differences in distributions start to appear. Second, if we measure a non-zero asymmetry, this means that the new particle ($\tilde{\chi}_2^0$ or Z_1) in the cascade decay has non-zero spin. An asymmetry study also tells about the relative chirality of sleptons and KK leptons. However, whether one can measure $A^{+-} \neq 0$ or not depends on the particular point in parameter space. For instance, in the focus point region, $\tilde{g}$ production dominates and equal numbers of quarks and anti-quarks are produced, which wash out A^{+-}. In the case of off-shell sleptons decays, the spin correlation is small, and it is not clear whether an asymmetry would be observable in this case. Also, we can easily find parameter space where two contributions from sleptons with different chiralities can cancel each other. Even if we measure a non-zero asymmetry, it is not clear whether the new particle has spin 1 or 1/2 for the degenerate mass spectrum. For a particular point like SPS1a in mSUGRA, we can tell that the new particle is indeed a SUSY partner. However, even in this case, we don't know the effect of wrong choice of jets, and further study is needed.

Acknowledgements

The work of KK and KM is supported in part by a US Department of Energy Outstanding Junior Investigator award under grant DE-FG02-97ER41209.

4.2 Collider Search for Level 2 Kaluza-Klein Gauge Bosons at Hadron Colliders

AseshKrishna Datta[1]*, Kyoungchul Kong*[2] *and Konstantin T. Matchev*[2]
[1] *MCTP, University of Michigan, Ann Arbor, USA* [21]
[2] *Institute for Fundamental Theory, Physics Dept., University of Florida, USA*

We contrast the experimental signatures of low-energy supersymmetry and the model of Universal Extra Dimensions, and discuss their discrimination at hadron colliders. We study the discovery reach of the Tevatron and LHC for level 2 Kaluza-Klein modes, which would indicate the presence of extra dimensions. We find that with 100 fb^{-1} *of data the LHC will be able to discover the* γ_2 *and* Z_2 *KK modes as separate resonances if their masses are below 2 TeV.*

4.2.1 Introduction

Supersymmetry (SUSY) and Extra Dimensions (ED) offer two different paths to a theory of new physics beyond the Standard Model (SM). They both address the hierarchy problem, play a role in a more fundamental theory aimed at unifying the SM with gravity, and offer a candidate particle for dark matter, compatible with present cosmology data. If either SUSY or ED exist at the TeV scale, signals of new physics should be found by the ATLAS and CMS experiments at the Large Hadron Collider (LHC) at CERN. However, as we discuss below, the proper interpretation of such discoveries may not be straightforward.

A particularly interesting scenario of TeV-size extra dimensions is offered by the so called Universal Extra Dimensions (UED) model, originally proposed in [143], where all SM particles are allowed to freely propagate into the bulk. The case of UED bears interesting analogies to SUSY and sometimes has been referred to as "bosonic supersymmetry" [165]. In principle, disentangling UED and supersymmetry appears highly non-trivial at hadron colliders [165, 178, 179]. For each SM particle, both models predict the existence of a partner (or partners) with identical interactions. Unfortunately, the masses of these new particles are model-dependent and cannot be used to unambiguously discriminate between the two theories[22]. Both theories have a good dark matter candidate [183, 184, 185, 186, 187] and the typical collider signatures contain missing energy. One would therefore like to have experimental discriminators which rely on the fundamental distinctions between the two models. In what follows we shall discuss methods for experimental discrimination between SUSY and UED and study the discovery reach for level 2 Kaluza-Klein (KK) gauge boson particles and the resolving power of the LHC to see them as separate resonances.

[21] Current address: Harish-Chandra Research Institute, Allahabad, India

[22] Notice that the recently proposed little Higgs models with T-parity [192, 193, 194, 195] are reminiscent of UED, and may also be confused with SUSY.

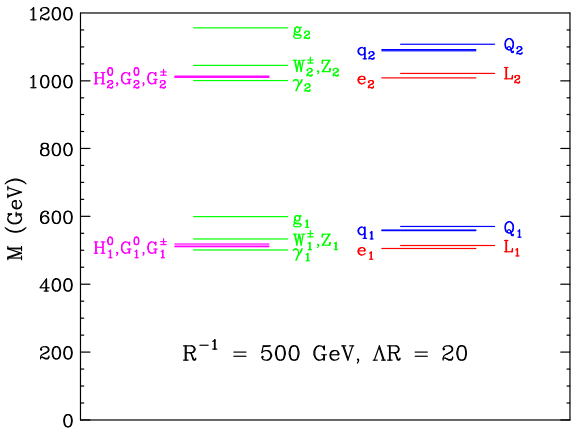

Fig. 4.2.1: One-loop-corrected mass spectrum of the $n = 1$ and $n = 2$ KK levels in Minimal UED, for $R^{-1} = 500$ GeV, $\Lambda R = 20$ and $m_h = 120$ GeV. We show the KK modes of gauge bosons, Higgs and Goldstone bosons and first generation fermions.

4.2.2 Phenomenology of Universal Extra Dimensions

The Minimal UED Model

Models of UED place all SM particles in the bulk of one or more compactified ED. In the simplest, most popular version, there is a single extra dimension of size R, compactified on an S_1/Z_2 orbifold [143].

A peculiar feature of UED is the conservation of KK number at tree level, which is a simple consequence of momentum conservation along the extra dimension. However, bulk and brane radiative effects [202, 203, 196] break KK number down to a discrete conserved quantity, the so-called KK parity, $(-1)^n$, where n is the KK level. KK parity ensures that the lightest KK partners (level one) are always pair-produced in collider experiments, just like in the R-parity conserving supersymmetry models discussed in Section 4.1.1. KK parity conservation also implies that the contributions to various low-energy observables [204, 205, 206, 207, 208, 209, 210, 211, 212, 213, 214] arise only at loop level and are small. As a result, limits on the scale R^{-1} of the extra dimension from precision electroweak data are rather weak, constraining R^{-1} to be larger than approximately 250 GeV [208]. An attractive feature of UED models with KK parity is the presence of a stable massive particle which can be a cold dark matter candidate [183, 184, 185, 186, 187].

In Fig. 4.2.1 we show the mass spectrum of the $n = 1$ and $n = 2$ KK levels in Minimal UED (MUED), for $R^{-1} = 500$ GeV, $\Lambda R = 20$ and SM Higgs boson mass $m_h = 120$ GeV. We include the full one-loop corrections from Ref. [196]. We have used RGE-improved couplings to compute the radiative corrections to the KK masses. It is well known that in UED the KK modes modify the running of the coupling constants at higher scales. We extrapolate the gauge coupling constants to the scale of the $n = 1$ and $n = 2$ KK modes, using the appropriate β functions dictated by the particle spectrum [215, 216, 217]. As a result, the spectrum shown in Fig. 4.2.1 differs slightly

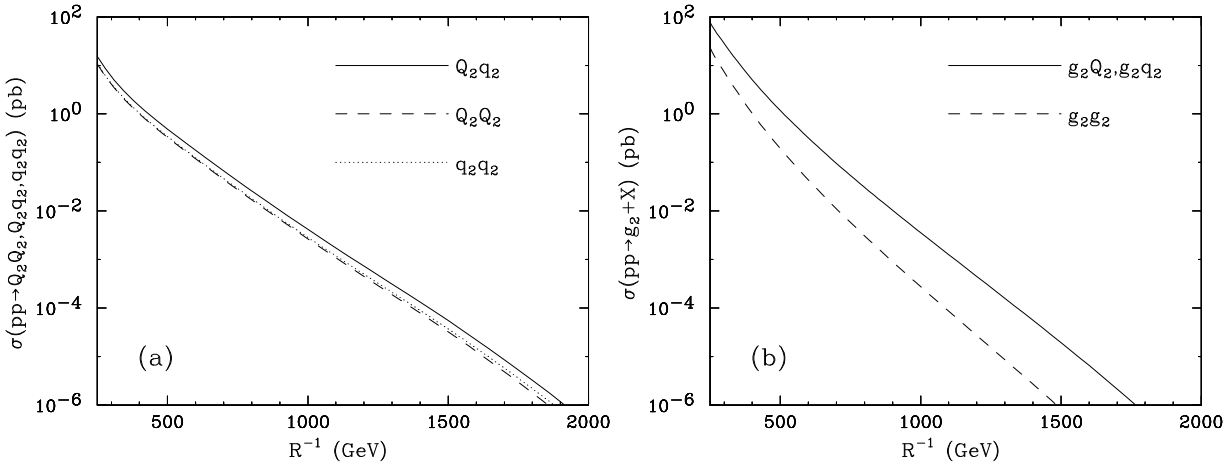

Fig. 4.2.2: Strong production of $n = 2$ KK particles at the LHC: (a) KK-quark pair production; (b) KK-quark/KK-gluon associated production and KK-gluon pair production. The cross-sections have been summed over all quark flavors and also include charge-conjugated contributions such as $Q_2\bar{q}_2$, $\bar{Q}_2q_2$, $g_2\bar{Q}_2$, etc.

from the one in Ref. [196]. Most notably, the colored KK particles are somewhat lighter, due to a reduced value of the strong coupling constant, and overall the KK spectrum at each level is more degenerate.

Comparison of UED and Supersymmetry

There is a wide variety of SUSY models, with very diverse phenomenology. Nevertheless, they all share the following common features which define a supersymmetric framework:

1. For each particle of the Standard Model, supersymmetry predicts a new particle (superpartner).
2. The spins of the superpartners differ by $1/2$ unit.
3. The couplings of the particles and their superpartners are equal, being related by supersymmetry
4. The generic collider signature of supersymmetric models with WIMP LSPs is missing energy.

The last property makes exact reconstruction of the event kinematics practically impossible. At a hadron collider, the center of mass energy is not known on an event-per-event basis. In addition, the momenta of *both* $\tilde{\chi}_1^0$ particles are unknown, and what is measured is only the transverse component of the sum of their momenta, provided there are no other sources of missing energy in the event (such as neutrinos, b-jets, τ-jets, etc.). This incomplete information is the main stumbling block in proving the basic properties of SUSY at the LHC.

In complete analogy, the discussion of Minimal UED model leads to the following generic features of UED:

1. For each particle of the Standard Model, UED models predict an infinite[23] tower of new particles (Kaluza-Klein partners).
2. The spins of the SM particles and their KK partners are the same.
3. The couplings of the SM particles and their KK partners are equal.
4. The generic collider signature of UED models with WIMP LKPs is missing energy.

Notice that defining features 3 and 4 are common to both SUSY and UED and cannot be used to distinguish the two cases. We see that while R-parity conserving SUSY implies a missing energy signal, the reverse is not true: a missing energy signal would appear in any model with a dark matter candidate, and even in models which have nothing to do with the dark matter issue, but simply contain new neutral quasi-stable particles. Similarly, the equality of the couplings (feature No. 3) is a celebrated test of SUSY, but from the above comparison we see that it is only a necessary, not sufficient condition in proving SUSY.

We are therefore forced to concentrate on the first two identifying features as the only promising discriminating criteria. Let us begin with feature 1: the number of new particles. The KK particles at $n = 1$ are analogous to superpartners in SUSY. However, the particles at the higher KK levels have no analogues in $N = 1$ supersymmetric models. Discovering the $n \geq 2$ levels of the KK tower would therefore indicate the presence of extra dimensions rather than SUSY. We shall concentrate on the $n = 2$ level and investigate the discovery opportunities at the LHC and the Tevatron (for linear collider studies of $n = 2$ KK gauge bosons, see Ref. [179, 167, 169, 170]). Notice that the masses of the KK modes are given roughly by $m_n \sim n/R$, where n is the KK level number, so that the particles at levels 3 and higher are rather heavy and their production is severely suppressed.

The second identifying feature – the spins of the new particles – also provides a tool for discrimination between SUSY and UED. Recently it was suggested that a charge asymmetry in the lepton-jet invariant mass distributions from a particular cascade can be used to discriminate SUSY from the case of pure phase space decays [178, 179, 176, 180]. The possibility of discriminating SUSY and UED by this method was the subject of Sec. 4.1. For the purposes of our study we implemented the relevant features of MUED in the CompHEP event generator [218]. The Minimal Supersymmetric Standard Model (MSSM) is already available in CompHEP (since version 41.10).

4.2.3 Collider Search for Level 2 KK Gauge Bosons

Phenomenology of Level 2 Fermions

In principle, there are two mechanisms for producing $n = 2$ KK quarks at the LHC: through KK-number conserving interactions, or through KK-number violating (but KK-parity conserving) interactions. The KK number conserving QCD interactions allow production of KK quarks either in pairs or singly (in association with the $n = 2$ KK mode of a gauge boson). The corresponding production cross sections are shown in Fig. 4.2.2 (the cross sections for producing $n = 1$ KK

[23] Strictly speaking, the number of KK modes is ΛR.

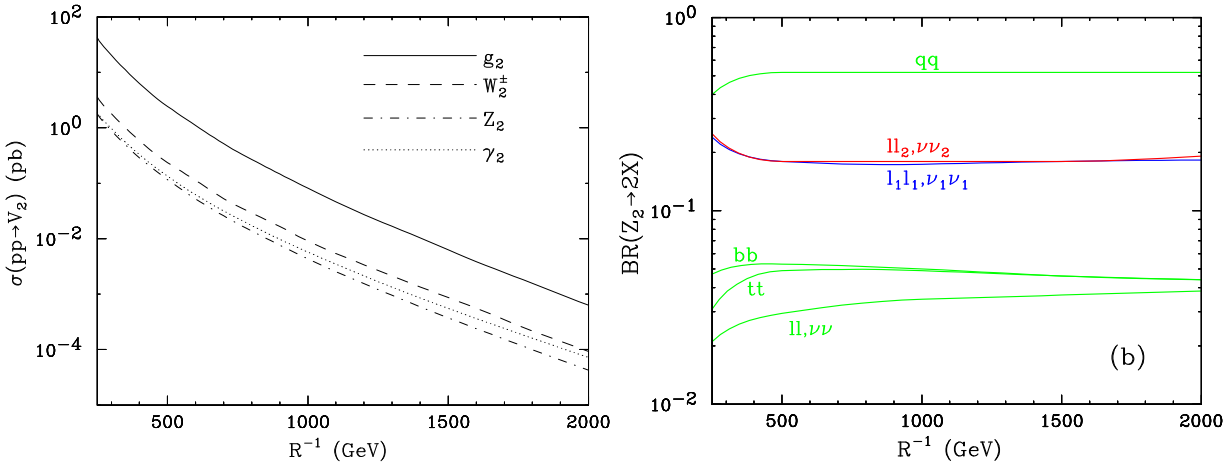

Fig. 4.2.3: (a) Cross sections for single production of level 2 KK gauge bosons through the KK number violating couplings. (b) Branching fraction of the Z_2 KK gauge boson and branching fractions of other n_2 KK gauge bosons are very similar.

quarks were calculated in [219, 220, 180]). In Fig. 4.2.2a we show the cross sections (pb) for $n = 2$ KK-quark pair production, while in Fig. 4.2.2b we show the results for $n = 2$ KK-quark/KK-gluon associated production and for $n = 2$ KK-gluon pair production. We plot the results versus R^{-1}, and one should keep in mind that the masses of the $n = 2$ particles are roughly $2/R$. In calculating the cross sections of Fig. 4.2.2, we consider 5 partonic quark flavors in the proton along with the gluon. We sum over the final state quark flavors and include charge-conjugated contributions. We used CTEQ5L parton distributions [221] and choose the scale of the strong coupling constant α_s to be equal to the parton level center of mass energy. All calculations are done with CompHEP [218] with our implementation of MUED. One could consider single production of $n = 2$ KK quarks through KK-number violation but the lowest-order coupling of an $n = 2$ KK quark to two SM particles is suppressed by the cutoff scale, which is unknown.

Having determined the production rates of level 2 KK quarks, we now turn to the discussion of their experimental signatures. To this end we need to determine the possible decay modes of Q_2 and q_2. At each level n, the KK quarks are among the heaviest states in the KK spectrum and can decay promptly to lighter KK modes. As can be seen from Fig. 4.2.1, the KK gluon is always heavier than the KK quarks, so the two body decays of KK quarks to KK gluons are closed. Instead, $n = 2$ KK quarks will decay to the KK modes of the electroweak gauge bosons which are lighter. The branching fractions for $n = 2$ KK quarks are almost independent of R^{-1}, unless one is close to threshold. This feature persists for all branching ratios of KK particles.

The case of the $SU(2)_W$-singlet quarks such as q_2 is simple, since they only couple to the hypercharge gauge bosons. At $n \geq 1$ the hypercharge component is almost entirely contained in the γ KK mode [196]. We therefore expect a singlet KK quark q_2 to decay to either $q_1\gamma_1$ or $q_0\gamma_2$, and in fact they have roughly same branching fractions (50%). The case of an $SU(2)_W$-doublet quark

Q_2 is much more complicated, since Q_2 couples to the (KK modes of the) weak gauge bosons as well, and many more two-body final states are possible. Since the weak coupling is larger than the hypercharge coupling, the decays to W and Z KK modes dominate, with $BR(Q_2 \to Q_0' W_2)/BR(Q_2 \to Q_0 Z_2) = 2$ and $BR(Q_2 \to Q_1' W_1)/BR(Q_2 \to Q_1 Z_1) = 2$. The branching fractions to the γ KK modes are only on the order of a few percent.

Level 2 Gauge Bosons

There are four $n = 2$ KK gauge bosons: the KK "photon" γ_2, the KK "Z-boson" Z_2, the KK "W-boson" $W_2^\pm$, and the KK gluon g_2. Recall that the Weinberg angle at $n = 2$ is very small, so that γ_2 is mostly the KK mode of the hypercharge gauge boson and Z_2 is mostly the KK mode of the neutral W-boson of the SM. An important consequence of the extra-dimensional nature of the model is that all four of the $n = 2$ KK gauge bosons are relatively degenerate; the masses are all roughly equal to $2/R$. Mass splittings are almost entirely due to radiative corrections, which in MUED yield the hierarchy $m_{g_2} > m_{W_2} \sim m_{Z_2} > m_{\gamma_2}$. The KK gluon receives the largest corrections and is the heaviest particle in the KK spectrum at each level n. The $W_2^\pm$ and Z_2 particles are degenerate to a very high degree.

In Fig. 4.2.3(a), we show single production cross sections for level 2 KK gauge bosons. Notice the roughly similar size of the four cross sections. This is somewhat surprising, since the cross sections scale as the corresponding gauge coupling squared, and one would have expected a wider spread in the values of the four cross sections. This is due to a couple of things. First, for a given R^{-1}, the masses of the four $n = 2$ KK gauge bosons are different, with $m_{g_2} > m_{W_2} \sim m_{Z_2} > m_{\gamma_2}$. Therefore, for a given R^{-1}, the heavier particles suffer a suppression. This explains to an extent why the cross section for γ_2 is not the smallest of the four, and why the cross section for g_2 is not as large as one would expect. There is, however, a second effect, which goes in the same direction. The coupling is also proportional to the mass corrections of the corresponding particles:

$$\frac{\bar{\delta} m_{V_2}}{m_{V_2}} - \frac{\bar{\delta} m_{f_2}}{m_{f_2}} \,. \tag{4.2.1}$$

Since the QCD corrections are the largest, for $V_2 = \{\gamma_2, Z_2, W_2^\pm\}$, the second term dominates. However, for $V_2 = g_2$, the first term is actually larger, and there is a cancellation, which further reduces the direct KK gluon couplings to quarks.

In Fig. 4.2.3(b), we show branching fraction of Z_2 only as an example. Again we observe that the branching fractions are very weakly sensitive to R^{-1}, just as the case of KK quarks. This can be understood as follows. The partial for the KK number conserving decays are proportional to the available phase space, while the partial width for the KK number violating decay is proportional to the mass corrections. Both the phase space and mass corrections are proportional to R^{-1}, which then cancels out in the branching fraction.

The electroweak KK modes γ_2, Z_2 and $W_2^\pm$ can be produced in the decays of heavier $n = 2$ particles such as the KK quarks and/or KK gluon. This is well-known from the case of SUSY,

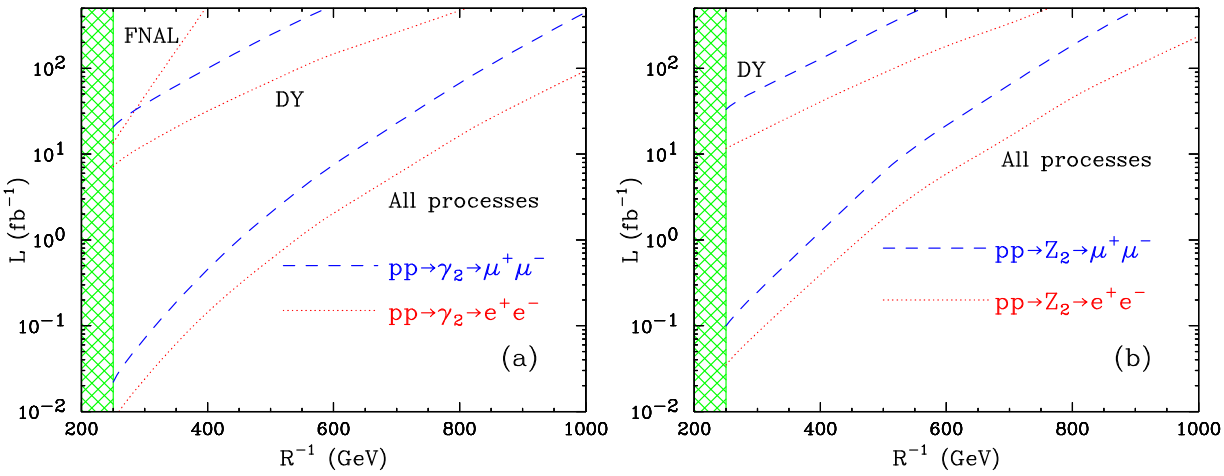

Fig. 4.2.4: 5σ discovery reach for (a) γ_2 and (b) Z_2. We plot the total integrated luminosity L (fb^{-1}) required for a 5σ excess of signal over background in the dielectron (red, dotted) and dimuon (blue, dashed) channel, as a function of R^{-1}. In each plot, the upper set of lines labelled "DY" makes use of the single V_2 production of Fig. 4.2.3 only, while the lower set of lines (labelled "All processes") includes indirect γ_2 and Z_2 production from $n = 2$ KK quark decays. The red dotted line marked "FNAL" in the upper left corner of (a) reflects the expectations for a $\gamma_2 \to e^+e^-$ discovery at Tevatron Run II. The shaded area below $R^{-1} = 250$ GeV indicates the region disfavored by precision electroweak data [208].

where the dominant production of electroweak superpartners is often indirect – from squark and gluino decay chains. The indirect production rates of γ_2, Z_2 and $W_2^\pm$ due to QCD processes can be readily estimated from Figs. 4.2.2 and branching fractions. $BR(Q_2 \to W_2^\pm)$, $BR(Q_2 \to Z_2)$ and $BR(q_2 \to \gamma_2)$ are among the largest branching fractions of the $n = 2$ KK quarks, and we expect indirect production from QCD to be a significant source of electroweak $n = 2$ KK modes.

The $n = 2$ KK modes can also be produced directly in pairs, through KK number conserving interactions. These processes, however, are kinematically suppressed, since we have to make *two* heavy particles in the final state. One would therefore expect that they will be the least relevant source of $n = 2$ KK gauge bosons. The only exception is KK gluon pair production which is important and is shown in Fig. 4.2.2b. We see that it is comparable in size to KK quark pair production and $q_2 g_2/Q_2 g_2$ associated production. We have also calculated the pair production cross sections for the electroweak $n = 2$ KK gauge bosons and confirmed that they are very small, hence we shall neglect them in our analysis below.

Analysis of the LHC reach for Z_2 and γ_2

We now consider the inclusive production of Z_2 and γ_2 and look for a dilepton resonance in both the e^+e^- and $\mu^+\mu^-$ channels. An important search parameter is the width of the reconstructed resonance, which in turn determines the size of the invariant mass window selected by the cuts. Since the intrinsic width of the Z_2 and γ_2 resonances is so small, the mass window is entirely

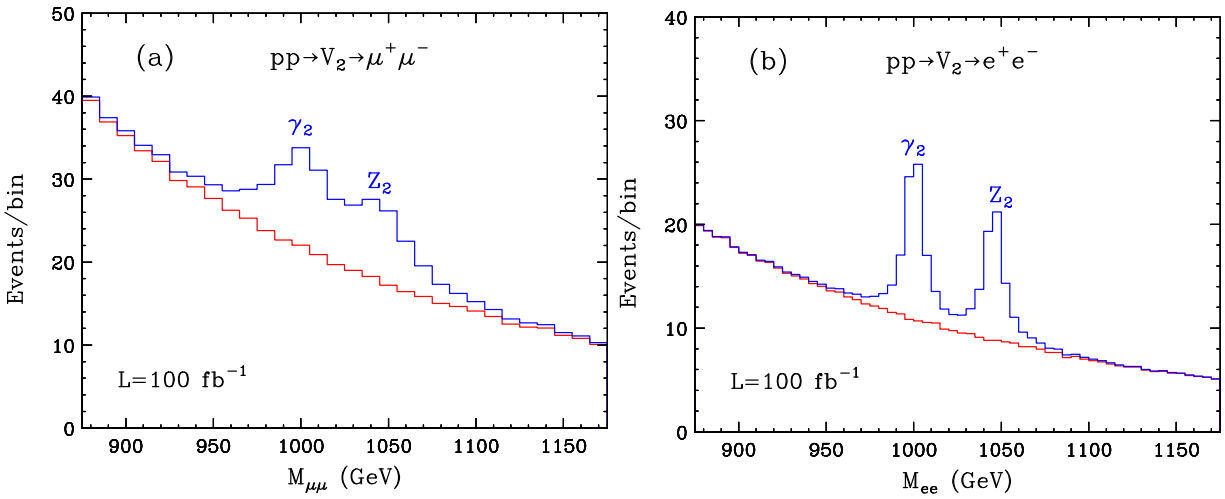

Fig. 4.2.5: The $\gamma_2 - Z_2$ diresonance structure in UED with $R^{-1} = 500$ GeV, for the (a) dimuon and (b) dielectron channels at the LHC with $\mathrm{L} = 100\ \mathrm{fb}^{-1}$. The SM background is shown with the (red) continuous underlying histogram.

determined by the mass resolution in the dimuon and dielectron channels. For electrons, the resolution in CMS is approximately constant, on the order of $\Delta m_{ee}/m_{ee} \approx 1\%$ in the region of interest [222]. On the other hand, the dimuon mass resolution is energy dependent, and in preliminary studies based on a full simulation of the CMS detector has been parametrized as [223] $\frac{\Delta m_{\mu\mu}}{m_{\mu\mu}} = 0.0215 + 0.0128\left(\frac{m_{\mu\mu}}{1\ \mathrm{TeV}}\right)$. Therefore in our analysis we impose the following cuts

1. Lower cuts on the lepton transverse momenta $p_T(\ell) > 20$ GeV.
2. Central rapidity cut on the leptons $|\eta(\ell)| < 2.4$.
3. Dilepton invariant mass cut for electrons $m_{V_2} - 2\Delta m_{ee} < m_{ee} < m_{V_2} + 2\Delta m_{ee}$ and muons $m_{V_2} - 2\Delta m_{\mu\mu} < m_{\mu\mu} < m_{V_2} + 2\Delta m_{\mu\mu}$.

With these cuts the signal efficiency varies from 65% at $R^{-1} = 250$ GeV to 91% at $R^{-1} = 1$ TeV. The main SM background to our signal is Drell-Yan, which we have calculated with the PYTHIA event generator [224].

With the cuts listed above, we compute the discovery reach of the LHC and the Tevatron for the γ_2 and Z_2 resonances. Our results are shown in Fig. 4.2.4. We plot the total integrated luminosity L (fb^{-1}) required for a 5σ excess of signal over background in the dielectron (red, dotted) and dimuon (blue, dashed) channels, as a function of R^{-1}. In each panel of Fig. 4.2.4, the upper set of lines labelled "DY" utilize only the single V_2 production cross sections from Fig. 4.2.3. The lower set of lines (labelled "All processes") include in addition indirect γ_2 and Z_2 production from the decays of $n = 2$ KK quarks to γ_2 and Z_2 (we ignore secondary γ_2 production from $Q_2 \to Z_2 \to \ell_2 \to \gamma_2$). The shaded area below $R^{-1} = 250$ GeV indicates the region disfavored by precision electroweak data [208]. Using the same cuts also for the case of the Tevatron, we find the Tevatron reach in $\gamma_2 \to e^+e^-$ shown in Fig. 4.2.4a and labelled "FNAL". For the Tevatron we

use electron energy resolution $\Delta E/E = 0.01 \oplus 0.16/\sqrt{E}$ [225]. The Tevatron reach in dimuons is worse due to the poorer resolution, while the reach for Z_2 is also worse since $m_{Z_2} > m_{\gamma_2}$ for a fixed R^{-1}.

Fig. 4.2.4 reveals that there are good prospects for discovering level 2 gauge boson resonances at the LHC. Within one year of running at low luminosity ($\mathrm{L} = 10\ \mathrm{fb}^{-1}$), the LHC will have sufficient statistics in order to probe the region up to $R^{-1} \sim 750$ GeV. Notice that in MUED, the "good dark matter" region, where the LKP relic density accounts for all of the dark matter component of the Universe, is at $R^{-1} \sim 500 - 600$ GeV [183, 185, 186]. This region is well within the discovery reach of the LHC for both $n = 1$ KK modes [165] and $n = 2$ KK gauge bosons (Fig. 4.2.4). If the LKP accounts for only *a fraction of* the dark matter, the preferred range of R^{-1} is even lower and the discovery at the LHC is easier.

From Fig. 4.2.4 we also see that the ultimate reach of the LHC for both γ_2 and Z_2, after several years of running at high luminosity ($\mathrm{L} \sim 300\ \mathrm{fb}^{-1}$), extends up to just beyond $R^{-1} = 1$ TeV. One should keep in mind that the actual KK masses are at least twice as large: $m_{V_2} \sim m_2 = 2/R$, so that the KK resonances can be discovered for masses up to 2 TeV.

While the $n = 2$ KK gauge bosons are a salient feature of the UED scenario, any such resonance by itself is not a sufficient discriminator, since it resembles an ordinary Z' gauge boson. If UED is discovered, one could then still make the argument that it is in fact some sort of non-minimal SUSY model with additional gauge structure containing neutral gauge bosons. Important corroborating evidence in favor of UED would be the simultaneous discovery of several, rather degenerate, KK gauge boson resonances. While SUSY also can accommodate multiple Z' gauge bosons, there would be no good motivation behind their mass degeneracy. A crucial question therefore arises: can we separately discover the $n = 2$ KK gauge bosons as individual resonances? For this purpose, one would need to see a double peak structure in the invariant mass distributions. Clearly, this is rather challenging in the dijet channel, due to relatively poor jet energy resolution. We shall therefore consider only the dilepton channels, and investigate how well we can separate γ_2 from Z_2.

Our results are shown in Fig. 4.2.5, where we show the invariant mass distribution in UED with $R^{-1} = 500$ GeV, for the (a) dimuon and (b) dielectron channels at the LHC with $\mathrm{L} = 100\ \mathrm{fb}^{-1}$. We see that the diresonance structure is easier to detect in the dielectron channel, due to the better mass resolution. In dimuons, with $\mathrm{L} = 100\ \mathrm{fb}^{-1}$ the structure also begins to emerge. We should note that initially the two resonances will not be separately distinguishable, and each will in principle contribute to the discovery of a bump, although with a larger mass window. In our reach plots in Fig. 4.2.4 we have conservatively chosen not to combine the two signals from Z_2 and γ_2, and instead show the reach for each one separately.

4.2.4 Conclusions

We studied the discovery reach for level 2 KK modes in UED at hadron colliders. We showed that the $n = 2$ KK gauge bosons offer the best prospects for detection, in particular the γ_2 and Z_2 resonances can be *separately* discovered at the LHC. However, this is not a proof of UED. These resonances could still be interpreted as Z' gauge bosons, but their close degeneracy is a smoking gun for UED. Furthermore, although we did not show any results to this effect in this paper, it is clear that the $W_2^\pm$ KK mode can also be looked for and discovered in its decay to SM leptons. One can then measure m_{W_2} and show that it is very close to m_{Z_2} and m_{γ_2}, which would further strengthen the case for UED. The spin discrimination is not so straightforward, and requires further study. The asymmetry method of Barr is discussed in Sec. 4.1.

While in this paper we concentrated on the Minimal UED model, it should be kept in mind that there are many interesting possibilities for extending the analysis to a more general setup. For example, non-vanishing boundary terms at the scale Λ can distort the MUED spectrum beyond recognition. The UED collider phenomenology is also very different in the case of a "fat" brane [226, 227], charged LKPs [228], KK graviton superwimps [229, 230] or resonances in two universal extra dimensions [191]. Notice that Little Higgs models with T-parity [192, 193, 194] are very similar to UED, and can also be confused with SUSY.

Acknowledegments

We thank H.-C. Cheng and B. Dobrescu for stimulating discussions. AD is supported by the US Department of Energy and the Michigan Center for Theoretical Physics. The work of KK and KM is supported in part by a US Department of Energy Outstanding Junior Investigator award under grant DE-FG02-97ER41209.

4.3 Universal extra dimensions with KK number violation

Cosmin Macesanu, Dept. of Physics, Syracuse University

We discuss in this section the phenomenological signals associated with a Universal Extra Dimensions (UED) model [143] with KK number violation. The breaking of KK number may arise in different ways, but here we take it to be a consequence of gravitational interactions. Such interactions are natural in a model in which matter and gravity both propagate in the bulk. If one adopts the framework advocated in the Arkani-Hamed, Dimopulos and Dvali (ADD) model [188, 231, 232], the size of the compactified extra dimensions where gravity propagates is of order inverse eV. Naturally, matter cannot propagate all the way into these extra dimensions (or one would observe eV spaced KK excitations of the SM particles). However, instead of being stuck on the 4D brane, the matter fields might be able to propagate a limited length of order $1/M$ into the bulk. One can moreover conjecture that the matter fields are confined close to the 4D brane by some interactions generated by physics at the string scale, M_D. Then one may expect that the two scales M and M_D are related, and roughly of the same order of magnitude.

The phenomenology of such a model differs significantly from that of the standard UED models [196, 165]. In the later case, there typically exists a lightest KK particle (LKP), which is stable due to KK number conservation. KK excitations of quarks and gluons, which dominate KK production at a hadron colider, will decay to the LKP, radiating semisoft quarks and leptons in the process. Being neutral and weakly interacting, the LKP would not leave energy in the detector, thus the experimental signal would consist of relatively soft jets and leptons plus missing energy (note also that while the absolute missing energy would be quite large, the observable transverse missing energy would be rather small). In the case of the UED model with KK number violation, the LKP will also decay by radiating a graviton and the SM partner of the LKP in our case. Although the coupling of an individual graviton to matter is extremely weak (of order $1/M_{Pl}^2$) the large number of gravitons available to contribute to the decay will give a sizeable total gravitational decay width $\Gamma_h \sim M^{N+3}/M_D^{N+2}$ (with N the number of extra dimensions), which for values of M_D not much larger than M is of the same order of magnitude as electroweak or strong decay widths. Moreover, since the masses of gravitons contributing to this decay may be significantly smaller that the mass of the KK matter particle, the momentum of the visible SM particle can be quite large.

One can in fact obtain different signals, depending of the parameters of the model. If the gravitational decay widths of the quark/gluon excitations are larger than the decays widths to the LKP, the KK particles produced at a hadron collider will decay gravitationally, leaving behind two high p_T jets [220]. If the opposite is true, then the KK quarks or gluons will first decay to the LKP, radiating soft jets and leptons. The LKP will in turn decay gravitationally, leaving behind a high p_T photon (assuming that the LKP is the photon excitation) and missing energy, taken away by the graviton. The phenomenology of this scenario was discussed in [226].

As a consequence of having high energy jets (or photons) in the final state, it will be much

easier to discover extra dimensions in a scenario with KK number violation. For example, for pair production processes the Tevatron Run II will be able to probe values of the inverse compactification scale $M = 1/R$ up to 400 GeV (in the case of the dijet signal) or 500 GeV (for the diphoton signal). At the LHC, one can probe values of $1/R$ close to 3 TeV, which is almost double the discovery reach compared to the case when the LKP is stable. Moreover, one may have a better chance of differentiating the UED model from competing models like SUSY by analyzing kinematical observables which are not accessible in the stable LKP scenario [180, 178].

Another particular behavior of models where the gravitational interaction violates KK number is the possibility of producing a single first level KK excitation of matter. Since these processes are gravity-mediated, the production cross section will depend on the strength of the gravitational interaction (the parameter M_D). Thus one can expect that the effective interaction strength is smaller than in the case of KK pair production (where the interaction strength is given by the strong coupling constant). However, this might be mitigated by the fact that one needs produce a single massive particle in the final state, rather that two. It is then possible that in the case when the fundamental gravity scale is not much larger than the collider energy, it would be easier to observe production of a single KK matter excitation rather than the usual pair production process.

There are two types of processes which lead to a single KK matter excitation in the final state: one in which gravitons play the role of virtual particles mediating the process, and one in which gravitons appear as final state real particles. We start the discussion with the first case [227]. The phenomenological signal for such a process will be either two jets plus missing transverse energy (associated with the graviton appearing in the decay of the KK quark/gluon), or a single jet plus a photon and missing energy (if the KK quark or gluon decays first to the LKP, and this particle decays gravitationaly). It turns out that for the most of the parameter space where the cross section is observable, the gravitational decay of KK quarks/gluons will take place, and the signal will be two jets plus missing energy. This can be understood by noting that an observable cross section requires a relatively strong gravitational interaction, which ensures in turn that the gravitational decay width of the produced KK excitation will be larger that the decay width to the LKP.

Some illustrative results for this type of process are presented in Fig. 4.3.1. The dashed and solid lines are contours in the (M_D, M) plane for a 5σ discovery at the Tevatron Run II with 2 fb^{-1} integrated luminosity (left panel), and at LHC with 100 fb^{-1} (right panel). The dashed lines correspond to $N = 2$ extra dimensions, while the solid lines correspond to $N = 6$. The contour lines correspond to an observable cross section of 25 fb at the Tevatron, with cuts of $p_T > 150$ GeV and $\not{E}_T > 300$ GeV on the transverse momentum of the observable jets and on the missing energy. At the LHC, the cross-section is 1 fb, and the corresponding cuts are $p_T > 800$ GeV and $\not{E}_T > 1.6$ TeV. The large cuts imposed on the missing energy and transverse momentum eliminate most of the Standard Model background, which in this kinematic range is due mostly to Z plus two jet production.

We observe that for small values of M_D, one can indeed probe a large range of values for

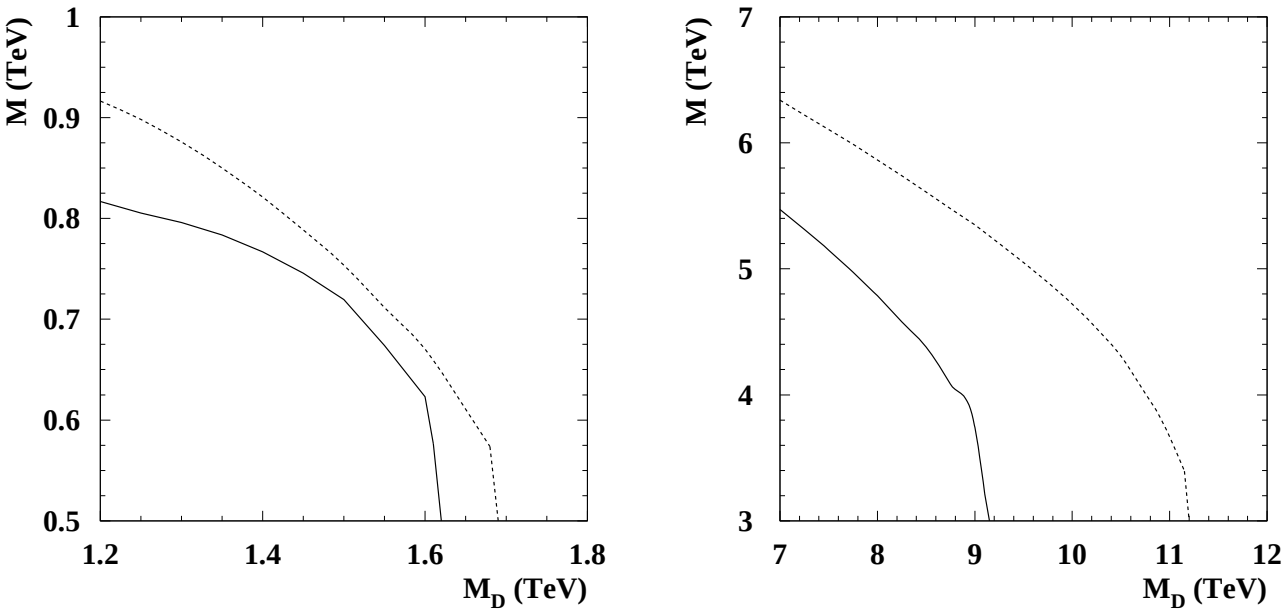

Fig. 4.3.1: Tevatron Run II (left) and LHC (right) 5σ discovery reach contours for single KK and SM quark or gluon production, for $N = 2$ (dashed lines) and $N = 6$ (solid lines) extra dimensions.

the compactification scale associated with matter, $1/M$, reaching to almost double the maximum accessible in pair production processes. However, this result is strongly dependent on the fundamental gravity scale M_D: the production cross-section behaves as $\sim 1/M_D^{10}$, and for larger values of this parameter, this process would become unobservable, as one can note from the abrupt drop of the contour lines in Fig. 4.3.1 once M_D has increased past a certain value. Note also that for these values of M_D, one would be able to observe KK gravitons through processes associated with typical ADD phenomenology. That is, SM particle production mediated by gravity, or processes with a graviton and a SM particle in the final state.

Additionally, one could observe the direct production of a photon and a photon KK excitation, or a lepton and KK lepton, through s-channel processes mediated by gravitons. The production cross sections for these processes will be of the same order of magnitude as for processes involving quarks or gluons and their KK excitations (since the strength of the effective interaction is the same in both cases). However, since the hadron collider background will be smaller for final state photons or leptons, one can expect that the reach in this channel will be somewhat larger than for processes involving quarks and gluons.

The second type of processes mediated by gravity are processes with a graviton and a KK matter excitation in the final state [233]. The KK excitation can decay either directly to another graviton and a gluon or quark, or first to the LKP, which in turn decays to a photon and a graviton. The signal will then be a single jet or photon, with missing energy due to the two gravitons in the

final state. Then one has to take into account contributions to this signal coming from the standard ADD-type processes with a KK graviton and a SM particle in the final state.

In the first case, with a jet in the final state, the cross section for production of a KK quark and gluon is smaller than the cross section for associated production of a SM quark or gluon and a KK graviton. This is due partly the fact that one has an extra massive particle in the final state, and partly to a suppression effect of the form factor associated with the graviton–KK matter interaction vertex [234]. As a consequence, one cannot directly observe the production of a single KK excitation plus a graviton in the jet plus missing energy channel. However, if we are in a region of parameter space where the KK quark or gluon decays first to the LKP, one may observe such production in the photon plus missing energy channel. For such a signal, the cross section for direct production of a SM photon and a graviton will be suppressed by the electroweak coupling constant as well as, in the LHC case, by the small $q\bar{q}$ content in the initial state.

We show in the left panels of Figs. 4.3.2,4.3.3 with solid curves the discovery reach for KK quark/gluon plus graviton at LHC in the photon + missing energy channel. The dashed curves show the upper limits in parameter space where the decay of the KK quark/gluon takes place through the LKP first, such that above those lines, the signal would be jet + $\not{E}_T$. We note that for small values of the matter compactification scale M, one can probe quite large values for the fundamental gravitational scale M_D, especially for the case of $N = 2$. This is due to an enhancement of the production cross section for very light gravitons [233], which is the dominant contribution for $N = 2$. Also, the cross section has a weaker dependence on M_D, $\sigma \sim 1/M_D^{N+2}$, compared to the $1/M_D^{10}$ dependence valid for the processes with KK production mediated by virtual gravitons.

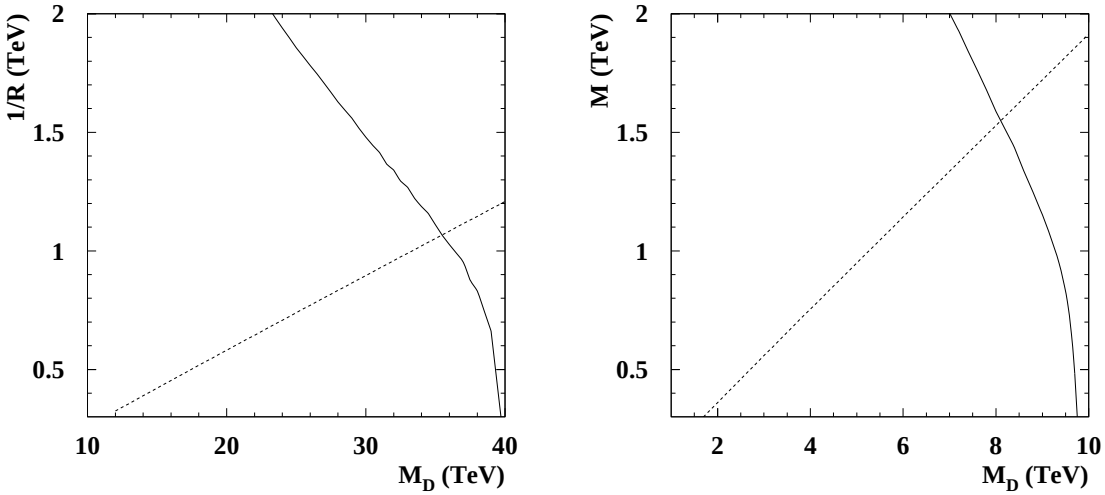

Fig. 4.3.2: Solid lines: the 5σ discovery reach at the LHC in the photon + $\not{E}_T$ channel for $N = 2$ (left panel) and $N = 4$ (right panel). For values of $M_D, 1/R$ below the dashed lines, the KK quarks and gluons decay first to the LKP.

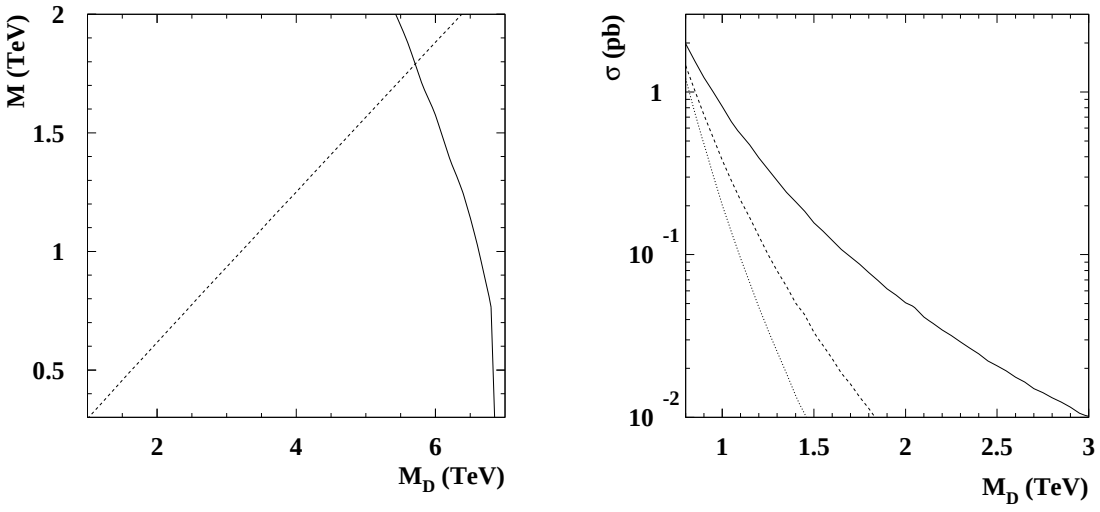

Fig. 4.3.3: Left panel: the 5σ discovery reach at the LHC in the photon + $\not{E}_T$ channel for $N = 6$. Right panel: the SM photon + $\not{E}_T$ cross-section at the Tevatron Run II, with $p_T > 100$ GeV. Solid, dashed and dotted lines correspond to $n = 2$, 4 and 6 extra dimensions respectively.

The Tevatron case is somewhat different. Here, the cross section for direct production of a SM photon and graviton plays a more important role than in the case of the LHC, due in part to the initial state containing a large $q\bar{q}$ fraction, which is required for the process with a photon in the final state. Conversely, the cross section for production of a quark/gluon excitation which decays to the LKP is highly supressed by large values of M_D. Then the cross section production for a single photon plus a graviton depends mostly on M_D, and is almost the same as the one evaluated for the simple ADD scenario (with no matter in extra dimensions). This cross section is shown in the right panel of Fig. 4.3.3 with a cut of $p_T > 100$ GeV on the photon transverse momentum (which corresponds to a SM background of ~ 80 fb). From such a process one can then set the same order of magnitude limits on the fundamental gravity scale as the limits obtained from the jet + $\not{E}_T$ signal in the ADD scenario [189, 190].

4.4 The Need for Beyond-SUSY Tools for the LHC

Albert De Roeck, CERN, Geneva, Switzerland

4.4.1 Introduction

One of the main missions of the LHC will be to test and discover new physics beyond the Standard Model (BSM) in the data. There is an impressive variety of proposals for BSM physics at the LHC, the most popular scenarios presently being supersymmetry and Extra Dimensions, but others include Technicolor, Little Higgs models, new gauge bosons, compositness, etc.

The experiments explore their sensitivity to these models mostly by means detector simulations using event generators. This is necessary since the main challenges at the LHC to discover new physics will be to find a signal on top of an often large background, and to have an efficient trigger path in place for the signature of this new physics channel. Hence, to prepare for LHC data taking, Monte Carlo event generators for these new processes are extremely useful tools. Also, once data is collected, event generators and programs to calculate cross sections will be indispensable tools for the analysis and interpretation of the data, whether a signal is observed or not.

The rapid increase of new models in the last few years has not been followed by an organized effort on specialized Monte Carlo generators. Often the experiments have made private implementations of (part of) the physics of such new scenarios or models. This contribution is a plea to have a more systematic approach to event generators for new physics for the LHC. It results from collecting information on the needs of the CMS and ATLAS experiments during their studies to prepare for physics. A number of suggestions are made on possible ways forward, taking the physics of Extra Dimensions (EDs) as an explicit example.

Since the first presentation of these ideas at the TeV4LHC workshop, this has been further developed at other workshops such as Les Houches 05, MC4BSM at FNAL in March 06, and the Tools for SUSY and BSM workshop at LAPP, Annecy in June 06. In particular after the Les Houches workshop, some action was taken as reported below.

4.4.2 Extra Dimensions as an example

Issues for the ED analyses for experimentalists at the LHC are as follows.

- Include new processes in Monte Carlo generators, usable for LHC (Tevatron) analyses. Hence they become a ”standard” which can be used for comparison between experiments.
- Include complete information into Monte Carlo generators, such as spin correlations. This will allow e.g. the study of measurability of spin effects (e.g. SUSY versus UED, Z’ versus KK states and so on).
- Cross checks between different codes/Monte Carlo results are important (problems have been found in the past).

- Agree on parameter space available for EDs at LHC (& ILC, CLIC, Tevatron). Under which conditions do e.g. astrophysical and other limits apply. How can certain scenarios (e.g MSLED) escape these limits? Presently the information is too scattered.
- Agree on a number of benchmark scenarios, like we have for SUSY and successfully used e.g. in LHC/ILC studies.
- Time to think about K-factors? These K-factors can be large and affect the search reach.
- The accuracy of the SM process background understanding is important (e.g. Drell-Yan, Z+jet, effects from PDFs..). This is particularly important for tails of distributions where the statistics and experimental checks will be limited.
- Use the same formalism in the models, e.g. for the definition of the effective Planck Scale.

So far the following generators are in use in the experiments for ED studies

- RS gravitons are included in the standard workhorses HERWIG and PYTHIA.
- ADD scenarios: several private codes for both the graviton radiation and graviton exchange processes, for PYTHIA or HERWIG, are circulating in the experiments. Recently the situation was improved by SHERPA, which contains complete ADD FeynmanRules and is now used in ATLAS/CMS.
- UEDs existed mainly in a private code for COMHEP (Matchev et al.) Now PYTHIA_UED [235] is available including UED without KK conservation.
- Plenty of other specific channels in private codes (e.g G. Azuelos et al.).
- Thanks to the Les Houches accord of 2001, an agreed exchange format exists such that one can think of a tool kit for ED processes.

Typically the specialized generators deal with the hard process only and workhorse generators such as PYTHIA and HERWIG, and now also Sherpa, deal with the hadronization and fragmentation aspects of event generation. The Les Houches accord [236] offers a common interface for communication between the generators. Hence one can construct a toolbox for generators for ED or more general BSM processes. Note that the SUSY generators are already organized in a way such that these can be used interchangeably to a large extent, albeit not quite in a toolbox format. Particularly useful has been the SPA (SUSY Parameter Analysis) [237] project.

The future of HEP software architecture will be based on frameworks. For the generators there is a proposal for such a framework called ThePEG [238]. Such a framework could well become in future the host of a possible toolkit for generators for BSM processes.

4.4.3 Wishlist for ED process generators

The variety of ED process is very large, with largely different signatures for different processes. A compiled wishlist (in 2005) of processes to become available or to be implemented is as follows:

- Universal Extra Dimensions with KK number conservation.

- Universal Extra Dimensions without KK number conservation.
- Bulk scalars with Higgs interference.
- Radions and interference with the Higgs.
- RS generator with SM fields in the bulk .
- Implementation of different running couplings.
- More flexible/complete generation of KK resonances in TeV^{-1} and RS models, which include many resonances, effects of brane kinematic terms.
- Branons.
- More sophisticated black hole generators? (remnant treatement, radiation phases, spin)
- String ball effects (black hole-like but different radiation/lower mass).
- Trans-Planckian effects, especially high-E_T dijet production.
- SUSY + ED scenarios.
- Thick branes, brain tension, rigid and soft branes.
- Even more recent scenarios (such as intersecting branes, Higgsless EWSB).

At this stage, for LHC studies, MCs of new scenarios are important if these imply new signatures and require new sorts of experimental checks or the need for new triggers.

4.4.4 K-factors, PDF and scale uncertainties

NLO estimates exist for Higgs production and SUSY particle production for a number of processes and variables. Recently K-factors have been determined also for a few ED processes. For example, it was shown that for ADD/RS dilepton production the K-factor can be large. At the LHC the factor is typical of order 1.6, shown in Fig. 4.4.1, larger than for the Drell-Yan background process[239]. K-factors can make a difference in both discovery and extracted limits and are already useful to have now for Tevatron analyses. Only a few processes have been calculated so far. E.g., even though we have the K-factor for a RS graviton decaying into $G \rightarrow$ dileptons, it can't be transported to the $G \rightarrow \gamma\gamma$ process.

Another important effect is the effect of the parton density functions (PDFs) and scale uncertainties. A recent analysis of PDF and scale uncertainties for EDs was reported in Ref. [240]. Earlier studies[241] showed that these uncertainties may reduce the search reach by up to a factor two, given the present PDF uncertainties. The HERA/LHC workshop [242, 243] offers a forum for the study of PDF uncertainties and strategies to reduce them.

Clearly understanding the SM background processes is imperative for BSM searches. Other contributions in this and the HERA/LHC workshop deal with these questions in detail.

4.4.5 Further items

Finally, for the physics TDR studies of CMS and ATLAS, it would have been useful to have agreed-upon benchmark points. Such points have been defined for SUSY studies and have been

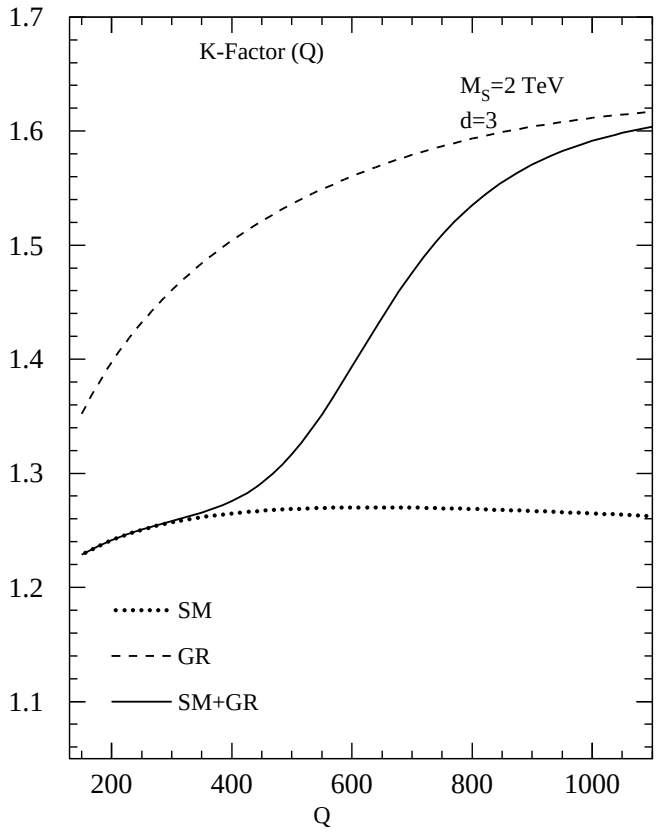

Fig. 4.4.1: The K-factor for the cross section $d\sigma/dQ$ at $M_s = 2$ TeV and $d = 3$. The plot is made for the LHC ($\sqrt{S} = 14$ TeV). Standard Model (dotted line), gravity (long dashed line), Standard Model plus gravity (solid line).

instrumental in common studies of ATLAS/CMS and the ILC study groups, as is demonstrated in the huge report of Ref. [244]. While it is getting late for benchmarks for the LHC now since data taking is approaching in 2008, one aspect of the benchmark selection studies remains useful, namely to get a complete review of the constraints of existing data (HEP or other) on the available parameter space.

Finally, a unification of different formalisms would be useful, e.g. for virtual graviton effects in ADD models for which there are at least three distinct formalisms.

4.4.6 Recent activities

As mentioned at the start: since the Les Houches 05 workshop some coherent activity has started. As a first step, the existing Monte Carlo generators and tools are cataloged and collected in one repository. In a next step one can try to unify them more and perhaps create a toolkit.

A BSM tool repository, which now contains a collection of 25 programs, is described in Ref. [235] and available under: http://www.ippp.dur.ac.uk/montecarlo/BSM/

Other useful information is the summary paper of the recent MC4BSM workshop [245], and a discussion forum for LHC tools is available under http://www-theory.lbl.gov/tools/.

4.4.7 Summary

The wishlist for BSM tools for the LHC is as follows:

- an ED or BSM Monte Carlo process tool box
  - include the (still many) missing processes into generators.
  - Keep track of details in the MC, such as spin correlations. These are likely to become very important when LHC will discover a new object.
  - Les Houches accords and frameworks such as ThePEG should facilitate this task
- SM background processes: These need to be known with high precision.
- Higher order QCD (EW) corrections to the processes
- ED constraints from existing data
- SUSY has the SPA project; do we need something similar for the EDs or other BSM processes?

On some of these items on the list activity is already ongoing, but some more central coordination and intiative would be extremely useful.

4.5 Collider Phenomenology of a Little Higgs Model with T-Parity

Jay Hubisz, Fermi National Accelerator Laboratory, Batavia, IL, USA

Little Higgs models are an interesting approach to solving the LEP paradox of precision data expectations to find a light Higgs but not finding such a state. The original littlest Higgs model was plagued by strong electroweak precision constraints, requiring a reintroduction of the fine tuning problem. An economical solution is to introduce a discrete symmetry called T-parity. T-parity solves the electroweak precision constraint issues, while also providing a dark matter candidate. We give the relic abundance of this dark matter candidate as a function of the parameters in the model. In addition, we discuss the LHC phenomenology, presenting the production cross sections and decay channels for the new particles in the model.

The turn-on date for the LHC is fast approaching. The electroweak hierarchy problem has many physicists convinced that the data which will pour out of this experiment will give many hints towards the way in which this problem is solved by nature. The most well studied extension of the Standard Model (SM) which stabilizes the electroweak hierarchy is supersymmetry.

Little Higgs models are a more recent attempt to solve the hierarchy problem by the introduction of additional global symmetries which are spontaneously broken at the TeV scale. In these theories, the Higgs is an approximate Goldstone boson of the global symmetry breaking pattern [246, 247, 248, 249, 250, 251, 252]. The interactions which explicitly violate these symmetries generate non-derivative interactions for these fields. In Little Higgs models, these interactions are introduced in a way such that any single interaction preserves enough of the global symmetries to keep the Higgs precisely massless [92]. However, all the interactions together break all the global symmetries. In this way, the quadratically divergent contributions to the Higgs mass are suppressed by additional loop factors.

We focus on the littlest Higgs model, based on an $SU(5)/SO(5)$ non-linear sigma model [109]. The earliest implementations of this structure were not reconcileable with electroweak precision constraints [253, 254, 255], but recently the structure has been extended to include a discrete symmetry which eliminates the tree-level contributions to SM electroweak observables [192, 193, 256]. This discrete symmetry is called T-parity. Most new particles introduced beyond the SM spectrum are odd under this parity, leading to drastically modified collider phenomenology [103, 94, 194].

4.5.1 Model description

The new interactions can be described by an $SU(5)/SO(5)$ non-linear sigma model, as we describe below. The breaking pattern $SU(5) \to SO(5)$ is accomplished by a symmetric tensor of $SU(5)$, Σ. The vacuum expectation value of this field is assumed to be near 1 TeV, so that fine tuning in the Higgs mass squared parameter is minimized. Embedded within the $SU(5)$ global symmetries is a $[SU(2) \times U(1)]^2$ gauge symmetry. The VEV Σ breaks this gauge symmetry down to the diagonal

subgroup which is then associated with the SM $SU(2)_L \times U(1)_Y$. The other gauge bosons become massive at the TeV scale.

In the non-linear sigma model parametrization, the field Σ can be written as

$$\Sigma = e^{2i\pi/f}\Sigma_0\,, \tag{4.5.1}$$

where π is a matrix containing all of the Goldstone degrees of freedom associated with the breaking of the $SU(5)$ global symmetry to the $SO(5)$ subgroup.

The Goldstone bosons associated with this breaking decompose under $SU(2)_L \times U(1)_Y$ as

$$3_0 \oplus 3_{1/2} \oplus 2_{1/2} \oplus 1_0\,. \tag{4.5.2}$$

The 3_0 and 1_0 are eaten by the gauge bosons that become massive at the scale f. We associate the $2_{1/2}$ with the Higgs multiplet. The $3_{1/2}$ is a triplet of $SU(2)_L$.

In addition to the new gauge and scalar degrees of freedom, a new vectorlike $SU(2)_L$ singlet quark is required in the theory to cancel the quadratic divergence due to the top quark Yukawa interaction. The top quark is a mixture of this singlet and the $T_3 = 1/2$ component of the $SU(2)_L$ third generation doublet. We label the orthogonal mass eigenstate T_+. This new colored state obtains a mass slightly larger than f.

The earliest implementations of this structure suffered from electroweak precision constraints. After electroweak symmetry breaking, mixing would be induced between the standard model gauge bosons and their TeV-scale partners. This mixing leads to violations of custodial $SU(2)$ [253, 254, 255] causing, for example, a tree-level shift in the ρ parameter, a tightly-constrained relation between the W and Z boson masses. T-parity is a postulated discrete symmetry which forbids mixing between the standard model fields, and their heavier counterparts.

T-parity exchanges the two copies of $SU(2) \times U(1)$. In this way, the diagonal subgroup (the SM gauge group) is T-even, while the other combinations, which receive f scale masses, are T-odd. In addition, if one wishes to implement this symmetry consistently throughout the entire model, the matter sector of the model must also be symmetric under this interchange. For every multiplet that transforms under $[SU(2) \times U(1)]_1$, there must be a partner multiplet that transforms under $[SU(2) \times U(1)]_2$. This discrete symmetry, while it eliminates the tree-level shifts in SM observables, drastically changes the phenomenology of little Higgs models.

Enforcing T-parity requires that the gauge couplings for the two $SU(2) \times U(1)$ gauge groups be equal. This fixes the mass spectrum of the new gauge bosons with respect to the overall breaking scale f:

$$M_{W_H^\pm} = M_{Z_H} = gf \quad M_{A_H} = \frac{g'f}{\sqrt{5}}\,, \tag{4.5.3}$$

where g and g' are the weak and hypercharge gauge couplings, respectively.

If the discrete symmetry is made exact, the lightest T-odd particle is stable and a potential dark matter candidate. In collider phenomenology, this lightest particle becomes a missing energy

signal, making observation of this new physics more complicated. In particular, it is likely that this type of model will look very much like supersymmetry in certain regions of parameter space. This is similar to studies of universal extra dimensions, where the signals are also similar to supersymmetry [165]. In the littlest Higgs model with T-parity, the heavy partner of the hypercharge gauge boson, the A_H, is the dark matter candidate, and can account for the WMAP observed relic density [194].

A consequence of implementing this discrete symmetry in the $SU(5)/SO(5)$ Littlest Higgs model is that the fermion spectrum must be substantially enlarged. This is due to constraints on four-fermion operators involving the standard model left handed quark and lepton doublets [193]. The additional T-odd fermions serve to cut these contributions off. In this analysis, we take these fermions to be rather heavy (out of reach for the LHC).

In addition, a T-odd partner of the T_+ is necessary, which we label T_-. This T-odd singlet changes the collider phenomenology, as the T_+ generically has a sizable branching fraction to missing energy: $T_+ \to T_- A_H$. In particular, earlier studies of the phenomenology of this new state [93, 102] are modified.

A more complete model description containing all details and interactions may be found in Ref. [194].

4.5.2 The dark matter Candidate

We calculate the relic density of the lightest T-odd particle assuming that T-parity is an exact symmetry, and that the T-odd fermions are heavy. The mass spectrum is sufficiently non-degenerate that coannihilation effects are unimportant, and only direct annihilation channels need be considered. The dominant channels are those involving s-channel Higgs exchange. As a result, the annihilation cross section is primarily a function of the Higgs and dark matter candidate masses. Imposing the constraints from WMAP [257] leads to Fig. 4.5.1. We see that there is a strong correlation between the scale f and the Higgs mass if the dark matter is to come purely from Little Higgs physics. This is due to the s-channel pole present when $m_{A_H} = m_H/2$. Noteably, larger values of f prefer larger Higgs masses than the SM best fit value.

We consider regions as ruled out where the relic density exceeds the 95% confidence limits imposed by the WMAP bound. In regions where the relic density of A_H is below the WMAP 95% confidence band, there is the possibility that there is another form of dark matter, such as an axion, which could make up the difference.

A study of the one-loop electroweak precision corrections in this model reveals that certain contributions to $\Delta\rho$ from one-loop diagrams arise with opposite sign as the terms which are logarithmic in the Higgs mass [258]. This effect is due to the contributions from singlet-doublet quark mass mixing in the third generation Yukawa couplings. Consequentially, the Higgs mass can be raised far above its standard electroweak precision bound while remaining consistent with LEP. Thus, for certain ranges of the parameters in the top-quark Yukawa sector, both dark matter and

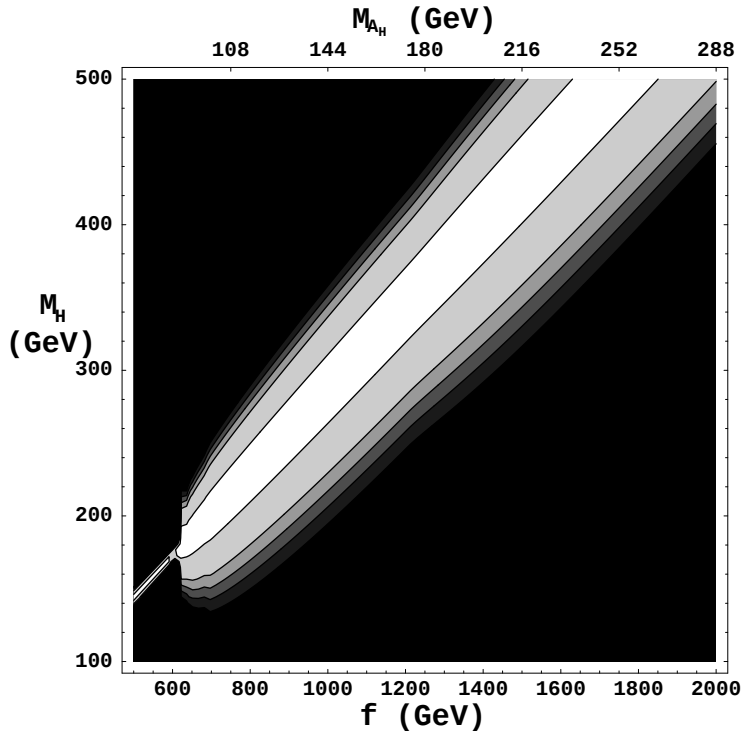

Fig. 4.5.1: Variation of the dark matter relic density with respect to the Higgs mass and the symmetry breaking scale, f. In order from lightest to darkest regions, the A_H makes up ($0-10\%$, $10-50\%$, $50-70\%$, $70-100\%$, 100%, $>100\%$) of the observed relic abundance.

EWP bounds may be satisfied simultaneously.

4.5.3 Collider Phenomenology

After entering all new interactions into COMPHEP [218], we calculate the production cross sections for the new particles in this model, comparing with the original little Higgs model, where the phenomenology was considered orginally in [103, 94]. We briefly discuss some of the signals, and summarize the primary decay modes of these particles.

Because SM particles are T-even while most new particles are T-odd, the energy cost of creating these particles is doubled due to the need to pair produce them. In addition, most new states are not charged under QCD, meaning that their production cross sections are somewhat small.

In the T-odd gauge boson sector, the only free parameter relevant for production cross section

calculations is the global symmetry breaking scale, f. The possible pairings are

$$\begin{aligned} pp &\to W_H^+ W_H^- \\ pp &\to W_H^\pm A_H \\ pp &\to W_H^\pm Z_H \,. \end{aligned} \tag{4.5.4}$$

The cross sections can be seen in Fig. 4.5.2. The dominant diagrams involve s-channel exchange of SM gauge bosons. Production of $W_H^\pm A_H$ is suppressed by the analog of the Weinberg angle in the T-odd gauge boson sector, which is of order v/f, which explains why the cross section for $pp \to W_H^\pm A_H$ is smaller than the others. The decays of the new gauge bosons are as follows:

$$\begin{aligned} W_H^\pm &\to W^\pm A_H \\ Z_H &\to A_H h \,. \end{aligned} \tag{4.5.5}$$

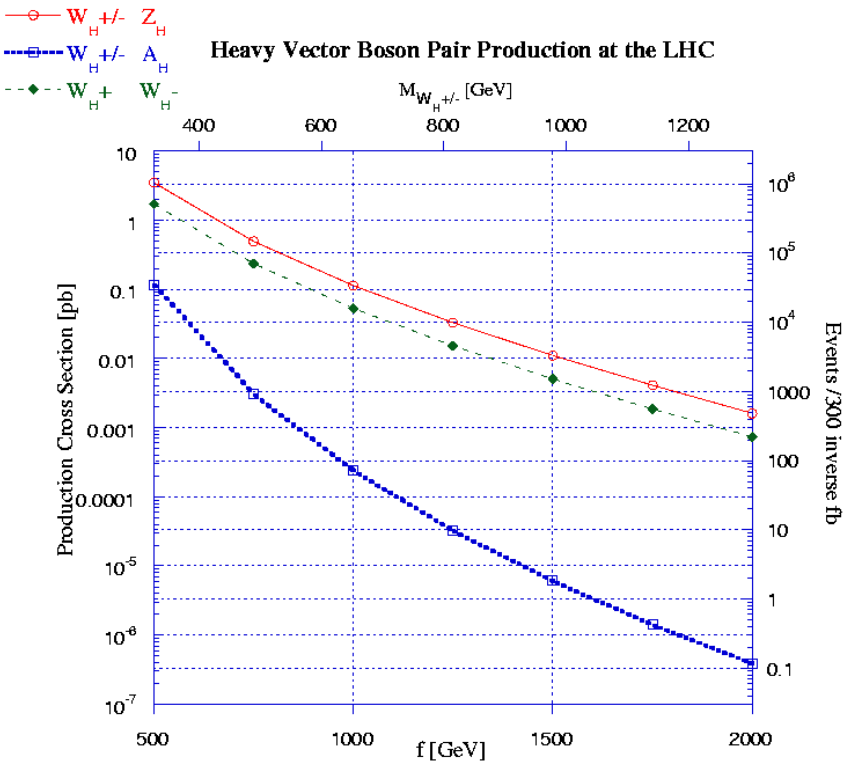

Fig. 4.5.2: Cross section for production of a pair of T-odd heavy vector bosons at the LHC as a function of the symmetry breaking scale f. The number of events for 300 fb^{-1} is plotted on the second y-axis. $M_{W_H^\pm}$ is plotted on the second x-axis. M_{Z_H} is degenerate in mass with $M_{W_H^\pm}$, and $M_{A_H} \sim .16f$.

In our analysis, we assume that the additional T-odd fermion doublets are significantly heavier than the new gauge bosons. This way they do not contribute significantly to the tree-level production cross sections, and are not themselves produced in large number.

It is also possible to pair produce the components of the scalar triplet. The triplet mass is proportional to the Higgs mass:

$$m_\Phi^2 \approx \frac{2m_H^2 f^2}{v^2}\,. \tag{4.5.6}$$

The degeneracy of the electromagnetic-charged eigenstates of the triplet is slightly split by electroweak symmetry breaking effects. The production cross sections are plotted in Fig. 4.5.3. When the Higgs is heavy enough, the relevant decay modes for the triplet are given by

$$\begin{aligned}
\phi^{++} &\to W^+ W_H^+ \to W^+ W^+ A_H \\
\phi^{+} &\to W^+ A_H \\
\phi^{P} &\to H A_H \\
\phi^{0} &\to Z A_H\,.
\end{aligned} \tag{4.5.7}$$

In the case that the triplet mass is below the threshold for the doubly charged components to decay through the above channel, they must decay directly to the three body final state. We note that in these regions, the Higgs is below 130 GeV. This region is excluded by WMAP, since such light values of the Higgs mass imply an excessive relic abundance, as shown in Fig. 4.5.1.

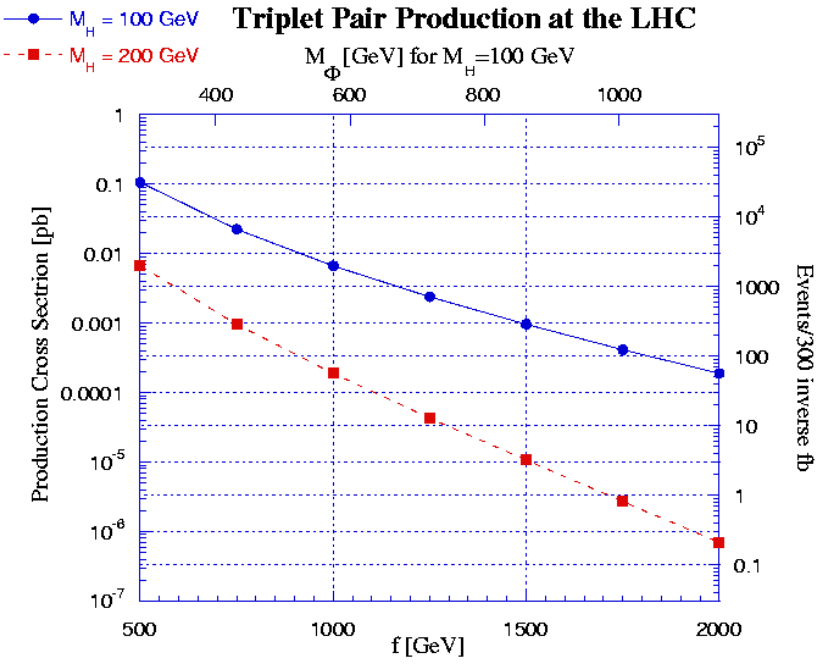

Fig. 4.5.3: Cross sections for the production of a pair of T-odd triplets at the LHC is plotted as a function of the symmetry breaking scale f, plotted for $m_H = 100, 200$ GeV since the triplet mass, M_Φ, is determined by f and m_H. The number of events for 300 fb^{-1} is plotted on the second y-axis. M_Φ for a Higgs mass of 100 GeV is plotted on the second x-axis, for a Higgs mass of 200 GeV simply scale the second x-axis by a factor of 2.

We also consider pair production of the T-odd colored fermion, T_-. In contrast to the gauge bosons and scalars, the T_- is produced primarily through gluon exchange. Therefore its production cross section, shown in Fig. 4.5.4, is comparatively large. The T_- decays through the channel $T_- \to tA_H$.

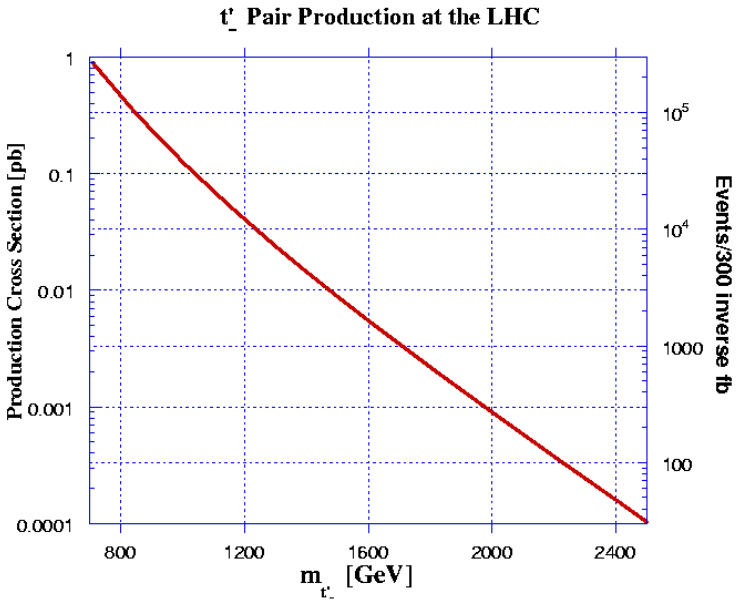

Fig. 4.5.4: Cross section for LHC production of a pair of T-odd heavy quarks T_-, plotted as a function of m_{T_-}. The number of events for 300 fb^{-1} is plotted on the second y-axis.

The backgrounds to these signals are likely to be considerable. A rough estimate is given in [194], but more thorough study is necessary.

The phenomenology of the T-even partner of the top quark is similar to the original Littlest Higgs implementation. The T_+ production cross sections are identical, as the top sector is not drastically modified. The primary difference is in the T_+ decay modes. A consistent implementation of T-parity in this model requires the introduction of a T-odd partner of the T_+, which we call the T_-. The T_- is generically lighter than the T_+. The mass difference between these two states is large enough in most of the available parameter space to allow the decay mode $T_+ \to T_- A_H \to tA_H A_H$. Thus, a sizeable fraction of the decay channels will have missing energy in the final state, which will complicate reconstruction of the T_+ width. The branching fractions of the T_+ are given in Fig. 4.5.5.

4.5.4 Conclusions

We have reviewed the phenomenology of the Littlest Higgs with T-parity in the limit that the partners of the standard model $SU(2)_L$ fermion doublets are taken to be above the reach of the

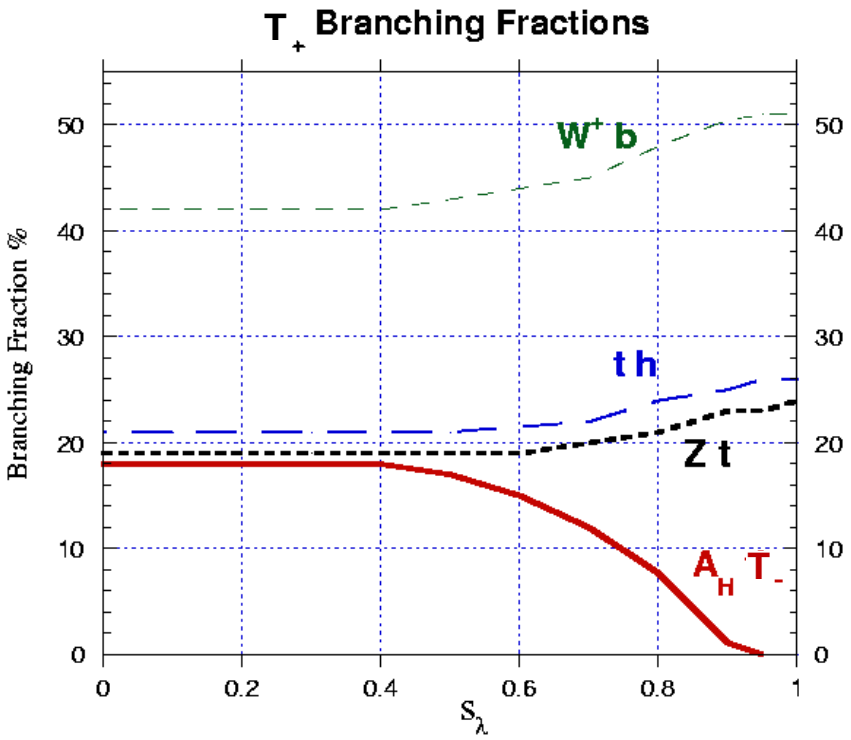

Fig. 4.5.5: Branching fractions for t'_+ decay as a function of s_λ, which parameterizes the ratio of masses of the T_+ and T_-; for $f = 1$ TeV.

LHC. We have shown that the T-parity symmetry provides a dark matter candidate that can account for the WMAP best fit value for the relic abundance. Due to the requirement of decaying to a missing energy signal, LHC phenomenology is more difficult. In particular, T-parity models may resemble supersymmetry in certain regions of parameter space.

4.6 Search for Low-Scale Technicolor at the Tevatron

Kenneth Lane, Dept. of Physics, Boston University

CDF and DØ each have more than $1\,\mathrm{fb}^{-1}$ *of data on tape, and their stores are increasing. This should be sufficient to carry out significant searches for low-scale technicolor in* $\rho_T \to W\pi_T$ *and* $\omega_T\,, \rho_T \to \gamma\pi_T$*, processes whose cross sections may be as large as several picobarn. We motivate and describe the Technicolor Straw Man framework for these processes and urge that they be sought soon in the Run 2 data.*

1. Preamble

Fig. 4.6.1 is from CDF in Run I. It shows a search for $\omega_T \to \gamma\pi_T$, with $\pi_T \to b$+jet, based on about 100 pb^{-1} of data, published in 1999 [259]. Note the $\sim 2\sigma$ excess near $M_{jj\gamma} - M_{jj} = 100$ GeV. This search has not been repeated in Run 2.[24] Fig. 4.6.2 is from CDF in Run II. It shows results of an unpublished CDF study looking for $\rho_T \to W^\pm\pi_T$.[25] The data were posted in July 2004 and are based on 162 pb^{-1} of data. There are small excesses in the dijet and Wjj masses near 110 GeV and 210 GeV, respectively. Assuming $M_{\omega_T} = M_{\rho_T} \simeq 230$ GeV, and taking into account losses from semileptonic b-decays, the excesses in Figs. 1 and 2 are in about the right place for $M_{\pi_T} \simeq 120$ GeV.

In December 2005, CDF reported on a search for WH-production with $W \to \ell\nu$ and $H \to b\bar{b}$ and a single b-tag, based on 320 pb^{-1} of data [261]. The dijet mass spectrum appears in Fig. 4.6.3.[26] There is a 2σ excess at $M_{jj} \simeq 110$ GeV. The Wjj spectrum was not reported and is not available. The expected rate for a ~ 100 GeV Higgs decaying to $b\bar{b}$ and produced in association with a W is about 0.1 pb. If the excess were real, it would correspond to a total WH cross section of about 5 pb, about 50 times the expected cross section.

A 2σ excess does not constitute convincing evidence of a signal, but does warrant follow-up investigation. Both experiments have now collected almost $1.5\,\mathrm{fb}^{-1}$. This summer, CDF and DØ will present new results for SUSY, large extra dimensions, Randall-Sundrum gravitons, Little Higgs, and other new physics searches. We hope they present the searches for technicolor as well. The most likely processes and search modes are:

$$\rho_T^\pm \to W^\pm\pi_T^0 \to \ell^\pm\nu_\ell + b\bar{b} \tag{4.6.1}$$

$$\rho_T^0 \to W^\pm\pi_T^\mp \to \ell^\pm\nu_\ell + b\bar{c}\,,\ b\bar{u} \tag{4.6.2}$$

$$\omega_T\,, \rho_T^0 \to \gamma\pi_T^0\,, \gamma\pi_T^{0\prime} \to \gamma b\bar{b} \tag{4.6.3}$$

$$\omega_T\,, \rho_T^0 \to e^+e^-\,,\ \mu^+\mu^-\,. \tag{4.6.4}$$

These processes (and more) are available in PYTHIA [7, 224].

[24] Both detectors induce jet backgrounds to photons that require much effort to suppress; the effort should be made.

[25] CDF's Run I version of this search is published in Ref. [260].

[26] I am grateful to Y.-K. Kim and her CDF collaborators for providing this figure.

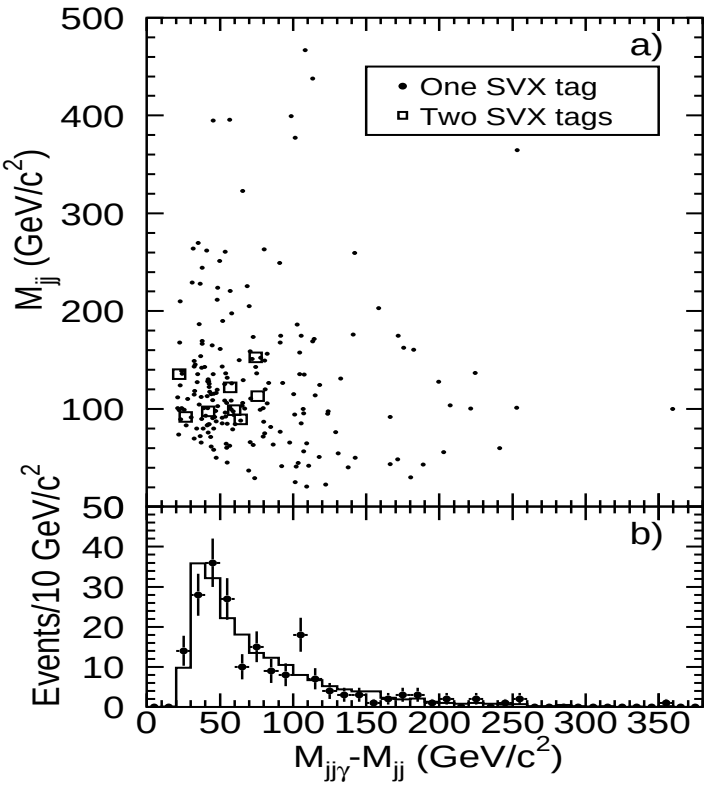

Fig. 4.6.1: (a) The distribution of M_{jj} vs. $M_{jj\gamma} - M_{jj}$ for events with a photon, b–tagged jet and a second jet, and (b) projection of this data in $M_{jj\gamma} - M_{jj}$; from Ref. [259].

In the rest of this section, we motivate low-scale technicolor — that technihadrons may be much lighter than ~ 1 TeV and, in fact, may be readily accessible at the Tevatron. Then we describe the Technicolor Straw Man Model (TCSM) and present some rate estimates for the most important color-singlet processes. The TCSM is described in more detail in Refs. [262, 263], and much of the last two subsections is taken from the second of these.

2. Low-Scale Technicolor

Technicolor (TC) is the only theory of electroweak symmetry breaking (EWSB) by new strong dynamics whose characteristic energy scale is at or below 1 TeV [264, 265]. It is the most natural scenario (not to mention the only precedent) for dealing with the Standard Model's naturalness problem: it banishes *elementary* scalar particles altogether. TC by itself, however, cannot explain — or even describe in a phenomenological way, as the standard model does — the origin of quark and lepton masses and mixings. The only known way to do that in the dynamical context of TC is *extended technicolor* (ETC) [266].

Two elements of the modern formulation of TC (see the reviews and references in Refs. [267, 268]) strongly suggest that its energy scale $\Lambda_{TC} \simeq 4\pi F_T$, where F_T is the technipion decay con-

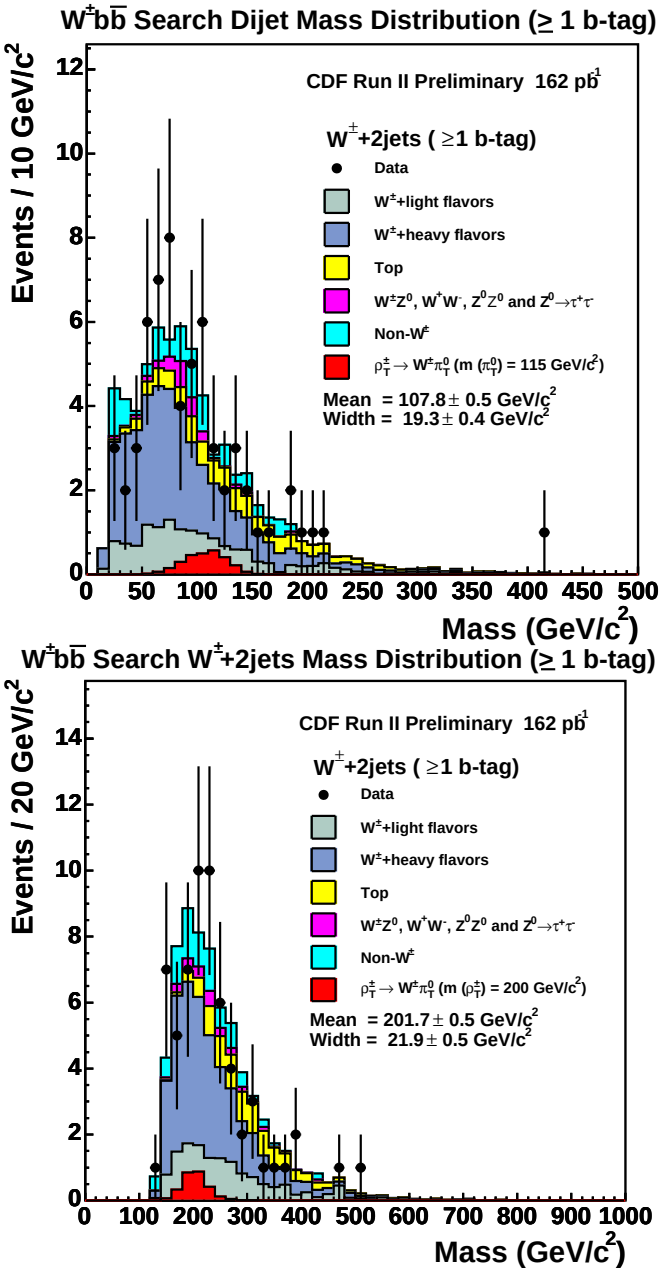

Fig. 4.6.2: (a) Invariant mass of the dijet system with $\geq$ 1 b-tagged jets, and (b) invariant mass of the $W + 2\,\mathrm{jet}$ system for the $\ell + 2\,\mathrm{jet}$ mode in $\geq$ 1 b-tagged jets; from Run 2 with $162\,\mathrm{pb}^{-1}$ (see http://www-cdf.fnal.gov/physics/exotic/r2a/20040722.lmetbj-wh-tc/).

stant — and therefore the masses of technihadrons (ρ_T and ω_T as well as π_T) — are *much* less than several TeV. They are the notions of *walking technicolor* (WTC) [269, 270, 271, 272] and *topcolor-assisted technicolor* (TC2) [273]. Assuming for simplicity that the technifermions form N_D electroweak doublets, then $F_T \simeq F_\pi/\sqrt{N_D}$, where $F_\pi = 246$ GeV. The EWSB condensate is

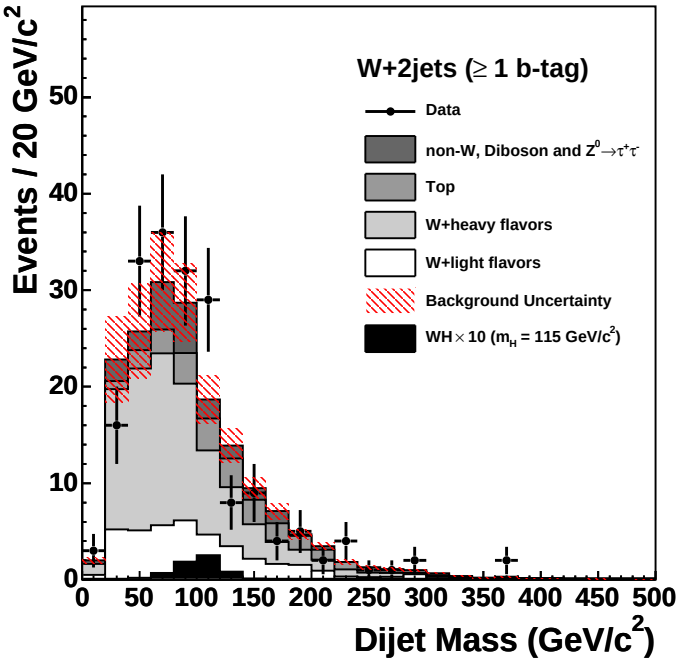

Fig. 4.6.3: Invariant mass of the $W + 2\,\mathrm{jet}$ system for the $\ell + 2\,\mathrm{jet}$ mode with ≥ 1 b-tagged jets; from Run 2 with $320\,\mathrm{pb}^{-1}$; see Ref. [261].

$\langle \bar{T}T \rangle_{TC} \simeq 4\pi F_T^3$.

Extended technicolor inevitably induces flavor-changing neutral current interactions of quarks and leptons. The most problematic of these are the $|\Delta S| = 2$ operators,

$$\mathcal{H}_{|\Delta S|=2} = \frac{g_{ETC}^2}{M_{ETC}^2} \sum_{ij} K_{ij}\, \bar{s}\Gamma_i d\, \bar{s}\Gamma_j d + \mathrm{h.c.}\,, \tag{4.6.5}$$

which require effective ETC gauge boson masses $M_{ETC}/g_{ETC}\sqrt{K_{ij}} \gtrsim 1000\ \mathrm{TeV}$. If TC were a QCD-like gauge theory, one in which asymptotic freedom sets in quickly near Λ_{TC}, the quark and lepton masses $m_{q,l} \simeq g_{ETC}^2 \langle \bar{T}T \rangle_{ETC}/M_{ETC}^2$ generated by such high-scale ETC interactions would be unacceptably small because $\langle \bar{T}T \rangle_{ETC} \simeq \langle \bar{T}T \rangle_{TC}$. This difficulty is cured by WTC, in which the technicolor gauge coupling α_{TC} runs very slowly, i.e., the interaction is close to conformally invariant, and the technifermion condensates $\langle \bar{T}T \rangle_{ETC}$ renormalized at the ETC scale are enhanced relative to $\langle \bar{T}T \rangle_{TC}$ by a factor not much less than M_{ETC}/Λ_{TC}. The small β_{TC}-function required for WTC is readily achieved by having many technidoublets transforming as the fundamental representation of the TC gauge group.[27] Thus, N_D is large and F_T is small.

[27] Walking could in principle be achieved by having a few technidoublets in higher-dimensional TC representations; see Refs. [274] and [275, 276]. It is difficult to see how this could be done without some number of doublets in the fundamental representation; see Ref. [277].

Even with the enhancements of walking technicolor, there is no satisfactory way in the context of ETC alone to understand the large mass of the top quark. Either the ETC mass scale generating m_t must be too close to Λ_{TC} or the ETC coupling must be fine-tuned.[28] So far, the most attractive scheme for m_t is that it is produced by the condensation of top quarks, induced at a scale near $1\ \mathrm{TeV}$ by new strong topcolor gauge interactions ($SU(3) \otimes U(1)$ in the simplest scheme). This top condensation scheme, topcolor-assisted technicolor, accounts for almost all the top mass, but for only a few percent of EWSB. Realistic models that provide for the TC2 gauge symmetry breaking and for the mixing of the heavy third generation with the two light generations typically require many ($N_D \simeq 10$ (!)) technifermion doublets. Therefore, in the following, we shall assume $F_T \lesssim 100$ GeV.[29]

3. The Technicolor Straw Man Model

The TCSM provides a simple framework for light technihadron searches. Its first and probably most important assumption is that the lowest-lying bound states of the lightest technifermions can be considered *in isolation*. The lightest technifermions are expected to be an isodoublet of color singlets, (T_U, T_D). Color triplets, not considered here, will be heavier because of $SU(3)_C$ contributions to their hard (chiral symmetry breaking) masses. We assume that all technifermions transform under technicolor $SU(N_{TC})$ as fundamentals. This leads us to make — with no little trepidation in a walking gauge theory — large-N_{TC} estimates of certain parameters. The electric charges of (T_U, T_D) are Q_U and $Q_D = Q_U - 1$; they are important parameters of the TCSM. The color-singlet bound states we consider are vector and pseudoscalar mesons. The vectors include a spin-one isotriplet $\rho_T^{\pm,0}$ and an isosinglet ω_T. Techni-isospin can be a good approximate symmetry in TC2, so that ρ_T and ω_T are nearly degenerate. Their mixing with each other and the photon and Z^0 is described by a neutral-sector propagator matrix.

The lightest pseudoscalar bound states of (T_U, T_D) are the color-singlet technipions. They also form an isotriplet $\Pi_T^{\pm,0}$ and an isosinglet $\Pi_T^{0\prime}$. However, these are not mass eigenstates. Our second important assumption for the TCSM is that the isovectors may be described as simple *two-state mixtures* of the longitudinal weak bosons $W_L^\pm$, Z_L^0 — the true Goldstone bosons of dynamical electroweak symmetry breaking — and mass-eigenstate pseudo-Goldstone technipions $\pi_T^\pm, \pi_T^0$:

$$|\Pi_T\rangle = \sin\chi\,|W_L\rangle + \cos\chi\,|\pi_T\rangle\,. \tag{4.6.6}$$

[28] A possible exception to this was proposed in Ref. [278]. In this model, $N_D = 4$ and F_T is not particularly small. The model is genuinely baroque, but that is probably true of any quasi-realistic ETC model.

[29] The question of the effect of technicolor on precisely measured electroweak quantities such as S, T, and U naturally arises because of the appearance of many technifermion doublets in low-scale technicolor. Calculations which show TC to be in conflict with precision measurements have been based on the assumption that TC dynamics are just a scaled-up version of QCD. However, because of its walking gauge coupling, this cannot be. In WTC there must be something like a tower of spin-one technihadrons reaching almost to the ETC scale, and these states must contribute significantly to the integrals over spectral functions involved in calculating S, T, and U. Therefore, in the absence of detailed experimental knowledge of this spectrum, including the spacing between states and their coupling to the electroweak currents, it is not possible to estimate these quantities reliably.

Assuming that $SU(N_{TC})$ gauge interactions dominate the binding of all technifermions into technihadrons, the decay constants of color-singlet and nonsinglet π_T are approximately equal, $F_T \simeq F_\pi/\sqrt{N_D}$, and the mixing factor $\sin\chi$ — another important TCSM parameter — is given by

$$\sin\chi \simeq F_T/F_\pi \simeq 1/\sqrt{N_D}\,, \tag{4.6.7}$$

so that $\sin^2\chi \ll 1$.

Similarly, $|\Pi_T^{0\prime}\rangle = \cos\chi'\,|\pi_T^{0\prime}\rangle + \cdots$, where χ' is another mixing angle and the ellipsis refer to other technipions needed to eliminate the two-technigluon anomaly from the $\Pi_T^{0\prime}$ chiral current. It is unclear whether, like ρ_T and ω_T, these neutral technipions will be degenerate. If π_T^0 and $\pi_T^{0\prime}$ are nearly degenerate *and* if their widths are roughly equal, there may be appreciable π_T^0–$\pi_T^{0\prime}$ mixing; then the lightest neutral technipions will be ideally-mixed $\bar{T}_U T_U$ and $\bar{T}_D T_D$ bound states. *Searches for these technipions ought to consider both possibilities: they are nearly degenerate or such that* $M_{\pi_T^\pm} = M_{\pi_T^0} \ll M_{\pi_T^{0\prime}}$.

Color-singlet technipion decays are mediated by ETC and (in the case of $\pi_T^{0\prime}$) $SU(3)_C$ interactions. In the TCSM they are taken to be:

$$\begin{aligned}
\Gamma(\pi_T \to \bar{f}' f) &= \frac{1}{16\pi F_T^2}\, N_f\, p_f\, C_{1f}^2\, (m_f + m_{f'})^2 \\
\Gamma(\pi_T^{0\prime} \to gg) &= \frac{1}{128\pi^3 F_T^2}\, \alpha_C^2\, C_{1g}^2\, N_{TC}^2\, M_{\pi_T^{0\prime}}^{\frac{3}{2}}\,.
\end{aligned} \tag{4.6.8}$$

The number of colors of fermion f is N_f and the fermion momentum is p_f. The QCD coupling α_C is evaluated at M_{π_T}; C_{1g}^2 is a Clebsch-Jordan coefficient of order one. The default values of these and other parameters are tabulated in Ref. [263]. Like elementary Higgs bosons, technipions are *expected* to couple to fermions proportional to the fermion mass. Thus, C_{1f} is an ETC-model dependent factor of order one *except* that TC2 implies a weak coupling to top quarks, $|C_{1t}| \lesssim m_b/m_t$. Thus there is no strong preference for technipions to decay to (or radiate from) top quarks. For $M_{\pi_T} < m_t + m_b$, these technipions are expected to decay mainly as follows: $\pi_T^+ \to c\bar{b}$, $u\bar{b}$, $c\bar{s}$ and possibly $\tau^+\nu_\tau$; $\pi_T^0 \to b\bar{b}$ and, perhaps $c\bar{c}$, $\tau^+\tau^-$; and $\pi_T^{0\prime} \to gg$, $b\bar{b}$, $c\bar{c}$, $\tau^+\tau^-$.

In the limit that the electroweak couplings $g, g' = 0$, the ρ_T and ω_T decay as

$$\begin{aligned}
\rho_T &\to \Pi_T\Pi_T = \cos^2\chi\,(\pi_T\pi_T) + 2\sin\chi\,\cos\chi\,(W_L\pi_T) + \sin^2\chi\,(W_L W_L)\,; \\
\omega_T &\to \Pi_T\Pi_T\Pi_T = \cos^3\chi\,(\pi_T\pi_T\pi_T) + \cdots\,.
\end{aligned} \tag{4.6.9}$$

The ρ_T decay amplitude is

$$\mathcal{M}(\rho_T(q) \to \pi_A(p_1)\pi_B(p_2)) = g_{\rho_T}\, \mathcal{C}_{AB}\, \epsilon(q)\cdot(p_1 - p_2)\,, \tag{4.6.10}$$

where $\epsilon(q)$ is the ρ_T polarization vector, $\alpha_{\rho_T} \equiv g^2_{\rho_T}/4\pi = 2.91(3/N_{TC})$ is scaled naively from QCD (and the parameter $N_{TC} = 4$ is used in calculations), and

$$\mathcal{C}_{AB} = \begin{cases} \sin^2\chi & \text{for } W_L^+W_L^- \text{ or } W_L^\pm Z_L^0 \\ \sin\chi\cos\chi & \text{for } W_L^\pm\pi_T^\mp, \text{ or } W_L^\pm\pi_T^0, Z_L^0\pi_T^\pm \\ \cos^2\chi & \text{for } \pi_T^+\pi_T^- \text{ or } \pi_T^\pm\pi_T^0. \end{cases} \tag{4.6.11}$$

The ρ_T decay rate to two technipions is then (for use in cross sections, we quote the energy-dependent width for a ρ_T mass of $\sqrt{\hat{s}}$):

$$\Gamma(\rho_T^0 \to \pi_A^+\pi_B^-) = \Gamma(\rho_T^\pm \to \pi_A^\pm\pi_B^0) = \frac{2\alpha_{\rho_T}\mathcal{C}_{AB}^2}{3} \frac{p^3}{\hat{s}}, \tag{4.6.12}$$

where $p = [(\hat{s} - (M_A + M_B)^2)(\hat{s} - (M_A - M_B)^2)]^{\frac{1}{2}}/2\sqrt{\hat{s}}$ is the π_T momentum in the ρ_T rest frame.

4. Sample TCSM Production Rates at the Tevatron

The $\rho_T \to \Pi_T\Pi_T$ decays are strong transitions, therefore we might expect the ρ_T to be quite wide. Almost certainly this is not so. The enhanced technifermion condensate in WTC magnifies technipion masses much more than it does technivector, so the channels $\rho_T \to \pi_T\pi_T$, $\omega_T \to \pi_T\pi_T\pi_T$ and even the isospin-violating decay $\omega_T \to \pi_T\pi_T$ are likely to be closed [274]. A ρ_T^0 of mass 200 GeV may then decay mainly to $W_L^\pm\pi_T^\mp$ or $W_L^+W_L^-$. These channels are also isospin-forbidden for the ω_T, so all its important decays are electroweak: $\omega_T \to \gamma\pi_T^0$, $Z^0\pi_T^0$, $W^\pm\pi_T^\mp$, and $\bar{f}f$ — especially e^+e^- and $\mu^+\mu^-$. Here, the Z and W are transversely polarized.[30] Furthermore, since $\sin^2\chi \ll 1$, the electroweak decays of ρ_T to the transverse gauge bosons γ, W, Z plus a technipion may be competitive with the open-channel strong decays. Thus, we expect ρ_T and ω_T to be *very narrow*. For masses accessible at the Tevatron, it turns out that $\Gamma(\rho_T) \sim 1$ GeV and $\Gamma(\omega_T) \lesssim 0.5$ GeV.

Within the context of the TCSM (and with plausible assumptions for its parameters), we expect that $\rho_T^{\pm,0}$ and ω_T with masses below about 250 GeV should be accessible in Tevatron Run II in one channel or another. Assuming $M_{\rho_T} < 2M_{\pi_T}$, the $\rho_T \to W\pi_T$ cross sections have rates of a few picobarn. An example is shown in Fig. 4.6.4 for $M_{\rho_T} = 210$ GeV and $M_{\pi_T} = 110$ GeV.[31] The parameter M_V against which these rates are plotted is described below; it hardly affects them. These cross sections were computed with EHLQ structure functions [17], and should be multiplied by a K-factor of about 1.4, typical of Drell-Yan processes such as these. Searches for these modes at the Tevatron require a leptonic decay of the W plus two jets with at least one b-tag.

[30] Strictly speaking, the identification of W and Z decay products as longitudinal or transverse is approximate, becoming exact in the limit of very large M_{ρ_T,ω_T}.

[31] This figure does not include contributions from transverse weak bosons, which are small for this choice of parameters.

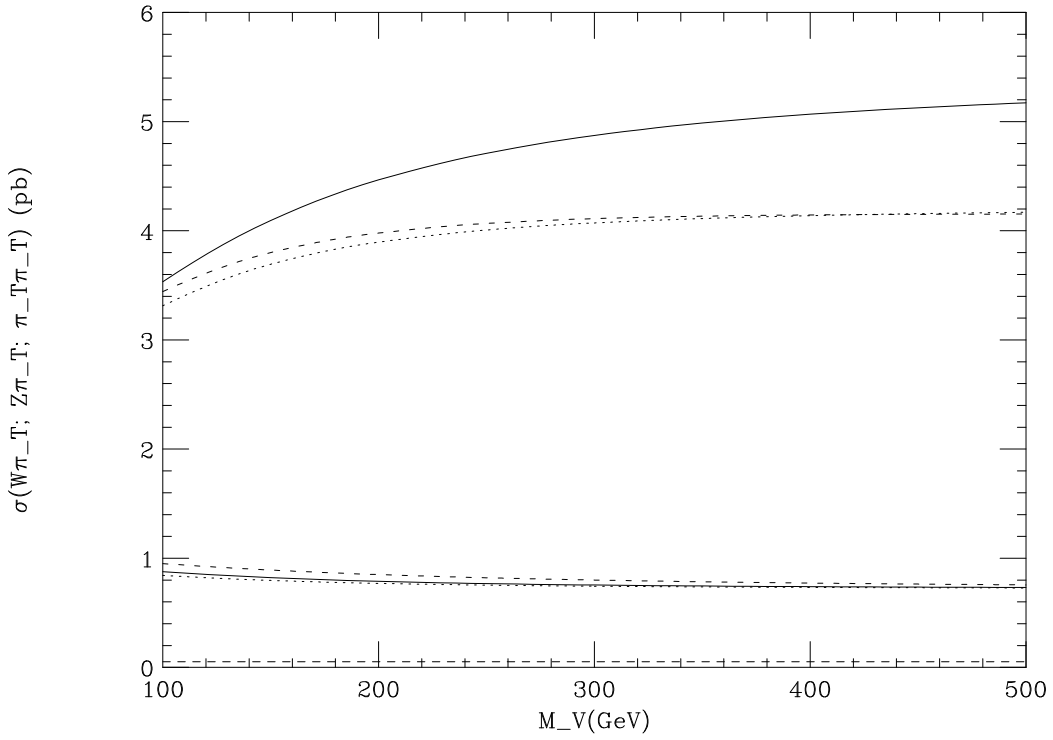

Fig. 4.6.4: Production rates in $p\bar{p}$ collisions at $\sqrt{s} = 2$ TeV for ω_T, ρ_T^0, $\rho_T^\pm \to W\pi_T$ (upper curves) and $Z\pi_T$ (lower curves) versus M_V, for $M_{\rho_T} = 210$ GeV and $M_{\omega_T} = 200$ (dotted curve), 210 (solid), and 220 GeV (short-dashed); $Q_U + Q_D = \frac{5}{3}$ and $M_{\pi_T} = 110$ GeV. Also shown is $\sigma(\rho_T \to \pi_T\pi_T)$ (lowest dashed curve). From Ref. [262].

The parameter M_V appears inversely in the amplitude for $\rho_T, \omega_T \to \gamma\pi_T$. It is a typical TC mass-scale and, for low-scale TC, should lie in the range 100–500 GeV. As long as the $\rho_T \to W\pi_T$ channels are open, $\gamma\pi_T^0$ and $\gamma\pi_T^{0\prime}$ production proceeds mainly through the ω_T resonance. Then M_V and the sum of the technifermion charges, $Q_U + Q_D$, control their rates, which are approximately proportional to $(Q_U + Q_D)^2/M_V^2$. Fig. 4.6.5 shows the $\gamma\pi_T$ cross sections v. M_V for the favorable case $Q_U + Q_D = \frac{5}{3}$. Again, a K-factor of about 1.4 should be applied. Here, $M_{\pi_T^{0\prime}} = M_{\pi_T^0}$ and about half the rate is $\gamma\pi_T^{0\prime}$. Note that the gg decays of the $\pi_T^{0\prime}$ will dilute the usefulness of the b-tag for these processes. On the other hand, decays involving b's have two b-jets.

Finally, for large M_V, ω_T decays mainly to $\bar{f}f$ pairs. The most promising modes at the Tevatron (and the LHC) then are e^+e^- and $\mu^+\mu^-$. Figs. 4.6.6 and 4.6.7 show the effect of changing M_V from 100 to 500 GeV on the e^+e^- invariant mass distributions. Note also the ω_T–ρ_T interference effect when their masses are close. This would be lovely to observe! The cross section for $M_{\omega_T} = M_{\rho_T} = 210$ GeV, integrated from 200 to 220 GeV and including the Drell-Yan background, increases from 0.12 to 0.25 pb^{-1} when M_V is increased from 100 to 500 GeV. A first search for $\omega_T, \rho_T \to e^+e^-$ was carried out by DØ in Run I and published in Ref. [279]. We look forward to a search based on Run II data soon; it shouldn't be difficult to carry out.

To sum up, there are nagging little hints of something at ~ 110 GeV in dijets with a b-tag coming from some parent at ~ 210 GeV. These have been around since Run I and deserve a closer

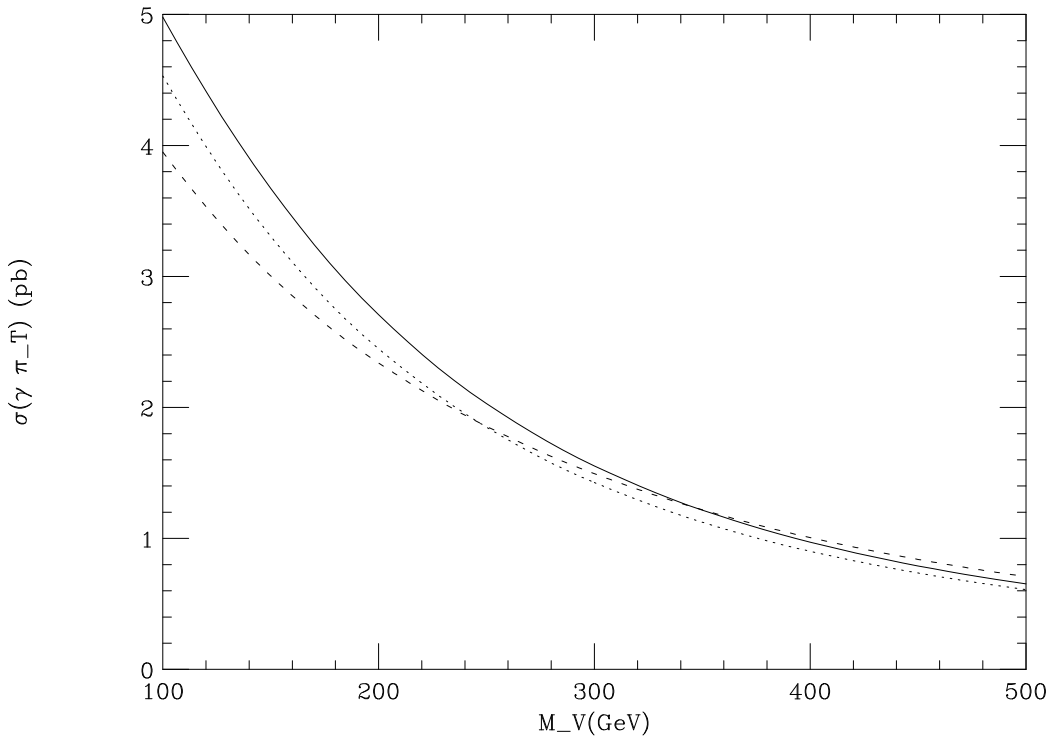

Fig. 4.6.5: Production rates in $p\bar{p}$ collisions at $\sqrt{s} = 2$ TeV for the sum of ω_T, ρ_T^0, $\rho_T^\pm \to \gamma\pi_T$ and $\gamma\pi_T^{0\prime}$ versus M_V, for $M_{\rho_T} = 210$ GeV and $M_{\omega_T} = 200$ (dotted curve), 210 (solid), and 220 GeV (short-dashed); $Q_U + Q_D = \frac{5}{3}$, and $M_{\pi_T} = M_{\pi_T^{0\prime}} = 110$ GeV. From Ref. [262].

look in Run II. We urge the Tevatron experimental collaborations to settle this soon.

Acknowledgements

I am grateful for many conversations with colleagues friends in CDF and DØ. I again thank Steve Mrenna for putting the TCSM into PYTHIA. Thanks also to David Rainwater and Bogdan Dobrescu of the TeV4LHC Landscapes project for their patience with me. This research was supported in part by the Department of Energy under Grant No. DE–FG02–91ER40676.

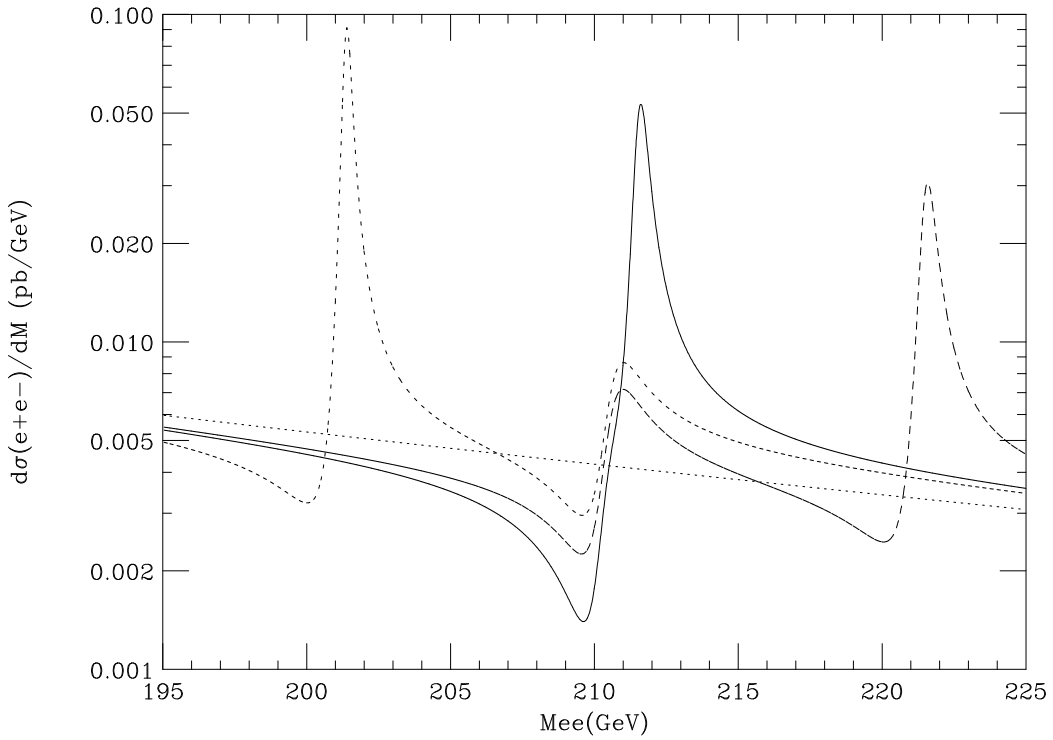

Fig. 4.6.6: Invariant mass distributions in $p\bar{p}$ collisions at $\sqrt{s} = 2$ TeV for ω_T, $\rho_T^0 \to e^+e^-$ for $M_{\rho_T} = 210$ GeV and $M_{\omega_T} = 200$ (short-dashed curve), 210 (solid), and 220 GeV (long-dashed); $M_V = 100$ GeV. The Standard Model background is the sloping dotted line. $Q_U + Q_D = \frac{5}{3}$ and $M_{\pi_T} = 110$ GeV. From Ref. [262].

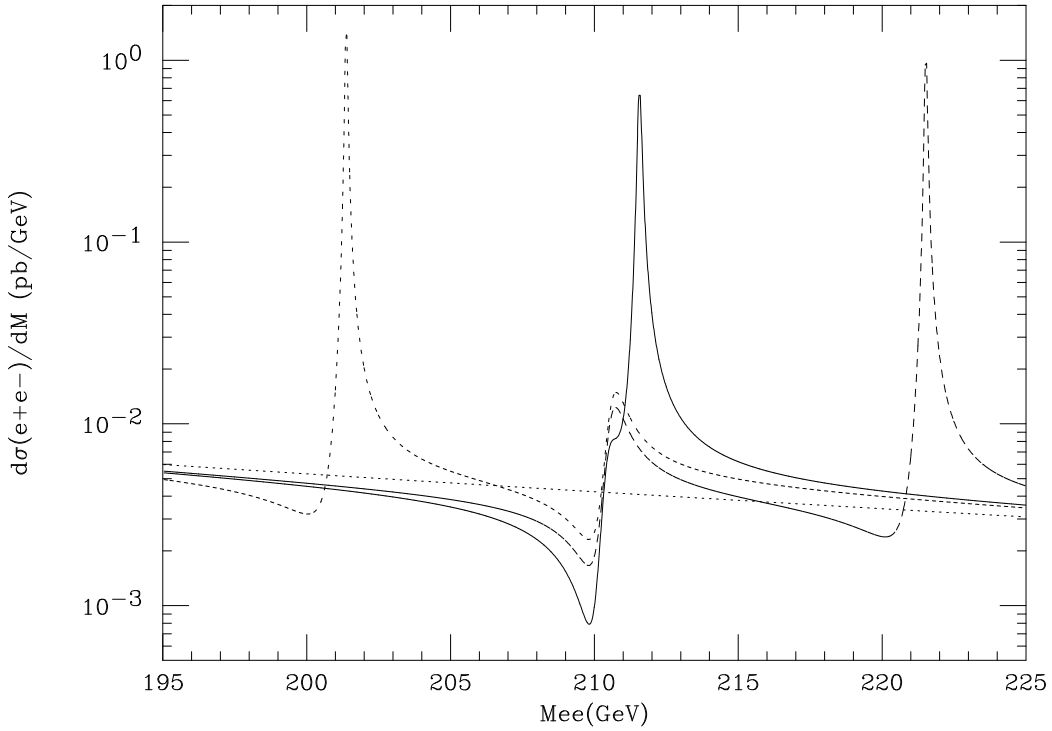

Fig. 4.6.7: Invariant mass distributions in $p\bar{p}$ collisions at $\sqrt{s} = 2$ TeV for ω_T, $\rho_T^0 \to e^+e^-$ for $M_{\rho_T} = 210$ GeV and $M_{\omega_T} = 200$ (short-dashed curve), 210 (solid), and 220 GeV (long-dashed); $M_V = 500$ GeV. The Standard Model background is the sloping dotted line. $Q_U + Q_D = \frac{5}{3}$ and $M_{\pi_T} = 110$ GeV. From Ref. [262].

4.7 Slepton Mass Measurements at the LHC

Andreas Birkedal[1], Craig Group[2] and Konstantin Matchev[2]

[1]*Santa Cruz Institute for Particle Physics*
[2]*Institute for Fundamental Theory, University of Florida*

The necessity of measuring slepton masses at the LHC is discussed, emphasizing their importance for cosmology. The possibility of making slepton mass determinations at the LHC in neutralino decays is investigated. It is demonstrated that by studying the shape of the dilepton invariant mass distribution in the decay $\tilde{\chi}_2^0 \to \tilde{\chi}_1^0 \ell^+ \ell^-$, one can determine whether the slepton is real or virtual. Furthermore, in case of virtual sleptons, it is possible to bound the slepton mass within a limited range. In this note this method is applied to the special case of mSUGRA via an approximate LHC detector simulation as a proof of technique study.

Low-energy supersymmetry remains the best-motivated extension of the standard model (SM). The search for superpartners is a prime objective of the LHC. Strong production of colored superpartners (squarks and the gluino) would dominate, and there is an extensive body of literature devoted to signatures. In contrast, direct production of non-colored superpartners (e.g. sleptons) is smaller, posing a challenge for their discovery [280, 281, 282, 283, 284, 285, 286]. A recent analysis [286] finds that CMS could discover right-handed sleptons with mass up to 200 GeV and left-handed sleptons up to 300 GeV with only 30 fb^{-1} of data.

Supersymmetric theories conserving R-parity also generically contain viable weakly-interacting massive particle (WIMP) dark matter candidates. This is typically is the lightest neutralino, $\tilde{\chi}_1^0$, for which the discovery signatures contain missing transverse energy due to two stable $\tilde{\chi}_1^0$'s in each event escaping the detector. A missing energy signal at the LHC would fuel the WIMP hypothesis. However, a missing energy signal at a collider only implies that particles have been created which are stable on a timescale characteristic of the detector size. To prove that the missing energy particle is indeed viable dark matter, one needs to calculate its relic abundance. To this end, one needs to measure all parameters which enter this calculation.

The relic abundance of a dark matter particle is determined in large part by its annihilation cross section $\sigma\left(\chi\chi \to \sum_i X_i\right)$, where χ is used to represent a generic dark matter particle, and X_i is any allowed final state. The post-WMAP determination of the dark matter abundance is accurate to about 10% [257]. Assuming a standard cosmology, one can then deduce a value for the cross section $\sigma\left(\chi\chi \to \sum_i X_i\right)$. This can in turn be translated into a model-independent prediction for the rates of $e^+e^- \to \chi\chi\gamma$, $q\bar{q} \to \chi\chi\gamma$, and $q\bar{q} \to \chi\chi\tilde{g}$ at colliders [287]. However, these searches are challenging at both the ILC [287] and LHC [230].

In typical models, slepton masses are among the key parameters in determining whether $\tilde{\chi}_1^0$ is a good dark matter candidate [288, 289, 290]. For example, if the slepton is light, then

slepton-mediated annihilation diagrams are important. In this case the slepton mass is required to determine the relic abundance. Conversely, if the slepton is heavy, its mass is unimportant for the relic abundance calculation [291, 292, 293, 294, 295, 296, 297, 298, 299, 300, 301, 302]. But, without a collider measurement of the slepton mass, there may be significant uncertainty in a relic abundance calculation.

To summarize, the importance of slepton discovery is two-fold. First, supersymmetry predicts a superpartner for every standard model particle. Therefore, the discovery of the superpartners of the leptons is an important step in verifying supersymmetry. Second, knowledge of slepton masses is *always* important for an accurate determination of the relic abundance of $\tilde{\chi}_1^0$.

Here we show that the LHC will indeed have sensitivity to slepton masses, even in the case of heavy sleptons, and describe the details of how slepton masses can be determined from neutralino decays. In a previous note [303] it was illustrated how this analysis can be done for the example of minimal supergravity (mSUGRA). It was shown that the difference between real and virtual sleptons can clearly be seen. Establishing the presence of a real slepton in a cascade decay by the method described is equivalent to a slepton discovery. In the case of virtual sleptons, it is possible to limit the allowed range of their masses with this method, which is equivalent to a rough indirect measurement of the slepton mass.

The previous analysis did not include backgrounds, detector effects, or realistic LHC event rates. The goal of this work is to confirm that dominant backgrounds can be reduced, find characteristics of the neutralino decays survive detector effects, and obtain realistic estimates of the LHC luminosity and event rate will provide suitable statistics for this study.

4.7.1 Slepton Phenomenology

Sleptons at the LHC

Direct slepton production suffers from large backgrounds, mostly due to W^+W^- and $t\bar{t}$ production [286]. Direct methods for slepton mass determination available at a linear colliders, such as threshold scans, are not applicable here. Fortunately, sleptons would be produced in sizable quantities at the LHC through cascade decays. These events can be easily triggered on and separated from the SM backgrounds. In principle, these slepton events present an opportunity for a slepton mass measurement. A common situation in supersymmetric models is the hierarchy $|M_1| < |M_2| < |\mu|$. In that case, sleptons affect the decay $\tilde{\chi}_2^0 \to \ell^{\pm}\tilde{\ell}^{\mp} \to \ell^{\pm}\ell^{\mp}\tilde{\chi}_1^0$. The resulting dilepton distribution, in principle, contains information about the slepton mass $m_{\tilde{\ell}}$. This situation is complicated by the fact that $\tilde{\chi}_2^0$ can also decay through a real or virtual Z: $\tilde{\chi}_2^0 \to Z\tilde{\chi}_1^0 \to \ell^{\pm}\ell^{\mp}\tilde{\chi}_1^0$. The Feynman diagrams for both decay channels are shown in Figure 4.7.1. In the next subsection we investigate the process $\tilde{\chi}_2^0 \to \ell^{\pm}\ell^{\mp}\tilde{\chi}_1^0$ in detail.

Slepton Masses through Neutralino Decays

What is the observable in these events that is sensitive to the slepton mass? We consider the dilepton invariant mass distribution, $m_{\ell\ell}$, in this analysis. It is already known that the endpoint

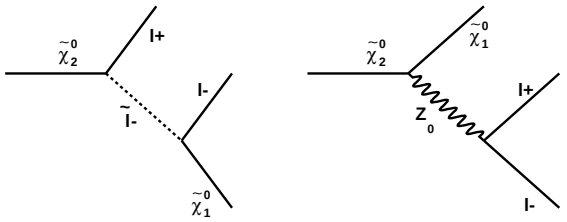

Fig. 4.7.1: Feynman diagrams for $\tilde{\chi}_2^0 \to \tilde{\ell}^{\pm}\ell^{\mp} \to \ell^{\pm}\ell^{\mp}\tilde{\chi}_1^0$ and $\tilde{\chi}_2^0 \to Z\tilde{\chi}_1^0 \to \ell^{\pm}\ell^{\mp}\tilde{\chi}_1^0$.

of the $m_{\ell\ell}$ spectrum contains information about the masses of the real particles involved in the decay [304].

- If the decay occurs through a real Z, $\tilde{\chi}_2^0 \to Z\tilde{\chi}_1^0 \to \ell^{\pm}\ell^{\mp}\tilde{\chi}_1^0$, then almost all such events will occur in the Z mass peak, and the endpoint information will be lost.
- In the case of a virtual intermediate particle ($\tilde{\chi}_2^0 \to Z^*\tilde{\chi}_1^0 \to \ell^{\pm}\ell^{\mp}\tilde{\chi}_1^0$ or $\tilde{\chi}_2^0 \to \tilde{\ell}^{\pm *}\ell^{\mp} \to \ell^{\pm}\ell^{\mp}\tilde{\chi}_1^0$), this process is a three-body decay and the endpoint value is:

$$m_{\ell\ell,max} = m_{\tilde{\chi}_2^0} - m_{\tilde{\chi}_1^0}\,. \tag{4.7.1}$$

- Finally, if the decay is through a real slepton ($\tilde{\chi}_2^0 \to \ell^{\pm}\tilde{\ell}^{\mp} \to \ell^{\pm}\ell^{\mp}\tilde{\chi}_1^0$), the endpoint is at:

$$m_{\ell\ell,max} = \sqrt{\frac{\left(m_{\tilde{\chi}_2^0}^2 - m_{\tilde{\ell}}^2\right)\left(m_{\tilde{\ell}}^2 - m_{\tilde{\chi}_1^0}^2\right)}{m_{\tilde{\ell}}^2}}. \tag{4.7.2}$$

The endpoint can be measured; however, its interpretation is ambiguous since it is not known *a priori* which formula is applicable (Eqn. 4.7.1 or Eqn. 4.7.2). More information is contained in the $m_{\ell\ell}$ distribution than just the value of the endpoint. One would expect the shapes of the Z and $\tilde{\ell}$ mediated distributions to be different. Furthermore, the shape of the total decay distribution (including both Z and $\tilde{\ell}$ contributions) changes as a function of the slepton mass. The slepton mass dependence is illustrated in Fig. 4.7.2, where the dilepton invariant mass distribution resulting from the interference of the Z and $\tilde{e}_R$-mediated diagrams is shown. Since the kinematic endpoint is kept fixed, this illustrates that the endpoint analysis is largely insensitive to the slepton mass. In all four cases, the slepton is virtual, but there exists a clear difference in the shape of the distribution. This implies that virtual slepton masses can be determined by studying the shape of the decay distributions. In the case of two-body decay through a real slepton, the $m_{\ell\ell}$ distribution will be triangular [305, 306].

4.7.2 Neutralino decay distributions at the LHC

We asssume in this analysis that LHC experiments have observed the dilepton mass distribution and have measured a kinematic endpoint at 59 GeV. What are the implications of this measurement for

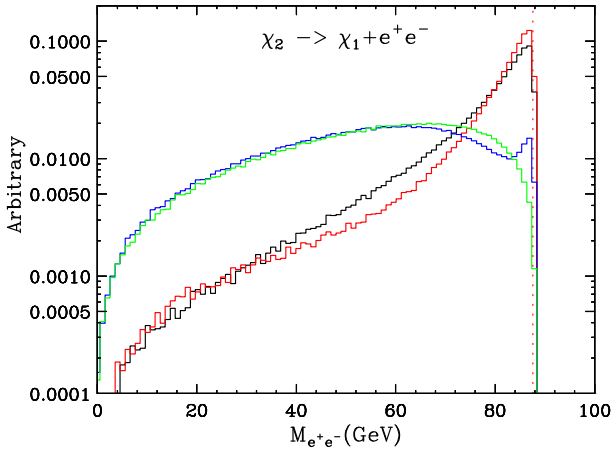

Fig. 4.7.2: $M_{e^+e^-}$ distributions for different selectron masses. We consider only the Z- and $\tilde{e}_R$-mediated diagrams. All parameters are held fixed except for $m_{\tilde{e}_R}$. The (green, blue, red, black) line is for a (300, 500, 1000 GeV, and ∞) mass selectron. The neutralino masses, $m_{\tilde{\chi}_1^0}$ and $m_{\tilde{\chi}_2^0}$, are kept constant, and their difference is 88 GeV.

the SUSY mass spectrum? Generally speaking, this reduces the parameter space by one degree of freedom. This is illustrated in Fig. 4.7.3, where a two-dimensional slice of the mSUGRA parameter space is defined by fixing $A_0 = 0$ and $\tan\beta = 10$. The measurement of the kinematic endpoint reduces the two-dimensional parameter space to one-dimensional line segments. These are the

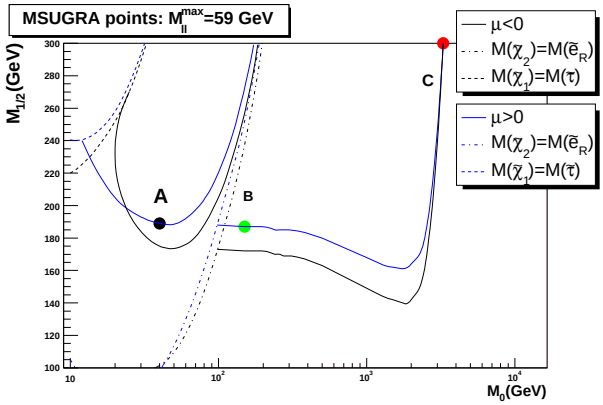

Fig. 4.7.3: Slepton mass determination in a slice of mSUGRA parameter space with $A_0 = 0$ and $\tan\beta = 10$. Here M_0 ($M_{1/2}$) is the universal scalar (gaugino) mass parameter. The effect on mSUGRA parameter space of fixing the dilepton kinematic endpoint of the $\chi_2^0 \to e^+e^-\chi_1^0$ decay to be $m_{\ell\ell,max} = 59$ GeV.

solid lines in Fig. 4.7.3. In mSUGRA, there is also the binary choice of $\mu > 0$ or $\mu < 0$, and their respective results are shown in blue and black. The dashed lines in the upper left corner indicate where $m_{\tilde{\chi}_1^0} = m_{\tilde{\tau}_1}$. Any points to the left of these lines are ruled out by constraints on charged dark matter. The dashed-dotted lines running through the middle of the plot indicate where $m_{\tilde{e}_R} = m_{\tilde{\chi}_2^0}$. This is where the slepton-mediated neutralino decays change from being three-body ($\tilde{e}_R$ is virtual

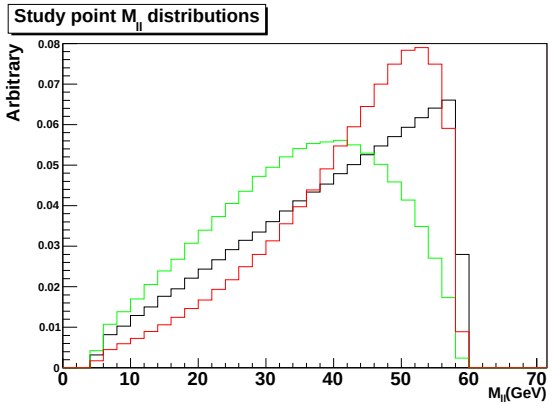

Fig. 4.7.4: Color-coded distributions for the 3 study points from Fig. 4.7.3. Points A, B, and C are shown in black, green, and red respectively. The distributions are normalized to one. Details are explained in the text.

to the right of these lines) to two-body ($\tilde{e}_R$ is real to the left of these lines). The three points labeled in Fig. 4.7.3 are the study points analyzed for this analysis. Point A is a low-mass SUSY point in which $m_{\tilde{l}_R} < m_{\tilde{\chi}_2^0}$, so that the decay channel through a real slepton is open. Point B is also a low mass point, however $m_{\tilde{l}_R} > m_{\tilde{\chi}_2^0}$ and therefore the real decay channel is closed. Finally, point C is a high-mass SUSY point which can decay only through virtual slepton or Z boson channels. This difference in the SUSY scale of point C is obvious in the rate of production shown in the Table 4.7.1.

The plot in Fig. 4.7.4 shows the invariant mass distribution expected from $\tilde{\chi}_2^0$ decays for the the three study points described above. These distributions are normalized to one so that their shapes may be compared. The black line displays the triangular shape of $\tilde{\chi}_2^0$ decay through a real slepton. Also, note the extreme difference in shape between the two virtual decays (red and green lines). ISAJET 7.69 [197] is employed for this and all other Monte Carlo-generated results in the analysis.

Event Rate

Depending on the SUSY model, and the particular point in its parameter space, SUSY events expected during the life of the LHC can vary by many orders of magnitude. The mSUGRA production cross sections, as well as the number of events expected for 10 fb^{-1} for the three study points for this analysis and dominant SM background ($t\bar{t}$ production) can be found in Table 4.7.1.

ID efficiencies, jet clustering, and energy smearing

As mentioned above, it was shown in a previous work that with reasonable statistics and a perfect detector it is possible to discriminate quite well between the regions of parameter space based on the shape of $m_{\ell\ell}$ distributions [303]. Here, major detector effects are included to study their affect on these distributions.

We include particle-level jet clustering, lepton ID efficiencies, and smearing parameteriza-

Point	M_0	$M_{\frac{1}{2}}$	$M_{\tilde{\ell}}$	σ	N(10fb^{-1})
A	40GeV	189 GeV	92 GeV	170 pb	$1.7 * 10^6$
B	150GeV	187 GeV	96 GeV	150 pb	$1.5 * 10^6$
C	3280GeV	300 GeV	3277 GeV	4.4 pb	44,000
$t\bar{t}$ (SM background)	NA	NA	NA	425 pb	$4.25 * 10^6$

Table 4.7.1: Event rates for mSUGRA study points at the LHC. All SUSY points have $\mu > 0$, $A_0 = 0$ and $tan(\beta) = 10$. In the second and third columns we show the point in the $(M_0, M_{\frac{1}{2}})$ plane. The forth column contains the mass of the lightest slepton. The total inclusive SUSY cross section as well as number of events produced for 10 fb^{-1} of integrated luminosity is also included.

tions for the muon, electron, photon, and jets. A basic cone algorithm ($R_{cone} = 0.7$) was used to combine all stable hadronically-interacting particles into jets. The jet energy was then conservatively smeared according to $\frac{\Delta E}{E} = \frac{120\%}{\sqrt{E}} + 7\%$, where E is in units of GeV. It should be noted that jets are used in this anlysis only as a tool to cut out the SM background. Their definitions affect only the signal multiplicity and the signal to background ratio. Jet characteristics do not affect the shapes of the distributions studied. A 90% ID efficiency was used for leptons. Photons and electrons were smeared according to $\frac{\Delta E}{E} = \frac{5\%}{\sqrt{E}} + 0.5\%$, with E given in GeV. Muons with $|\eta| < 1$ were smeared according to $\frac{\Delta P}{P} = .01\%P + 1\%$ while muons with $|\eta| > 1$ were smeared by $\frac{\Delta P}{P} = .04\%P + 2\%$, where P is in units of GeV. Missing transverse energy is calculated by taking the magnitude of the vector E_T sum of all leptons, photons, and jets reconstructed in the event.

Backgrounds and kinematic cuts

Variable	Cuts
N_{jets}(P$_T$ >50GeV, $\|\eta\|$ <2)	4
N_{jets}(P$_T$ >100GeV, $\|\eta\|$ <2)	1
$\not{E}_T$	max(100GeV,.2M_{eff})
N_{leps}(P$_T$ >20GeV, $\|\eta\|$ <2.5)	2 (opposite sign)

Table 4.7.2: Base Cuts

In this analysis, there are two main types of backgrounds to be considered: those which come from the Standard Model, and those which arise from SUSY processes. In general, any SM or SUSY process which contains opposite-sign lepton pairs in the final state must be considered. After applying the standard set of cuts shown in Table 4.7.2, $t\bar{t} \rightarrow W^+W^-$ is the dominant SM background. The events surviving these base cuts as a function of $M_{\text{eff}} \equiv \not{E}_T + \sum_{i=1}^{4} P_{T_i}^{Jet}$ with 10 fb^{-1} of data are shown in Fig. 4.7.5. The total number of events surviving the base cuts are included in the legend for each sample. The low-mass slepton points (A and B) statistically dominate the background, while the the high-mass slepton point (point C) clearly needs more than 10 fb^{-1}

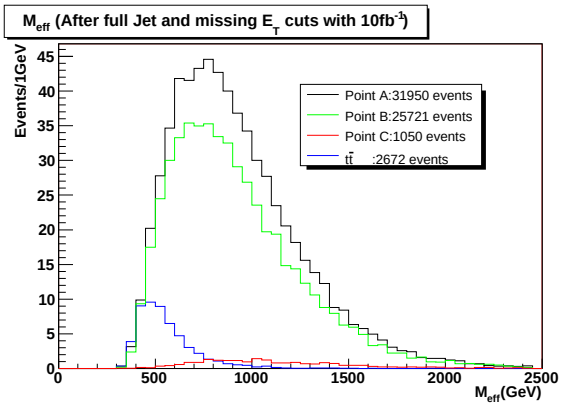

Fig. 4.7.5: The number of events per GeV surviving the base cuts of Table 4.7.2 versus M_{eff} for the low-mass virtual decay, real decay, and the high mass-points, as well as the $t\bar{t}$ background. The total number of events surviving the cuts appears in the legend for each sample.

for any statistical study. A cut on M_{eff} has not been included in the analysis but could be used to increase the significance. More luminosity as well as an optimized cut on M_{eff} will be necessary to apply this analysis to high slepton mass points (such as point C).

The cuts in Table 4.7.2 are designed to cut out SM events so exotic physics can be studied. However, lepton pairs that come from unrelated SUSY decays in the cascade are indistinguishable from the pairs which originate from a single neutralino decay. These SUSY background events will pass the base cuts with high efficiency, therefore they must be dealt with in a different manner than the Standard Model background.

Background subtraction

Both SUSY and SM backgrounds are uncorrelated in the sense that the opposite sign leptons do not originate from the decay of a single parent particle (except for the $Z \to \ell^+\ell^-$ decays). A *subtracted distribution* will be used to reduce both of these uncorrelated backgrounds. The idea is that $\mu^{\pm}e^{\mp}$ distributions will have the same rate and distribution as the uncorrelated $e^{\pm}e^{\mp}$ and $\mu^{\pm}\mu^{\mp}$ distributions [307]. Thus, distributions such as:

$$\left.\frac{d\sigma}{dM}\right|_{\text{sub}} = \left.\frac{d\sigma}{dM}\right|_{e^+e^-} + \left.\frac{d\sigma}{dM}\right|_{\mu^+\mu^-} - \left.\frac{d\sigma}{dM}\right|_{e^+\mu^-} - \left.\frac{d\sigma}{dM}\right|_{e^-\mu^+} \tag{4.7.3}$$

will be independent of these uncorrelated backgrounds.

Results

The goal of this work is to extract information from the shape of the invariant mass distributions. An immediate concern is whether or not this subtraction method preserves the shape of the distribution.

Fig. 4.7.6 puts this concern to rest. The reconstructed invariant mass distributions for all opposite-sign electron pairs added to the same distribution for opposite-sign muon pairs is shown

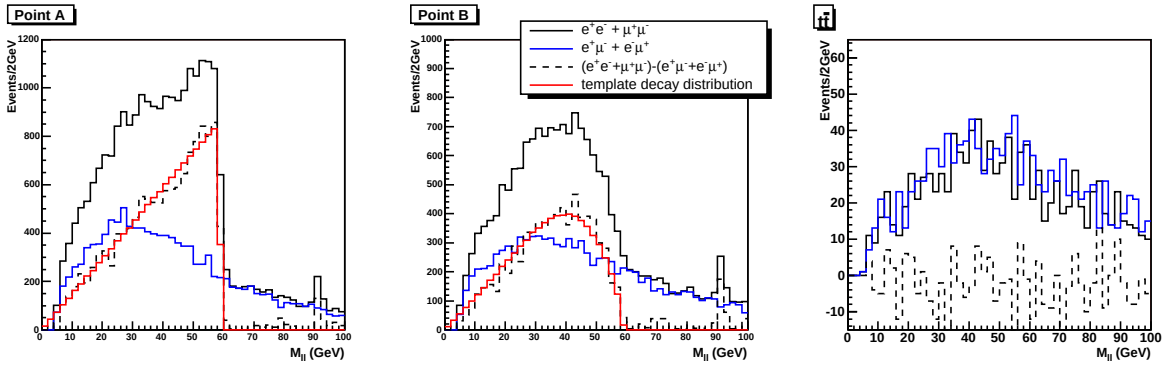

Fig. 4.7.6: The plots show the various lepton pair distributions, as well as, the subtracted and template distributions for points A and B and the $t\bar{t}$ background. For points A and B, the template distributions(red line) match the subtracted distributions (black dashed line) quite well. See the text for more information.

in solid black. This distribution contains signal events as well as SUSY background. In solid blue, the opposite-sign invariant mass distributions of opposite+sign electron–muon mixed pairs are shown. This distribution should be similar to the opposite-sign same-flavor SUSY background as long as $M_{\tilde{\mu}} \simeq M_{\tilde{e}}$. The dotted black line is the subtracted distribution defined in Eq. 4.7.3 (solid black minus solid blue). This distribution should be independent of the SUSY background and represents experimental results after background subtraction with 10 fb^{-1} of LHC data. The actual decay distribution (template distribution) for the SUSY point is shown in red. This template represents the theoretical distribution expected without any cuts, smearing, or misidentification. The template distribution is normalized to the subtracted distribution over the range 0–60 GeV. The subtracted distribution of Fig. 4.7.6 matches the shape of the template quite well for the two low-mass points: A (left) and B (center). Finally, shown on the right of Fig. 4.7.6 is the invariant mass distribution for the $t\bar{t}$ background. The subtraction method effectively reduces this background to zero (within statistical fluctuations).

Several conclusions may be drawn from these results:

- The subtraction method does not distort the shape of the invariant mass distribution of the decay products of the $\tilde{\chi}_2^0$, or any other correlated lepton pair contribution (notice that the Z peak survives).
- Smearing effects from the detector do not distort the shape of the invariant mass distribution of the decay products of the $\tilde{\chi}_2^0$.
- With as little at 10 fb^{-1} of integrated luminosity, an analysis based on shapes of lepton pairs' invariant mass distributions will be possible in the case of a light slepton at the LHC (points A and B).
- The subtraction method described above is relevant for both standard model and SUSY background subtractions.

As stated above, if the slepton is heavy (point C), it is clear from Fig. 4.7.5 that it is not pos-

sible to do a shape analysis without more luminosity and a further optimization of cuts. Therefore, this point is not included in Fig. 4.7.6.

4.7.3 Conclusions

In this report we addressed the importance of measuring slepton masses at the LHC. An inability to significantly bound the slepton masses would introduce large uncertainties into any subsequent calculation of the neutralino dark matter abundance. Dilepton invariant mass distributions from neutralino decays were identified as one avenue for determining slepton masses at the LHC. We investigated the decay $\tilde{\chi}_2^0 \rightarrow e^+e^-\tilde{\chi}_1^0$ for a specific value of the dilepton kinematic endpoin, performing an analysis in the mSUGRA paradigm with $A_0 = 0$ and $\tan\beta = 10$ – though this analysis is clearly extendible to more general theories. In a previous note it was shown that whether the intermediate slepton is real or virtual can be determined based on the shape of the lepton pair invariant mass distribution. This provides one clean bound on the slepton mass. In the case of light virtual sleptons, one can place significant lower and upper bounds on the slepton mass. For very heavy virtual sleptons, only a lower bound can be placed. However, this bound is generally above 1 TeV, except for the case of cancellation between Z and slepton diagrams with $\mu < 0$. This work extends the previous analysis to include detector affects, dominant backgrounds, and realistic event rates for the LHC. We conclude that statistics will be reasonable for studies if the slepton is light (points A and B) with as little at 10 fb^{-1} of integrated luminosity. Furthermore, the shape of the lepton invariant mass distribution is not distorted due to the background subtraction methods described or major detector effects included in the simulation. This result adds reassurance that constraints on the slepton mass based on the shape of invariant mass distributions from neutralino decays will be a useful technique at the LHC.

Further studies are needed to determine mass constraints based on the results including detector simulation and background subtraction. In addition, more effort will extend this method to the general MSSM. Furthermore, the exact extent to which this measurement assists the determination of the neutralino dark matter density needs to be quantified.

4.8 Light stop searches

Sabine Kraml[1] *and Are R. Raklev*[1,2]
[1] *CERN, Geneva, Switzerland*
[2] *University of Bergen, Norway*

If searches at the Tevatron find an excess in $c\bar{c}\,\not{E}_T$ events, this will hint at a light stop with $m_{\tilde{t}_1} \lesssim m_t$, decaying into $c\tilde{\chi}_1^0$. The nature of this excess may be confirmed at the LHC using the signature of 2b-jets + 2 same-sign letpons + jets + $\not{E}_T$, stemming from gluino-pair production followed by gluino decays into top and stop.

4.8.1 Introduction

Within the MSSM, electroweak baryogenesis motivates a very light $\tilde{t}_1$ with $m_{\tilde{t}_1} \lesssim m_t$ [308, 309, 310, 311]; see also Sec. 4.9. The Tevatron reach for such a light stop was studied in Ref. [312]. It was found that if the $\tilde{t}_1$ decays into $c\tilde{\chi}_1^0$, giving a signature of $c\bar{c} + \not{E}_T$, the Tevatron can cover the baryogenesis-motivated region with 4 fb^{-1} of integrated luminosity provided the $\tilde{t}_1$–$\tilde{\chi}_1^0$ mass difference is large enough, that is $\gtrsim 30$ GeV, see Fig. 4.8.1. For smaller mass differences, especially in the stop coannihilation region where $m_{\tilde{t}_1} - m_{\tilde{\chi}_1^0} \lesssim 25$ GeV, the c-jets are too soft and hence the number of events not significant enough for a discovery.

Should an excess of c-jets plus missing energy events be observed at the Tevatron, this will trigger dedicated searches for light stops at the LHC. Although stop pair production has a large cross section in the interesting mass range (see Table 4.8.1) the signal will be buried in the background at the LHC. Moreover, an interpretation of $c\bar{c}\not{E}_T$ as a signal of light stops is equivocal, and gives only weak bounds on the stop mass. The alternative at the LHC is to exploit gluino pair production with the gluinos decaying into top and stop as proposed in Ref. [313, 314]: since gluinos are Majorana particles, they can decay either into $t\tilde{t}_1^*$ or $\bar{t}\tilde{t}_1$. Pair-produced gluinos therefore give same-sign top quarks in half of the gluino-to-stop decays. If the stops decay into $c\tilde{\chi}_1^0$ and the W's from the $t \to bW$ decay leptonically, we obtain

$$pp \to \tilde{g}\tilde{g} \to bb\,l^+l^+ \,(\text{or } \bar{b}\bar{b}\,l^-l^-) + \text{jets} + \not{E}_T\,. \tag{4.8.1}$$

This peculiar signature has little background and could be used to prove that the Tevatron excess of $c\bar{c}\not{E}_T$ indeed originated from $\tilde{t}_1\tilde{t}_1^*$ production.

4.8.2 Simulation and Results

To demonstrate the use of the signature in Eq. (4.8.1), we performed a case study for the LST1 benchmark point with $m_{\tilde{g}} = 660$ GeV, $m_{\tilde{t}_1} = 150$ GeV, and $m_{\tilde{\chi}_1^0} = 105$ GeV. All other squarks (in particular the sbottoms) are taken to be heavier than the gluinos. This suppresses the SUSY background, and gluinos decay to 100% into $t\tilde{t}_1$. Sleptons are also assumed to be fairly heavy, $m_{\tilde{l}} \sim 250$ GeV. A neutralino relic density within the WMAP bound is achieved by annihilation

$m_{\tilde{t}_1}$ [GeV]	120	130	140	150	160	170	180
$\sigma(\tilde{t}_1\tilde{t}_1^*)$, Tevatron	5.43	3.44	2.25	1.50	1.02	0.71	0.50
$\sigma(\tilde{t}_1\tilde{t}_1^*)$, LHC	757	532	382	280	209	158	121

Table 4.8.1: NLO cross sections in pb for $\tilde{t}_1$ pair-production at the Tevatron and the LHC, computed with PROSPINO2 [315].

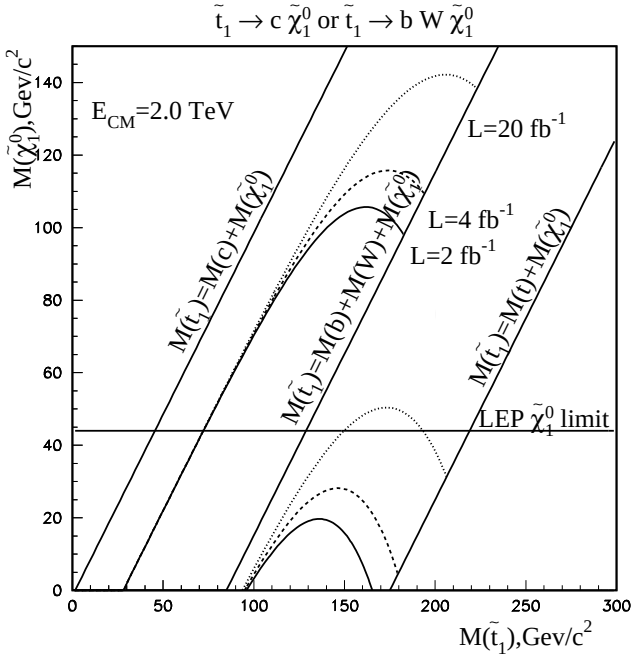

Fig. 4.8.1: Tevatron reach for a light stop, from Ref. [312].

through a Higgs for $m_A = 250$ GeV. Assuming BR$(\tilde{t}_1 \to c\tilde{\chi}_1^0) \simeq 1$, experiments at the Tevatron should see a clear excess in the $c\bar{c} + \not{E}_T$ channel for this scenario [312].

At the LHC, gluino pair production has a cross section of 5.4 pb at LST1. We generated events equivalent to 30 fb^{-1} of integrated luminosity with PYTHIA 6.321[7]. The events were run through the detector simulation program AcerDET 1.0 [316] to simulate a generic LHC detector. In the SM background we included $t\bar{t}$, W+jet, Z+jet, $WW/WZ/ZZ$ and QCD $2 \to 2$ events, assuming that FCNCs are too small to lead to significant same-sign top production. Other sources of SM background were found to be negligible; see Ref. [313] for details on the simulation and the LST1 benchmark point. We applied the following cuts to isolate the signal:

- Two same-sign leptons (e or μ) with $p_T^{\rm lep} > 20$ GeV.
- At least four jets with $p_T^{\rm jet} > 50$ GeV, at least two of which are b-tagged.[32]

[32]We assume a b-tagging efficiency of 43%. Light-jet rejection is set according to the p_T parametrization for a low

Cut	2lep 4jet	$p_T^{\rm lep}$	$p_T^{\rm jet}$	$2b$	$\not{E}_T$	$2t$	SS
$\tilde{g}\tilde{g}$ signal	10839	6317	4158	960	806	628	330
SUSY bkgd	1406	778	236	40	33	16	5
SM bkgd	25.3M	1.3M	35977	4809	1787	1653	12

Table 4.8.2: Number of events left for 30 fb^{-1} of data after each stage of cuts.

- Missing transverse energy $\not{E}_T > 100$ GeV.
- Two combinations of the two hardest leptons and b-jets with $m_{bl} < 160$ GeV.

The effects of these cuts are summarized in Table 4.8.2: "2lep 4jet" is the cut on two leptons and four jets; "2b" the requirement of two b-jets; "$\not{E}_T$" the cut on missing transverse energy and "SS" the requirement of two same-sign leptons. Note the central importance of the same-sign cut in removing the SM background, which at that point consists only of $t\bar{t}$ events. The cuts on transverse momentum and invariant mass "$2t$" were used to further reduce the background. We find that the signature of Eq. (4.8.1) is easily separated from both SM and SUSY backgrounds.

Isolating this same-sign top signature at the LHC would strengthen the interpretation of the signal observed at the Tevatron. The next aim would be to measure the masses of the newly discovered particles. With the missing energy and momentum of the neutralino, reconstruction of a mass peak would be impossible. The well-studied alternative to this [304, 199, 200, 318, 201], is to use the SM decay products' invariant-mass distributions. Their endpoints can be given in terms of the SUSY masses, and these equations can then in principle be solved to give the masses. However, among the four possible endpoints, one is simply a relationship between SM masses, and two are linearly dependent, so that we are left with three unknown masses and only two equations. Also, because of the information lost with the escaping neutrino, the distributions of interest all fall very gradually to zero. Determining exact endpoints in the presence of background, taking into account smearing from the detector, etc., would be be very difficult.

We attacked this problem with an extension of the endpoint method, deriving the complete shapes of the invariant-mass distributions for m_{bc} and m_{lc}; for details see Ref. [313]. Fitting to the whole invariant mass distribution greatly reduces the uncertainty involved in endpoint determination, and may give additional information on the masses. Extending this method to include spin effects propounds the possibility of comfirming the scalar nature of the stop. Fitting to the m_{bc} and m_{lc} distributions can in principle be used to determine both of the two linearly independent parameters

$$(m_{bc}^{\max})^2 = \frac{(m_t^2 - m_W^2)(m_{\tilde{t}_1}^2 - m_{\tilde{\chi}_1^0}^2)(m_1^2 + m_2^2)}{2m_t^2 m_{\tilde{t}_1}^2} \quad \text{and} \quad a = \frac{m_2^2}{m_1^2}, \tag{4.8.2}$$

luminosity environment, given in Ref. [317].

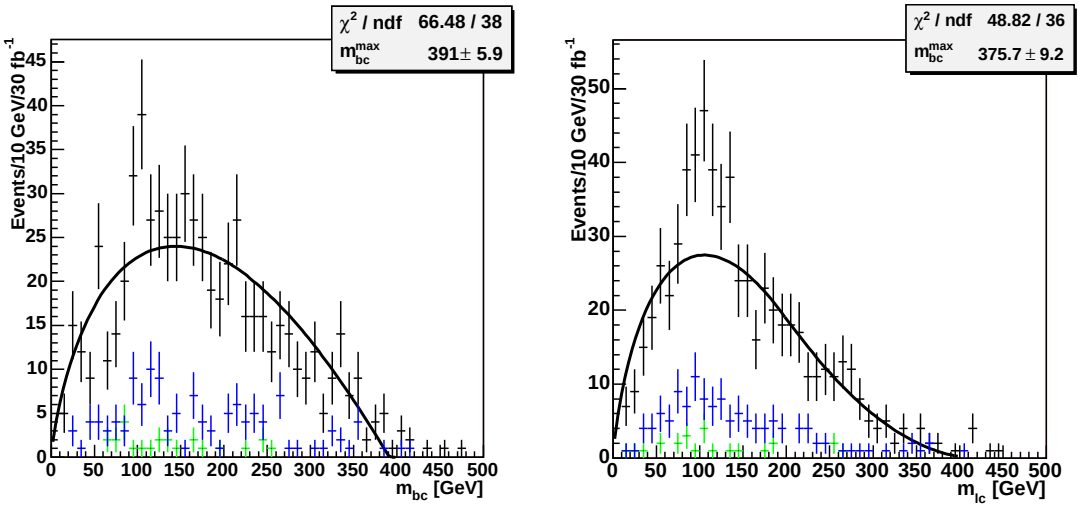

Fig. 4.8.2: Invariant-mass distributions m_{bc} (left) and m_{lc} (right) for LST1, together with fits of the calculated distributions. Also shown are the contributions from the SM background (green) and the SUSY background (blue).

where

$$m_1^2 = m_{\tilde{g}}^2 - m_t^2 - m_{\tilde{t}_1}^2 \quad \text{and} \quad m_2^4 = m_1^4 - 4m_t^2 m_{\tilde{t}_1}^2 . \tag{4.8.3}$$

For light stops, models typically have $m_t m_{\tilde{t}_1} \ll m_{\tilde{g}}^2$ and hence $a \approx 1$. The distributions are sensitive to such values only at very low invariant masses, so that a cannot be determined in our case. We shoe the m_{bc} and m_{lc} distributions for LST1, and the fits to them, in Fig. 4.8.2.

In fitting the m_{bc} and m_{lc} distributions, the b-jets and leptons are paired through the cut on invariant mass. In some events the W decays to a tau, which in turn decays leptonically; these events are an additional, irreducible background to our distributions. The likelihoods in the b-tagging routine should help to discriminate c-jets from other jets. We assume a 20% probability of identifying a c-jet directly from the b-tagging likelihood. For events where one or both c-jets are missed, they are chosen as the two hardest remaining jets with $p_T^{\text{jet}} < 100$ GeV. This upper bound is applied to avoid picking jets from the decay of heavy squarks. Note that the c-jets are expected to be relatively soft if our signal exists and, depending on the $\tilde{t}_1$–$\tilde{\chi}_1^0$ mass difference, the final results are somewhat sensitive to the exact value of this cut. Information from the Tevatron on the kinematic distribution of the excess c-jets can hence be helpful for determining the appropriate value. Finally, our c-jet candidates are paired to the top candidates by their angular separation, and by requiring consistency with the endpoints of the invariant-mass distributions we are not looking at. The precision of our mass determination is limited by systematics from these issues and others that affect the distributions, such as final-state radiation, finite-width effects and cuts.[33]

The combined result of the two distributions, with statistical error, is $m_{bc}^{\max} = 389.8 \pm$

[33] For a more thorough discussion of these issues, details on deriving invariant-mass distributions in cascade decays, and the possible inclusion of spin effects, see Ref. [305].

5.3 GeV, which compares well to the nominal value of 391.1 GeV. However, the quality of the fits are rather low, with large χ^2 values, and the two separate results lie on either side of the nominal value, fortuitously cancelling, indicating that the systematic errors can be significant. All in all, additional information, e.g. a measurement of the effective-mass scale of events, would be necessary to determine the masses of the SUSY particles involved, in particular the mass of the light stop.

Finally, we want to comment on the robustnest of our method. We checked that the signal of Eq. (4.8.1) remains significant enough for a 5σ discovery for gluino masses up to $m_{\tilde{g}} \sim 900$ GeV and for sbottom masses lighter than the gluino. We also checked that lowering the stop mass to $m_{\tilde{t}_1} = 120$ GeV does not considerably reduce the significance of the signal. This implies that the same-sign signature can be used to search for a light stop even in the stop-coannihilation region.

4.8.3 Conclusions

If experiments at the Tevatron discover a light stop in the channel $p\bar{p} \to \tilde{t}_1\tilde{t}_1^* \to c\bar{c} + \not{E}_T$ (or see a significant excess of $c\bar{c} + \not{E}_T$ events), this may be confirmed at the LHC using gluino pair production followed by gluino decays into top and stop. The signature of 2 b-jets + 2 same-sign leptons + jets + $\not{E}_T$ discussed in this contribution has little background and will help determine whether what has been discovered is indeed a light scalar top. The kinematic distribution of the c-jets in the Tevatron signal may be useful for reducing systematic errors from mistagging at the LHC.

Acknowledgements

S.K. is supported by an APART (Austrian Programme of Advanced Research and Technology) grant of the Austrian Academy of Sciences. A.R.R. acknowledges support from the Norwegian Research Council and the European Community through a Marie Curie Fellowship for Early Stage Researchers Training.

4.9 Tevatron-LHC-ILC synergy: light stops, baryogenesis and dark matter

Csaba Balázs[1], Marcela Carena[2], Arjun Menon[1,3], David E. Morrissey[4] and Carlos Wagner[1,3]

[1]*Argonne National Laboratory*
[2]*Fermi National Accelerator Laboratory*
[3]*University of Chicago*
[4]*University of Michigan*

After highlighting the basics and the consequences of electroweak baryogenesis in the Minimal Supersymmetric Standard Model (MSSM), the viability that the MSSM simultaneously provides the measured baryon asymmetry and dark matter abundance is summarized. Examining a few benchmark points within this scenario, we demonstrate a synergy between the Tevatron, the LHC and the ILC.

4.9.1 Electroweak baryogenesis and neutralino dark matter

The cosmological energy density of both main components of matter, baryons and dark matter, is known with a remarkable precision [257]. In units of the critical density $\rho_c = 3H_0^2/(8\pi G_N)$[34], they are:

$$\Omega_B h^2 = 0.0224 \pm 0.0009 \quad \text{and} \quad \Omega_{DM} h^2 = 0.1126^{+0.0161}_{-0.0181} \,. \tag{4.9.1}$$

at 95% CL. According to the observations, the baryon density is dominated by baryons while anti-baryons are only secondary products in high energy processes. The source of this baryon–anti-baryon asymmetry is one of the major puzzles of particle physics and cosmology.

Assuming that inflation washes out any initial baryon asymmetry after the Big Bang, there should be a dynamic post-inflation mechanism to regenerate the asymmetry. Any microscopic mechanism for baryogenesis must fulfill the three Sakharov requirements [319]:

- $\mathrm{baryon\ number\ (B)\ violation}$
- $\mathrm{CP\ violation}$
- $\mathrm{departure\ from\ equilibrium.}$

These requirements are satisfied in the MSSM during the electroweak phase transition. This is the basis for electroweak baryogenesis (EWBG) [320, 321, 322, 323, 324]. Baryon number violation occurs in the MSSM due to quantum transitions between inequivalent SU(2) vacua that violate $(B+L)$ [325]. These transitions are exponentially suppressed at low temperatures in the electroweak broken phase [326, 327], but become active at high temperatures when the electroweak symmetry is restored [328, 329, 330, 331, 332]. If the electroweak phase transition is first order, bubbles of broken phase nucleate within the symmetric phase as the universe cools below the critical temperature. These provide the necessary departure from equilibrium.

[34] $H_0 = h \times 100\ km/s/Mpc$ is the present value of the Hubble constant, $h = 0.71^{+0.04}_{-0.03}$, and G_N is Newton's constant.

To generate the observed baryon asymmetry the electroweak phase transition has to be *strongly* first order [333],

$$v(T_c)/T_c \gtrsim 1\,, \tag{4.9.2}$$

where $v(T_c)$ denotes the Higgs vacuum expectation value at the critical temperature T_c.

For sufficiently light Higgs bosons, a first-order phase transition can be induced by the loop effects of light bosonic particles, with masses of the order of the weak scale and large couplings to the Higgs fields. Within the MSSM the most important contribution comes from a light stop. Detailed calculations show that for the mechanism of electroweak baryogenesis to work, the lightest stop mass must be less than the top mass but greater than about 120 GeV to avoid color breaking minima. Simultaneously, the Higgs boson involved in breaking the electroweak symmetry must be lighter than 120 GeV [334, 335, 336, 337, 338, 339, 309, 340, 341, 342, 343, 344], and only slightly above the present experimental bound [345],

$$m_h \gtrsim 114\ \text{GeV}\,, \tag{4.9.3}$$

which is valid for a Standard Model (SM) Higgs boson.

To avoid generating too large a contribution to $\Delta\rho$, the light stop must be mostly right-handed. Since the stops generate the most important radiative contribution to the Higgs boson mass in the MSSM [346, 347, 348], the other stop must be considerably heavier in order to raise the Higgs boson mass above the experimental bound, Eq. (4.9.3). For the stop soft supersymmetry breaking masses, this implies [309]

$$m_{U_3}^2 \lesssim 0 \quad \text{and} \quad m_{Q_3}^2 \gtrsim (1\ \text{TeV})^2\,. \tag{4.9.4}$$

where U_3 (Q_3) is the soft mass of the third-generation electroweak singlet up-type (doublet) scalar quarks at the electroweak scale. A similar balance is required for the combination of soft SUSY breaking parameters defining the stop mixing [309]:

$$5 \lesssim \tan\beta \lesssim 10 \quad \text{and} \quad 0.3 \lesssim |A_t - \mu^*/\tan\beta|/m_{Q_3} \lesssim 0.5\,. \tag{4.9.5}$$

In addition to a strong electroweak phase transition, a CP-violating source is needed to generate a chiral charge asymmetry. This translates into the following bounds on the chargino sector:

$$|\arg(\mu\, M_2)| \gtrsim 0.1 \quad \text{and} \quad \mu, M_2 \lesssim 500\ \text{GeV}\,. \tag{4.9.6}$$

These conditions are relevant to the abundance of neutralino dark matter, since the masses and mixing in the neutralino (and chargino) sector are directly affected by the value of the soft gaugino masses (M_i) and the higgsino mass parameter (μ) at the weak scale.

Low energy supersymmetry also provides a natural solution to the origin of dark matter in the form of the lightest supersymmetric particle (LSP). In this summary, we consider only the case where the LSP is the lightest neutralino. To assess the viability of simultaneous generation of

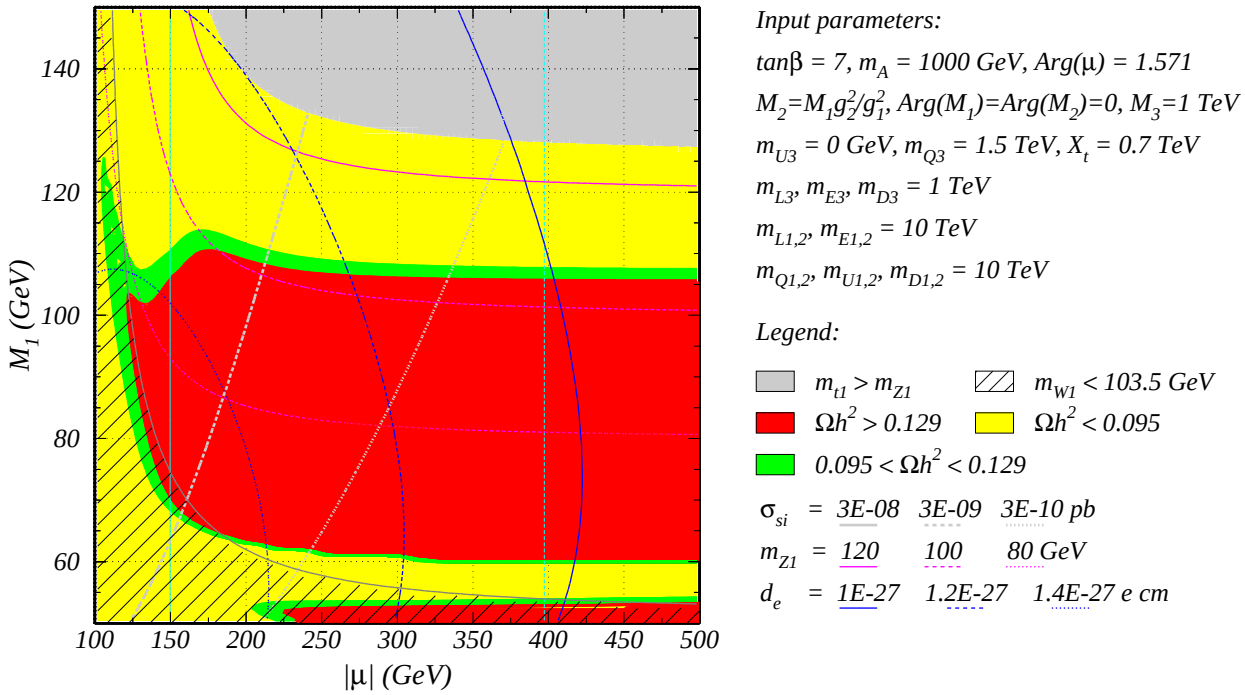

Fig. 4.9.1: Neutralino relic density as a function of M_1 vs. $|\mu|$ for $m_A = 1000$ GeV and $\arg(\mu) = \pi/2$.

the observed baryon–anti-baryon asymmetry and neutralino dark matter, we focus on the narrow parameter region of the MSSM defined by equations (4.9.3)-(4.9.6). As established earlier, in this parameter region EWBG is expected to yield the observed amount of baryon density of the Universe. To further simplify the analysis, we assume that the gaugino mass parameters M_1 and M_2 are related by the standard unification relation, $M_2 = (g_2^2/g_1^2)\, M_1 \simeq 2\, M_1$. The first and second generation sfermion soft masses are taken to be very large, $m_{\tilde{f}} \gtrsim 10$ TeV, to comply with the electron electric dipole moment (EDM) constraints in the presence of sizable phases.[35] Only a phase directly related to EWBG is introduced, namely $\arg(\mu)$, and for convenience we set the phases of A_f equal and opposite to it. For simplicity, we neglect the mixing between CP-even and CP-odd Higgs bosons due to these phases.

We compute the relic neutralino abundance as described in Ref. [349]. Fig. 4.9.1 shows the typical neutralino relic density dependence on $|\mu|$ and M_1 for typical parameters inspired by EWBG: $\tan\beta = 7$, $m_A = 1000$ GeV, and $\arg(\mu) = \pi/2$. The green (medium gray) bands show the region of parameter space where the neutralino relic density is consistent with WMAP at 95% CL. The regions in which the relic density is above or below this experimental bound are indicated by the red (dark gray) and yellow (light gray) areas, respectively. Finally, in the (medium-light) gray

[35] As was shown in Ref. [349], EDM limits strongly constrain the EWBG mechanism in the MSSM.

region at the upper right corner, the lightest stop becomes the LSP, while in the hatched area at the lower left corner the mass of the lightest chargino is lower than is allowed by LEP data[36].

In the upper allowed band the mass difference between the neutralino LSP and the light stop is less than about 20-25 GeV, and stop-neutralino coannihilation as well as stop-stop annihilation are very efficient in reducing the neutralino abundance. There is an area below the disallowed band in which the neutralino mass lies in the range 40-60 GeV and the neutralino annihilation cross section is enhanced by s-channel resonant h exchange. The relic density is also quite low for smaller values of $|\mu|$. In these regions, the neutralino LSP acquires a significant Higgsino component allowing it to couple more strongly to the Higgs bosons and the Z. For higher M_1 values, the lightest neutralino and chargino masses are also close enough that chargino-neutralino coannihilation and chargino-chargino annihilation substantially increase the effective cross section.

In summary, the requirement of a consistent generation of baryonic and dark matter in the MSSM leads to a well-defined scenario with a light stop and a light Higgs boson, light neutralinos and charginos, sizeable CP-violating phases, and moderate values of $5 \lesssim \tan\beta \lesssim 10$. These properties will be tested in a complementary way by the Tevatron, the LHC and a prospective ILC, as well as through direct dark matter detection experiments in the near future. The first tests of this scenario will probably come from electron EDM measurements, stop searches at the Tevatron and Higgs searches at the LHC within the next few years.

4.9.2 Tevatron-LHC-ILC synergy

A stop lighter than the top quark was and is being searched for at LEP and the Tevatron, respectively, in various decay modes. The Tevatron reach depends on the decay properties of the lightest stop, and also on the specific values of the light chargino and neutralino masses [350, 351, 352, 353, 354]. Here we focus on the case in which the neuralino is the lightest (LSP) and the lighter stop is the next-to-lightest supersymmetric partner (NLSP). In such a case, the Tevatron can find a light stop provided its mass is smaller than about 200 GeV [312], a region that overlaps substantially with the interesting one for EWBG.

To assess the light stop collider reach in the EWBG scenario, we conducted a random scan over the following range of MSSM parameters:[37]

$$-(80\ \mathrm{GeV})^2 < m^2_{\tilde{U}_3} < 0, \quad 100 < |\mu| < 500\ \mathrm{GeV}, \quad 50 < M_1 < 150\ \mathrm{GeV},$$
$$200 < m_A < 1000\ \mathrm{GeV}, \quad 5 < \tan\beta < 10\,. \tag{4.9.7}$$

The result of the scan, projected to the stop mass versus neutralino mass plane, is shown by Figure 4.9.2. The region where $m_{\tilde{Z}_1} > m_{\tilde{t}_1}$ is inconsistent with a neutralino LSP, while for $m_{\tilde{t}_1} > m_W + m_b + m_{\tilde{Z}_1}$ the three-body decay $\tilde{t}_1 \to W^+ \bar{b} \tilde{Z}_1$ becomes accessible and dominant. For

[36] See $http://lepsusy.web.cern.ch/lepsusy/www/inos\_moriond01/charginos\_pub.html$

[37] Parameters which are not scanned over are fixed as in the right side of Fig. 4.9.1.

models marked by dots the neutralino relic density is below or within the 2σ WMAP bound. The lower left corner is excluded by the LEP chargino mass limit of 103.5 GeV.

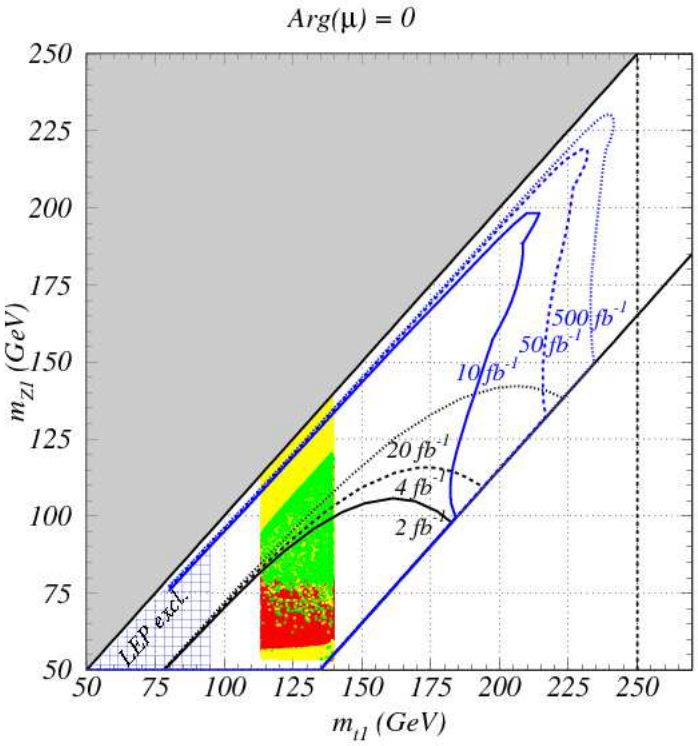

Fig. 4.9.2: Discovery reach of the Tevatron (black contours) and an ILC (blue contours) for production of light stop quarks in the decay channel $\tilde{t}_1 \to c\chi_1^0$.

Overlayed on Fig.4.9.2 is the Tevatron light stop search sensitivity in the $cc\not{E}_T$ channel for 2, 4 and 20 pb^{-1} pf integrated luminosity [312]. The Tevatron can cover a considerable region of parameter space of the EWBG-motivated scenario. In the Tevatron covered region, resonant annihilation via the light Higgs produces acceptable amount of dark matter. Coannihilation with the lightest stop is dominant where the stop-neutralino mass gap is small. As is apparent from the figure, under the present missing-energy triggering requirements, the Tevatron will not be able to detect a light stop in this region of parameter space. This region, on the other hand, is easily covered by even a 500 GeV ILC.

For the detailed exploration of the collider phenomenology in this scenario, the common strategy of selecting and analysing individual parameter space points, or benchmark points, was used at Les Houches in 2005. The benchmark points were defined taking into account the discussion of the parameter values presented in the previous section. All benchmark points were selected such that the baryon asymmetry of the universe and the relic neutralino density is predicted to be close to those measured by WMAP, and pass all known low energy, collider and astronomy con-

straints. The most important of these are the SUSY particle masses, the electron EDM, $B(b \to s\gamma)$, and direct WIMP detection. A crucial constraint is the LEP II Higgs boson direct exclusion mass limit of $m_h > 114.4$ GeV. In the calculations of the supersymmetric spectrum and the baryon asymmetry, we used tree-level relations except for the Higgs mass, which was calculated at one loop. In the parameter region of interest, the one-loop calculation results in about a 6-8 GeV lower lightest Higgs mass than the two-loop result [355, 356]. Thus, if the soft supersymmetric parameters defining the benchmark points are used in a two-loop calculation, the resulting lightest Higgs mass is found to be inconsistent with LEP II. A two-loop-level consistency with the LEP II limit can be achieved only when a baryon asymmetry calculation becomes available using two-loop Higgs boson masses.

The main difference between the Les Houches benchmark points lies in the mechanism that ensures the neutralino relic density also complies with WMAP. Keeping the unification-motivated ratio of the gaugino mass parameters M_2/M_1 close to 2 (together with the baryogenesis required $100 \lesssim |\mu| \lesssim 500$ GeV) induces a lightest neutralino with mostly bino admixture. A bino typically overcloses the universe, unless there is a special situation that circumvents this. For example, as in the supergravity-motivated minimal SUSY scenario mSUGRA, neutralinos can coannihilate with sfermions, resonantly annihilate via Higgs bosons, or acquire a sizable Higgsino admixture in special regions of the parameter space. This lowers the neutralino density to a level that is consistent with observation.

Benchmark point LHS-1 features strong stop-neutralino coannihilation which lowers the relic density of neutralinos close to the WMAP central value. Sizable coannihilation occurs only when the neutralino–stop mass difference is small, less than about $30 - 40\%$. A small neutralino-stop mass gap poses a challenge for the Tevatron and the LHC while an ILC could cover this region efficiently.

Point LHS-2, resonant annihilation of neutralinos via s-channel Higgs resonances lowers the neutralino abundance to the measured level. In this case, the neutralino mass must be very close to half of the lightest Higss boson mass. This point features a stop that, given enough luminosity, can be discovered at the Tevatron due to the large difference between the stop and the neutralino masses. Even the heavier stop can possibly be produced at the LHC together with the third generation sleptons. On the other hand, the resonance feature implies that the lightest Higgs boson can decay into neutralinos, which would reduce its visible width and therefore could make its discovery more challenging.

Point LHS-3 satisfies the WMAP relic density constraint partly because the lightest neutralino acquires some wino admixture and because it coannihilates with the lightest stop and chargino. The multiple effects lowering the relic density allow for a little larger neutralino-stop mass gap than in LHS-1. This point has a neutralino-stop mass gap that makes it detectable at the Tevatron and the LHC.

LHS-4, a variation of LHS-1, is defined in detail in Ref. [357]. Here the small neutralino-

stop mass difference makes the light stop inaccessible at the Tevatron and the LHC. On the other hand, an ILC could measure the parameters with precision. The discovery potential of this point is discussed in detail in Ref. [357].

In summary, the four benchmark points offer various challenges for the three colliders. The Tevatron could resolve the stop quark in points LHS-2 and LHS-3, where the $\tilde{t}_1$ decays into $\tilde{\chi}_1^{\pm} b$, but not in LHS-1 and LHS-4, where it decays into $\tilde{\chi}_1^0 c$ with a small phase space. The LHC on the other hand may explore LHS-1 and LHS-2 as described in the Les Houches 2005 proceedings. In principle these methods are also applicable for LHS-4 and LHS-3; the small mass differences at these points, however, make the analysis much more difficult. In LHS-1, LHS-2 and LHS-3 the LHC can pair produce the heavier stop, which is needed to pin down the stop sector so crucial for baryogenesis. At an ILC, one can perform precision measurements of the light stop. Moreover, the weak ino sector including the important phase(s) can be measured precisely (see Ref. [358] and references therein).

Acknowledgements

Research at the HEP Division of ANL is supported in part by the US DOE, Division of HEP, Contract W-31-109-ENG-38. Fermilab is operated by Universities Research Association Inc. under contract no. DE-AC02-76CH02000 with the DOE.

4.10 Discovering SUSY at the LHC with Same-Sign Di-Muons

Salavat Abdoulline[1]*, Darin Acosta*[2]*, Paolo Bartalini*[2]*, Richard Cavanaugh*[2]*, Alexey Drozdetskiy*[2]*, Sven Heinemeyer*[3]*, Andrey Korytov*[2]*, Guenakh Mitselmakher*[2]*, Yuriy Pakhotin*[2]*, Bobby Scurlock*[2]*, Georg Weiglein*[4]

[1] *Fermi National Laboratory, Chicago, IL, USA*

[2] *University of Florida, Gainesville, FL, USA*

[3] *Dept. de Física Teórica, Universidad de Zaragoza, Spain*

[4] *IPPP, University of Durham, UK*

Within the framework of the Constrained Minimal Supersymmetric Standard Model (CMSSM) we analyze the discovery potential of the LHC for the same-sign di-muon signature. The analysis focuses on parameter space that will not be probed by the Tevatron, and that is favored by current electroweak precision data and cosmological observations. With an integrated luminosity of 10 fb^{-1}, corresponding to the first phase of LHC operations, fermionic mass parameters $m_{1/2}$ can be probed up to $m_{1/2} < 650$ GeV. For $\tan\beta = 10$ this covers the full range favored by current low-energy precision data. For larger $\tan\beta$ values, the highest favored $m_{1/2}$ values require a larger integrated luminosity.

4.10.1 Introduction

Theories based on Supersymmetry (SUSY) [13, 359, 360] are widely considered as the theoretically most appealing extension of the Standard Model (SM) [361, 362, 363]. They are consistent with the approximate unification of the gauge coupling constants at the GUT scale and provide a way to cancel the quadratic divergences in the Higgs sector, stabilizing the huge hierarchy between the GUT and Fermi scales. Furthermore, in SUSY theories, breaking of the electroweak symmetry is naturally induced at the Fermi scale, and the lightest supersymmetric particle can be neutral, weakly interacting and stable, providing therefore a natural solution for the dark matter problem.

SUSY predicts the existence of scalar partners $\tilde{f}_L$, $\tilde{f}_R$ to each SM chiral fermion, and spin–1/2 partners to the gauge and scalar Higgs bosons. So far, the direct search for SUSY particles has not been successful. One can only set lower bounds of $\mathcal{O}(100)$ GeV on their masses [32]. The search reach is currently extended in various ways in the ongoing Run II at the upgraded Fermilab Tevatron [364]. The LHC [22, 5] and the proposed e^+e^- International Linear Collider (ILC) [365, 366, 367, 368, 369] have very good prospects for exploring SUSY at the TeV scale, which is favored from naturalness arguments. From the interplay of both machines detailed information on the SUSY spectrum can be expected in this case [244].

In the Minimal Supersymmetric Standard Model (MSSM), no further assumptions are made on the structure of the soft SUSY-breaking parameters, and a parameterization of all possible SUSY-breaking terms is used. The high dimensionality makes analyses in the MSSM without any further constraints quite cumbersome. For this reason, simplifying assumptions that may be

more or less well-motivated are often made, so as to reduce the parameter space to a manageable dimensionality. Following many previous studies, we work here in the framework of the constrained MSSM (CMSSM), in which the soft supersymmetry-breaking scalar and gaugino masses are each assumed to be equal at some GUT input scale. In this case, the new independent MSSM parameters are just four in number: the universal gaugino mass $m_{1/2}$, the scalar mass m_0, the trilinear soft supersymmetry-breaking parameter A_0, and the ratio $\tan\beta$ of Higgs vacuum expectation values [38].

The non-discoveries of supersymmetric particles and the Higgs boson at LEP and the Tevatron (so far) impose significant lower bounds on $m_{1/2}$ and m_0. An important further restriction is provided by the density of dark matter in the universe, which is tightly constrained by WMAP and other astrophysical and cosmological data [370, 257]. These have the effect within the CMSSM, assuming that the dark matter consists largely of neutralinos [371, 372], of reducing the available parameter space and allowing only thin strips in ($m_{1/2}$, m_0)-planes (for fixed A_0 and $\tan\beta$) [373, 374].

An important discovery signal for SUSY at the LHC is the same-sign di-muon signature. A typical decay chain for a signal event is similar to the following one: $gq \to \tilde{g}\tilde{q}_L$, where $\tilde{g} \to \tilde{t}t \to \tilde{\chi}_1^+ + X \to W^+ + \tilde{\chi}_1^0 + X \to \tilde{\chi}_1^0 + X + \mu^+ + \nu$ and $\tilde{q}_L \to \tilde{\chi}_1^+ + Y \to W^+ + \tilde{\chi}_1^0 + Y \to \tilde{\chi}_1^0 + Y + \mu^+ + \nu$. Here we see two $\tilde{\chi}_1^0$ stable neutral heavy SUSY particles providing MET, two high P_T μ^+ and high E_T jets included into X, Y decay chain parts. Two same-sign muons with relatively high p_T (at least $p_T > 10$ GeV) significantly reduce background contamination with respect to the "multi-jets only" signature, as well as provide high trigger efficiency. Additional cuts on missing transverse energy as well as jet E_T increase signal to background significance even further. A recent published theoretical study of that signature for the Tevatron can be found in Ref. [375].

The outline of the contribution is as follows. In Sec. 4.10.2 we review the CMSSM landscape. We review the lower bounds on SUSY masses from the LEP and Tevatron searches and describe briefly the effects of cold dark matter (CDM) density. We also outline the regions of CMSSM parameter space that are favored by electroweak precision observables (where also Tevatron data plays an important role). Within the region allowed by direct searches and favored by precision data we perform a simulated experimental analysis for the same-sign di-muon signature at the LHC. The reach within the CMSSM parameter space for various SUSY mass scales is then explored in Sec. 4.10.3. We find that for $\tan\beta = 10$ the full range of $m_{1/2}$ values, favored at the 90% C.L. by current electroweak precision data, can be probed with the same-sign di-muon signature in the first phase of LHC operations (10 fb^{-1}). For higher $\tan\beta$ values, the largest $m_{1/2}$ values favored by precision data will require a higher integrated luminosity.

[38] An economical way to ensure the universality assumed in the CMSSM is by gravity-mediated SUSY breaking in a minimal supergravity (mSUGRA) scenario. The mSUGRA scenario predicts in particular a relation between the gravitino mass and m_0, which is not necessarily fulfilled in the CMSSM. For simplicity, we do not make the distinction between the CMSSM and the mSUGRA scenario, and use the phrase "CMSSM" for both.

4.10.2 The CMSSM landscape

Here we briefly review the parameters of the CMSSM, their experimental bounds and the regions of parameter space favored by current electroweak precision data.

The CMSSM

The study presented below has been performed in the framework of the CMSSM, in which the soft SUSY-breaking scalar and gaugino masses are each assumed to be equal at some GUT input scale. The new independent MSSM parameters are: the universal gaugino mass $m_{1/2}$, the scalar mass m_0, the trilinear soft supersymmetry-breaking parameter A_0, and the ratio $\tan\beta$ of Higgs vacuum expectation values. Also, the sign of the Higgs mixing parameter μ is in principle still undetermined. The anomalous magnetic moment of the muon, $(g-2)_\mu$, shows a 2-3 σ discrepancy from the SM expectation [376, 377, 378]. SUSY effects can easily account for this deviation if μ is positive [379]. For this reason, in the rest of this contribution, we restrict our attention to $\mu > 0$. Even in view of the possible size of experimental and theoretical uncertainties, it is very difficult to reconcile $\mu < 0$ with the present data on $(g-2)_\mu$.

We furthermore assume that the CMSSM gives the right amount of CDM density (with the lightest neutralino being the dark matter particle) to be in the range $0.094 < \Omega_{\rm CDM}h^2 < 0.129$ favored by a joint analysis of WMAP and other astrophysical and cosmological data [370, 257]. This strongly reduced the available CMSSM parameter space and allows only thin strips in ($m_{1/2}$,m_0)-planes (for fixed A_0 and $\tan\beta$) [373, 374]. For simplicity the experimental analysis was performed for $A_0 = 0$ and certain fixed values of $\tan\beta$: 10, 20, and 35.

Limits from LEP and the Tevatron

The four LEP experiments actively searched for SUSY particles without seeing any significant excess of signal over background [380, 381, 382, 383]. Limits of ~ 100 GeV could be set on the masses of all electrically charged SUSY particles. Within the CMSSM, the mass of the lightest neutralino was limited to be above ~ 50 GeV.

The search for SUSY particles has been continued at the Tevatron in Run II [364]. Currently, the limits for scalar quarks (except scalar tops and bottoms) and gluinos have been extended to 350 GeV [384]. Assuming that the Tevatron will not discover SUSY even with 8 fb^{-1} per detector, these bounds will be extended to about 450 GeV [384].

Within the CMSSM these SUSY particle limits can be translated into limits on $m_{1/2}$, m_0, A_0 and $\tan\beta$. Assuming the CDM density constraints (see above), values of $\mathcal{O}(50)$ GeV can be excluded for $m_{1/2}$ and m_0 (depending on the choice of A_0 and $\tan\beta$). In our analysis below we discard all CMSSM parameter combinations that are not in agreement with the anticipated future exclusion bounds for SUSY particles or Higgs bosons [345, 385, 386, 387, 388] from the Tevatron and LEP searches.

Indications from electroweak precision observables

Measurements at low energies may provide interesting indirect information about the masses

of particles that are too heavy to be produced directly. A prime example is the use of precision electroweak data from LEP, the SLC, the Tevatron and elsewhere to predict (successfully) the mass of the top quark and to provide an indication of the possible mass of the hypothetical Higgs boson [389, 390]. Predicting the masses of supersymmetric particles is much more difficult than for the top quark or even the Higgs boson, because the renormalizability of the Standard Model and the decoupling theorem imply that many low-energy observables are insensitive to heavy sparticles. Nevertheless, present data on electroweak precision observables can already provide interesting information on the scale of SUSY.

We consider the following observables: the W boson mass, M_W, the effective weak mixing angle at the Z boson resonance, $\sin^2\theta_{\rm eff}$, the anomalous magnetic moment of the muon, $(g-2)_\mu$, the rare decay $\mathrm{BR}(b \to s\gamma)$ and the mass of the lightest CP-even Higgs boson, m_h. Within the CMSSM, a χ^2 analyses for fixed values of $A_0/m_{1/2}$ for $\tan\beta = 10$ and 50 with $\mu > 0$ was performed [374, 391]. A remarkably high sensitivity of the current data for the electroweak precision observables to the scale of SUSY was observed. For $\tan\beta = 10$, a preference for low values of $m_{1/2} \sim 300$ GeV was found. This increases to $m_{1/2} \sim 450, 550, 600$ GeV for $\tan\beta = 20, 35, 50$. As an example, showing also the impact of future Tevatron measurements, we reproduce here the result for the *upper* limit on $m_{1/2}$ at the 90% C.L. Fig. 4.10.1 [391] shows this upper limit for various top-quark mass measurements (m_t enters the prediction of the precision observables) and possible future uncertainties that could be realized during RunII at the Tevatron [39]. We fixed m_0 via the CDM constraint, varied A_0 from -2 $m_{1/2}$ to +2 $m_{1/2}$, and set $\tan\beta = 10$. The upper limit on $m_{1/2}$ does not exceed 650 GeV for $169 < m_t < 178$ GeV (depending only slightly on the experimental precision of m_t). Only for m_t values outside this interval much are larger upper bounds obtained. The bounds increase to about 850 GeV for $\tan\beta = 20$, 1000 GeV for $\tan\beta = 35$, and about 1200 GeV for $\tan\beta = 50$. Consequently we will focus on $m_{1/2} < 900$ GeV in our analysis.

Experimental analysis

In this study we used the following values of the parameters: $\mathrm{sign}(\mu) > 0$, $A_0 = 0$, $\tan\beta = 10, 20, 35$ and 20 $(m_{1/2}, m_0)$-points. All points were chosen so as to satisfy recent theoretical and experimental constraints [373]. The top quark mass, m_t, was fixed to $m_t = 175$ GeV.

The study is based on the assumption of 10 fb^{-1} integrated luminosity collected at CMS. The points are analyzed in view of the same-sign di-muon signature. More recent results on the two same-sign di-muon signature analysis with CMS are now available in the CMS Physics TDR, vol.2 [392].

Simulation and Reconstruction

[39] Also, the M_W measurement will be improved during RunII, possibly down to an uncertainty of $\delta M_W^{\rm RunII} \approx 20$ MeV, compared to the current uncertainty of $\delta M_W = 32$ MeV today. This will slightly tighten the constraints from precision observables. However, the impact is expected to be substantially smaller than from the improved m_t measurements.

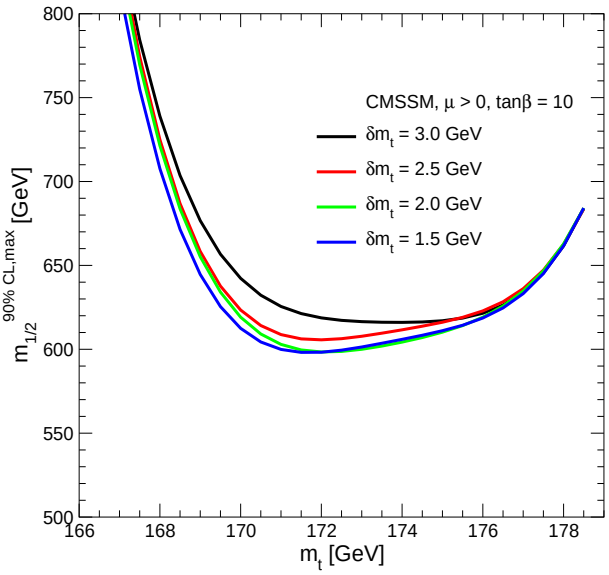

Fig. 4.10.1: The dependence of the *upper* limit on $m_{1/2}$ at the 90% C.L. on m_t and its uncertainty δm_t [391].

The points chosen for this analysis are shown in Fig. 4.10.2. Points 2, 11, 16, 19 are CMSSM benchmark points taken from Ref. [393] (two of them, points 2 and 16, were modified for a top-quark mass of 175 GeV as used for all other points). All points shown on the plot by empty markers have a cross section too small for a target integrated luminosity of 10 fb^{-1} and are not considered in the study. On the other hand, these are exactly the points that are disfavored by current electroweak precision data [40].

Coupling constants and cross sections at leading order (LO) for SUSY processes were calculated with ISASUGRA 7.69 [394]. Next-to-Leading Order (NLO) corrections were calculated with the PROSPINO program [315] and used in the analysis. The cross sections for the SM processes were calculated using PYTHIA 6.220 [83] and CompHEP 4.2p1 [395]. For several SM processes ($t\bar{t}, ZZ, Zb\bar{b}$), the NLO correction are known and were used [396]. All events were generated with PYTHIA 6.220. Some preselection cuts were applied at the generator level: events were kept if at least two same-sign muons with $p_T > 10$ GeV and $|\eta| < 2.5$. After the event generation, a GEANT-based simulation CMSIM [397] was performed.

Data digitization and reconstruction were done with the ORCA [397] reconstruction package. Pile-up events were not taken into account in this study (and muon isolation cuts were not used). Muon reconstruction was performed using an algorithm implemented for the CMS High-Level Triggers (HLT) [398] based on the muon and tracker sub-detector information. Jets were reconstructed with the Iterative Cone Algorithm with a cone size of 0.5[399]. Jet E_T corrections were applied and missing E_T calculated as described in Ref. [398].

[40] For larger $\tan\beta$ values it is possible to find non-disfavored points that have a too small cross section.

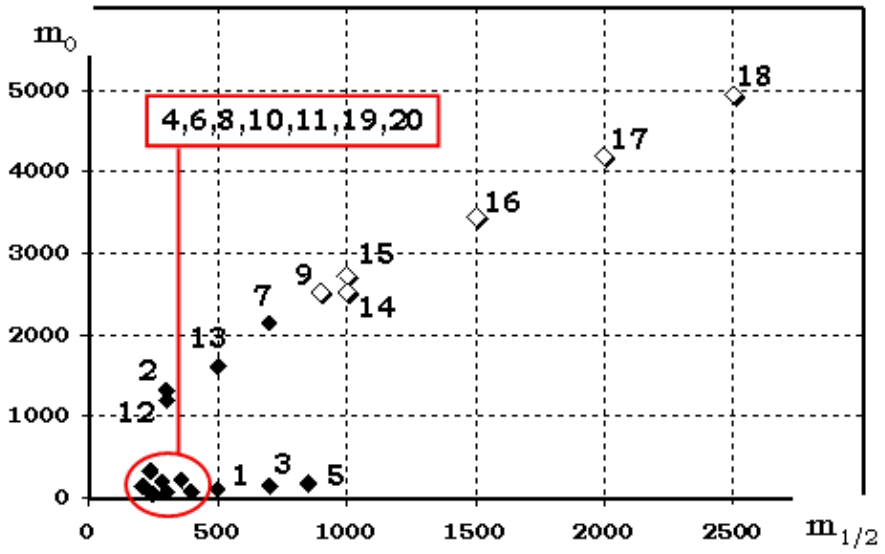

Fig. 4.10.2: The CMSSM benchmark points investigated in this analysis.

We checked that all events satisfying the selection criteria passed both L1 and HLT muon triggers (single and di-muon triggers). Details on the trigger threshold and efficiencies can be found in Ref. [398].

Background processes

Several of the important backgrounds were studied in detail, while for several of the rare processes only an estimate was made based on the cross section and branching ratio to the final state signature.

The cross sections and numbers of generated and selected events for the important sources of backgrounds are listed in Tab. 4.10.1. In all tb, tqb, $\bar{t}b$, $\bar{t}qb$ processes, the top quark was forced to decay to Wb and the W was forced to decay into a muon and neutrino. The muon from that decay chain was required to have $p_T > 10$ GeV and $|\eta| < 2.5$ at the CompHEP generation level. In the $Zb\bar{b}$ process, the Z was allowed to be off mass shell (Z/γ^*) and was forced to decay to $\mu^+\mu^-$. The invariant mass of the two muons from the initial Z/γ^* was required to be larger than 5 GeV at the CompHEP generation level.

In Tab. 4.10.2 the estimates of other potential background processes are shown. No detailed simulation was performed for these processes. An estimate was obtained from the process cross section (calculated with CompHEP) and the branching fraction into muons.

The main conclusion here is that all but the $t\bar{t}W$, $t\bar{t}Z$ processes are negligible and they are neglected in this analysis. Both $t\bar{t}W$ and $t\bar{t}Z$ backgrounds need, however, further future investigation.

Process	σ, pb	$N_{\mathrm{generated}}$	N_{selected}	N1	N2
tb	0.212	18,999	1,000	2,120	112
tqb	5.17	28,730	1,000	51,700	1,798
$\bar{t}b$	0.129	13,588	745	1,290	71
$\bar{t}qb$	3.03	28,359	1,000	30,300	1,067
ZZ	18(NLO)	433,489	1,000	180,000	256
ZW	26.2	368,477	1,000	262,000	727
WW	26.2	894,923	41	702,000	39.7
$t\bar{t}$	886(NLO)	931,380	15,000	8,860,000	142,691
$Zb\bar{b}$	232(NLO)	359,352	2,000	2,320,000	12,924
All					160,000

Table 4.10.1: Cross sections and numbers of events for the SM processes for which a detailed simulation was performed for an integrated luminosity of 10 fb^{-1}. $N_{\mathrm{generated}}$ is the unweighted number of generated events, N_{selected} is the unweighted number of pre-selected events, N_1 is the number of events for an integrated luminosity of 10 fb^{-1}, N_2 is the number of events after pre-selection cuts (at least two same-sign muons with $p_T > 10$ GeV.)

Process	σ, pb	N1	N2
WWW	0.129	1,290	< 15
ZWW	0.0979	979	< 10
ZZW	0.0305	305	< 3
ZZZ	0.00994	99.4	< 1
WWWW	0.000574	negl.	negl.
ZWWW	0.000706	negl.	negl.
ZZWW	0.000442	negl.	negl.
ZZZW	0.000572	negl.	negl.
ZZZZ	0.0000161	negl.	negl.
$\mathrm{t\bar{t}W}$	0.556	5,560	< 200
$\mathrm{t\bar{t}Z}$	0.65	6,500	< 200
$\mathrm{t\bar{t}WW}$	negl.	negl.	negl.
$\mathrm{t\bar{t}ZW}$	negl.	negl.	negl.
$\mathrm{t\bar{t}ZZ}$	negl.	negl.	negl.

Table 4.10.2: Cross sections and event numbers for the SM processes for which only an estimate was obtained for an integrated luminosity of 10 fb^{-1}. N_1 is the estimated number of events for integrated luminosity of 10 fb^{-1}, N_2 is the estimated number of events.

Selection and cut optimization

The distributions of kinematic variables such as missing E_T, jet E_T, muon p_t (as chosen for this study), are very different for SUSY and SM processes as shown in Fig. 4.10.3. Suitable cuts

on these variables help reducing the SM background.

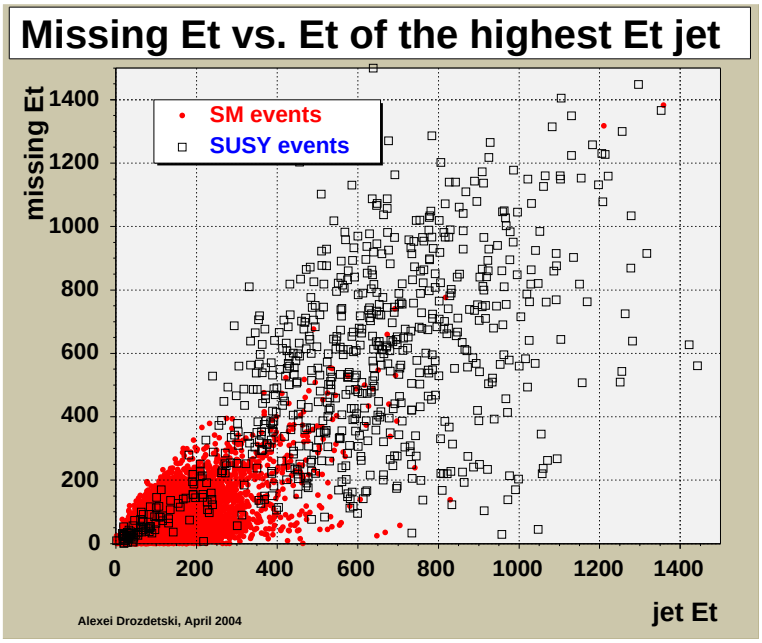

Fig. 4.10.3: Missing transverse energy vs. jet E_T for SUSY (open squares) and SM events (points) after full simulation and reconstruction.

A set of five variables (missing E_T, E_{T,jet_1}, E_{T,jet_3}, p_{T,μ_1}, p_{T,μ_2}) was chosen. For each variable a set of possible selection cuts was defined. A combination of selection variables and cuts was performed, leading to different sets of cuts. The significance, signal-over-background ratio and number of expected events for 10 fb^{-1} were calculated for each set of cuts. Only the two sets of cuts shown in the Tab. 4.10.3 were finally chosen to be applied in the analysis, since they cover all CMSSM points with significance greater than 5σ.

set	miss. E_T, GeV	E_{T,jet_1}, GeV	E_{T,jet_3}, GeV	P_{T,μ_1}, GeV	P_{T,μ_2}, GeV
1	> 200	> 0	> 170	> 20	> 10
2	> 100	> 300	> 100	> 10	> 10

Table 4.10.3: Chosen cut sets. E_{T,jet_1} is the E_T of the leading jet (maximum E_T) (GeV), E_{T,jet_3} is the E_T of the third highest-E_T jet (GeV), P_{T,μ_1} and P_{T,μ_2} are the two highest-p_T values of the same-sign muons (GeV).

SUSY points characteristics

For each CMSSM point, the LO cross section was calculated as well as the number of events, for an integrated luminosity of 10 fb^{-1}. NLO corrections were applied for all CMSSM points and corrected values were used for this analysis.

Two other parameters were calculated for each CMSSM point: the statistical significance and the signal-to-background ratio. The significance was calculated using the following expression [400]: $S_{12} = 2(\sqrt{N_S + N_B} - \sqrt{N_B})$, where N_B is the total number of background events and N_S is the number of signal events for each point in the $(m_{1/2}, m_0)$-plane.

Six points (numbers 9 and 14-18) were excluded from the analysis because of their small cross section. These are exactly the points that are disfavored by current electroweak precision data. This selection is affected by our initial choice of benchmark points, where most have $\tan\beta = 10$, only one has $\tan\beta = 20$, and three have $\tan\beta = 35$. For $\tan\beta > 10$ it is in principle possible to find non-disfavored points that have a too-small cross section.

Results

Details concerning the expected number of signal and background events as well as the significance at each point studied are listed in the Tab. 4.10.4.

	N_{set1}	$S_{12,\text{set1}}$	S/B_{set1}	N_{set2}	$S_{12,\text{set2}}$	S/B_{set2}
SM	69.5±6.0			432±8.8		
1	95.9±6.7	9.05	1.38	184±9.3	8.06	0.43
2	282±20	20.8	4.06	560±29	21.4	1.3
3	17.7±1.1	2	0.25	30.4±1.4	1.44	0.07
4	365±73	25	5.26	1590±152	48.4	3.7
5	6.54±0.37	0.77	0.094	9.6±0.45	0.46	0.002
6	277±35	20.6	4.0	1030±67	35	2.4
7	6.7±0.35	0.78	0.096	8.31±0.39	0.4	0.019
8	188±17	15.5	2.71	530±28	20.5	1.2
10	515±78	31.7	7.41	1950±151	56.1	4.5
11	137±11	12.1	1.98	322±18	13.4	0.75
12	409±30	27.1	5.89	781±42	28.1	1.8
13	58.8±3.3	6	0.85	86.9±4	4	0.2
19	377±59	26.5	5.43	1220±106	39.8	2.8
20	279±36	20.6	4.01	996±67	34	2.3

Table 4.10.4: The CMSSM benchmark points: the expected "final" number of events after all cuts, N, the significance values, S_{12}, and the signal-to-background ratio, S/B. The errors quoted on $N_{\text{set1,set2}}$ account for Monte Carlo statistics only. The indices, set1 and set2, are for cut sets # 1 and #2 respectively, and the "SM" row gives the expected number of the SM background events after all cuts for all considered processes.

The number of points out of reach (significance less than 5σ) for 10 fb^{-1} varies from nine to ten. Results are also illustrated at Fig. 4.10.4. For the benchmark CMSSM points with significance

greater than 5σ the signal to background ratios are greater than 0.4 (the excess of SUSY events over the SM is greater than 40%). The interpretation of these results in terms of SUSY masses etc. can be found in Sec. 4.10.3.

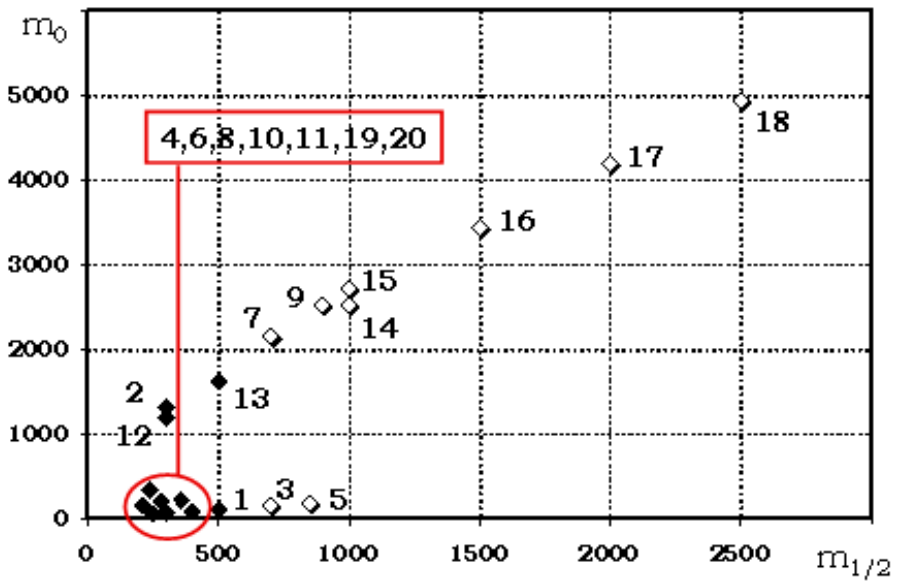

Fig. 4.10.4: The black points in the $(m_{1/2}, m_0)$-plane have significance greater than five. The white points are not reachable.

First estimate of systematic effects

The stability of the significance as a function of the uncertainty on the signal acceptance and the background normalization was verified. A correlated variation of the SM event number ($+30\%$) and expected number of SUSY events (-30%) was applied. As a result, (Tab. 4.10.5) the significance of only one CMSSM point (# 13) drops below discovery level.

4.10.3 Experimental reach in the CMSSM

Figure 4.10.4 shows which CMSSM points have a significance greater than 5σ when plotted in ($m_{1/2}$,m_0)-plane. An approximate sensitive area for 10 fb^{-1} is well defined on the $m_{1/2}$ parameter axis. The largest benchmark value of $m_{1/2}$ giving a significance higher than 5σ has $m_{1/2} = 500$ GeV. It can be expected that also slightly larger values, $m_{1/2} \lesssim 650$ GeV can be tested with 10 fb^{-1} at CMS. For $\tan\beta = 10$ this covers the whole range preferred by electroweak precision data. For $\tan\beta = 35$, however, a large interval of $m_{1/2}$ values, 650 GeV $\lesssim m_{1/2} \lesssim 1000$ GeV remains unexplored. Higher luminosities are required to cover this part of the CMSSM parameter space. This gap becomes even larger for largerer $\tan\beta$ values. It should also be noticed that at

	S_{12}, set#1	S/B, set#1	S_{12}, set#2	S/B, set#2
1	6.09	0.743	5.15	0.23
2	14.9	2.19	14.4	0.7
3	1.26	0.137	0.889	0.038
4	18.2	2.83	34.5	2
5	0.476	0.0507	0.283	0.012
6	14.7	2.15	24.3	1.3
7	0.425	0.0516	0.245	0.01
8	10.8	1.46	13.7	0.66
10	23.5	3.99	40.5	2.4
11	8.31	1.07	8.71	0.4
12	19.8	3.17	19.2	0.97
13	3.93	0.456	2.5	0.11
19	18.6	2.93	27.9	1.5
20	14.8	2.16	23.6	1.2

Table 4.10.5: CMSSM benchmark points: results after the variation for cuts set #1 and #2.

large $\tan\beta$ the production of τ's increases compared to μ production. This might lead to a weaker signal and correspondingly weaker coverage.

We now turn to the discovery reach in the physical spectrum. For each $\tan\beta$ value we show in Tab. 4.10.6 the point with the highest $m_{1/2}$ value. For $\tan\beta = 10$ we show a second point with the highest m_0. The CMSSM parameters are given together with some examples of the corresponding physical spectrum [41]. If a signal at the LHC is seen in the initial phase or running with 10 fb^{-1}, within the CMSSM framework this corresponds to scalar quark masses below ~ 1800 GeV and gluino masses below ~ 1200 GeV. Scalar lepton masses are strongly correlated with m_0. In the chargino/neutralino sector the light masses are below ~ 400 GeV, while the heavy masses can go up to ~ 650 GeV. The heavy Higgs masses can be as high as ~ 1400 GeV. For the four cases shown in Tab. 4.10.6, the heavy Higgs bosons can certainly not observed at the LHC directly. On the other hand, observation of SUSY particles at the LHC with 10 fb^{-1} would in the framework of the CMSSM guarantee that several charginos and neutralinos could be detected at the ILC.

The bounds on m_0 are obtained only indirectly via the requirement of the correct CDM density and the choice $A_0 = 0$. In order to get a full overview of the CMS capabilities, more extended studies will be necessary. These should involve more CMSSM benchmark points with $m_{1/2} < 650$ GeV and $m_0 > 1500$ GeV and various A_0 values. Also, for larger $\tan\beta$, more points

[41] It should be noted that the m_h evaluation has a large theoretical error. While with the most advanced code [401, 355, 356] a theory error of up to 3 GeV was estimated [402], this error is even larger in the calculation as implemented in ISASUGRA 7.69. Therefore the low value for $\tan\beta = 20$ does not rule out this parameter point.

have to be studied in order to correctly assess the LHC potential.

4.10.4 Conclusions

Within the framework of the Constrained Minimal Supersymmetric Standard Model (CMSSM), we have analyzed the discovery potential of the LHC for the same-sign di-muon signature. The analysis was performed in the parameter space that is bounded from below by the non-observation of SUSY particles at the Tevatron. Indications for upper bounds are derived with the help of electroweak precision data, where the top-quark mass measurement at the Tevatron plays a crucial role. At the 90% C.L. the fermionic mass parameter $m_{1/2}$ is bounded from above by $m_{1/2} \leq 650, 1000$ GeV for $\tan\beta = 10, 35$. The analysis concentrated on 200 GeV $\leq m_{1/2} \leq$ 1000 GeV. We furthermore used $A_0 = 0$ and $m_t = 175$ GeV. All benchmark points that entered the analysis also fulfilled the requirement that the lightest neutralino gives the right amount of CDM density. This fixes to a large extent the scalar mass parameter m_0.

The analysis was performed for the first phase of LHC operations, corresponding to an integrated luminosity of 10 fb^{-1}. We found that $m_{1/2}$ can be tested up to $m_{1/2} < 650$ GeV. This covers the full range favored by current low-energy precision data for $\tan\beta = 10$, but leaves unexplored regions for larger $\tan\beta$ values – then a higher integrated luminosity would be necessary. Thus, if SUSY in its simple version of the CMSSM with $A_0 = 0$ and $\tan\beta = 10$ is realized in nature, it will be discovered already in the first phase of LHC running. For larger $\tan\beta$ values, the preferred range of $m_{1/2}$ is larger, and more luminosity has to be collected to cover the correspondingly higher $m_{1/2}$ values. In order to get a full overview of the LHC potential more extended studies will be necessary. These should involve more CMSSM benchmark points with larger m_0 values, $A_0 \neq 0$ and larger $\tan\beta$.

Acknowledgements

We would like to thank A. Birkedal, N. Marinelli, K. Matchev, L. Pape, A. De Roeck, M. Spira, M. Spiropulu, G. Wrochna, for their special help and contributions to the analysis. We thank B. Heinemann for helpful discussions on the Tevatron results. S.H. was partially supported by CICYT (grant FPA2004-02948) and DGIID-DGA (grant 2005-E24/2).

$\tan\beta$	10	10	20	35
$m_{1/2}$	500	300	240	500
m_0	107	1330	330	1620
sign(μ)	+	+	+	+
$m_{\tilde{t}_1}$	813.02	914.14	448.95	1257.40
$m_{\tilde{t}_2}$	1015.81	1230.46	606.35	1557.96
$m_{\tilde{b}_1}$	972.28	1216.66	552.76	1540.94
$m_{\tilde{b}_2}$	1000.59	1422.56	593.76	1718.06
$m_{\tilde{u}_L}$	1047.11	1451.59	619.98	1891.29
$m_{\tilde{u}_R}$	1011.73	1447.76	607.91	1877.60
$m_{\tilde{d}_L}$	1050.16	1453.76	625.09	1892.97
$m_{\tilde{d}_R}$	1008.09	1448.01	607.96	1876.51
$m_{\tilde{g}}$	1154.04	791.75	601.89	1237.18
$m_{\tilde{\tau}_1}$	213.62	1321.88	323.45	1441.49
$m_{\tilde{\tau}_2}$	358.84	1337.29	370.18	1562.59
$m_{\tilde{\nu}_\tau}$	347.87	1333.95	354.88	1559.54
$m_{\tilde{e}_L}$	358.00	1342.14	369.93	1650.46
$m_{\tilde{e}_R}$	221.03	1333.49	344.24	1629.05
$m_{\tilde{\nu}_e}$	348.89	1339.45	361.04	1648.21
$m_{\tilde{\chi}_1^0}$	200.38	119.67	92.28	206.06
$m_{\tilde{\chi}_2^0}$	386.88	233.35	174.04	400.77
$m_{\tilde{\chi}_3^0}$	631.76	434.46	327.81	582.35
$m_{\tilde{\chi}_4^0}$	646.55	452.22	348.19	599.03
$m_{\tilde{\chi}_1^\pm}$	387.55	234.03	174.19	401.85
$m_{\tilde{\chi}_2^\pm}$	646.00	451.72	348.18	598.98
m_h	118.19	115.41	113.29	118.87
m_H	717.66	1399.04	456.33	1400.62
m_A	712.79	1389.77	453.32	1391.45
$m_{H^\pm}$	721.93	1401.22	463.65	1403.49

Table 4.10.6: Three points, one for each $\tan\beta$ value with the highest $m_{1/2}$, and one for $\tan\beta = 10$ with the highest m_0 value (with $A_0 = 0$ and $m_t = 175$ GeV) are shown together with some examples of the corresponding physical spectrum. All masses are in GeV.

4.11 Collider Searches and Dark Matter Detection Prospects in mSUGRA

Howard Baer[1], Alexander Belyaev[2], Tadas Krupovnickas[1,3], Jorge O'Farrill[1] and Xerxes Tata[4]

[1] *Florida State University at Tallahassee, USA*
[2] *Michigan State University at East Lansing, USA*
[3] *Brookhaven National Laboratory, USA*
[4] *University of Hawai'i, USA*

In recent years, supersymmetric models have become increasingly constrained by a variety of measurements [403, 404]. These include determination of the branching fraction $BF(b \to s\gamma)$ [405, 406, 407, 408], the muon anomalous magnetic moment $a_\mu = (g-2)_\mu/2$ [409, 410] and most recently, the tight restriction on the relic dark matter density from the Big Bang, as determined by the WMAP experiment [257]. Analyses of WMAP and other data sets have determined a preferred range for the abundance of cold dark matter [257]:

$$\Omega_{CDM}h^2 = 0.1126^{+0.0161}_{-0.0181}\,, \quad 2\sigma \text{ level}\,. \tag{4.11.1}$$

For phenomenologically viable ranges of parameters, the lightest neutralino in the minimal supergravity (mSUGRA) framework is usually the lightest SUSY particle [411, 412, 413, 414]. Since R-parity is assumed to be conserved, this neutralino is stable and provides a good candidate for cold dark matter. The possibility that dark matter, like visible matter, is made up of several components cannot be excluded at this point. In our analysis we therefore interpret the WMAP measurement (4.11.1) as an *upper* bound, $\Omega_{\widetilde{Z}_1}h^2 < 0.129$, on the neutralino relic density, unless stated otherwise. mSUGRA is characterized by four SUSY parameters together with a sign choice,

$$m_0,\ m_{1/2},\ A_0,\ \tan\beta \ \text{ and } sign(\mu)\,. \tag{4.11.2}$$

Here m_0 is the common mass of all scalar particles at M_{GUT}, $m_{1/2}$ is the common gaugino mass at M_{GUT}, A_0 is the common trilinear soft term at M_{GUT}, $\tan\beta$ is the ratio of Higgs field vacuum expectation values at the scale M_Z, and finally the magnitude – but not the sign – of the superpotential μ term is determined by the requirement of radiative electroweak symmetry breaking (REWSB).

Evaluations of the neutralino relic density [415, 416, 288, 417, 418, 419, 420, 421, 301, 422, 423] show four qualitatively different viable regions of mSUGRA parameter space consistent with recent WMAP and other data sets [257]. These include 1.) the bulk region at low m_0 and $m_{1/2}$ where neutralinos may annihilate in the early universe via t-channel slepton exchange, 2.) the stau co-annihilation region where $m_{\widetilde{Z}_1} \simeq m_{\tilde{\tau}_1}$ [415, 416], 3.) the axial Higgs A annihilation corridor at large $\tan\beta$ [288, 417, 418, 419, 420, 421], and 4.) the hyperbolic branch/focus poin (HB/FP) region where the neutralino has a significant higgsino component and can readily annihilate to WW and ZZ pairs in the early universe [301, 418]. Somewhat less popular but still viable scenarios in the literature include a region of squark–neutralino co-annihilation which can exist for particular

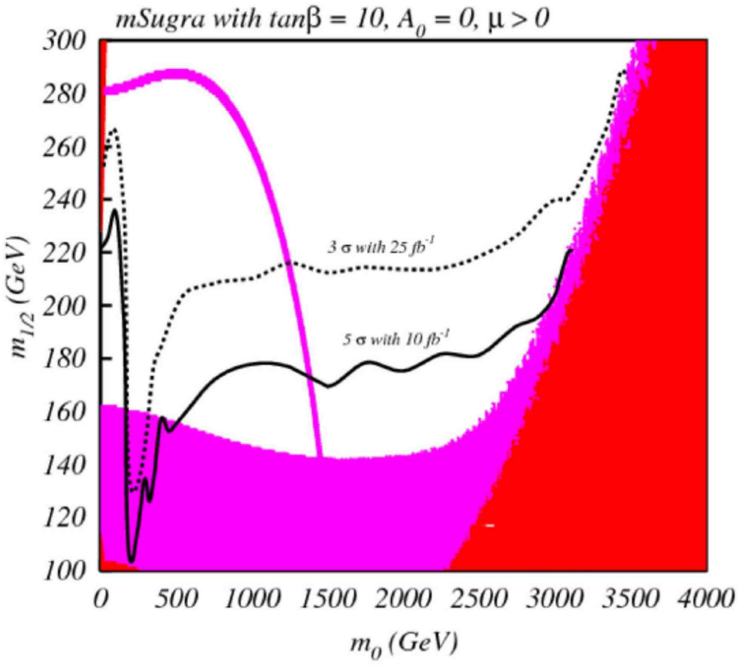

Fig. 4.11.1: The reach of Fermilab Tevatron in the m_0 *vs.* $m_{1/2}$ mSUGRA parameter plane, with $\tan\beta = 10$, $A_0 = 0$, $\mu > 0$ and $m_t = 175$ GeV assuming a 5σ signal with 10 fb^{-1} (solid) and a 3σ signal with 25 fb^{-1} (dashed) of integrated luminosity. The red (magenta) region is excluded by theoretical (experimental) constraints. The region below the magenta contour has $m_h < 114.1$ GeV, in violation of the Higgs mass limit from LEP II.

values of the A_0 parameter that give rise, for instance, to $m_{\tilde{t}_1} \simeq m_{\widetilde{Z}_1}$ [422, 423]. Also, Ref. [424] showed that for a large value of the top quark mass, $m_t = 180$ GeV, there exists a narrow band just above the LEP II exclusion contour where neutralinos can annihilate through a light Higgs resonance ($m_h \simeq 2m_{\widetilde{Z}_1}$). The latter scenario seems to be currently disfavored due to the new top quark mass measurement, which pushes the light Higgs annihilation corridor into the region already excluded by LEP II searches for the Higgs boson.

We first turn our attention to mSUGRA's prospects at the Tevatron. There, $\widetilde{W}_1\widetilde{Z}_2$ production can lead to trilepton plus $\not\!\!E_T$ final states which can be above SM background levels for significant regions of parameter space. This channel was found to be the most promising at the Tevatron. We extend the trilepton search results presented in Ref. [425] to large values of $m_0 > 1$ TeV, including the HB/FP region. Here, we adopt the set of cuts labelled SC2 in Ref. [425], which generally give the best reach. From Fig. 4.11.1 [426], we see that the 5σ reach for 10 fb^{-1} approaches $m_{1/2} \sim 175$ GeV for $m_0 \sim 1000 - 2000$ GeV, corresponding to a reach in $m_{\widetilde{W}_1}(m_{\tilde{g}})$ of 125(525) GeV.

Tevatron also provides us with a very important measurement of the top quark mass. The impact of variation of m_t on the allowed mSUGRA parameter space is shown in Fig. 4.11.2 [426]. The boundary of the allowed parameter space exhibits very strong sensitivity to the precise value of m_t.

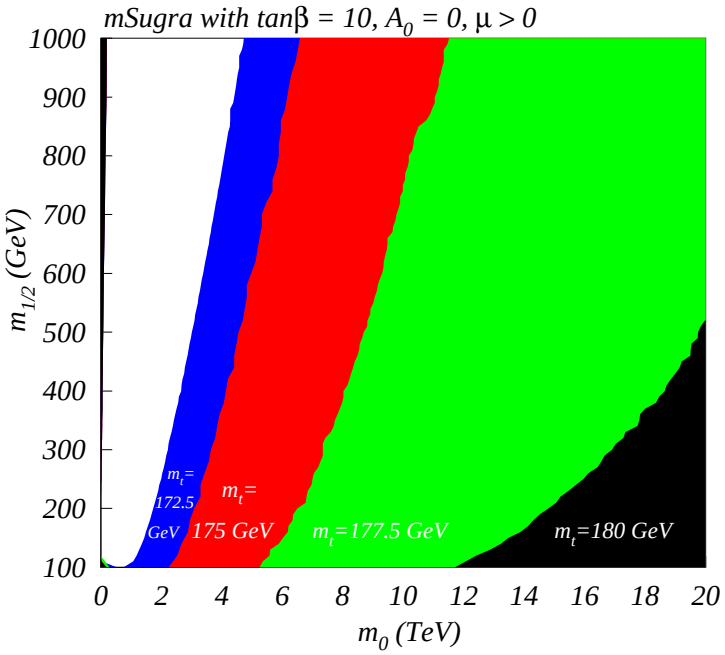

Fig. 4.11.2: Boundary of the mSUGRA m_0 *vs.* $m_{1/2}$ parameter plane, with $\tan\beta = 10$, $A_0 = 0$ and $\mu > 0$, for $m_t = 172.5$, 175, 177.5 and 180 GeV.

The CERN LHC is expected to accumulate a significant data sample in 2008 with pp collisions at $\sqrt{s} = 14$ TeV. While the initial luminosity is expected to be ~ 10 fb^{-1} per year, an integrated luminosity of several hundred fb^{-1} is ultimately anticipated. When analyzing the prospects of mSUGRA at the LHC, we adopt the approach of optimizing kinematic cuts for different scenarios using computer code, rather than a detailed case-by-case study. In our study all events have to pass the following pre-cuts:

- $E_T^{miss} > 200$ GeV;
- Number of jets, $N_j \geq 2$,

and then we try a large set of combinations of cuts on the most important variables on signal and background [427]. We divide the events into signal types according to the number of isolated leptons (or photons for the isolated γ signal). In the case of an E_T^{miss} signal there can be any number of leptons: 0-lepton signal has no leptons, 1-lepton signal has 1 lepton, 2-OS-lepton signal has 2 opposite sign leptons, 2-SS-lepton signal has 2 same sign leptons, 3-lepton signal has 3 leptons, ≥ 4-lepton has more than 3 leptons, and $Z \rightarrow \ell^+\ell^-$ has at least 2 OS, same-flavor leptons with invariant mass in the interval $(M_Z - \Delta M_Z, M_Z + \Delta M_Z)$ (ΔM_Z is varied during the optimization procedure). Finally, the isolated γ signal has any number of leptons plus at least one photon (the cut on the number of photons is varied during the optimization procedure). The resulting reaches for different channels are shown in Fig. 4.11.3.

Next we turn our attention to a future Linear Collider (LC). We explore two possibilities for

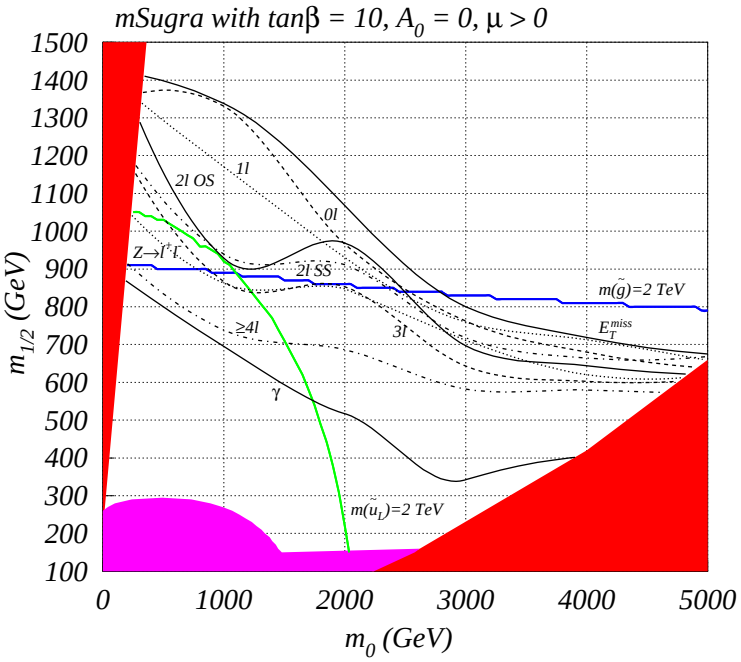

Fig. 4.11.3: The reach of the CERN LHC in the mSUGRA m_0 *vs.* $m_{1/2}$ parameter plane, with $\tan\beta = 10$, $A_0 = 0$, $\mu > 0$ and $m_t = 175$ GeV, assuming 100 fb^{-1} of integrated luminosity. The red (magenta) regions are excluded by theoretical (experimental) constraints discussed in the text. We show the reach in the 0ℓ, 1ℓ, OS, SS, 3ℓ, $\geq 4\ell$, γ and Z channels, as well as in the "inclusive" $\not{E}_T$ channel.

center-of-mass energy: 500 GeV and 1 TeV. It is difficult to create a cut optimization algorithm for the LC which would work well throughout all mSUGRA parameter space, primarily because different sparticle processes (or at least different sparticle kinematics) are accessed in different regions. Therefore we restrict ourselves to creating the best sets of cuts for phenomenologically different regions of parameter space. We find several such regions [428, 424]:

- At low m_0 with $m_{1/2} \sim 300 - 500$ GeV, slepton pair production occurs at large rates. For low $\tan\beta \sim 10$, the reach due to selectron, smuon or stau pair production is roughly the same. However, stau pair production extends the reach of LC in the case of larger $\tan\beta$ values.
- There exists a small region around $m_0 \sim 200 - 500$ GeV and $m_{1/2} \sim 300 - 350$ GeV where neither slepton nor chargino pairs are kinematically accessible, but where $e^+e^- \to \widetilde{Z}_1\widetilde{Z}_2$ is. In this case, the decay $\widetilde{Z}_2 \to \widetilde{Z}_1 h$ was usually found to be dominant.
- For larger m_0 values, chargino pair production occurs at a large rate. We found that this region cannot be treated by applying the same set of cuts throughout. This is due to the fact that in the lower range of m_0 the chargino $\widetilde{W}_1$ and neutralino $\widetilde{Z}_1$ mass gap is large, and consequently the visible decay products are hard, while for larger m_0 the opposite is the case.

In Fig. 4.11.4, we show LC reach contours for $\tan\beta = 10$.

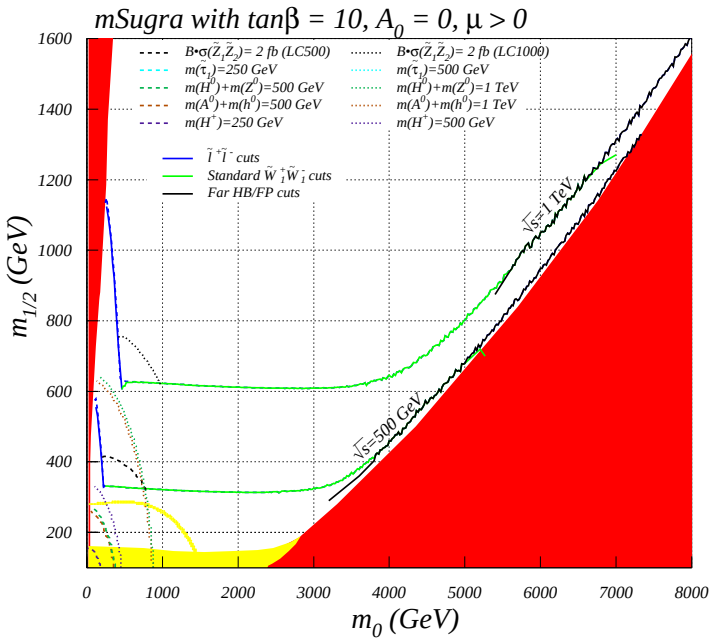

Fig. 4.11.4: Reach of a linear collider for supersymmetry in the mSUGRA model for $\sqrt{s} = 500$ and 1000 GeV, for $\tan\beta = 10$, $A_0 = 0$, $\mu > 0$ and $m_t = 175$ GeV. The slepton pair production reach is denoted by the blue contour, while lower-m_0 cuts for chargino pair production yield the green contour. Larger-m_0 chargino pair cuts yield the black contour in the HB/FP region. The red region is theoretically excluded, while the yellow region is excluded by LEP II measurements. Below the yellow contour, $m_h \leq 114.4$ GeV.

One can summarize all the collider reaches and compare them with the constraints from WMAP measurements. The resulting contours are shown in Fig. 4.11.5. The striking feature of Fig. 4.11.5 is that the reach of the 1 TeV LC bypasses the reach of LHC in the far HB/FP region, which is favored by dark matter (DM) constraints.

One can also include the direct and indirect searches of relic neutralinos in the analysis. The bounds from future experiments were summarized in Ref. [429]. We considered neutrino signals from neutralino annihilation in the core of the Earth or the Sun, γ's from neutralino annihilation in the core of the galaxy, positrons and antiprotons from neutralino annihilation in the galactic halo, and direct searches for neutralino DM via neutralino scattering off nuclei. The projected reaches from all these experiments, along with the favored DM density regions and the collider reaches are presented in Fig. 4.11.6. The intriguing point is that almost the entire HB/FP region (up to $m_{1/2} \sim 1400$ GeV) can be explored by the cubic-km-scale IceCube ν telescope [430, 431]. It can also be explored (apparently at later times) by the Stage 3 direct DM detectors such as ZEPLIN4 [432], XENON [433] and WARP [434].

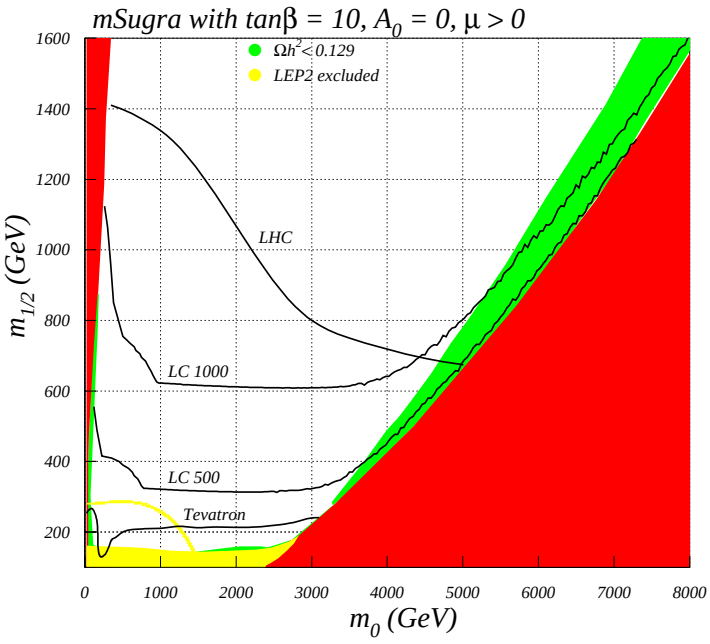

Fig. 4.11.5: Reach of a $\sqrt{s} = 0.5$ and 1 TeV LC for sparticles in mSUGRA for $\tan\beta = 10$, $A_0 = 0$, $\mu > 0$ and $m_t = 175$ GeV. We also show the Fermilab Tevatron reach assuming 10 fb^{-1} of integrated luminosity (for isolated trileptons), and the CERN LHC reach assuming 100 fb^{-1} of data. Finally, the green shaded region shows points where the relic density $\Omega_{\widetilde{Z}_1} h^2 < 0.129$ as dictated by WMAP.

In conclusion, Tevatron still has a chance of discovering mSUGRA, although the region of the parameter space which will be probed is relatively small. Nevertheless, the more accurately measured top quark mass will give us the information about which part of mSUGRA parameter space is still theoretically allowed. After accumulating 100 fb^{-1} of integrated luminosity, LHC will have probed gluino masses as large as ~ 3 TeV. However, the reach of the LHC peters out in the far HB/FP region. It does not seem possible to extend the LHC reach using $\widetilde{W}_1\widetilde{Z}_2 \rightarrow 3\ell$ production [435], and b-jet tagging extends the gluino reach by just $10-15\%$ [436]; thus, accessing the far-HB/FP region seems to be a real challenge for the LHC. That provides even more support for the case of a future LC, preferably with a large center-of-mass energy (of order 1 TeV). It is very encouraging that direct and indirect DM search experiments will be able to probe the far-HB/FP before the LC can be expected to start operating, even if these experiments alone do not shed light on the physics origin of DM. If we interpret this DM as the neutralino of mSUGRA, these experiments, together with absence of signals at the LHC, will point to the HB/FP region, and make a strong case for the construction of a TeV LC.

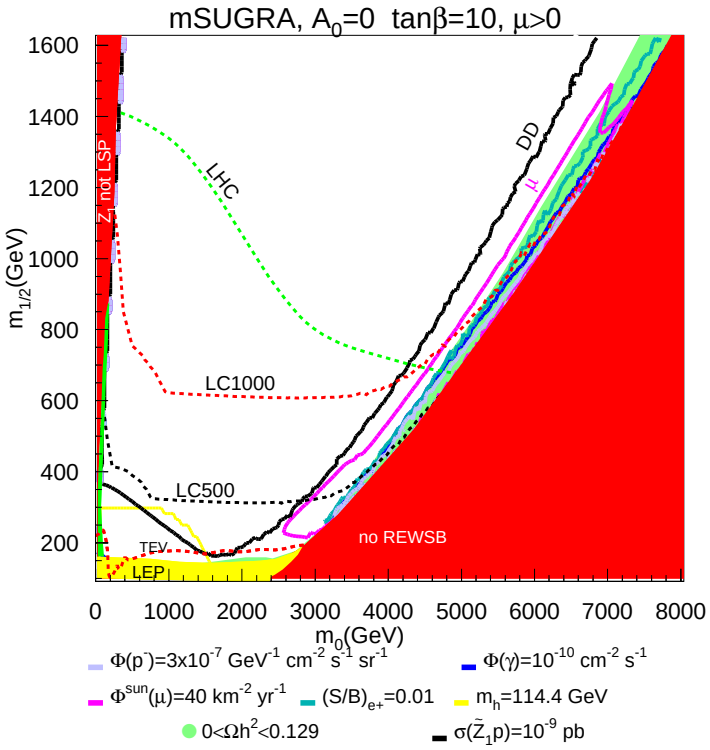

Fig. 4.11.6: A plot of the reach of direct, indirect and collider searches for neutralino dark matter in the m_0 *vs.* $m_{1/2}$ plane, for $\tan\beta = 10$, $A_0 = 0$, $\mu > 0$ and $m_t = 175$ GeV. We include the reaches of Tevatron, LHC, and linear colliders of $E_{cm} = 500$ GeV and $E_{cm} = 1$ TeV (dashed lines). We also show the reaches of Stage 3 direct dark matter detection experiments (DD) and the IceCube ν telescope (μ), $\Phi(\gamma) = 10^{-10}$ γs/cm^2/s contour, $S/B > 0.01$ contour for halo produced positrons and the antiproton flux rate $\Phi(\bar{p}) = 3 \times 10^{-7}$ $\bar{p}$s/cm^2/s/sr (solid lines).

4.12 A Quick Guide to SUSY Tools

Peter Z. Skands[42]*, Fermi National Accelerator Laboratory, Batavia, IL, USA*

The last decade has seen the emergence of a wide range of automated calculations for supersymmetric extensions of the Standard Model. This guide contains a brief summary of these, with the main focus on hadron collider phenomenology, as well as a brief introduction to the so-called SUSY Les Houches Accord. See also the Les Houches Web Repository for BSM Tools: http://www.ippp.dur.ac.uk/montecarlo/BSM/

4.12.1 Introduction

Among the most enticing possibilities for observable new physics both at the Tevatron and at the LHC is supersymmetry (SUSY); for reviews, see e.g. Refs. [437, 438, 439]. At the most fundamental level, imposing SUSY on a quantum field theory represents the most general (and only) possible way of extending the Poincaré group of spacetime symmetries [440, 441]. At the same time it furnishes a desirable relation between the bosonic and fermionic degrees of freedom. Empirically, however, SUSY can at most be a broken symmetry if it exists in nature, due to the non-observation of mass-degenerate (or lighter) spin-partners for each of the Standard Model (SM) particles.

However, even a softly-broken supersymmetry can have quite amazing properties, as long as the mass splittings introduced by the breaking are smaller than a TeV or so. Among the most well-known consequences of such SUSY are radiative breaking of electroweak symmetry, an elegant solution to the so-called hierarchy problem, a natural weakly-interacting dark matter candidate (in theories with conserved R-parity), and unification of the strong, weak, and electromagnetic gauge couplings at a (very) high energy scale.

For collider phenomenology, the most immediately relevant consequences are 1) a minimal extension of the SM Higgs sector to two doublets, 2) promotion of each of the Standard Model fields (plus the extra Higgs content) to superfields, resulting in a spin-partner for each SM particle, with mass splittings inside each boson–fermion doublet $\lesssim 1$ TeV, and 3) the special properties which accompany a conserved R-parity, namely production of the new states only in pairs, followed by individual cascade decays down to the Lightest Supersymmetric Particle (LSP) which is stable and (usually) escapes detection.

The large interest in ($N = 1$) supersymmetric extensions of the SM and their phenomenological consequences has carried with it the need for automated tools to calculate SUSY mass spectra and couplings, cross sections, decay rates, dark matter relic densities, event rates, precision observables, etc. To handle communication between the many tools, the SUSY Les Houches Accord [442, 443, 444] (SLHA) is now in widespread use. Section 4.12.2 contains a brief introduction to this accord. Next, in Section 4.12.3, an overview of the presently available state-of-the-art tools

[42]skands@fnal.gov

is given, divided into four main categories. A more extensive collection of tools for BSM physics as well as an online repository can be found in [445]. Another recent and comprehensive tools review is the Les Houches Guidebook to MC Generators [446].

4.12.2 The SUSY Les Houches Accord

Given the long history of the subject, it is not surprising that several different conventions for defining SUSY theories have been proposed over the years, many of which are in active use by different groups. While this is not a problem per se (unique translations can always be constructed), it does entail a few practical problems, in particular when the results of one group are compared to or used in the calculations of a different group.

In addition, even when the theoretical conventions are identical, there remains the purely technical issue that each program has its own native way of inputting and outputting parameters, each of which is unintelligible to most other programs.

The SLHA was proposed to solve both these problems. Due to the large parameter space of unconstrained supersymmetric models, the SLHA in its present form [442] (SLHA1) is limited to the Minimal Supersymmetric Standard Model (MSSM), with conservation of R-parity, CP, and flavour. Extensions to more general models are underway [444] (SLHA2).

Technically, the accord is structured into 3 ASCII files (or strings): 1) model definition and measured SM parameters, 2) SUSY mass and coupling spectrum, and 3) decay tables. Though admittedly not elegant, the ASCII format was chosen for its robustness across platforms and compilers. In general, all input parameters used for a calculation are copied to the output, so that any subsequent calculation also has access to the exact input parameters used for the previous one.

The SLHA Conventions The backbone of the Accord is a unique set of conventions for defining the SUSY parameters, fields, and couplings. These conventions, which have also been adapted for the Supersymmetry Parameter Analysis (SPA) project [237], largely resemble the widely used Gunion–Haber conventions [447], with a few differences as noted explicitly in Ref. [442]. Simply stated, to define a SUSY model, one needs the field content, the superpotential, the SUSY breaking terms, and the gauge couplings. For the field content, the SLHA assumes that of the MSSM, while SLHA2 will include extensions for the NMSSM.

The MSSM superpotential is specified by the measured SM particle masses (giving the Yukawa couplings) and by the μ term. In SLHA1, only the third-generation Yukawas are included. The gauge couplings are specified in terms of $M_{\rm Z}$, G_F, $\alpha_s(M_{\rm Z})^{\overline{\rm MS}}$, and the fine structure constant at zero momentum transfer. All of these are the usual SM ones that one can get from a review text, i.e. no SUSY corrections should be included here. SLHA2 will include masses for all 3 generations, as well as the CKM matrix.

The SUSY breaking terms can be specified either by giving the parameters for a minimal version of a particular SUSY breaking model (SUGRA, GMSB, or AMSB), or individually, either

by starting from a minimal model and successively adding non-universal terms, or simply by giving all terms explicitly. For higher-order calculations, these parameters are interpreted in the modified dimensional reduction ($\overline{\rm DR}$) scheme [448, 449, 450], either at the (derived) unification scale or at a user-specifiable scale. As mentioned, CP, R-parity, and flavour are assumed conserved in SLHA1.

In the spectrum output, three kinds of parameters are given: 1) pole masses of all (s)particles, 2) mixing matrices, and 3) Lagrangian parameters. While the precise definition of the mixing matrix elements are left up to each spectrum calculator, the Lagrangian parameters are defined as $\overline{\rm DR}$ ones at one or several user-specifiable scales Q.

The SLHA Decay Tables A somewhat separate and self-contained aspect of the SLHA is the possibility to pass total widths and partial branching ratios via a file structure similar to that of the rest of the Accord. A common use for this is to improve or extend the width calculations of an event generator by the numbers calculated with a specialised package.

Note! An important potential pitfall when using these files is on-shell intermediate resonances in final states with more than 2 particles. If not treated properly, large problems both with double-counting and with incorrect population of phase space can occur. Please see [442] for an explicit description of the correct procedure to adopt in these cases.

4.12.3 Computing SUSY

This Section contains an overview of SUSY calculational tools, divided into 1) spectrum calculators, 2) observables calculators, 3) matrix element and event generators, and 4) data fitting programs. For links and references, the reader should consult the recently constructed online repository for BSM tools [445].

Spectra Given assumptions about the underlying supersymmetric theory (field content, superpotential, supersymmetry breaking terms) and a set of measured parameters (SM particle masses, gauge couplings, electroweak symmetry breaking), the masses and couplings of all particles in the spectrum can be computed. This is the task of spectrum calculators, also called RGE packages.

The most commonly used all-purpose spectrum calculators are ISAJET [451], SOFTSUSY [452], SPHENO [453], and SUSPECT [454], all compatible with SLHA. In general, the codes agree with each other to within a percent or so, though larger discrepancies can occur, in particular at large $\tan\beta$. For mSUGRA, a useful online tool for comparison between them (and different versions of them) exists [455]. Other recent comparison studies are found in Refs. [456, 457]. Though PYTHIA [7] also contains an internal spectrum calculator [458], the resulting spectrum is very approximate and should not be used for serious studies.

There are also a few spectrum calculators with more specialised areas of application, such as CPSUPERH [459], FEYNHIGGS [401], and NMHDECAY [460]. NMHDECAY computes the entire mass spectrum in the NMSSM (and has a limit which is equivalent to the MSSM), but

couplings and decay widths are so far only calculated for the Higgs sector, though improvements are underway. It is compatible with an extension of the SLHA [444]. The program FEYNHIGGS deals with the Higgs sector of the MSSM, for which it contains higher-precision calculations than the general-purpose programs mentioned above. It is also able to handle both minimal flavor violation (MFV) and CP violation, and is compatible with the SLHA, hence can be used to e.g. provide a final adjustment to the Higgs sector of a general spectrum calculated by one of the other codes. Finally, CPSUPERH deals with the Higgs sector in the MSSM with explicit CP violation and contains a number of refinements which makes it interesting also in the CP conserving case.

Observables This includes programs that calculate one or more of the following: cross sections, decay partial widths, dark matter relic density, and indirect/precision observables. Note that we here focus on calculations relevant for hadron colliders and that matrix element and event generators, which also calculate many of these things, are treated separately below.

For hadron collider cross sections, PROSPINO [315] can be used to calculate inclusive SUSY-NLO cross sections, both total and differential. It also calculates LO cross sections and gives the corresponding K-factors.

For partial decay widths, several specialised packages exist. For the MSSM, SPHENO calculates tree-level decays of all (s)particles (soon to include RPV[43]), SDECAY [461] computes sparticle decay widths including NLO SUSY-QCD effects, and both FEYNHIGGS [401] and HDECAY [462] compute Higgs partial widths with higher-order corrections. Recently, HDECAY, SDECAY, and SUSPECT were combined into one package, SUSY-HIT [463]. NMHDECAY [460] computes partial widths for all Higgs bosons in the NMSSM.

For the density of dark matter, DARKSUSY [464], ISATOOLS [465], and MICROMEGAS [466] represent the publically available state-of-the-art tools. All of these work for the MSSM, though a special effort has been put into MICROMEGAS to make it easily extendable [467], recently resulting in an implementation of the NMSSM [468], and work on CP violation is in progress.

For precision observables, NMHDECAY includes a check against LEP Higgs searches, $\mathrm{b} \to \mathrm{s}\gamma$, and can be interfaced to MICROMEGAS for the relic density. ISAJET/ISATOOLS include calculations of $\mathrm{b} \to \mathrm{s}\gamma$, $(g-2)_\mu$, $\mathrm{B_s} \to \mu^+\mu^-$, $\mathrm{B}_d \to \tau^+\tau^-$, and neutralino-nucleon scattering cross sections. SPHENO includes $\mathrm{b} \to \mathrm{s}\gamma$, $(g-2)_\mu$, as well as the SUSY contributions to the ρ parameter due to sfermions. Finally, SUSPECT also includes a calculation of $\mathrm{b} \to \mathrm{s}\gamma$.

Matrix Element and Event Generators By a matrix element generator, we mean a program that, given a set of fields and a Lagrangian, is able to generate Feynman diagrams for any process and square them. Note, however, that many of the codes are able to do quite a bit more than that. An event generator is a program that, given a matrix element, is able to generate a series of random

[43] RPV in SPheno is not yet public, but a private version is available from the author

exclusive events in phase space, often including resonance decays, parton showers, underlying event, hadronisation, and hadron decays.

The automated tools for generating matrix elements for SUSY are AMEGIC++ [469], CALCHEP [470], COMPHEP [218], GRACE-SUSY [471], SUSY-MADGRAPH [472], and O'MEGA [473]. All of these work at leading order, except GRACE, and all currently only deal with the MSSM, except CALCHEP, which contains an NMSSM implementation.

CALCHEP and COMPHEP provide internal event generators, while the event generator SHERPA [474] is built on AMEGIC++, GR@PPA [475] builds on GRACE, SUSY-MADEVENT [476] builds on SUSY-MADGRAPH, and WHIZARD [477] builds on O'MEGA. Of these, most are matrix-element-level event generators. That is, they provide events consisting of just a few partons and their four-momenta, corresponding to the given matrix element convoluted with phase space. These events must then be externally interfaced [236, 478] e.g. to PYTHIA or HERWIG for resonance decays, parton showering, underlying event, and hadronisation. The exception is SHERPA, which contains its own parton shower and underlying event models (similar to the PYTHIA ones), and for which a cluster-based hadronisation model is being developed.

In addition, both HERWIG [479] and PYTHIA contain a large number of internal hardcoded leading-order matrix elements, including R-parity violating (RPV) decays in both cases [480, 481, 482], and RPV single sparticle production in HERWIG [480]. In PYTHIA, the parton shower off SUSY resonance decays is merged to the real NLO jet emission matrix elements [483], an interface to CALCHEP and NMHDECAY exists for the NMSSM [484], and an implementation of the hadronisation of R-hadrons is available [127, 123].

Two other event generators should be mentioned. ISAJET [451] also contains a large amount of SUSY phenomenology, but its parton shower and hadronisation machineries are much less sophisticated than those of HERWIG, PYTHIA, and SHERPA. The active development of SUSYGEN [485] (which among other things includes RPV single sparticle production) is currently at a standstill, though basic maintenance is still being carried out.

Fitters Roughly speaking, the tools described above all have one thing in common: given a set of fundamental parameters (themselves not directly observable) they calculate the (observable) phenomenological and experimental consequences. However, if SUSY is at some point discovered, a somewhat complementary game will ensue: given a set of observed masses, cross sections, and branching ratios, how much can we say about the fundamental parameters?

The fitting programs FITTINO [171] and SFITTER [172] attempt to address this question. In a spirit similar to codes like ZFITTER [486], they combine the above tools in an automated statistical analysis, taking as input a set of measured observables and yielding as output a set of fundamental parameters.

Obviously, the main difficulty does not lie in determining the actual central values of the parameters, although this can require significant computing resources in itself; by far the most im-

portant aspect of these tools is a proper and thorough error analysis. Statistical uncertainties can be treated rigorously, and are included in both programs. Theoretical and systematic uncertainties are trickier. In a conventional analysis, these uncertainties are evaluated by careful consideration of both the experimental setup and of the particular theoretical calculations involved. In an automated analysis, which has to deal simultaneously with the entire parameter space of supersymmetry, a 'correct' evaluation of these errors poses a truly formidable challenge, one that cannot be considered fully dealt with yet.

Acknowledgments

The TeV4LHC series of workshops have been highly enjoyable, and I am thankful for all the hard work put in by the organisers. This work was supported by Universities Research Association, Inc. under Contract No. DE-AC02-76CH03000 with the United States Department of Energy.

4.13 SFITTER

Remy Lafaye[1]*, Tilman Plehn*[2]*, Dirk Zerwas*[3]
[1] *CERN, Geneva, Switzerland*
[2] *MPI for Physics, Munich, Germany and University of Edinburgh, Scotland*
[3] *LAL Université de Paris-Sud, Orsay Cedex, France*

The impact of Tevatron measurements on the determination of supersymmetric parameters is presented.

4.13.1 Introduction

The supersymmetric extension [487] of the Standard Model is a well-motivated framework which can link particle physics and astrophysics and provides us with a consistent and perturbative description of physics up to the unification scale. If supersymmetry is discovered, it will be crucial to determine the fundamental SUSY–breaking parameters at an unknown high scale from weak-scale measurements [488]. Large production cross sections for strongly interacting supersymmetric particles at the LHC combined with the typical cascade decays can provide a wealth of measurements [22, 365, 489, 369, 244]. A precise theoretical link of masses and couplings at the high scale and the weak scale are available, for example via Spheno, SuSpect, SoftSUSY [453, 454, 452]. These renormalization group analyses have to be combined with highly efficient parameter extraction tools such as Fittino [171, 490] and SFitter [491, 172] to properly determine the underlying fundamental parameters.

In the following we explore the SPS1a [198] parameter point (m_0= 100 GeV,$m_{1/2}$= 250 GeV,A_0= -100 GeV,$\tan\beta$= 10 and $\mu > 0$) using the standard set of measurements as listed in Ref. [244], corresponding to an integrated luminosity of 300 fb^{-1} at the LHC. The focus of this particular study is the determination of the expected errors on the supersymmetric parameters using SFitter.

4.13.2 Finding and Fitting

Two separate tasks have to be considered for a proper determination of supersymmetric parameters: finding the correct point in parameter space, and determining the errors on the parameters. For complex parameter spaces with an increasing number of dimensions, the allowed parameter space might not be sampled completely using a standard fit alone, if the starting point of a fit is arbitrary. To avoid domain walls created by unphysical parameter regions, which can confine the fit to a 'wrong' parameter region, combining the fit with an initial evaluation of a multi-dimensional grid offers one possible solution. In the general MSSM, the weak-scale parameters can vastly outnumber the collider measurements, so that a complete parameter fit is technically not possible. We then have to limit ourself to a subset of parameters and carefully estimate the quantitative effect of fixing certain parameters. We implemented both a grid and a fit approach which can be combined,

including a general correlation matrix and the option to exclude parameters of the model from the fit/grid by fixing them to an arbitrary value.

4.13.3 mSUGRA at the LHC

The masses which could be measured in the SPS1a parameter point at the LHC provide a sufficiently large dataset to perform a fit of the mSUGRA parameters. In particular, if the starting point of the fit is far away from the true parameters (m_0=$m_{1/2}$=1 TeV, $\tan\beta$=50, A_0=0 i.e. the central value of the entire allowed region), the fit converges to the true values. The sign of μ is fixed to its true value.

	SPS1a	ΔLHC$_{\text{masses}}$	ΔLHC$_{\text{edges}}$
m_0	100	3.9	1.2
$m_{1/2}$	250	1.7	1.0
$\tan\beta$	10	1.1	0.9
A_0	-100	33	20

Table 4.13.1: Results for mSUGRA at the LHC: all nominal values and the absolute errors for mass and edge measurements. Mass values are given in GeV.

Using the LHC measurements of particle masses, all SUSY breaking parameters can be determined at the percent level (Table 4.13.1). It is particularly interesting to note that the results using LHC measurements can be improved significantly when we resort to the measured edges and thresholds instead. Because the mass values are extracted from the kinematic endpoints in long decay chains, the resulting masses are strongly correlated. In order to restore the initial sensitivity when we extract the SUSY breaking parameters from the measured masses we would need the full correlation matrix.

The precision obtained with the previous fits neglects theoretical errors. Indeed, if we take into account reasonable theoretical errors, such as 3 GeV [356, 492] on the lightest Higgs boson, 3% on colored supersymmetric partners, 1% on neutralinos and sleptons, the error on the $m_0$mass increases. Already at the LHC, the experimental precision will necessitate a vigorous theoretical effort [237, 493] to fully exploit the available experimental information.

4.13.4 Impact of the Tevatron Data

At the parameter point SPS1a most of the supersymmetric particles are out of reach of the Tevatron. However, we observe an indirect effect from the measurement of the top mass. The top mass and Yukawa coupling are crucial parameters in the renormalization group analysis and strongly influences the mass predictions of supersymmetric particles. Even though we use a point in the so-called bulk region of the mSUGRA parameter space, we note that this dependence becomes dominant for the focus point region [494]. For SPS1a a 4 GeV shift in the top mass shifts the mass of the lightest Higgs boson by 1.5 GeV.

	SPS1a	m_t=175	m_t=179	m_t=171
m_0	100	100 ± 6	97.9 ± 6	101 ± 6
$m_{1/2}$	250	250 ± 5	250 ± 6	249 ± 5
$\tan\beta$	10	10 ± 5	7.5 ± 2	12.6 ± 6
A_0	-100	-100 ± 110	-37 ± 140	-152 ± 88

Table 4.13.2: Results of the fit with a shifted top mass. All mass values are given in GeV.

As a first scenario we assume one year of low-luminosity running at the LHC, corresponding to an integrated luminosity of 10 fb^{-1}. The experimental errors on the SUSY masses are scaled from the edges measurements, even though this might be an optimistic assumption. The expected precision on the LHC top mass measurement of around 1 GeV will be dominated by systematic errors and will not be available after one year of running. Therefore, we use the Tevatron measurement instead. To illustrate the influence of the Tevatron, we generate the spectrum with a top mass of 175 GeV and fit the SUSY masses assuming a top mass shifted by 4 GeV. As shown in Table 4.13.2, the systematic effect on the extraction of $\tan\beta$ and $A_0$is non-negligible: while the error of the fitted parameters is indeed independent of the top mass we assume for the fit, the central values shift by up to 0.7σ.

The discovery and in particular a mass measurement of the lightest Higgs boson with only 10 fb^{-1} will be challenging at the LHC, as would several other measurements of edges and mass differences. Therefore, a natural early–LHC scenario is the observation of only the main decay chain $\tilde{q}_L \to q\tilde{\chi}_2 \to q\ell\tilde{\ell}_R \to q\ell\ell\tilde{\chi}_1$. We show the resulting mSUGRA parameters and their errors in Table 4.13.3.

If the lightest Higgs boson is sitting at the edge of the LEP2 exclusion bound, one could expect 6 events per fb^{-1} per experiment in the $WH + ZH$ channels at the Tevatron. A Higgs mass determination with a precision around 4-5 GeV could be obtained. Again, we fit the mSUGRA parameters assuming evidence of a Higgs at the LEP limit with mass uncertainty of 4.5 GeV. Our results are shown in Table 4.13.3. This hint of a light Higgs reduces the expected error on m_0, $\tan\beta$ and A_0 significantly.

	SPS1a	$\Delta\text{LHC}_{\text{edges}}$	$\Delta\text{LHC}_{\text{edges}}^{\text{Higgs}}$
m_0	100	14	9
$m_{1/2}$	250	10	9
$\tan\beta$	10	144	31
A_0	-100	2400	685

Table 4.13.3: Main decay chain only and impact of a hint of a Higgs boson with a mass extraction to 5 GeV at the Tevatron. All mass values are given in GeV.

	SPS1a	ΔLHC $\Delta m_t = 2$	ΔLHC $\Delta m_t = 1.5$	ΔLHC $\Delta m_t = 1$
m_0	100	1.28	1.28	1.26
$m_{1/2}$	250	1.01	1.00	0.99
$\tan\beta$	10	1.29	1.21	1.11
A_0	-100	26.5	25.4	24.0
$y_t^{\rm os}$	175	1.2	1.1	0.8

Table 4.13.4: Results of the fit including a top mass measurement with errors of 2 GeV, 1.5 GeV, 1 GeV. The errors on the top–Yukawa model parameter $y_t^{\rm os}$ from the fit are given in the last line. For the SUSY masses we assume an integrated luminosity of 300 fb^{-1} and an analysis based on kinematic endpoints directly. All masses are in GeV.

4.13.5 Top mass as model parameter

To carefully study the impact of the top mass measurement on the determination of supersymmetric parameters, we have to fit the supersymmetric parameters together with the top mass [171, 490, 495]. The top mass appears as an mSUGRA model parameter, just like e.g. m_0. For example, SuSpect (in agreement with the Susy Les Houches Accord specifications [442]) requires the input of an on–shell (pole) top mass from which it computes the running top Yukawa coupling. We refer to this input mSUGRA model parameter as $y_t^{\rm os}$ to differentiate it from the direct top quark mass measurement and use 175 GeV as its central value.

At the high scale the Higgs field has not yet acquired a vacuum expectation value, which means that all fermions are still massless and the top model parameter should be written as the top Yukawa coupling y_t. Naturally, this Lagrangian parameter would be renormalized in $\overline{\rm MS}$. Note that such a replacement of a high–scale model parameter by a weak-scale model parameter ($y_t^{\rm os}$) is nothing new to mSUGRA; the same happens with $\tan\beta$, which as a ratio of two vacuum expectation values is by definition a weak-scale parameter.

The top mass also appears as a measured observable at the LHC, typically renormalized in

	SPS1a	ΔLHC$_{\rm edges}$ $\Delta m_t = 2$	ΔLHC$_{\rm edges}$ $\Delta m_t = 1$
m_0	100	22.6	17.4
$m_{1/2}$	250	16.1	12.6
$\tan\beta$	10	253.4	190.
A_0	-100	4173	3108
$y_t^{\rm os}$	175	2.0	1.0

Table 4.13.5: Results of the fit including Top mass measurement with errors of 2 GeV and 1 GeV in the minimal LHC scenario with only one decay chain measured with 10 fb^{-1}. The errors on the top quark model parameter from the fit are given in the last line. All masses are in GeV.

the on–shell scheme. In this section, the symbol m_t is reserved for this observable top mass. The central value we expect to extract from data is identical to our parameter $y_t^{\rm os}$, i.e. 175 GeV.

It is instructive to start from the most precise set of measurements (edges), corresponding to an integrated luminosity of 300 fb^{-1}. We show the results in Table 4.13.4 assuming an experimental error on the top mass m_t of 2 GeV, 1.5 GeV and 1 GeV. Due to the high precision of supersymmetric and Higgs measurements, the top–Yukawa model parameter is strongly constrained directly (as the top mass) and indirectly at the same time. Indeed, as shown in the last line of Table 4.13.4, the error on the top–Yukawa model parameter is smaller than that from direct measurement. The strongest impact of the top mass measurement we observe is in the $\tan\beta$ determination via the measurement of the lightest Higgs mass. The precision on $\tan\beta$ improves by about 20% if the top mass measurement improves from 2 GeV to 1 GeV accuracy.

If we perform the same fit assuming errors for an integrated luminosity of 10 fb^{-1}, the improvement of the $\tan\beta$ measurement is limited to 5% and the top–Yukawa model parameter error is essentially the same as that of the direct m_t measurement.

As this scenario is arguably optimistic on the LHC side, we also study the "minimal" scenario described above. The results are shown in Table 4.13.5. Because of the absence of any Higgs boson mass measurement, $\tan\beta$ and A_0 are undetermined. While the top mass parameter error is not improved with respect to the direct measurement, the errors on both m_0 and $m_{1/2}$ are reduced if the top mass precision is improved from 2 GeV to 1 GeV at the Tevatron. This sensitivity is essentially due to the lepton-lepton edge measurement. These studies show the importance of measuring Standard Model parameters in general and the top mass in particular with high precision.

4.13.6 Conclusions

If SUSY is discovered, sophisticated tools such as Fittino and SFitter will be necessary to determine the fundamental parameters of the theory. Even in the absence of a discovery at the Tevatron, its top quark measurement will impact the precision with which high–scale SUSY breaking parameters will be measured in the early years of LHC running.

5 Summary and Outlook

This report includes numerous results and new ideas relevant to the search for new physics at the LHC, Tevatron and elsewhere. Here we reiterate only a few conclusions, with the hope that the reader will read the detailed contributions presented in Sections 2, 3 and 4.

Experimental techniques developed by the CDF and D0 collaborations may be used at the LHC to improve the capability to reconstruct electrons, photons, muons, taus, jets and missing transverse energy. The background rates to reconstruction of some of these objects at the LHC may be predicted based on the Tevatron data.

When a signal for new physics will be observed at CMS or ATLAS, it would be useful to try to fit the signal by assuming the existence of a single particle beyond the ones discovered already. We have presented several representative examples, including Z' and W' bosons, vectorlike quarks, and $SU(2)_w$-triplet scalars, long-lived charged particles. If the signal cannot be convincingly explained by the existence of a single new particle, then one should attempt to explain it in models containing several new particles.

Much of model-based phenomenology presented here focuses on LHC signatures, or disentangling information from a new discovery at LHC. This is not unexpected, since many ideas for new physics lie at scales beyond the reach of Tevatron. However, there are many cases where Tevatron would first make a discovery, guiding searches at the LHC. An example is Technicolor, for which there are possible hints in the Run I data, yet to be re-examined now in Run II. If these hints should turn out to be real evidence, such a discovery would refocus the very thinly spread phenomenological preparation for LHC running into a concentrated effort, likely helping us to be readier to analyze LHC data in a useful way. Another possibility is supersymmetry with a light stop. Tevatron has considerable reach yet left to explore for such a scenario. Were a discovery made, it would similarly narrow the LHC focus down in a highly useful way, and make preliminary SUSY measurements which could give us strong hints for where else to look in the LHC data for the rest of the SUSY spectrum. In some cases, the lower-QCD background environment at Tevatron could provide a cleaner measurement of some of the SUSY sector than at the LHC.

Given that the Tevatron produces $p\overline{p}$ collisions, while the LHC will produce pp collisions, there are physics scenarios where there is a complementarity between the two colliders. If a resonance will be discovered at the Tevatron in a certain invariant mass distribution, then the observation of the same resonance at the LHC would provide complementary information about the couplings of the new particle to different quark flavors. Clearly, the synergy between the Tevatron and the LHC is a vast subject that requires much work beyond what has been presented during the TeV4LHC workshops. More generally, both the experimental and theoretical particle physics comunities need to intensify the preparations for the start-up of explorations of the energy frontier at the LHC.

References

[1] B. W. Lee, C. Quigg and H. B. Thacker, Phys. Rev. **D16**, 1519 (1977).

[2] D0, V. M. Abazov *et al.*, Phys. Rev. Lett. **95**, 151805 (2005), [hep-ex/0504032].

[3] D0, V. M. Abazov *et al.*, Phys. Rev. Lett. **94**, 041801 (2005), [hep-ex/0408146].

[4] G. Choudalakis, K. Makhoul, M. Klute, C. Henderson, B. Knuteson, R. Culbertson, "Physics of jet fake rates and consistency check with Vista", CDF note 8076, Jan. 2006.

[5] Volume 1 of the CMS physics TDR, CERN/LHCC 2006-001.

[6] P. Bartalini, R. Chierici and A. De Roeck, CMS Note 2005/013.

[7] T. Sjostrand *et al.*, Comput. Phys. Commun. **135**, 238 (2001), [hep-ph/0010017].

[8] CompHEP, E. Boos *et al.*, Nucl. Instrum. Meth. **A534**, 250 (2004), [hep-ph/0403113].

[9] P. Nason *et al.*, hep-ph/0003142.

[10] M. Heldmann and D. Cavalli, An improved tau-identification for the atlas experiment, ATL-PHYS-PUB-2006-008.

[11] D0, V. M. Abazov *et al.*, Phys. Rev. **D71**, 072004 (2005), [hep-ex/0412020].

[12] D0, V. M. Abazov *et al.*, DØ note 4742-CONF (2005).

[13] H. P. Nilles, Phys. Rept. **110**, 1 (1984).

[14] H. E. Haber and G. L. Kane, Phys. Rept. **117**, 75 (1985).

[15] See http://lhc.web.cern.ch/lhc/.

[16] ATLAS, W. W. Armstrong *et al.*, CERN-LHCC-94-43.

[17] E. Eichten, I. Hinchliffe, K. D. Lane and C. Quigg, Rev. Mod. Phys. **56**, 579 (1984).

[18] M. Spira, Nucl. Phys. Proc. Suppl. **89**, 222 (2000).

[19] P. Fayet, Phys. Lett. **B69**, 489 (1977).

[20] M. L. Mangano, M. Moretti, F. Piccinini, R. Pittau and A. D. Polosa, JHEP **07**, 001 (2003), [hep-ph/0206293].

[21] M. L. Mangano, http://mlm.home.cern.ch/mlm/alpgen/.

[22] TDR, ATLAS Collaboration, CERN-LHCC-99-14 and CERN-LHCC-99-15.

[23] G. Buchalla and A. J. Buras, Nucl. Phys. **B400**, 225 (1993).

[24] A. J. Buras, Phys. Lett. **B566**, 115 (2003), [hep-ph/0303060].

[25] D0, V. M. Abazov *et al.*, Phys. Rev. Lett. **94**, 071802 (2005), [hep-ex/0410039].

[26] D. Collaboration, DØnote 4733-CONF (2005).

[27] CDF, A. Abulencia *et al.*, Phys. Rev. Lett. **95**, 221805 (2005), [hep-ex/0508036].

[28] BABAR, B. Aubert *et al.*, Phys. Rev. Lett. **94**, 221803 (2005), [hep-ex/0408096].

[29] CDF, D. Acosta *et al.*, Phys. Rev. Lett. **93**, 032001 (2004), [hep-ex/0403032].

[30] CDF, F. Abe *et al.*, Phys. Rev. **D57**, 3811 (1998).

[31] CDF, F. Abe *et al.*, Phys. Rev. Lett. **71**, 1685 (1993).

[32] Particle Data Group, S. Eidelman *et al.*, Phys. Lett. **B592**, 1 (2004).

[33] CDF, R. Bernhard *et al.*, hep-ex/0508058.

[34] I. Bertram *et al.*, FERMILAB-TM-2104, 2000.

[35] J. Conway *et al.*, CDF Note 6428.

[36] P. Burikham, T. Figy and T. Han, Phys. Rev. **D71**, 016005 (2005), [hep-ph/0411094].

[37] M. Carena, A. Daleo, B. A. Dobrescu and T. M. P. Tait, Phys. Rev. **D70**, 093009 (2004), [hep-ph/0408098].

[38] CDF, A. Abulencia *et al.*, hep-ex/0602045.

[39] ATLAS Computing Group, ATLAS Computing Technical Design Report, CERN-LHCC-2005-022, 2005.

[40] M. Schaefer, F. Ledroit and B. Trocmé, 2005, ATL-PHYS-PUB-2005-010.

[41] S. Bityukov and N. Krasnikov, Durham 2002, Advanced statistical techniques in particle physics, p. 77-80.

[42] S. Dimopoulos and L. Susskind, Nucl. Phys. **B155**, 237 (1979).

[43] S. Weinberg, Phys. Rev. **D19**, 1277 (1979).

[44] M. E. Peskin and T. Takeuchi, Phys. Rev. Lett. **65**, 964 (1990).

[45] M. E. Peskin and T. Takeuchi, Phys. Rev. **D46**, 381 (1992).

[46] C. Csaki, C. Grojean, H. Murayama, L. Pilo and J. Terning, Phys. Rev. **D69**, 055006 (2004), [hep-ph/0305237].

[47] C. Csaki, C. Grojean, L. Pilo and J. Terning, Phys. Rev. Lett. **92**, 101802 (2004), [hep-ph/0308038].

[48] Y. Nomura, JHEP **11**, 050 (2003), [hep-ph/0309189].

[49] C. Csaki, C. Grojean, J. Hubisz, Y. Shirman and J. Terning, Phys. Rev. **D70**, 015012 (2004), [hep-ph/0310355].

[50] G. Cacciapaglia, C. Csaki, C. Grojean and J. Terning, Phys. Rev. **D71**, 035015 (2005), [hep-ph/0409126].

[51] R. Foadi, S. Gopalakrishna and C. Schmidt, Phys. Lett. **B606**, 157 (2005), [hep-ph/0409266].

[52] C. Schwinn, Phys. Rev. **D71**, 113005 (2005), [hep-ph/0504240].

[53] G. Cacciapaglia, C. Csaki, C. Grojean, M. Reece and J. Terning, Phys. Rev. **D72**, 095018 (2005), [hep-ph/0505001].

[54] R. Sekhar Chivukula, D. A. Dicus and H.-J. He, Phys. Lett. **B525**, 175 (2002), [hep-ph/0111016].

[55] R. Barbieri, A. Pomarol and R. Rattazzi, Phys. Lett. **B591**, 141 (2004), [hep-ph/0310285].

[56] G. Burdman and Y. Nomura, Phys. Rev. **D69**, 115013 (2004), [hep-ph/0312247].

[57] G. Cacciapaglia, C. Csaki, C. Grojean and J. Terning, Phys. Rev. **D70**, 075014 (2004), [hep-ph/0401160].

[58] H. Davoudiasl, J. L. Hewett, B. Lillie and T. G. Rizzo, Phys. Rev. **D70**, 015006 (2004), [hep-ph/0312193].

[59] H. Davoudiasl, J. L. Hewett, B. Lillie and T. G. Rizzo, JHEP **05**, 015 (2004), [hep-ph/0403300].

[60] R. Barbieri, A. Pomarol, R. Rattazzi and A. Strumia, Nucl. Phys. **B703**, 127 (2004), [hep-ph/0405040].

[61] J. L. Hewett, B. Lillie and T. G. Rizzo, JHEP **10**, 014 (2004), [hep-ph/0407059].

[62] R. Foadi, S. Gopalakrishna and C. Schmidt, JHEP **03**, 042 (2004), [hep-ph/0312324].

[63] R. Casalbuoni, S. De Curtis and D. Dominici, Phys. Rev. **D70**, 055010 (2004), [hep-ph/0405188].

[64] R. S. Chivukula, E. H. Simmons, H.-J. He, M. Kurachi and M. Tanabashi, Phys. Rev. **D70**, 075008 (2004), [hep-ph/0406077].

[65] H. Georgi, Phys. Rev. **D71**, 015016 (2005), [hep-ph/0408067].

[66] M. Perelstein, JHEP **10**, 010 (2004), [hep-ph/0408072].

[67] H. Georgi, hep-ph/0508014.

[68] A. Birkedal, K. Matchev and M. Perelstein, Phys. Rev. Lett. **94**, 191803 (2005), [hep-ph/0412278].

[69] M. Papucci, hep-ph/0408058.

[70] E. Asakawa and S. Kanemura, Phys. Lett. **B626**, 111 (2005), [hep-ph/0506310].

[71] J. Bagger *et al.*, Phys. Rev. **D49**, 1246 (1994), [hep-ph/9306256].

[72] J. Bagger *et al.*, Phys. Rev. **D52**, 3878 (1995), [hep-ph/9504426].

[73] M. S. Chanowitz, Czech. J. Phys. **55**, B45 (2005), [hep-ph/0412203].

[74] A. Dobado, M. J. Herrero and J. Terron, Z. Phys. **C50**, 205 (1991).

[75] A. Dobado, M. J. Herrero and J. Terron, Z. Phys. **C50**, 465 (1991).

[76] Z. Sullivan, Phys. Rev. **D66**, 075011 (2002), [hep-ph/0207290].

[77] P. Langacker and S. Uma Sankar, Phys. Rev. **D40**, 1569 (1989).

[78] Particle Data Group, D. E. Groom *et al.*, Eur. Phys. J. **C15**, 1 (2000).

[79] Z. Sullivan, hep-ph/0306266.

[80] CDF, D. Acosta *et al.*, Phys. Rev. Lett. **90**, 081802 (2003), [hep-ex/0209030].

[81] CDF, T. Affolder *et al.*, Phys. Rev. Lett. **87**, 231803 (2001), [hep-ex/0107008].

[82] Z. Sullivan, in production, 2006.

[83] T. Sjostrand, L. Lonnblad and S. Mrenna, hep-ph/0108264.

[84] J. S. Conway *et al.*, Shw, in *Proceedings of the Workshop on Physics at Run II – Supersymmetry/Higgs*, p. 39, Fermilab, 1998, [hep-ph/0010338].

[85] B. W. Harris, E. Laenen, L. Phaf, Z. Sullivan and S. Weinzierl, Phys. Rev. **D66**, 054024 (2002), [hep-ph/0207055].

[86] Z. Sullivan, Phys. Rev. **D70**, 114012 (2004), [hep-ph/0408049].

[87] J. Campbell and R. K. Ellis, Phys. Rev. **D65**, 113007 (2002), [hep-ph/0202176].

[88] B. A. Dobrescu and C. T. Hill, Phys. Rev. Lett. **81**, 2634 (1998), [hep-ph/9712319].

[89] R. S. Chivukula, B. A. Dobrescu, H. Georgi and C. T. Hill, Phys. Rev. **D59**, 075003 (1999), [hep-ph/9809470].

[90] B. A. Dobrescu, Phys. Rev. **D63**, 015004 (2001), [hep-ph/9908391].

[91] H.-J. He, C. T. Hill and T. M. P. Tait, Phys. Rev. **D65**, 055006 (2002), [hep-ph/0108041].

[92] N. Arkani-Hamed, A. G. Cohen and H. Georgi, Phys. Lett. **B513**, 232 (2001), [hep-ph/0105239].

[93] M. Perelstein, M. E. Peskin and A. Pierce, Phys. Rev. **D69**, 075002 (2004), [hep-ph/0310039].

[94] T. Han, H. E. Logan, B. McElrath and L.-T. Wang, Phys. Rev. **D67**, 095004 (2003), [hep-ph/0301040].

[95] T. G. Rizzo, Phys. Rev. **D35**, 1677 (1987).

[96] H.-J. He, T. Tait and C. P. Yuan, Phys. Rev. **D62**, 011702 (2000), [hep-ph/9911266].

[97] D. Choudhury, T. M. P. Tait and C. E. M. Wagner, Phys. Rev. **D65**, 053002 (2002), [hep-ph/0109097].

[98] D. E. Morrissey and C. E. M. Wagner, Phys. Rev. **D69**, 053001 (2004), [hep-ph/0308001].

[99] T. C. Andre and J. L. Rosner, Phys. Rev. **D69**, 035009 (2004), [hep-ph/0309254].

[100] R. Mehdiyev, S. Sultansoy, G. nel and M. Yilmaz, ATLAS note: ATL-PHYS-PUB-2005-021.

[101] H. Collins, A. K. Grant and H. Georgi, Phys. Rev. **D61**, 055002 (2000), [hep-ph/9908330].

[102] G. Azuelos *et al.*, Eur. Phys. J. **C39S2**, 13 (2005), [hep-ph/0402037].

[103] G. Burdman, M. Perelstein and A. Pierce, Phys. Rev. Lett. **90**, 241802 (2003), [hep-ph/0212228].

[104] B. A. Dobrescu, C. T. Hill and T. M. Tait, In preparation.

[105] J. A. Aguilar-Saavedra, Phys. Lett. **B625**, 234 (2005), [hep-ph/0506187].

[106] M.-C. Chen and S. Dawson, Phys. Rev. **D70**, 015003 (2004), [hep-ph/0311032].

[107] M.-C. Chen and S. Dawson, hep-ph/0409163.

[108] M.-C. Chen, S. Dawson and T. Krupovnickas, hep-ph/0504286.

[109] N. Arkani-Hamed, A. G. Cohen, E. Katz and A. E. Nelson, JHEP **07**, 034 (2002), [hep-ph/0206021].

[110] T. Blank and W. Hollik, Nucl. Phys. **B514**, 113 (1998), [hep-ph/9703392].

[111] M. Czakon, J. Gluza, F. Jegerlehner and M. Zralek, Eur. Phys. J. **C13**, 275 (2000), [hep-ph/9909242].

[112] M. L. Perl *et al.*, Int. J. Mod. Phys. **A16**, 2137 (2001), [hep-ex/0102033].

[113] H1, A. Aktas *et al.*, Eur. Phys. J. **C36**, 413 (2004), [hep-ex/0403056].

[114] DELPHI, J. Abdallah *et al.*, Eur. Phys. J. **C26**, 505 (2003), [hep-ex/0303024].

[115] CDF, F. Abe *et al.*, Phys. Rev. **D46**, 1889 (1992).

[116] CDF, D. Acosta *et al.*, Phys. Rev. Lett. **90**, 131801 (2003), [hep-ex/0211064].

[117] CDF, C. Pagliarone, Searches for new physics at tevatron, in *Proc. of 15th Conference on High Energy Physics (IFAE 2003), Lecce, Italy, Apr 2003*, 2003.

[118] M. T. Eads, *A search for charged massive stable particles at D0*, PhD thesis, Northern Illinois University, 2005, UMI-31-85434.

[119] A. Nisati, S. Petrarca and G. Salvini, Mod. Phys. Lett. **A12**, 2213 (1997), [hep-ph/9707376].

[120] P. Zalewski, "Study of the NLSP from the GMSB models in the CMS detector at the LHC", CMS-CR-1999-019, 1999.

[121] G. Polesello *et al.*, "Measuring the SUSY Breaking Scale at the LHC in the Slepton NLSP Scenario of GMSB Models", ATL-PHYS-2002-006, 2002.

[122] S. Hellman, D. Milstead and M. Ramstedt, "A Strategy to Discover and Identify Gluino R-hadrons with the ATLAS Experiment at the LHC", ATL-PHYS-PUB-2006-005, 2005.

[123] A. C. Kraan, J. B. Hansen and P. Nevski, hep-ex/0511014.

[124] H. Baer, K.-m. Cheung and J. F. Gunion, Phys. Rev. **D59**, 075002 (1999), [hep-ph/9806361].

[125] S. Raby and K. Tobe, Nucl. Phys. **B539**, 3 (1999), [hep-ph/9807281].

[126] A. Mafi and S. Raby, Phys. Rev. **D62**, 035003 (2000), [hep-ph/9912436].

[127] A. C. Kraan, Eur. Phys. J. **C37**, 91 (2004), [hep-ex/0404001].

[128] N. Arkani-Hamed and S. Dimopoulos, JHEP **06**, 073 (2005), [hep-th/0405159].

[129] G. F. Giudice and A. Romanino, Nucl. Phys. **B699**, 65 (2004), [hep-ph/0406088].

[130] J. Polchinski and M. B. Wise, Phys. Lett. **B125**, 393 (1983).

[131] G. F. Giudice and A. Romanino, Phys. Lett. **B634**, 307 (2006), [hep-ph/0510197].

[132] J. R. Ellis and D. V. Nanopoulos, Phys. Lett. **B110**, 44 (1982).

[133] J. L. Hewett, B. Lillie, M. Masip and T. G. Rizzo, JHEP **09**, 070 (2004), [hep-ph/0408248].

[134] W. Kilian, T. Plehn, P. Richardson and E. Schmidt, Eur. Phys. J. **C39**, 229 (2005), [hep-ph/0408088].

[135] V. S. Kaplunovsky and J. Louis, Phys. Lett. **B306**, 269 (1993), [hep-th/9303040].

[136] C. H. Chen, M. Drees and J. F. Gunion, Phys. Rev. **D55**, 330 (1997), [hep-ph/9607421].

[137] S. Raby, Phys. Rev. **D56**, 2852 (1997), [hep-ph/9702299].

[138] G. D. Starkman, A. Gould, R. Esmailzadeh and S. Dimopoulos, Phys. Rev. **D41**, 3594 (1990).

[139] R. N. Mohapatra and S. Nussinov, Phys. Rev. **D57**, 1940 (1998), [hep-ph/9708497].

[140] M. Drees, An introduction to supersymmetry, in *Proc. of the Inaugural Conference of the Asia Pacific Centre for Theoretical Physics*, 1996, [hep-ph/9611409].

[141] R. Barbieri, L. J. Hall and Y. Nomura, Phys. Rev. **D63**, 105007 (2001), [hep-ph/0011311].

[142] C. Friberg, E. Norrbin and T. Sjostrand, Phys. Lett. **B403**, 329 (1997), [hep-ph/9704214].

[143] T. Appelquist, H.-C. Cheng and B. A. Dobrescu, Phys. Rev. **D64**, 035002 (2001), [hep-ph/0012100].

[144] G. Ingelman and C. Wetterich, Phys. Lett. **B174**, 109 (1986).

[145] P. H. Frampton and P. Q. Hung, Phys. Rev. **D58**, 057704 (1998), [hep-ph/9711218].

[146] H. Fritzsch, Phys. Lett. **B78**, 611 (1978).

[147] P. Fishbane, S. Meshkov and P. Ramond, Phys. Lett. **B134**, 81 (1984).

[148] P. A. M. Dirac, Proc. Roy. Soc. Lond. **A133**, 60 (1931).

[149] P. A. M. Dirac, Phys. Rev. **74**, 817 (1948).

[150] G. 't Hooft, Nucl. Phys. **B79**, 276 (1974).

[151] A. M. Polyakov, JETP Lett. **20**, 194 (1974).

[152] T. Sjostrand, S. Mrenna and P. Skands, JHEP **05**, 026 (2006), [hep-ph/0603175].

[153] B. Andersson, G. Gustafson, G. Ingelman and T. Sjöstrand, Phys. Rept. **97**, 31 (1983).

[154] http://www.thep.lu.se/~torbjorn/Pythia.html.

[155] C. Peterson, D. Schlatter, I. Schmitt and P. M. Zerwas, Phys. Rev. **D27**, 105 (1983).

[156] CDF, F. Abe *et al.*, Phys. Rev. **D45**, 1448 (1992).

[157] G. Altarelli, R. K. Ellis, G. Martinelli and S.-Y. Pi, Nucl. Phys. **B160**, 301 (1979).

[158] S. J. Brodsky and J. F. Gunion, Phys. Rev. Lett. **37**, 402 (1976).

[159] CERN Program Libary Long Writeup W5013.

[160] U. Sarid and S. D. Thomas, Phys. Rev. Lett. **85**, 1178 (2000), [hep-ph/9909349].

[161] S. Hellman, M. Johansen and D. Milstead, "Mass Measurements of R-hadrons with the ATLAS Experiment at the LHC", ATL-PHYS-PUB-2006-015, 2005.

[162] B. Baldwin *et al.*, "Technical Design of the Central Muon System", D0 Internal Note, 1998.

[163] W. Beenakker, R. Hopker, M. Spira and P. M. Zerwas, Z. Phys. **C69**, 163 (1995), [hep-ph/9505416].

[164] W. Beenakker, R. Hopker, M. Spira and P. M. Zerwas, Nucl. Phys. **B492**, 51 (1997), [hep-ph/9610490].

[165] H.-C. Cheng, K. T. Matchev and M. Schmaltz, Phys. Rev. **D66**, 056006 (2002), [hep-ph/0205314].

[166] J. L. Feng, M. E. Peskin, H. Murayama and X. Tata, Phys. Rev. **D52**, 1418 (1995), [hep-ph/9502260].

[167] M. Battaglia, A. Datta, A. De Roeck, K. Kong and K. T. Matchev, JHEP **07**, 033 (2005), [hep-ph/0502041].

[168] G. Bhattacharyya, P. Dey, A. Kundu and A. Raychaudhuri, Phys. Lett. **B628**, 141 (2005), [hep-ph/0502031].

[169] B. Bhattacherjee and A. Kundu, Phys. Lett. **B627**, 137 (2005), [hep-ph/0508170].

[170] S. Riemann, hep-ph/0508136.

[171] P. Bechtle, K. Desch and P. Wienemann, Comput. Phys. Commun. **174**, 47 (2006), [hep-ph/0412012].

[172] R. Lafaye, T. Plehn and D. Zerwas, hep-ph/0404282.

[173] P. Meade and M. Reece, hep-ph/0601124.

[174] A. Datta, G. L. Kane and M. Toharia, hep-ph/0510204.

[175] N. Arkani-Hamed, G. L. Kane, J. Thaler and L.-T. Wang, hep-ph/0512190.

[176] A. J. Barr, Phys. Lett. **B596**, 205 (2004), [hep-ph/0405052].

[177] A. J. Barr, hep-ph/0511115.

[178] A. Datta, K. Kong and K. T. Matchev, Phys. Rev. **D72**, 096006 (2005), [hep-ph/0509246].

[179] M. Battaglia, A. K. Datta, A. De Roeck, K. Kong and K. T. Matchev, hep-ph/0507284.

[180] J. M. Smillie and B. R. Webber, JHEP **10**, 069 (2005), [hep-ph/0507170].

[181] K. Kong and K. T. Matchev, (2006).

[182] A. Alves, O. Eboli and T. Plehn, hep-ph/0605067.

[183] G. Servant and T. M. P. Tait, Nucl. Phys. **B650**, 391 (2003).

[184] M. Kakizaki, S. Matsumoto, Y. Sato and M. Senami, Nucl. Phys. **B735**, 84 (2006), [hep-ph/0508283].

[185] F. Burnell and G. D. Kribs, Phys. Rev. **D73**, 015001 (2006), [hep-ph/0509118].

[186] K. Kong and K. T. Matchev, JHEP **01**, 038 (2006), [hep-ph/0509119].

[187] H.-C. Cheng, J. L. Feng and K. T. Matchev, Phys. Rev. Lett. **89**, 211301 (2002), [hep-ph/0207125].

[188] N. Arkani-Hamed, S. Dimopoulos and G. R. Dvali, Phys. Lett. **B429**, 263 (1998), [hep-ph/9803315].

[189] G. F. Giudice, R. Rattazzi and J. D. Wells, Nucl. Phys. **B544**, 3 (1999), [hep-ph/9811291].

[190] E. A. Mirabelli, M. Perelstein and M. E. Peskin, Phys. Rev. Lett. **82**, 2236 (1999), [hep-ph/9811337].

[191] G. Burdman, B. A. Dobrescu and E. Ponton, hep-ph/0601186.

[192] H.-C. Cheng and I. Low, JHEP **09**, 051 (2003), [hep-ph/0308199].

[193] H.-C. Cheng and I. Low, JHEP **08**, 061 (2004), [hep-ph/0405243].

[194] J. Hubisz and P. Meade, Phys. Rev. **D71**, 035016 (2005), [hep-ph/0411264].

[195] H.-C. Cheng, I. Low and L.-T. Wang, hep-ph/0510225.

[196] H.-C. Cheng, K. T. Matchev and M. Schmaltz, Phys. Rev. **D66**, 036005 (2002), [hep-ph/0204342].

[197] F. E. Paige, S. D. Protopopescu, H. Baer and X. Tata, hep-ph/0312045.

[198] B. C. Allanach *et al.*, Eur. Phys. J. **C25**, 113 (2002), (see www.ippp.dur.ac.uk/˜georg/sps/).

[199] H. Bachacou, I. Hinchliffe and F. E. Paige, Phys. Rev. **D62**, 015009 (2000), [hep-ph/9907518].

[200] B. C. Allanach, C. G. Lester, M. A. Parker and B. R. Webber, JHEP **09**, 004 (2000), [hep-ph/0007009].

[201] B. K. Gjelsten, D. J. Miller and P. Osland, JHEP **12**, 003 (2004), [hep-ph/0410303].

[202] H. Georgi, A. K. Grant and G. Hailu, Phys. Lett. **B506**, 207 (2001), [hep-ph/0012379].

[203] G. von Gersdorff, N. Irges and M. Quiros, Nucl. Phys. **B635**, 127 (2002), [hep-th/0204223].

[204] K. Agashe, N. G. Deshpande and G. H. Wu, Phys. Lett. **B511**, 85 (2001), [hep-ph/0103235].

[205] K. Agashe, N. G. Deshpande and G. H. Wu, Phys. Lett. **B514**, 309 (2001), [hep-ph/0105084].

[206] T. Appelquist and B. A. Dobrescu, Phys. Lett. **B516**, 85 (2001), [hep-ph/0106140].

[207] F. J. Petriello, JHEP **05**, 003 (2002), [hep-ph/0204067].

[208] T. Appelquist and H.-U. Yee, Phys. Rev. **D67**, 055002 (2003), [hep-ph/0211023].

[209] D. Chakraverty, K. Huitu and A. Kundu, Phys. Lett. **B558**, 173 (2003), [hep-ph/0212047].

[210] A. J. Buras, M. Spranger and A. Weiler, Nucl. Phys. **B660**, 225 (2003), [hep-ph/0212143].

[211] J. F. Oliver, J. Papavassiliou and A. Santamaria, Phys. Rev. **D67**, 056002 (2003), [hep-ph/0212391].

[212] A. J. Buras, A. Poschenrieder, M. Spranger and A. Weiler, Nucl. Phys. **B678**, 455 (2004), [hep-ph/0306158].

[213] E. O. Iltan, JHEP **02**, 065 (2004), [hep-ph/0312311].

[214] S. Khalil and R. Mohapatra, Nucl. Phys. **B695**, 313 (2004), [hep-ph/0402225].

[215] K. R. Dienes, E. Dudas and T. Gherghetta, Nucl. Phys. **B537**, 47 (1999), [hep-ph/9806292].

[216] A. Perez-Lorenzana and R. N. Mohapatra, Nucl. Phys. **B559**, 255 (1999), [hep-ph/9904504].

[217] H.-C. Cheng, B. A. Dobrescu and C. T. Hill, Nucl. Phys. **B573**, 597 (2000), [hep-ph/9906327].

[218] A. Pukhov *et al.*, hep-ph/9908288.

[219] T. G. Rizzo, Phys. Rev. **D64**, 095010 (2001), [hep-ph/0106336].

[220] C. Macesanu, C. D. McMullen and S. Nandi, Phys. Rev. **D66**, 015009 (2002), [hep-ph/0201300].

[221] CTEQ, H. L. Lai *et al.*, Eur. Phys. J. **C12**, 375 (2000), [hep-ph/9903282].

[222] D. Acosta, private communication.

[223] D. Bourilkov, talk given at the LPC Muon Meeting, Fermilab, December 2004.

[224] T. Sjostrand, L. Lonnblad, S. Mrenna and P. Skands, hep-ph/0308153 (2003), [hep-ph/0308153].

[225] CDF-II, R. Blair *et al.*, FERMILAB-PUB-96-390-E.

[226] C. Macesanu, C. D. McMullen and S. Nandi, Phys. Lett. **B546**, 253 (2002), [hep-ph/0207269].

[227] C. Macesanu, S. Nandi and M. Rujoiu, Phys. Rev. **D71**, 036003 (2005), [hep-ph/0407253].

[228] M. Byrne, Phys. Lett. **B583**, 309 (2004), [hep-ph/0311160].

[229] J. L. Feng, A. Rajaraman and F. Takayama, Phys. Rev. Lett. **91**, 011302 (2003), [hep-ph/0302215].

[230] J. L. Feng, S. Su and F. Takayama, hep-ph/0503117.

[231] N. Arkani-Hamed, S. Dimopoulos and G. R. Dvali, Phys. Rev. **D59**, 086004 (1999), [hep-ph/9807344].

[232] I. Antoniadis, N. Arkani-Hamed, S. Dimopoulos and G. R. Dvali, Phys. Lett. **B436**, 257 (1998), [hep-ph/9804398].

[233] C. Macesanu, S. Nandi and C. M. Rujoiu, Phys. Rev. **D73**, 076001 (2006), [hep-ph/0510350].

[234] C. Macesanu, A. Mitov and S. Nandi, Phys. Rev. **D68**, 084008 (2003), [hep-ph/0305029].

[235] P. Skands *et al.*, Presented at Les Houches Workshop on Physics at TeV Colliders, Les Houches, France, 2-20 May 2005.

[236] E. Boos *et al.*, hep-ph/0109068.

[237] J. A. Aguilar-Saavedra *et al.*, Eur. Phys. J. **C46**, 43 (2006), [hep-ph/0511344].

[238] L. Lonnblad, Nucl. Instrum. Meth. **A559**, 246 (2006).

[239] P. Mathews, V. Ravindran, K. Sridhar and W. L. van Neerven, Nucl. Phys. **B713**, 333 (2005), [hep-ph/0411018].

[240] M. C. Kumar, P. Mathews and V. Ravindran, hep-ph/0604135.

[241] ATLAS, S. Ferrag, hep-ph/0407303.

[242] S. Alekhin *et al.*, hep-ph/0601013.

[243] S. Alekhin *et al.*, hep-ph/0601012.

[244] LHC/LC Study Group, G. Weiglein *et al.*, Phys. Rept. **426**, 47 (2006), [hep-ph/0410364].

[245] J. Hubisz and P. Skands, Presented at Miniworkshop on Monte Carlo Tools for Beyond the Standard Model Physics (MC4BSM), Batavia, Illinois, 20- 21 Mar 2006.

[246] H. Georgi and A. Pais, Phys. Rev. **D12**, 508 (1975).

[247] H. Georgi and A. Pais, Phys. Rev. **D10**, 539 (1974).

[248] M. J. Dugan, H. Georgi and D. B. Kaplan, Nucl. Phys. **B254**, 299 (1985).

[249] H. Georgi and D. B. Kaplan, Phys. Lett. **B145**, 216 (1984).

[250] H. Georgi, D. B. Kaplan and P. Galison, Phys. Lett. **B143**, 152 (1984).

[251] D. B. Kaplan, H. Georgi and S. Dimopoulos, Phys. Lett. **B136**, 187 (1984).

[252] D. B. Kaplan and H. Georgi, Phys. Lett. **B136**, 183 (1984).

[253] C. Csaki, J. Hubisz, G. D. Kribs, P. Meade and J. Terning, Phys. Rev. **D67**, 115002 (2003), [hep-ph/0211124].

[254] C. Csaki, J. Hubisz, G. D. Kribs, P. Meade and J. Terning, Phys. Rev. **D68**, 035009 (2003), [hep-ph/0303236].

[255] J. L. Hewett, F. J. Petriello and T. G. Rizzo, JHEP **10**, 062 (2003), [hep-ph/0211218].

[256] I. Low, JHEP **10**, 067 (2004), [hep-ph/0409025].

[257] WMAP, D. N. Spergel *et al.*, Astrophys. J. Suppl. **148**, 175 (2003), [astro-ph/0302209].

[258] J. Hubisz, P. Meade, A. Noble and M. Perelstein, JHEP **01**, 135 (2006), [hep-ph/0506042].

[259] CDF, F. Abe *et al.*, Phys. Rev. Lett. **83**, 3124 (1999), [hep-ex/9810031].

[260] CDF, A. A. Affolder *et al.*, Phys. Rev. Lett. **84**, 1110 (2000).

[261] CDF, A. Abulencia *et al.*, Phys. Rev. Lett. **96**, 081803 (2006), [hep-ex/0512051].

[262] K. D. Lane, Phys. Rev. **D60**, 075007 (1999), [hep-ph/9903369].

[263] K. Lane and S. Mrenna, Phys. Rev. **D67**, 115011 (2003), [hep-ph/0210299].

[264] S. Weinberg, Phys. Rev. **D19**, 1277 (1979).

[265] L. Susskind, Phys. Rev. **D20**, 2619 (1979).

[266] E. Eichten and K. D. Lane, Phys. Lett. **B90**, 125 (1980).

[267] K. Lane, hep-ph/0202255.

[268] C. T. Hill and E. H. Simmons, Phys. Rept. **381**, 235 (2003), [hep-ph/0203079].

[269] B. Holdom, Phys. Rev. **D24**, 1441 (1981).

[270] T. W. Appelquist, D. Karabali and L. C. R. Wijewardhana, Phys. Rev. Lett. **57**, 957 (1986).

[271] K. Yamawaki, M. Bando and K.-i. Matumoto, Phys. Rev. Lett. **56**, 1335 (1986).

[272] T. Akiba and T. Yanagida, Phys. Lett. **B169**, 432 (1986).

[273] C. T. Hill, Phys. Lett. **B345**, 483 (1995), [hep-ph/9411426].

[274] K. D. Lane and E. Eichten, Phys. Lett. **B222**, 274 (1989).

[275] D. D. Dietrich, F. Sannino and K. Tuominen, Phys. Rev. **D72**, 055001 (2005), [hep-ph/0505059].

[276] N. Evans and F. Sannino, hep-ph/0512080.

[277] K. D. Lane and M. V. Ramana, Phys. Rev. **D44**, 2678 (1991).

[278] T. Appelquist, M. Piai and R. Shrock, Phys. Rev. **D69**, 015002 (2004), [hep-ph/0308061].

[279] D0, V. M. Abazov *et al.*, Phys. Rev. Lett. **87**, 061802 (2001), [hep-ex/0102048].

[280] F. del Aguila and L. Ametller, Phys. Lett. **B261**, 326 (1991).

[281] H. Baer, C.-h. Chen, F. Paige and X. Tata, Phys. Rev. **D49**, 3283 (1994), [hep-ph/9311248].

[282] H. Baer, C.-h. Chen, F. Paige and X. Tata, Phys. Rev. **D53**, 6241 (1996), [hep-ph/9512383].

[283] N. V. Krasnikov, JETP Lett. **65**, 148 (1997), [hep-ph/9611282].

[284] S. I. Bityukov and N. V. Krasnikov, Phys. Atom. Nucl. **62**, 1213 (1999), [hep-ph/9712358].

[285] S. I. Bityukov and N. V. Krasnikov, hep-ph/9806504.

[286] Y. M. Andreev, S. I. Bityukov and N. V. Krasnikov, Phys. Atom. Nucl. **68**, 340 (2005), [hep-ph/0402229].

[287] A. Birkedal, K. Matchev and M. Perelstein, Phys. Rev. **D70**, 077701 (2004), [hep-ph/0403004].

[288] M. Drees and M. M. Nojiri, Phys. Rev. **D47**, 376 (1993), [hep-ph/9207234].

[289] T. Nihei, L. Roszkowski and R. Ruiz de Austri, JHEP **03**, 031 (2002), [hep-ph/0202009].

[290] A. Birkedal-Hansen and E.-h. Jeong, JHEP **02**, 047 (2003), [hep-ph/0210041].

[291] A. Birkedal-Hansen and B. D. Nelson, Phys. Rev. **D64**, 015008 (2001), [hep-ph/0102075].

[292] A. Birkedal-Hansen, Nucl. Phys. Proc. Suppl. **124**, 155 (2003), [hep-ph/0204176].

[293] P. Binetruy, A. Birkedal-Hansen, Y. Mambrini and B. D. Nelson, hep-ph/0308047.

[294] S. Mizuta, D. Ng and M. Yamaguchi, Phys. Lett. **B300**, 96 (1993), [hep-ph/9210241].

[295] A. Corsetti and P. Nath, Phys. Rev. **D64**, 125010 (2001), [hep-ph/0003186].

[296] V. Bertin, E. Nezri and J. Orloff, JHEP **02**, 046 (2003), [hep-ph/0210034].

[297] A. Birkedal-Hansen and B. D. Nelson, Phys. Rev. **D67**, 095006 (2003), [hep-ph/0211071].

[298] A. Birkedal-Hansen, hep-ph/0306144.

[299] J. L. Feng, K. T. Matchev and T. Moroi, Phys. Rev. Lett. **84**, 2322 (2000), [hep-ph/9908309].

[300] J. L. Feng, K. T. Matchev and T. Moroi, Phys. Rev. **D61**, 075005 (2000), [hep-ph/9909334].

[301] J. L. Feng, K. T. Matchev and F. Wilczek, Phys. Lett. **B482**, 388 (2000), [hep-ph/0004043].

[302] J. L. Feng and K. T. Matchev, Phys. Rev. **D63**, 095003 (2001), [hep-ph/0011356].

[303] A. Birkedal, R. C. Group and K. Matchev, hep-ph/0507002.

[304] I. Hinchliffe, F. E. Paige, M. D. Shapiro, J. Soderqvist and W. Yao, Phys. Rev. **D55**, 5520 (1997), [hep-ph/9610544].

[305] D. J. Miller, P. Osland and A. R. Raklev, JHEP **03**, 034 (2006), [hep-ph/0510356].

[306] K. Kong and K. Matchev, These Proceedings.

[307] A. Bartl *et al.*, ECONF **C960625**, SUP112 (1996).

[308] D. Delepine, J. M. Gerard, R. Gonzalez Felipe and J. Weyers, Phys. Lett. **B386**, 183 (1996), [hep-ph/9604440].

[309] M. Carena, M. Quiros and C. E. M. Wagner, Nucl. Phys. **B524**, 3 (1998), [hep-ph/9710401].

[310] J. M. Cline and G. D. Moore, Phys. Rev. Lett. **81**, 3315 (1998), [hep-ph/9806354].

[311] C. Balazs, M. Carena and C. E. M. Wagner, Phys. Rev. **D70**, 015007 (2004), [hep-ph/0403224].

[312] R. Demina, J. D. Lykken, K. T. Matchev and A. Nomerotski, Phys. Rev. **D62**, 035011 (2000), [hep-ph/9910275].

[313] S. Kraml and A. R. Raklev, Phys. Rev. **D73**, 075002 (2006), [hep-ph/0512284].

[314] B. C. Allanach *et al.*, hep-ph/0602198.

[315] W. Beenakker, R. Hopker and M. Spira, hep-ph/9611232.

[316] E. Richter-Was, hep-ph/0207355.

[317] ATLAS, CERN-LHCC-97-16.

[318] C. G. Lester, CERN-THESIS-2004-003.

[319] A. D. Sakharov, Pisma Zh. Eksp. Teor. Fiz. **5**, 32 (1967).

[320] A. G. Cohen, D. B. Kaplan and A. E. Nelson, Ann. Rev. Nucl. Part. Sci. **43**, 27 (1993), [hep-ph/9302210].

[321] M. Quiros, Helv. Phys. Acta **67**, 451 (1994).

[322] V. A. Rubakov and M. E. Shaposhnikov, Usp. Fiz. Nauk **166**, 493 (1996), [hep-ph/9603208].

[323] A. Riotto and M. Trodden, Ann. Rev. Nucl. Part. Sci. **49**, 35 (1999), [hep-ph/9901362].

[324] M. Quiros and M. Seco, Nucl. Phys. Proc. Suppl. **81**, 63 (2000), [hep-ph/9903274].

[325] G. 't Hooft, Phys. Rev. **D14**, 3432 (1976).

[326] N. S. Manton, Phys. Rev. **D28**, 2019 (1983).

[327] F. R. Klinkhamer and N. S. Manton, Phys. Rev. **D30**, 2212 (1984).

[328] D. Bodeker, Phys. Lett. **B426**, 351 (1998), [hep-ph/9801430].

[329] P. Arnold and L. G. Yaffe, Phys. Rev. **D62**, 125014 (2000), [hep-ph/9912306].

[330] P. Arnold, Phys. Rev. **D62**, 036003 (2000), [hep-ph/9912307].

[331] G. D. Moore and K. Rummukainen, Phys. Rev. **D61**, 105008 (2000), [hep-ph/9906259].

[332] G. D. Moore, Phys. Rev. **D62**, 085011 (2000), [hep-ph/0001216].

[333] A. I. Bochkarev and M. E. Shaposhnikov, Mod. Phys. Lett. **A2**, 417 (1987).

[334] M. Carena, M. Quiros and C. E. M. Wagner, Phys. Lett. **B380**, 81 (1996), [hep-ph/9603420].

[335] M. Laine, Nucl. Phys. **B481**, 43 (1996), [hep-ph/9605283].

[336] M. Losada, Phys. Rev. **D56**, 2893 (1997), [hep-ph/9605266].

[337] G. R. Farrar and M. Losada, Phys. Lett. **B406**, 60 (1997), [hep-ph/9612346].

[338] B. de Carlos and J. R. Espinosa, Nucl. Phys. **B503**, 24 (1997), [hep-ph/9703212].

[339] D. Bodeker, P. John, M. Laine and M. G. Schmidt, Nucl. Phys. **B497**, 387 (1997), [hep-ph/9612364].

[340] M. Laine and K. Rummukainen, Nucl. Phys. **B535**, 423 (1998), [hep-lat/9804019].

[341] M. Losada, Nucl. Phys. **B537**, 3 (1999), [hep-ph/9806519].

[342] M. Losada, Nucl. Phys. **B569**, 125 (2000), [hep-ph/9905441].

[343] M. Laine and M. Losada, Nucl. Phys. **B582**, 277 (2000), [hep-ph/0003111].

[344] M. Laine and K. Rummukainen, Nucl. Phys. **B597**, 23 (2001), [hep-lat/0009025].

[345] ALEPH, DELPHI, L3 and OPAL Collaborations, and the LEP Working Group for Higgs boson searches, Phys. Lett. **B565**, 61 (2003), [hep-ex/0306033].

[346] J. R. Ellis, G. Ridolfi and F. Zwirner, Phys. Lett. **B257**, 83 (1991).

[347] Y. Okada, M. Yamaguchi and T. Yanagida, Prog. Theor. Phys. **85**, 1 (1991).

[348] H. E. Haber and R. Hempfling, Phys. Rev. Lett. **66**, 1815 (1991).

[349] C. Balazs, M. Carena, A. Menon, D. E. Morrissey and C. E. M. Wagner, Phys. Rev. **D71**, 075002 (2005), [hep-ph/0412264].

[350] CDF, A. A. Affolder *et al.*, Phys. Rev. Lett. **84**, 5704 (2000), [hep-ex/9910049].

[351] D0, S. Abachi *et al.*, Phys. Rev. Lett. **76**, 2222 (1996).

[352] M. Carena, D. Choudhury, R. A. Diaz, H. E. Logan and C. E. M. Wagner, Phys. Rev. **D66**, 115010 (2002), [hep-ph/0206167].

[353] E. L. Berger, B. W. Harris and Z. Sullivan, Phys. Rev. Lett. **83**, 4472 (1999), [hep-ph/9903549].

[354] C.-L. Chou and M. E. Peskin, Phys. Rev. **D61**, 055004 (2000), [hep-ph/9909536].

[355] S. Heinemeyer, W. Hollik and G. Weiglein, Eur. Phys. J. **C9**, 343 (1999), [hep-ph/9812472].

[356] G. Degrassi, S. Heinemeyer, W. Hollik, P. Slavich and G. Weiglein, Eur. Phys. J. **C28**, 133 (2003), [hep-ph/0212020].

[357] M. Carena *et al.*, Phys. Rev. **D72**, 115008 (2005), [hep-ph/0508152].

[358] G. Moortgat-Pick *et al.*, hep-ph/0507011.

[359] H. E. Haber and G. L. Kane, Phys. Rept. **117**, 75 (1985).

[360] R. Barbieri, Riv. Nuovo Cim. **11N4**, 1 (1988).

[361] S. L. Glashow, Nucl. Phys. **22**, 579 (1961).

[362] S. Weinberg, Phys. Rev. Lett. **19**, 1264 (1967).

[363] A. Salam, Originally printed in *Svartholm: Elementary Particle Theory, Proceedings Of The Nobel Symposium Held 1968 At Lerum, Sweden*, Stockholm 1968, 367-377.

[364] SUGRA Working Group, S. Abel *et al.*, hep-ph/0003154.

[365] ECFA/DESY LC Physics Working Group, J. A. Aguilar-Saavedra *et al.*, hep-ph/0106315.

[366] American Linear Collider Working Group, T. Abe *et al.*, hep-ex/0106055.

[367] American Linear Collider Working Group, T. Abe *et al.*, hep-ex/0106056.

[368] American Linear Collider Working Group, T. Abe *et al.*, hep-ex/0106057.

[369] ACFA Linear Collider Working Group, K. Abe *et al.*, hep-ph/0109166.

[370] C. L. Bennett *et al.*, Astrophys. J. Suppl. **148**, 1 (2003).

[371] H. Goldberg, Phys. Rev. Lett. **50**, 1419 (1983).

[372] J. R. Ellis, J. S. Hagelin, D. V. Nanopoulos, K. A. Olive and M. Srednicki, Nucl. Phys. **B238**, 453 (1984).

[373] J. R. Ellis, K. A. Olive, Y. Santoso and V. C. Spanos, Phys. Lett. **B565**, 176 (2003).

[374] J. R. Ellis, S. Heinemeyer, K. A. Olive and G. Weiglein, JHEP **02**, 013 (2005), [hep-ph/0411216].

[375] K. T. Matchev and D. M. Pierce, Phys. Rev. **D60**, 075004 (1999), [hep-ph/9904282].

[376] A. Czarnecki and W. J. Marciano, Phys. Rev. **D64**, 013014 (2001), [hep-ph/0102122].

[377] M. Knecht, Lect. Notes Phys. **629**, 37 (2004), [hep-ph/0307239].

[378] Muon g-2, G. W. Bennett *et al.*, Phys. Rev. Lett. **92**, 161802 (2004), [hep-ex/0401008].

[379] T. Moroi, Phys. Rev. **D53**, 6565 (1996), [hep-ph/9512396].

[380] K. Desch, Prepared for International Conference on 20 Years of SUGRA and Search for SUSY and Unification (SUGRA 20), Boston, Massachusetts, 17-20 Mar 2003.

[381] J. B. de Vivie, Prepared for 32nd International Conference on High-Energy Physics (ICHEP 04), Beijing, China, 16-22 Aug 2004.

[382] A. C. Kraan, hep-ex/0505002.

[383] G. Pasztor, PoS **HEP2005**, 346 (2006), [hep-ex/0512054].

[384] B. Heinemann.

[385] ALEPH, hep-ex/0602042.

[386] D0, V. M. Abazov *et al.*, Phys. Rev. Lett. **95**, 151801 (2005), [hep-ex/0504018].

[387] CDF, A. *et al*. Abulencia, Phys. Rev. Lett. **96**, 011802 (2006), [hep-ex/0508051].

[388] R. Eusebi, *Search for charged Higgs in $t\bar{t}$ decay products from proton-antiproton collisions at $\sqrt{s} = 1.96\,\mathrm{TeV}$*, PhD thesis, University of Rochester, 2005, CDF Collaboration. hep-ex/0510065, CDF Note 7250.

[389] M. W. Grunewald, hep-ex/0304023.

[390] C. Diaconu, talk given at Lepton-Photon 2005, Uppsala, Sweden, June 2005.

[391] J. R. Ellis, S. Heinemeyer, K. A. Olive and G. Weiglein, JHEP **05**, 005 (2006), [hep-ph/0602220].

[392] Volume 2 of the CMS physics TDR, CERN/LHCC 2006-021.

[393] M. Battaglia *et al.*, Eur. Phys. J. **C33**, 273 (2004), [hep-ph/0306219].

[394] H. Baer *et al.*, (1999), hep-ph/0001086.

[395] A. P. etal., (1999), [hep-ph/9908288].

[396] V. Bartsch, PhD thesis, CMS, 2003.

[397] CMS, see http://cmsdoc.cern.ch/cmsim/cmsim.html, http://cmsdoc.cern.ch/orca/.

[398] CMS, the TriDAS Project Technical Design Report, Volume 2, CERN, 2002.

[399] H. Wellisch, CMS Note 1999/034.

[400] S. I. Bityukov and N. V. Krasnikov, hep-ph/0204326.

[401] S. Heinemeyer, W. Hollik and G. Weiglein, Comput. Phys. Commun. **124**, 76 (2000), [hep-ph/9812320].

[402] G. Degrassi, S. Heinemeyer, W. Hollik, P. Slavich and G. Weiglein, Eur. Phys. J. **C 28**, 133 (2003), [hep-ph/0212020].

[403] H. Baer *et al.*, JHEP **07**, 050 (2002), [hep-ph/0205325].

[404] H. Baer *et al.*, hep-ph/0210441.

[405] CLEO, D. Cronin-Hennessy *et al.*, Phys. Rev. Lett. **87**, 251808 (2001), [hep-ex/0108033].

[406] Belle, K. Abe *et al.*, Phys. Lett. **B511**, 151 (2001), [hep-ex/0103042].

[407] H. Baer and M. Brhlik, Phys. Rev. **D55**, 3201 (1997), [hep-ph/9610224].

[408] H. Baer, M. Brhlik, D. Castano and X. Tata, Phys. Rev. **D58**, 015007 (1998), [hep-ph/9712305].

[409] Muon g-2, G. W. Bennett *et al.*, Phys. Rev. Lett. **89**, 101804 (2002), [hep-ex/0208001].

[410] H. Baer *et al.*, Phys. Rev. **D64**, 035004 (2001).

[411] A. H. Chamseddine, R. Arnowitt and P. Nath, Phys. Rev. Lett. **49**, 970 (1982).

[412] R. Barbieri, S. Ferrara and C. A. Savoy, Phys. Lett. **B119**, 343 (1982).

[413] N. Ohta, Prog. Theor. Phys. **70**, 542 (1983).

[414] L. J. Hall, J. D. Lykken and S. Weinberg, Phys. Rev. **D27**, 2359 (1983).

[415] J. R. Ellis, T. Falk and K. A. Olive, Phys. Lett. **B444**, 367 (1998), [hep-ph/9810360].

[416] J. R. Ellis, T. Falk, K. A. Olive and M. Srednicki, Astropart. Phys. **13**, 181 (2000), [hep-ph/9905481].

[417] H. Baer and M. Brhlik, Phys. Rev. **D53**, 597 (1996), [hep-ph/9508321].

[418] H. Baer and M. Brhlik, Phys. Rev. **D57**, 567 (1998), [hep-ph/9706509].

[419] H. Baer *et al.*, Phys. Rev. **D63**, 015007 (2001), [hep-ph/0005027].

[420] G. F. R. Ellis, H. van Elst and R. Maartens, Class. Quant. Grav. **18**, 5115 (2001), [gr-qc/0105083].

[421] A. B. Lahanas and V. C. Spanos, Eur. Phys. J. **C23**, 185 (2002), [hep-ph/0106345].

[422] C. Boehm, A. Djouadi and M. Drees, Phys. Rev. **D62**, 035012 (2000), [hep-ph/9911496].

[423] J. R. Ellis, K. A. Olive and Y. Santoso, Astropart. Phys. **18**, 395 (2003), [hep-ph/0112113].

[424] H. Baer, T. Krupovnickas and X. Tata, JHEP **06**, 061 (2004), [hep-ph/0405058].

[425] H. Baer, M. Drees, F. Paige, P. Quintana and X. Tata, Phys. Rev. **D61**, 095007 (2000), [hep-ph/9906233].

[426] H. Baer, T. Krupovnickas and X. Tata, JHEP **07**, 020 (2003), [hep-ph/0305325].

[427] H. Baer, C. Balazs, A. Belyaev, T. Krupovnickas and X. Tata, JHEP **06**, 054 (2003), [hep-ph/0304303].

[428] H. Baer, A. Belyaev, T. Krupovnickas and X. Tata, JHEP **02**, 007 (2004), [hep-ph/0311351].

[429] H. Baer, A. Belyaev, T. Krupovnickas and J. O'Farrill, JCAP **0408**, 005 (2004), [hep-ph/0405210].

[430] The IceCube, J. Ahrens *et al.*, Nucl. Phys. Proc. Suppl. **118**, 388 (2003), [astro-ph/0209556].

[431] F. Halzen and D. Hooper, JCAP **0401**, 002 (2004), [astro-ph/0310152].

[432] D. B. Cline *et al.*, Nucl. Phys. Proc. Suppl. **124**, 229 (2003).

[433] Xenon, Y. Suzuki, Low energy solar neutrino detection by using liquid xenon, hep-ph/0008296, 2000.

[434] R. Brunetti *et al.*, WARP liquid argon detector for dark matter survey, astro-ph/0405342, 2004.

[435] H. Baer, T. Krupovnickas, S. Profumo and P. Ullio, JHEP **10**, 020 (2005), [hep-ph/0507282].

[436] P. G. Mercadante, J. K. Mizukoshi and X. Tata, Phys. Rev. **D72**, 035009 (2005), [hep-ph/0506142].

[437] S. P. Martin, hep-ph/9709356.

[438] X. Tata, hep-ph/9706307.

[439] D. J. H. Chung *et al.*, Phys. Rept. **407**, 1 (2005).

[440] S. Coleman and J. Mandula, Phys. Rev. **159**, 1251 (1967).

[441] R. Haag, J. T. Lopuszanski and M. Sohnius, Nucl. Phys. **B**, 257 (1975).

[442] P. Skands *et al.*, JHEP **07**, 036 (2004), [hep-ph/0311123].

[443] Beyond the Standard Model Working Group, B. C. Allanach *et al.*, hep-ph/0402295.

[444] B. C. Allanach *et al.*, The SUSY Les Houches Accord II Project, FERMILAB-CONF-05-517-T. To appear in Les Houches 'Physics at TeV Colliders 2005' BSM Working Group: Summary report, 2006.

[445] P. Skands *et al.*, A repository for beyond-the-standard-model tools, FERMILAB-CONF-05-521-T. To appear in Les Houches 'Physics at TeV Colliders 2005' BSM Working Group: Summary report. See also:
http://www.ippp.dur.ac.uk/montecarlo/BSM/, 2006.

[446] M. A. Dobbs *et al.*, hep-ph/0403045.

[447] J. F. Gunion and H. E. Haber, Nucl. Phys. **B272**, 1 (1986), [Erratum-ibid. **B402**, 567 (1993)].

[448] W. Siegel, Phys. Lett. **B84**, 193 (1979).

[449] D. M. Capper, D. R. T. Jones and P. van Nieuwenhuizen, Nucl. Phys. **B167**, 479 (1980).

[450] I. Jack, D. R. T. Jones, S. P. Martin, M. T. Vaughn and Y. Yamada, Phys. Rev. **D50**, 5481 (1994), [hep-ph/9407291].

[451] H. Baer, F. E. Paige, S. D. Protopopescu and X. Tata, hep-ph/9305342.

[452] B. C. Allanach, Comput. Phys. Commun. **143**, 305 (2002).

[453] W. Porod, Comput. Phys. Commun. **153**, 275 (2003), [hep-ph/0301101].

[454] A. Djouadi, J.-L. Kneur and G. Moultaka, hep-ph/0211331.

[455] G. Belanger, S. Kraml and A. Pukhov, Phys. Rev. **D72**, 015003 (2005), [hep-ph/0502079].

[456] B. C. Allanach, S. Kraml and W. Porod, JHEP **03**, 016 (2003), [hep-ph/0302102].

[457] B. C. Allanach, A. Djouadi, J. L. Kneur, W. Porod and P. Slavich, JHEP **09**, 044 (2004), [hep-ph/0406166].

[458] S. Mrenna, Comput. Phys. Commun. **101**, 232 (1997), [hep-ph/9609360].

[459] J. S. Lee *et al.*, Comput. Phys. Commun. **156**, 283 (2004).

[460] U. Ellwanger, J. F. Gunion and C. Hugonie, JHEP **02**, 066 (2005), [hep-ph/0406215].

[461] M. Muhlleitner, A. Djouadi and Y. Mambrini, Comput. Phys. Commun. **168**, 46 (2005), [hep-ph/0311167].

[462] A. Djouadi, J. Kalinowski and M. Spira, Comput. Phys. Commun. **108**, 56 (1998).

[463] A. Djouadi, M. M. Muhlleitner and M. Spira, hep-ph/0609292.

[464] P. Gondolo *et al.*, JCAP **0407**, 008 (2004), [astro-ph/0406204].

[465] H. Baer, C. Balazs, A. Belyaev and J. O'Farrill, JCAP **0309**, 007 (2003), see http://www.phy.bnl.gov/$"sim$isajet/.

[466] G. Belanger, F. Boudjema, A. Pukhov and A. Semenov, Comput. Phys. Commun. **149**, 103 (2002), [hep-ph/0112278].

[467] G. Bélanger, F. Boudjema, A. Pukhov and A. Semenov, micrOMEGAS2.0 and the relic density of dark matter in a generic model, To appear in Les Houches 'Physics at TeV Colliders 2005' BSM Working Group: Summary report, 2006.

[468] G. Belanger, F. Boudjema, C. Hugonie, A. Pukhov and A. Semenov, JCAP **0509**, 001 (2005), [hep-ph/0505142].

[469] F. Krauss, R. Kuhn and G. Soff, JHEP **02**, 044 (2002), [hep-ph/0109036].

[470] A. Pukhov, hep-ph/0412191.

[471] Minami-Tateya, H. Tanaka, M. Kuroda, T. Kaneko, M. Jimbo and T. Kon, Nucl. Instrum. Meth. **A389**, 295 (1997).

[472] J. Reuter *et al.*, hep-ph/0512012.

[473] M. Moretti, T. Ohl and J. Reuter, hep-ph/0102195.

[474] T. Gleisberg *et al.*, JHEP **02**, 056 (2004), [hep-ph/0311263].

[475] S. Tsuno, hep-ph/0501174.

[476] F. Maltoni and T. Stelzer, JHEP **02**, 027 (2003), [hep-ph/0208156].

[477] W. Kilian, (2001), LC-TOOL-2001-039.

[478] J. Alwall *et al.*, hep-ph/0609017.

[479] G. Corcella *et al.*, JHEP **01**, 010 (2001), [hep-ph/0011363].

[480] H. K. Dreiner, P. Richardson and M. H. Seymour, JHEP **04**, 008 (2000), [hep-ph/9912407].

[481] P. Z. Skands, Eur. Phys. J. **C23**, 173 (2002), [hep-ph/0110137].

[482] T. Sjostrand and P. Z. Skands, Nucl. Phys. **B659**, 243 (2003), [hep-ph/0212264].

[483] E. Norrbin and T. Sjostrand, Nucl. Phys. **B603**, 297 (2001), [hep-ph/0010012].

[484] A. Pukhov and P. Skands, (2005), FERMILAB-CONF-05-520-T.

[485] N. Ghodbane, hep-ph/9909499.

[486] D. Y. Bardin *et al.*, Comput. Phys. Commun. **133**, 229 (2001), [hep-ph/9908433].

[487] J. Wess and B. Zumino, Nucl. Phys. **B70**, 39 (1974).

[488] G. A. Blair, W. Porod and P. M. Zerwas, Eur. Phys. J. **C27**, 263 (2003), [hep-ph/0210058].

[489] American Linear Collider Working Group, T. Abe *et al.*, Resource book for Snowmass 2001, 30 Jun - 21 Jul 2001, Snowmass, Colorado.

[490] P. Bechtle, K. Desch, W. Porod and P. Wienemann, hep-ph/0511006.

[491] R. Lafaye, T. Plehn and D. Zerwas, hep-ph/0512028.

[492] S. Heinemeyer, W. Hollik, H. Rzehak and G. Weiglein, Eur. Phys. J. **C39**, 465 (2005), [hep-ph/0411114].

[493] S. P. Martin, Phys. Rev. **D72**, 096008 (2005), [hep-ph/0509115].

[494] M. Drees and S. P. Martin, hep-ph/9504324.

[495] B. C. Allanach and C. G. Lester, Phys. Rev. **D73**, 015013 (2006), [hep-ph/0507283].